NUMERICAL MODELLING IN LARGE STRAIN PLASTICITY
WITH APPLICATION TO TUBE COLLAPSE ANALYSIS

By

JOSE M. GOICOLEA RUIGOMEZ
Ing. Caminos

A Thesis submitted for the degree of
Doctor of Philosophy

In the Faculty of Engineering of the
University of London

King's College London

October 1985

ABSTRACT

Numerical methods are proposed for the analysis of 2 or 3-dimensional large strain plasticity problems. A Finite Difference program, with 2-dimensional continuum elements and explicit time integration, has been developed and applied to model the axisymmetric crumpling of circular tubes.

New types of mixed elements (Triangles-Quadrilaterals for 2-D, Tetrahedra-Bricks for 3-D) are proposed for the spatial discretization. These elements model accurately incompressible plastic flow, without unwanted "zero-energy" deformation modes or tangling over of the mesh. Elastic-plastic, rate dependent laws are modelled with a "radial return" algorithm. The transmission of heat generated by plastic work and material dependence on temperature are also included, enabling a fully coupled thermo-mechanical analysis.

A 2-D and axisymmetric computer program has been developed, implementing the numerical techniques described. Computational efficiency was essential, as large scale, costly applications were intended. An important part of the program was the contact algorithm, enabling the modelling of interaction between surfaces.

The axisymmetric crumpling of tubes under axial compression ("concertina" mode) has been analyzed Numerically. Quasi-static experiments on Aluminium tubes were modelled, using velocity scaling. Very large strains are developed in the crumpling process; with the help of tension tests, material laws valid for such strain ranges were developed. Good agreement was obtained between numerical predictions and experimental results. Modelling choices such as mesh refinement, element type and velocity scaling were studied, and found to have an important influence on the numerical predictions. Finally, a large scale impact analysis of a steel tube at 176m/s was performed. The results compared well with experiment, indicating differences with the behaviour of low velocity crumpling mechanisms.

To conclude, Finite Difference procedures with explicit time-

marching techniques are proposed for large strain plasticity problems, at low or medium impact velocities. A fairly robust code has been developed and applied successfully to a range of large strain and tube crumpling problems.

ACKNOWLEDGEMENTS

I wish to express my sincere gratitude to the following:

Dr. G.L. England who supervised this work, for his constant support and guidance throughout the period of research;

Dr. J. Marti from Principia, for his invaluable expert advice on theoretical and numerical matters, and his friendly support and suggestions;

Dr. E. Alarcon, for his help and motivation in the initial stages of work;

The staff and technicians of the Civil Engineering Department at King's College, for their help and cooperation;

My wife, Tereca Marin, for her help in the preparation of figures, and her unending patience and encouragement during the research period.

I would also like to thank the following bodies for sponsoring my research at the various stages: The British Council, The Spanish Government (Ministry of Education), Principia Mechanica Ltd. (UK), and the Committee of Vicechancellors and Principals (UK).

TABLE OF CONTENTS

BASIC NOTATION

A	Area; Mass damping coefficient (eqn. 4.56)
B	Stiffness damping coefficient (eqn. 4.56); strain-rate parameter (eqn. 4.50)
$\mathbf{B}$ (B_{ij})	Left Cauchy-Green deformation tensor (eqn. 2.12)
B_{iJ}	Gradient operator for Finite Elements (eqn. 3.6)
c	Stress wave velocity
$\mathbf{C}$ (C_{ijkl})	Constitutive tensor for Jaumann rate of Cauchy stress (eqn. 3.23)
$\mathbf{C}$ (C_{IJ})	Right Cauchy-Green tensor (eqn. 2.12)
$\mathbf{C}$	Damping matrix (eqn. 3.30)
$\underline{\mathbf{C}}$ $(\underline{C}_{ijkl})$	Constitutive tensor for Truesdell rate of Cauchy stress (sect. 3.5.2)
CST	Constant strain elements
$\mathbf{d}$ (d_{ij})	Rate of deformation tensor (eqn. 2.15)
$\mathbf{d}$ (d_i)	Penetration in contact (eqn. 4.68)
$\mathbf{D}$ (D_{IJKL})	Constitutive tensor (total Lagrangian) (eqns. 2.47, 3.21)
D	Diameter
E	Young's modulus of Elasticity
$\mathbf{E}$ (E_{IJ})	Green's strain tensor (eqn. 2.17)
F	Force; Yield function (eqn. 2.54)
$\mathbf{F}$ $(F^{I}{}_{J})$	Deformation gradient tensor (eqn. 2.7)
FD	Finite Difference (method)
FE	Finite Element (method)
G	Elastic shear modulus (eqn. 2.45)
$\mathbf{g}$ (g_{ij})	Metric tensor (eqn. 2.2)
$h,h_{\alpha},h_{\gamma},h'$	Height; Plastic hardening moduli (eqns. 4.44, 4.45)
$\mathbf{h}$ (h_i)	Heat flow rate (eqn. 2.32)
$\mathbf{I}$	Identity tensor
ID	Inner diameter
J	Jacobian of motion (eqn. 2.10)
K,$\mathbf{K}$	Stiffness, stiffness matrix (eqns. 3.10, 3.11)
L	Length
$\mathbf{l}$ (l_{ij})	Velocity gradients (eqn. 2.14)
m,M,$\mathbf{m}$,$\mathbf{M}$	Mass, mass matrices (eqn. 3.8)
MD	Mixed Discretization (sect. 4.2.2)
MTB(C)	Mixed Tetrahedra-Brick (Corrected) elements

MTQ(C) Mixed Triangles-Quadrilateral (Corrected) elements

N,n Normal vectors

n Time instant corresponding to n Δt

N Shape functions for FE (eqn. 3.5)

OD Outer Diameter

P Internal forces

q Body heat supply

r,R Radius; External force (eqn. 3.8)

R (R_{ij}) Rotation tensor (eqn. 2.11)

S,s Surface; Distance along a curve

S (S_{IJ}) 2nd Piola-Kirchhoff stress tensor (eqn. 2.25)

s (s_{ij}) Cauchy deviatoric stresses (eqn. 2.59)

t Time; Thickness

T Temperature

u Internal energy

u (u_i) Displacements

U (U_{IJ}) Right stretch tensor (eqn. 2.11)

V Volume

V (V_{ij}) Left stretch tensor (eqn. 2.11)

v,**v** (v_i) Velocity (eqn. 2.6)

w (w_{ij}) Spin tensor (eqn. 2.15)

W Work, Energy

x (x_i),
 (x,y,z) Spatial coordinates (eqn. 2.5)

X Particle (sect. 2.2.1)

X (X_I) Lagrangian coordinates (eqn. 2.4)

X Vector product (eqn. 2.30)

Y Yield stress

α Thermal expansion coefficient; Back stress (eqn. 2.61);
 Mixed Discretization correction coefficient (eqn. 4.19)

β Proportion of critical damping; Radial return coefficient
 (eqn. 4.32)

γ Plastic flow arbitrary multiplier (eqn. 2.55)

Δ Increment

δ_{ij} Kronecker delta

ϵ^p Effective plastic strain (eqn. 2.60b)

$\epsilon(\epsilon_{ij})$ Small strain tensor (eqn. 2.43)

λ Lame's Elastic constant

μ Coefficient of Coulomb friction (eqn. 7.11)

ν	Poisson's ratio
ρ	Mass density; Radius of curvature
θ	Angular coordinate
$\sigma\ (\sigma_{ij})$	Cauchy stress tensor (eqn. 2.24)
∂	Partial derivative
$\emptyset_t^*, \emptyset_{t*}$	Pull-back, push-forward of tensors (eqns. 2.21, 2.22)
χ	Mesh coordinates (sect. 3.4)
ω	Angular frequency

CHAPTER 1

INTRODUCTION

1.1 OBJECTIVES

1.2 NON-LINEAR MODELLING

1.3 LAYOUT

1.1 OBJECTIVES

This work consists of a theoretical part (mathematical and numerical models, chapters 2-4), and a practical part (applications and numerical simulation of large strain tube collapse analysis, chapters 5-7).

The motivation for the theoretical part of the work lies in the author's interest in non-linear solid mechanics modelling, understood broadly as encompassing the following phenomena:

- large strains and large displacements (geometric nonlinearities);

- plastic and viscoplastic behaviour (material nonlinearities);

- contacts and impact (nonlinear boundary conditions);

- thermomechanical coupling.

On the practical side, the source of motivation was the research program on tube collapse mechanisms being carried out at the Civil Engineering department of King's College, University of London (Andrews, England and Ghani, 1983). Such mechanisms are efficient energy dissipating systems (Johnson and Reid, 1978), for use in impact situations. Additionally, tubes are frequent structural components for aerospace vehicles and other equipment or components which may suffer accidental collisions.

The objective of this work was the development of numerical methods of simulation for nonlinear analysis, capable of modelling tube collapse mechanisms. More specifically, the attention was restricted to collapse through axisymmetric sequential folding (Concertina mode). Numerical predictions for tube collapse should be obtained and compared to experimental results, available from previous work on aluminium tubes by Ghani (1982). This objective posed some important challenges, such as the development of a numerical model for large strains and large displacements, with elastic-plastic behaviour, capable of modelling arbitrary tube-tube and tube-platen contacts (chapters 2, 3, 4). Reliable data would have to be obtained for the

TIME = 0.00 ms

TIME = 0.77 ms

TIME = 1.37 ms

TIME = 2.09 ms

TIME = 2.93 ms

TIME = 3.62 ms
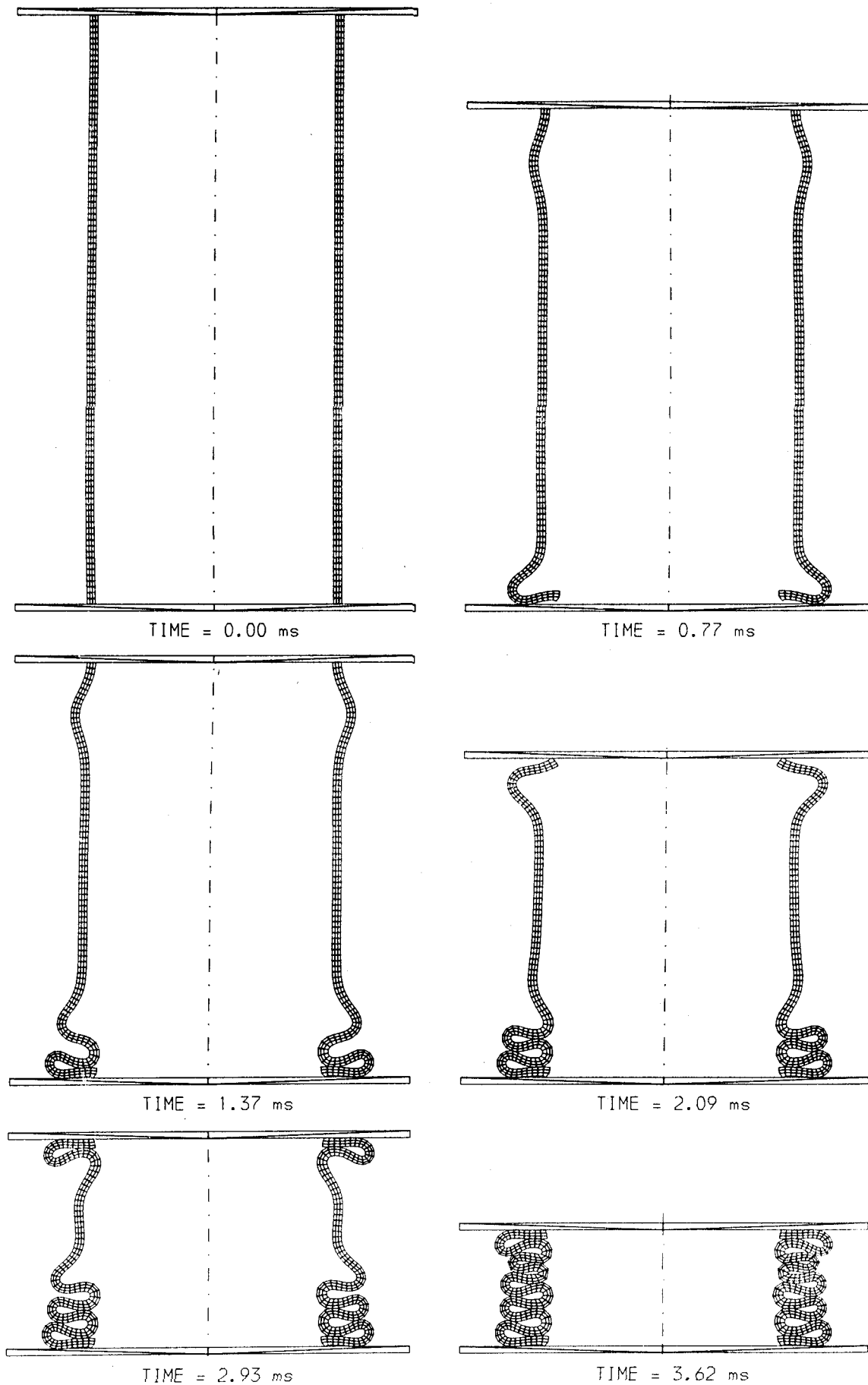
Figure 1.1: TYPICAL RESULTS FOR AXISYMMETRIC TUBE COLLAPSE ANALYSIS
OD=38.1mm, t_o=1.22mm, L=88.9mm – TUBE9, GEOMETRY F (SEE TABLE 7.4)

constitutive behaviour of the Aluminium at large strains (chapter 6).

With this objective in mind, a Finite Difference method with explicit time integration was chosen. The method uses a Finite Element topology, and can therefore be applied to irregular meshes in arbitrary continua. An efficient contact logic was essential for the success of the simulations. A typical example of the results obtained is shown in figure 1.1.

1.2 NON-LINEAR MODELLING

Within the past decade there has been considerable interest in nonlinear solid mechanics simulations, due to the great problem-solving power available from the new generations of digital computers. The possibility of detailed solutions for highly complex non-linear problems has occassioned renewed interest and pressure for powerful mathematical descriptions and numerical techniques which implement them efficiently.

In many aspects of non-linear numerical modelling, choices are available: explicit or implicit time integration, Lagrangian or Eulerian meshes, total Lagrangian or Cauchy stress formulations. Each of these choices has its own advantages and drawbacks. On the other hand, non-linear mechanics is a field under constant development, and new approaches are being explored which attempt to combine efficiently the advantages of different techniques (e.g. Element By Element method, Arbitrary Lagrangian Eulerian descriptions).

The procedure chosen for this work (Explicit Finite Difference) is ideally suited for steeply non-linear, short duration transient phenomena (wave propagation type problems). A natural application is for impact scenarios, e.g. the missile impact tests done at UKAEA Winfrith reported by Barr (1983a) (sect. 7.4). Explicit Finite Difference techniques are also useful for slow loading phenomena, in order to take advantage of the non-linear robustness and capabilities, through the use of velocity scaling or dynamic relaxation (chapters 4, 6, 7).

1.3 **LAYOUT**

In chapter 2 a number of essential solid mechanics concepts are introduced and discussed briefly. Non-linear numerical models and techniques to implement those concepts into numerical codes are reviewed in chapter 3. The Explicit Finite Difference model and computer code developed here are described in chapter 4, while chapter 5 contains some validation examples which test the main aspects of the formulation. Chapter 6 concerns the derivation of a material constitutive law for Aluminium alloy through tensile tests, with some applications to the numerical simulation of the tensile tests themselves. Chapter 7 contains applications to tube collapse analysis, comparing the results with experimental data for quasi-static collapse of Aluminium tubes. The constitutive law from chapter 6 is used for the numerical predictions. An analysis for a medium velocity (176 m/s) tube impact is also described. Finally, conclusions and some suggestions for further work are given in chapter 8.

CHAPTER 2

CONTINUUM MECHANICS DESCRIPTIONS

2.1 INTRODUCTION

2.2 KINEMATICS

2.2.1 Configurations

2.2.2 Deformation tensors

2.2.3 Deformation and spin rates

2.2.4 Strains

2.2.5 Transformations

2.3 STRESS

2.3.1 Cauchy

2.3.2 Piola-Kirchhoff

2.4 BALANCE LAWS

2.4.1 Balance of mass

2.4.2 Balance of momentum

2.4.3 Balance of energy

2.5 CONSTITUTIVE RELATIONS

2.5.1 Rate equations

2.5.2 Elasticity

   2.5.2.1 Hyperelastic materials

   2.5.2.2 Hypoelastic materials

2.5.3 Plasticity

   2.5.3.1 Von Mises model

   2.5.3.2 Other plasticity models

2.1 **INTRODUCTION**

The advances made in digital computing within the last decades have opened up new fields for engineers and scientists. Problems previously regarded as unsolvable, only approached through experiments and simplified empirical formulae, can now be analyzed numerically in great detail. In the field of continuum mechanics this has greatly increased the interest in detailed mathematical descriptions, amenable *to be used in numerical models with discretization techniques (e.g.* Finite Element or Finite Difference methods).

Having said this, there still exists a certain degree of confusion in the specialist literature. On the part of the mathematicians, rigorous mechanical descriptions are often presented in ways difficult to be grasped by engineers and implemented in numerical production codes. As a result, many engineers still cling on to outdated and much less powerful notations. On the other hand, *theoretical presentations are not unique,* causing some degree of confusion to researchers first approaching seriously these topics.

An effort has been made in this chapter to present a brief overview of certain continuum mechanics concepts, indispensable in a rigorous treatment, without unnecessary mathematical fuss. The purpose of this exposition is:

- to introduce the nomenclature and definitions of concepts used in later chapters;

- to discuss the significance of and interpret some concepts with a view to numerical modelling (basis of this work);

- to ensure certain completeness for the ideas presented in this thesis.

It must be stressed, however, that this exposition does not pretend to be complete. Only the concepts which are relevant for the rest of this thesis will be dwelt upon. In particular, emphasis is laid on solid mechanics and elastic-plastic behaviour. A number of results will be presented without proof. For a more complete

discussion of these topics, the interested reader is referred to Fung (1965), Malvern (1969), and Billington and Tate (1981) for the general concepts, and to Marsden and Hughes (1983) for a more detailed and up-to-date mathematical description.

In the following presentation, the ambient space is assumed to be an Euclidean point space (i.e. interior product defined), and where necessary this will be particularized to R^3. The coordinate bases may be curvilinear and arbitrary, although when equations are given in component form, often orthonormal bases (not necessarily cartesian) are assumed for simplicity. The usual conventions for tensor notation are employed: repeated indices indicate summation over their range unless explicitly stated, and commas indicate covariant derivatives. Vectors and tensors are represented by boldface characters. Superposed dots indicate material time derivatives.

Given two tensors **A** and **B** the product **AB** is understood to be contracting the near indices with opposite variance:

$$(\mathbf{AB})^{ij} = A^{ik}B_k{}^j \qquad\qquad (2.1)$$

If the indices have the same variance, e.g. both are contravariant, the metric tensor **g** is necessary to lower one:

$$(\mathbf{AB})^{ij} = A^{ik}g_{kl}B^{lj} = A^{ik}B_k{}^j \qquad\qquad (2.2)$$

When the tensor components are referred to orthonormal bases the vertical position of the indices is irrelevant, as the metric tensor is unity.

A colon indicates doubly contracted product:

$$\mathbf{A:B} = A^{ij}B_{ij} \qquad\qquad (2.3)$$

2.2 KINEMATICS

A body (or continuum) is a set whose elements, called material particles, have a one-to-one correspondence with a region V of the

Euclidean point space. The following kinematics concepts are intended
to provide a description of the motion of deformable bodies.

2.2.1 CONFIGURATIONS

Each particle X of the body B may be identified by its position **X**
in the $\underline{\text{original configuration}}$, V_0, which is taken as reference:

$$\textbf{X} = k(X) \tag{2.4}$$

X (components X^I) are called Material or Lagrangian coordinates of the
particle. The motion of the body at a later time is given by the time-
dependent positions **x** of the particles in the $\underline{\text{current configuration}}$,
V:

$$\textbf{x} = \textbf{x}(\textbf{X},t) \tag{2.5}$$

x (components x^i) are the spatial or Eulerian coordinates. Hereafter
upper case indices shall refer to Lagrangian coordinates, and lower
case to Eulerian. The velocities are defined as

$$\textbf{v} = \dot{\textbf{x}} \tag{2.6}$$

where the dot signifies a material time derivative, i.e. following the
particle X.

2.2.2 DEFORMATION TENSORS

Central to deformation measurements is the deformation gradient
tensor:

$$\textbf{F} = \partial\textbf{x}/\partial\textbf{X} \tag{2.7}$$

with components $F^i{}_I = x^i{}_{,I}$.

The tensor **F** is used as the base for a number of strain and
deformation measures. An element of a curve d**X** is transformed by

$dx = FdX$. The inverse of F gives the spatial gradients of the material coordinates:

$$F^{-1} = \partial X/\partial x$$

$$((F^{-1})^I{}_i = X^I{}_{,i})$$

(2.9)

F constitutes a two-point tensor. Another interpretation that relates F to transformations between configurations is given in section 2.2.5.

The Jacobian of the motion is

$$J = \det(F) \tag{2.10}$$

The polar decomposition of F gives

$$F = RU = VR \tag{2.11}$$

where R is an orthogonal (rotation) tensor, $RR^T = I$. U and V are positive definite, and are called the right and left stretch tensors respectively. Equations (2.11) represent two ways to visualize the deformation: first stretching (U) and then rotating (R), or first rotating (R) and then stretching (V)

Other deformation measures are the Cauchy-Green tensors:

$$C = F^T F \qquad \text{(right Cauchy-Green)}$$

(2.12)

$$B = FF^T \qquad \text{(left Cauchy-Green)}$$

The length of an element of curve is given by $ds^2 = dx\,dx$ in the current configuration, and $dS^2 = dX\,dX$ in the original configuration. The significance of C and B is given by the relations

$$ds^2 = dX\,C\,dX$$

(2.13)

$$dS^2 = dx\,B^{-1}\,dx$$

2.2.3 DEFORMATION AND SPIN RATES

The spatial velocity gradient tensor is defined as:

$$\mathbf{l} = \partial\mathbf{v}/\partial\mathbf{x} \tag{2.14}$$

$$(\mathbf{l}^i{}_j = \mathbf{v}^i{}_{,j})$$

which can be decomposed into symmetric and skew-symmetric parts:

$$\mathbf{d} = (\mathbf{l}+\mathbf{l}^T)/2$$

$$\tag{2.15}$$

$$\mathbf{w} = (\mathbf{l}-\mathbf{l}^T)/2$$

These are called the rate of deformation (or velocity strain) and spin rate tensors respectively. The rate of change of length of an element of curve is given by

$$d\dot{s} = (d\mathbf{x}d d\mathbf{x})/ds \tag{2.16}$$

2.2.4 STRAINS

A measure of the total strain is given by the Green strain tensor, defined as

$$\mathbf{E} = (\mathbf{C} - \mathbf{I})/2 \tag{2.17}$$

where $\mathbf{I}$ is the Identity tensor. It is trivial to see that

$$ds^2-dS^2 = 2d\mathbf{X}\mathbf{E}d\mathbf{X} \tag{2.18}$$

and that the rate of $\mathbf{E}$ is given by

$$\dot{\mathbf{E}} = \mathbf{F}^T\mathbf{d}\mathbf{F} \tag{2.19}$$

2.2.5 TRANSFORMATIONS

For the tensors defined above, some of the indices refer to the original configuration (upper case), while others are related to the current configuration (lower case). Here some transformation laws are given to find the corresponding tensor in the alternative configuration.

Although the transformed tensors will be considered as different tensorial entities, one way to visualize the transformation is as a mere change of base. Imagine a base $(O, \mathbf{e}_i)$ fixed in space throughout the motion, and another base $(O'(t), \mathbf{e}'_i(t))$ which deforms and translates with the body. In this convected curvilinear base, the coordinates of a material point remain constant throughout the motion, and equal to the material coordinates, X^I. The spatial components of F provide the matrix for the change of coordinates between the two bases. Given a 2nd order contravariant tensor $\mathbf{a}$ by its convected material components, $\underline{a}^{IJ}$, the spatial components are

$$a^{ij} = (\partial x^i / \partial X^I)(\partial x^j / \partial X^J)\underline{a}^{IJ} \tag{2.20}$$

Hence F provides a means for transforming between spatial and material coordinates. a^{ij} and $\underline{a}^{IJ}$ are the components in different bases of the same tensor, $\mathbf{a}$. If now one assumes components $\underline{a}^{IJ}$ to apply to the spatial basis, a new tensor is obtained:

$$\mathbf{A} = \underline{a}^{IJ} \, \mathbf{e}_I \otimes \mathbf{e}_J \tag{2.21a}$$

where $\otimes$ signifies a tensorial product. $\mathbf{A}$ is called the **pull-back** of $\mathbf{a}$, and may be obtained as

$$\mathbf{A} = F^{-1}\mathbf{a}F^{-T} = \emptyset_t^*(\mathbf{a}) \tag{2.21b}$$

while the **push-forward** is defined by the inverse relation:

$$\mathbf{a} = \emptyset_{t*}(\mathbf{A}) = F\mathbf{A}F^T \tag{2.22}$$

These relations may be trivially generalized to tensors of any rank.

Elements of area and volume in reference and current configurations are transformed by the following transport formulae:

$$nda = JF^{-T}NdA \qquad (2.23a)$$

$$dv = JdV \qquad (2.23b)$$

These relations may be used to express integral balance laws (sect. 2.4) in either configuration. Eqn. (2.23a) conditions the form of the Piola transformations for the stress tensor (eqn. 2.25)

2.3 STRESS

2.3.1 CAUCHY

The concept of stress rests upon the Cauchy postulate that the action of the rest of the material upon any volume element of it is of the same form as distributed surface forces. A traction vector **t**(**n**) may be defined at each point, as the force exerted per unit infinitesimal area, for each orientation **n**.

Applying equilibrium considerations, it may be deduced that a stress tensor σ must exist, such that for every orientation **n**

$$\mathbf{t}(\mathbf{n}) = \mathbf{n}\,\sigma \qquad (2.24)$$

σ is called the Cauchy or true stress tensor, and it is related to the current configuration.

2.3.2 PIOLA-KIRCHHOFF

If both the force and the area components of the concept of stress are transformed back into the original configuration, a new stress tensor is obtained:

$$S = JF^{-1}\sigma F^{-t} = J\emptyset_t^{*}(\sigma) \qquad (2.25)$$

This relation is called the backward Piola transformation. It defines the 2nd Piola-Kirchhoff stress tensor **S**, which is a stress measure referred to the original configuration.

2.4 BALANCE LAWS

Balance laws (mass, momentum, angular momentum, and energy) may be stated alternatively in integral form or as field equations. Integral forms provide "weaker" expressions for the same principles. This will be commented further in section 4.3.

2.4.1 BALANCE OF MASS

Conservation of mass implies that the mass of the material ocupying a certain region V of the body remains constant throughout the motion:

$$(d/dt)\int_V \rho dV = 0 \qquad (2.26)$$

where ρ is the mass density.

As a field equation, balance of mass is expressed by the continuity equation:

$$\dot{\rho} + \rho \text{div}(\mathbf{v}) = 0 \qquad (2.27)$$

2.4.2 BALANCE OF MOMENTUM

For a region V of the body with boundary S, the integral form of the equation of linear momentum balance is

$$(d/dt)\int_V \rho \mathbf{v} dV = \int_V \rho \mathbf{f} dV + \int_S \mathbf{n}\sigma dS \qquad (2.28)$$

where **f** is the body force per unit mass. The corresponding

differential expression is Cauchy's equation of motion,

$$\rho \dot{\mathbf{v}} = \text{div}(\sigma) + \rho \mathbf{f} \tag{2.29}$$

The integrals in eqn. (2.28) involve vectors, and as pointed out by Marsden and Hughes (1978), may not provide a covariant statement of the momentum balance principle in a general manifold. However, for the Euclidean space to which this exposition refers, the objection is not relevant. The integral expression is better suited for finite difference numerical models (section 4.3), for which weak variational global expressions (as employed in Finite Elements) are not obtained.

Taking moments in eqn. (2.28) with respect to the origin, the balance of angular momentum is expressed by

$$(d/dt)\int_V \rho(\mathbf{x}\mathbf{X}\mathbf{v})dV = \int_V \rho(\mathbf{x}\mathbf{X}\mathbf{f})dV + \int_S \mathbf{x}\mathbf{X}(\mathbf{n}\,\sigma)dS \tag{2.30}$$

where $\mathbf{x}\mathbf{X}\mathbf{v}$ denotes vector product of $\mathbf{x}$ and $\mathbf{v}$. The corresponding field equation states simply the symmetry of σ:

$$\sigma = \sigma^T \tag{2.31}$$

Symmetry of S may be deduced from eqns. (2.25) and (2.31).

2.4.3 BALANCE OF ENERGY

In a continuum, the first law of thermodynamics may be expressed as

$$(d/dt)\int_V \rho u\,dV = \int_V (\rho q + \sigma : d)dV + \int_S \mathbf{h}\mathbf{n}\,dS \tag{2.32}$$

where u is the internal energy per unit mass
q is the rate of body heat supply per unit mass
h is the heat flux vector; for an oriented infinitesimal area
the heat flow rate is given by H = $\mathbf{h}\mathbf{n}$dS

The corresponding field equation is

$$\rho \dot{u} = \sigma{:}d + \rho q + \text{div}(h) \qquad (2.33)$$

The term $\sigma{:}d$ represents the stress work per unit volume and time. σ and d are said to be conjugate stress and strain measures. An alternative representation of the energy balance principle involves the use of S and $\dot{E}$, also conjugate:

$$\rho_o \dot{u} = S{:}\dot{E} + \rho_o q + \frac{\rho_o}{\rho}\, \text{div}(h) \qquad (2.34)$$

2.5 CONSTITUTIVE RELATIONS

The balance laws provide a set of equations which are not sufficient to determine the behaviour of a material body. Some further equations are necessary, stating the relation between kinematic and dynamic variables (constitutive equations).

Constitutive equations are based on judgement, a-priori knowledge of how the material behaves. However, certain general principles must be satisfied in their formulation. For our purpose, the most important principle is that of objectivity, which states that constitutive equations must be invariant under changes of reference frame, in order to represent the material behaviour objectively.

For a homogeneous material it may be seen (Billington and Tate, 1981), that an objective relation between Cauchy stress and deformation takes the form:

$$\sigma = R\; p(C^t(s), T^t(s))\; R^T \qquad (2.35)$$

where R is the rotation tensor (eqn. 2.11) and T the temperature. The notation $C^t(s)$ signifies the history of C (eqn. 2.12) from $-\infty < s < t$. Note that in general the complete history of the deformation C (or of E equivalently, eqn. (2.17)) are required, while for R only the instantaneous current value is used, for rotating the stresses.

The second Piola-Kirchhoff stress S is objective as such (being related to a fixed reference configuration). In terms of it eqn.

(2.35) may be rephrased as

$$S = \varrho(C^t(s), T^t(s))$$ (2.36)

The advantage of using the 2nd Piola-Kirchhoff stress tensor for total formulations is evident (see also sect. 3.5.1).

Some types of Elastic and Plastic rate equations are discussed below. For simplicity, attention is centred on the isothermal case.

2.5.1 RATE EQUATIONS

Materials without memory or with smooth memory may be described with rate equations, e.g.

$$\overset{o}{\sigma} = g(\mathbf{d}, \sigma, \mathbf{F})$$ (2.37)

where $\overset{o}{\sigma}$ is a stress rate which is objective for rigid body rotations. The choice of objective rate is not unique. A variety of options are available, the two most widely used being the Jaumann rate

$$\overset{\triangledown}{\sigma} = \dot{\sigma} + \sigma \mathbf{w} + \mathbf{w}^\mathsf{T}\sigma$$ (2.38)

and the Truesdell rate,

$$\overset{o}{\sigma} = \dot{\sigma} - \sigma \mathbf{l}^\mathsf{T} - \mathbf{l}\sigma + \sigma\,\mathrm{tr}(\mathbf{l})$$ (2.39)

In equation (2.37) $\overset{o}{\sigma}$ provides the constitutive part of the stress increment. Eqns. (2.38) or (2.39) define the remaining terms that must be added for objectivity. Formulations based on either objective rate may be made equivalent by adjusting the constitutive law, g. However, if g is postulated a-priori, independently of the choice of objective rate, both formulations give rise to different constitutive behaviour.

The need for special objective rates is avoided if the equations are formulated in a material setting, e.g.

$$\dot{S} = \underline{g}(E, \dot{E}, S) \tag{2.40}$$

$\dot{S}$ is the material time rate of a tensor on the current configuration (2nd Piola-Kirchhoff), which is already objective.

2.5.2 ELASTICITY

Elastic materials are those for which a natural, stress-free state exists, to which the body returns upon removal of all external forces. The stress depends on the deformation from this natural state:

$$S = f(\mathbf{C}, t) \tag{2.41}$$

A perfect memory of the natural state, with no memory of intermediate states, is exhibited.

For linear elasticity and small strains the relation is as follows:

$$\sigma = \mathbf{c} : \epsilon \tag{2.42}$$

(in component form $\sigma^{ij} = c^{ij}{}_{kl} \epsilon^{kl}$)

$\mathbf{c}$ is termed the elasticity tensor, and ϵ is the small strain tensor:

$$\epsilon_{ij} = (u_{i,j} + u_{j,i})/2 \tag{2.43}$$

where $\mathbf{u}$ are displacements. For isotropic materials, and provided σ and ϵ are both symmetric, $\mathbf{c}$ must take the form

$$c_{ijkl} = \lambda \delta_{ij} \delta_{kl} + 2G \delta_{ik} \delta_{jl} \tag{2.44}$$

where λ and G are called Lame's constants. This gives rise to the classic generalized Hooke's law:

$$\sigma_{ij} = \lambda \epsilon_{kk} \delta_{ij} + 2G \epsilon_{ij} \tag{2.45}$$

2.5.2.1 HYPERELASTIC MATERIALS

The concept of Hyperelasticity was introduced by Green and given its present name by Truesdell (e.g. Truesdell and Toupin, 1960). It postulates the existence of a strain-energy function from which the stresses may be derived as

$$S = \rho_0 \, (\partial W / \partial E) \tag{2.46}$$

Assuming the necessary differentiability, the elasticity tensor is defined as

$$D = \rho_0 \, (\partial^2 W / \partial E^2) \tag{2.47}$$

and a rate equation may be written as

$$\dot{S} = D : \dot{E} \tag{2.48}$$

(in component form $\dot{S}^{IJ} = D^{IJ}{}_{KL} \dot{E}^{KL}$)

For a constant value of D, a linear hyperelastic total equation is obtained:

$$S = D : E \tag{2.49}$$

2.5.2.2 HYPOELASTIC MATERIALS

The term Hypoelastic, also introduced by Truesdell (Truesdell and Toupin, 1960), characterizes a material for which the behaviour is defined in the current configuration by an incrementally linear relationship of the form:

$$\overset{\circ}{\sigma} = c : d \tag{2.50}$$

(in component form $\overset{\circ}{\sigma}{}^{ij} = c^{ij}{}_{kl} d^{kl}$)

An objective stress rate must be used for eqn. (2.50) (see section

2.5.1).

Hypoelastic behaviour is very convenient for descriptions based on the current configuration. Material data based on true stress - natural strain relationships (see section 6.1) give rise naturally to hypoelastic interpretations.

For isotropic materials eqn. (2.50) takes the form

$$\overset{\circ}{\sigma} = \lambda \text{tr}(\mathbf{d})\mathbf{I} + 2G\mathbf{d} \qquad (2.51)$$

(in orthonormal components $\overset{\circ}{\sigma}_{ij} = \lambda d_{kk} \delta_{ij} + 2G d_{ij}$)

2.5.3 PLASTICITY

For most solids, behaviour may be assumed elastic only within a certain stress range. Beyond the elastic range yield occurs, deformations being characterized by permanent changes occasioned by slip or dislocations at the atomic level (Plastic flow).

After yield, Elastic and Plastic deformations are assumed to happen concurrently (Elastic-Plastic materials). More restrictive idealizations are provided by rigid-plastic models (only plastic deformations). An additive decomposition of the rate of deformation is assumed here:

$$\mathbf{d} = \mathbf{d}^e + \mathbf{d}^p \qquad (2.52)$$

where superindices e and p indicate elastic and plastic components respectively. Additive decomposition of strains in this fashion was proposed by Hill (1950). Lee (1969) has proposed a multiplicative decomposition of deformation gradients instead, $F = F^e F^p$, while Green and Naghdi (1965) have advocated an additive decomposition of total strain, $E = E^e + E^p$.

Classical plasticity is formulated in terms of the current configuration (Hill, 1950). Hence the popularity of an additive decomposition of the rates of deformation, eqn. (2.52), coupled with

hypoelastic behaviour, for Elastic-Plastic material descriptions (e.g. Wilkins (1964), Hibbit, Marcal and Rice (1970)). In this case

$$\overset{\circ}{\sigma} = \mathbf{c}:\mathbf{d}^e = \mathbf{c}:(\mathbf{d}-\mathbf{d}^p) \qquad (2.53)$$

The yield criterion determines the limit of the elastic range:

$$F(\sigma,\mathbf{Q}) = 0 \qquad (2.54)$$

where $\mathbf{Q}$ is a set of plastic hardening parameters. For $F<0$ the material behaves elastically. Two additional sets of relations must be provided to determine fully the stress-strain behaviour:

- Flow rule $\qquad \mathbf{d}^p = \dot{\gamma}\mathbf{R}(\sigma,\mathbf{Q}) \qquad (2.55a)$

- Hardening rule $\qquad \overset{\circ}{\mathbf{Q}} = \dot{\gamma}\mathbf{H}(\sigma,\mathbf{Q}) \qquad (2.55b)$

where γ is an arbitrary multiplier, whose value is determined from the simultaneous solution of eqns. (2.54), (2.55). An objective rate $\overset{\circ}{\mathbf{Q}}$ must be used in eqn. (2.55b).

Drucker (1951) postulated a criterion for stable work-hardening materials. This involves the work done by a set of self-equilibrating forces, requiring:

$$\dot{\sigma}:\mathbf{d} > 0 \qquad (2.56a)$$
$$\sigma:\mathbf{d}^p \geqslant 0 \qquad (2.56b)$$

The equal sign in (2.56b) holds for perfectly plastic materials (no hardening). A consequence of Drucker's postulate is the associativity of plastic flow: for a smooth part of the yield surface,

$$\mathbf{d}^p = \dot{\gamma}(\partial F/\partial\sigma) \qquad (2.57)$$

which in a nine-dimensional stress space may be interpreted as the normality of d^p to the surface $F(\sigma,\mathbf{Q})$.

2.5.3.1 VON MISES MODEL

Particularly useful and simple models are derived from the yield criterion of Von Mises (1913). This may be written as

$$F = (3/2)s:s - Y^2 = 0 \qquad (2.58)$$

where s are the deviatoric Cauchy stresses,

$$s = \sigma - (1/3)tr(\sigma)I \qquad (2.59a)$$

(in orthonormal components, $s_{ij} = \sigma_{ij} - (1/3)\sigma_{kk}\delta_{ij}$ (2.59b)

Y is the yield strength of the material, which coincides with the yield stress in uniaxial tension (see section 6.1). The Von Mises yield condition is independent of volumetric stresses, which are assumed to behave elastically.

An isotropic hardening model is obtained by making Y a function of the effective plastic strain, ϵ^p:

$$Y = Y(\epsilon^p) \qquad (2.60a)$$

with $\epsilon^p = \int d\epsilon^p = \int\sqrt{(2/3)d^p: d^p}\ dt$ (2.60b)

A more general hardening model, incorporating Bauschinger effect, may be obtained by combining isotropic hardening with the kinematic hardening proposed by Prager (1956) and Ziegler (1959), giving the yield condition

$$F = (3/2)(s-\alpha):(s-\alpha) - Y^2 \qquad (2.61)$$

α is called the back-stress and represents a kinematic hardening parameter (translation of the Von Mises circle). The associative flow rule is

$$d^p = \dot{\gamma}(s-\alpha) \qquad (2.62)$$

and the hardening laws.

$$\overset{\circ}{\alpha} = (2/3)h_\alpha \dot{p} \qquad\qquad (2.63a)$$

$$\dot{Y} = h_Y \dot{\epsilon}^p \qquad\qquad (2.63b)$$

Imposing the consistency condition ($\dot{F}$ = 0) during loading, and combining eqns. (2.51), (2.53), (2.61)-(2.63), the stress-strain relation is found to be

$$\overset{\circ}{\sigma} = \mathbf{c}:[\mathbf{d} - (\mathbf{s}-\alpha)(3/2)\mathbf{d}:(\mathbf{s}-\alpha)/Y^2(1+h'/3G)] \qquad (2.64)$$

where $h' = h_Y + h_\alpha$ (plastic modulus). Purely isotropic hardening is obtained with $h_\alpha = 0$, and purely kinematic with $h_Y = 0$.

In a uniaxial test, law (2.64) will provide an Elastoplastic hardening modulus of

$$h = 1/[1/E + 1/h'] \qquad\qquad (2.65)$$

where $E = G(3\lambda+2G)/(\lambda+G)$ (Young's modulus of elasticity).

2.5.3.2 OTHER PLASTICITY MODELS

Plasticity in soils is generally considerably more complicated than the above Von Mises model. Pressure dependent yield, anisotropy, dilatation and non-associativity, hysteretic cyclic behaviour, pore pressure, are important features for soil plasticity. An excellent review of this topic has been given by Marti and Cundall (1980).

The mathematical theory of plasticity is a field still under development. Very refined phenomenological models have been proposed (e.g. Mroz (1967), Prevost (1978)). These models are based on multiple-surface idealizations. They provide elaborate stress-strain laws requiring considerable computational cost for numerical modelling, thus in practice they are hardly used. This fact has been acknowledged by Ortiz and Popov (1983), who propose simpler, one-surface models for metal plasticity.

Finally, a principle to be held present when choosing a plasticity model, is that it can only be as reliable and as sophisticated as the experimental information on which the determination of the model parameters is based. For example, there is little point in using anything other than a Von Mises isotropic hardening model in a metal, if all the information available is a uniaxial stress-strain law. On the other hand, the added complication of some models may not be necessary if the loading is mainly monotonic.

CHAPTER 3

NONLINEAR NUMERICAL MODELS FOR SOLID MECHANICS

3.1 INTRODUCTION

3.2 FINITE DIFFERENCE METHODS

3.3 FINITE ELEMENT METHODS

3.4 MESH DESCRIPTIONS

    3.4.1 Lagrangian

    3.4.2 Eulerian

    3.4.3 Arbitrary Lagrangian-Eulerian

3.5 LARGE DISPLACEMENT FORMULATIONS

    3.5.1 Total Lagrangian

    3.5.2 Cauchy stress - velocity strain

    3.5.3 Updated Lagrangian

3.6 TIME INTEGRATION

    3.6.1 Central difference (explicit)

    3.6.2 Trapezoidal rule (implicit)

    3.6.3 Operator split methods

3.7 PRACTICAL CONSIDERATIONS FOR DISCRETE MESHES

    3.7.1 "Locking up" for incompressible flow

    3.7.2 "Hourglassing"

3.8 CONCLUSIONS

3.1 INTRODUCTION

The Governing equations in solid mechanics are the equations of motion, which can be written in component form as

$$\sigma_{ij,j} + \rho(f_i - \ddot{u}_i) = 0 \qquad (3.1)$$

where σ_{ij} is the Cauchy stress tensor, ρ the mass density, f_i are body forces per unit mass (typically gravity), and u_i displacements. These equations originate from the balance of momentum principle (section 2.4.2). This principle may be stated alternatively in integral form (eqn. 2.28).

The partial differential eqns. of motion (3.1) depend upon 3 space and 1 time variables. The numerical models described here perform independent semidiscretizations in space and time. First eqns. (3.1) are discretized in space, yielding a system of ordinary differential eqns. in time. These are then integrated with a time-stepping procedure.

The discretization of the continuum may be achieved either with Finite Element (FE) or Finite Difference (FD) methods. Both methods have had separate historical developments, although some degree of convergence has been reached lately in the literature (e.g. Belytschko, 1983). The theoretical principles for both methods are different: local truncation errors for FD, global error norms for FE. However, FE methods are also based on independent shape functions for each element. As a result, FE and FD formulations often produce equivalent algorithms (e.g. Kunar and Minowa, 1981).

Other numerical methods need only a discretization in the boundary: the Boundary Element Methods (BEM). These were first proposed for solid mechanics by Rizzo (1967) and Cruse (1969). Considerable advantage can be gained by the reduction and simplification of the discretization. For nonlinear problems, however, BEM lose much of their appeal. Volume integrals appear which require an additional discretization of the continuum (e.g. Garcia, 1981). For this reason BEM will not be reviewed here.

Time integration may be performed either by modal analysis methods or by direct integration (time-marching). Modal analysis requires transformations into the frequency domain which are only valid in a linear regime, for which reason they must be ruled out for nonlinear models. As to time-marching procedures two main alternatives exist, explicit or implicit methods. Both have advantages and disadvantages, which will be reviewed briefly in this chapter. Recent alternative procedures based on operator splitting methods will also be considered.

3.2 FINITE DIFFERENCE METHODS

Finite Difference methods have been used for a long time by engineers within relaxation procedures (e.g. Southwell, 1940). Finite Difference operators provide local approximations for a system of coupled differential equations. Due to this fact, a one-step global solution is not possible and recourse must be made to relaxation and iterative techniques. Additionally, FD methods have been associated normally with regular zoning (at least topologically regular). For these two reasons, FD methods were eclipsed by the Finite Element boom in the 1960's for structural and solid mechanics applications. FD has always been popular, however, in other areas such as Eulerian fluid mechanics (e.g. Nichols, Hirt, and Hotchkiss, 1980).

For a regular mesh with "I" and "J" lines along the two coordinate directions, standard finite difference approximations for the gradient of a vector u are given by:

$$u_{i,1}^{I+1/2,J+1/2} = \frac{1}{\Delta x_1} (u_i^{I+1,J+1/2} - u_i^{I,J+1/2})$$

$$u_{i,2}^{I+1/2,J+1/2} = \frac{1}{\Delta x_2} (u_i^{I+1/2,J+1} - u_i^{I+1/2,J}) \tag{3.2}$$

Eqns. (3.2) require the mesh to be topologically and geometrically regular.

The use of contour integral formulas (Wilkins, 1964) allows the application of FD approximations to topologically and geometrically irregular meshes. The basic idea is to employ Gauss' theorem in order

to express the gradient of a field in a cell in terms of a contour integral. Considering cell V^E enclosed by contour S^E, and the gradient of the displacement vector **u**,

$$\int_{V^E} u_{i,j} dV = \int_{S^E} u_i n_j dS \qquad (3.3)$$

If the gradient is assumed constant in the cell, then

$$u_{i,j} = \frac{1}{V^E} \int_{S^E} u_i n_j dS \qquad (3.4)$$

The contour integral may be evaluated assuming a linear variation of u along the edge of the cell.

Contour integrals may be used for any 2-D polygon or 3-D polyhedron, to interpolate a value for the gradient at the centre of the cell, knowing the values at the corner nodes. For the particular cases of triangles and tetrahedra, an alternative technique is available (e.g. Marti, 1981), in which the gradients are interpolated directly by inverting the spatial finite difference equations. This technique has been followed in the present work, and will be detailed in section 4.2.1.

For explicit time-marching models the semi-discrete equations of motion become uncoupled. This means that only local approximations to the partial differential equations (3.1) are performed within each time-step, no iterations being needed for a FD operator. Such a fact was exploited in the development of the first FD "Hydrocodes" at the U.S. national laboratories in the 1950's. These were oriented mainly towards sensitive nuclear and defence applications. Little publicity was given until the 1960's (Wilkins (1964), Maenchen and Sack (1964), Noh (1964)). At this time Finite Element Methods had just been introduced for solid mechanics (Clough, 1960), and techniques were being developed for linear analysis. Not much attention was given to FD for solid mechanics by the engineering community, as indeed FE methods seemed much more powerful and indeed advantageous for linear systems, being able to provide a one-step global solution.

Interest in the nonlinear and wave-propagation regimes for specialized engineering applications in the late 1960's and 1970's

created a resurgence of the Hydrocodes (Bertholf and Benzley (1968), Wilkins (1975)), and a certain degree of convergence between FD and FE literature (Belytschko (1978), Krieg and Key (1976), Goudreau and Hallquist (1982)). Explicit finite-difference methods were popularized to wider sectors of the engineering community, and new codes were created such as PISCES (Hancock, 1976), the rock mechanics codes of Cundall and Marti (1979), and PR3D for solid mechanics impact by Marti (1981).

3.3 FINITE ELEMENT METHODS

The first application of Finite Element techniques for continua was by Clough (1960), although the theoretical bases for the method had already been set by Courant (1943) and applications to structural analysis had been proposed earlier (Argyris and Kelsey, 1954).

Finite Element discretizations rely on two essential ingredients: a variational or weak form of the eqns. of motion (3.1), and a construction of approximate solutions based on generalized nodal coordinates and independent element shape functions.

The domain V is subdivided into elements V^E, interconnected by nodes. An approximate solution is constructed within an element E as a product of shape functions $N_I(x)$ and the nodal displacements $u_I^E(t)$:

$$u(x,t) = u_I^E(t)N_I(x) \qquad (3.5)$$

where I is summed over the nodes of the element. The shape functions are chosen so that u is continuous over the element boundaries, although its gradient need not be continuous (C^0 continuity). The shape functions N_I so defined are independent of time; eqn. (3.5) constitutes in fact a local separation of variables (semidiscretization).

The discrete form of the gradient operator may be written as

$$u_{i,j} = B_{jI}u_{iI} \qquad (3.6)$$

where

$$B_{jI} = \frac{\partial N_I}{\partial x_j}$$

Let the solid continuum be V with boundary S, consisting of S_u and S_T, where

$$u = u^* \quad \text{on } S_u$$

$$\sigma n = T^* \quad \text{on } S_T$$

A weak form of the eqns. of motion (3.1) may be obtained by using either Galerkin weighed residuals or the virtual work principle, both of which yield the same result:

$$\int_V v_{i,j}\sigma_{ij}dV + \int_V \rho v_i \ddot{u}_i dV = \int_V \rho v_i f_i dV + \int_{S_T} v_i T_i^* dS \qquad (3.7)$$

where v is the test function (or variation) and u the trial function.

Eqns. (3.7) require only C^0 continuity for both trial and test functions, as opposed to (3.1), for which C^1 continuity is needed. If the approximations defined in (3.5) are used for u and v, and because (3.7) must hold for arbitrary v, the global discrete equations are deduced:

$$M\ddot{u} + P(u) = R \qquad (3.8)$$

where the global coefficient matrices M, P, R are assembled from individual element matrices that take the form:

$$M^E = \int_{V^E} \rho N_I N_J \delta_{ij} dV \qquad \text{(mass matrix)}$$

$$P^E = \int_{V^E} B_{jI}\sigma_{ij}dV \qquad \text{(internal forces)} \qquad (3.9)$$

$$R^E = \int_{V^E} f_i N_I dV + \int_{S_T^E} N_I T_i dS \qquad \text{(external forces)}$$

(3.8) is a system of ordinary differential equations of second order in time; integration of these is discussed in section 3.6. For a linear model (small deformations and elastic behaviour), (3.8) becomes

$$M\ddot{u} + Ku = R \tag{3.10}$$

The stiffness matrix K is assembled from element matrices of the type

$$K^E = \int_{V^E} B_{jJ} C_{ijkl} B_{lK} dV \tag{3.11}$$

In static analysis the inertia term may be dropped from eqns. (3.8):

$$P(u) = R \tag{3.12}$$

which for the linear case becomes

$$Ku = R \tag{3.13}$$

For linear analysis, a solution is obtained merely by inverting the stiffness matrix K in eqns. (3.10) or (3.13). In a nonlinear case, eqns. (3.8) or (3.12) must be solved in a number of steps using Newton-Raphson or iterative techniques. It is interesting to note the ability of FE to give a one-step solution to the linear problem, which FD methods lack, having to approach the global solution through relaxation and iteration. Hence the popularity of FE for linear problems. For nonlinear behaviour, however, this advantage disappears, as both FE and FD have to perform some sort of iterations.

For large systems, the assemblage of matrix K is undesirable, as core memory limits may be exceeded and recourse must be made to slow, costly disk Input/Output. This fact accounts for the popularization of relaxation techniques for equation solving (e.g. Flanagan and Belytschko, 1981a), which avoid the assemblage of global coefficient matrices. The FE operators are used only at a local level. In this case FE become conceptually very similar to FD methods with general topology, specially as they often provide equivalent algorithms for the local approximations (Kunar and Minowa, 1981).

3.4 MESH DESCRIPTIONS

Let a particle X of body B be defined by its position at t=0 (reference configuration), **X** . At time t (current configuration) the position of the particle will be

$$\mathbf{x} = \mathbf{x}(\mathbf{X},t) \tag{3.14}$$

x are called the spatial coordinates, and **X** the material coordinates of X. Eqns. (3.14) describe the motion of B.

For the discretization of B three types of meshes may be used, depending on the motion of the nodes of the mesh. The position of a point of the mesh, initially coincident with particle X, will be given by $\chi = \chi(\mathbf{X},t)$.

3.4.1 LAGRANGIAN

In a Lagrangian description the mesh follows the motion of the body,

$$\chi(\mathbf{X},t) = \mathbf{x}(\mathbf{X},t) \tag{3.15}$$

A given node remains coincident with the same material particle throughout the motion. Each element will contain the same domain of material throughout the deformation, thus enforcing implicitly the continuity equation.

Motion of the boundary does not present difficulties, as it always coincides with the mesh boundary. For a scalar field $g(\chi,t)$, the material time derivative (i.e. following the particle) coincides with the partial time derivative:

$$\dot{g} = \frac{\partial g}{\partial t} \tag{3.16}$$

The only disadvantage of this description comes from the fact that the mesh can become excessively distorted for certain problems (e.g. fluids, high velocity impact). In some cases, "rezoning" techniques

may be used to circumvent this problem (e.g. Kalsi and Marti, 1985).

3.4.2 EULERIAN

In an Eulerian description the mesh is fixed in space, i.e.

$$\chi(X,t) = X \qquad (3.17)$$

Nodes are no longer coincident with material particles through time, and the material flows through the cells. Continuity must be enforced explicitly. The material time derivative of $g(\chi,t)$ includes a flux term:

$$\dot{g} = \frac{\partial g}{\partial t} + \frac{\partial g}{\partial x}\frac{dx}{dt} = \frac{\partial g}{\partial t} + \frac{\partial g}{\partial x}v \qquad (3.18)$$

Numerical computations for the flux of scalar fields tend to smear their values, which will not be defined as sharply as for a Lagrangian mesh. Material boundaries are difficult to describe, as they move relative to the mesh. On the credit side, distortion is not a problem, making Eulerian meshes preferrable to Lagrangian meshes for very large deformations.

3.4.3 ARBITRARY LAGRANGIAN-EULERIAN

Arbitrary Lagrangian-Eulerian (ALE) descriptions attempt to combine the advantages of Lagrangian and Eulerian meshes. The mesh moves with an arbitrarily defined motion, $\chi(X,t)$. $d\chi/dt=0$ for an Eulerian mesh, $d\chi/dt=v$ for a Lagrangian mesh. χ can be defined so as to follow the material in the boundary, but without causing excessive distortion in the interior. ALE formulations have been developed by Noh (1964) and Hirt et al. (1974) in FD formats, and by Donea et al. (1977) and Belytschko and Kennedy (1978) in FE.

Material derivatives are given by

$$\dot{g} = \frac{\partial g}{\partial t} + \frac{d\chi}{dt}\frac{\partial g}{\partial x} \qquad (3.19)$$

With an ALE description properties still need to be fluxed through cells, and some smearing may occur as a result.

A crucial aspect in ALE descriptions is the definition of the arbitrary motion of the mesh χ for internal points. Generally a complex rezoning algorithm is necessary for optimizing the new mesh positions at each step. Such a general rezoning algorithm has been proposed for 2-D by Giuliani (1982). Schreurs (1983) has proposed a mesh optimizing algorithm based on the deformation of a fictitious material from an "ideal" mesh. In fact ALE techniques would be equivalent to Lagrangian descriptions in which rezoning is performed at every step. Some applications (e.g. metal forming) may not need such frequent rezoning, and Lagrangian techniques with rezoning at wider intervals could be preferrable.

3.5 LARGE DISPLACEMENT FORMULATIONS

Several formulations are possible depending on which configurations the stress and deformation tensors are referred to. Three alternatives widely used in solid mechanics are presented below.

3.5.1 TOTAL LAGRANGIAN

The 2nd Piola-Kirchhoff stress tensor S and the Green strain tensor E, both of which relate to the reference configuration, are used to describe the material behaviour. Hibbit, Marcal and Rice (1970) proposed this description in the first published large-strain, large-displacement nonlinear formulation for general purpose FE codes.

A constitutive relation is given by

$$S = S(E) \tag{3.20}$$

and in rate form by

$$\dot{S} = D : \dot{E} \tag{3.21}$$

$$(\dot{S}_{IJ} = D_{IJKL}\dot{E}_{KL} \text{ components})$$

S and E being material tensors, their material rates are objective. This formulation is advantageous for Hyperelastic materials, whose behaviour is described on the reference configuration. In this case, calling W the strain energy functional per unit mass,

$$D = \frac{\partial^2 W}{\partial E^2} = \lambda \delta_{IJ}\delta_{KL} + 2G\delta_{IK}\delta_{JL}$$

$$S = \frac{\partial W}{\partial E} \tag{3.22}$$

Elastic-plastic material behaviour is best described on the current configuration, x (Hill, 1950). It is possible to transform such a law into one of the type (3.21) (e.g. Hibbit et al. (1970), Krieg and Key (1976)), but complex and computationally expensive transformations are necessary. However, Simo and Ortiz (1985) suggest that total Lagrangian, Hyperelastic-type formulations provide a more rigorous approach for incremental, non-linear calculations. Such rigour is not justified in explicit calculations with very small steps.

3.5.2 CAUCHY STRESS-VELOCITY STRAIN

A description based on the current configuration may be used to model the behaviour of materials with smooth memory. In the simplest case, the Jaumann rate of Cauchy stress ($\overset{\triangledown}{\sigma}$) and the rate of deformation tensor (velocity strain, **d**) are related by

$$\overset{\triangledown}{\sigma} = C : d \tag{3.23}$$

$$(\overset{\triangledown}{\sigma}_{ij} = C_{ijkl}d_{kl} \text{ in component form})$$

48

where C is the constitutive tensor. For an elastic-plastic material (hypoelastic with associated plasticity) C takes the form

$$C_{ijkl} = \lambda \delta_{ij}\delta_{kl} + 2G(\delta_{ik}\delta_{jl} - \eta n_{ij}n_{kl}) \qquad (3.24)$$

where $\eta > 0$ for plastic loading, $= 0$ otherwise
n is the unit normal to the yield surface

The Jaumann derivative used in eqn. (3.23) provides the constitutive part of the stress rate. To obtain the total stress rate the rotational components must be added:

$$\dot{\sigma}_{ij} = \overset{\triangledown}{\sigma}_{ij} + w_{ip}\sigma_{pj} + w_{jp}\sigma_{pi} \qquad (3.25)$$

If the material behaviour is anisotropic, C must be updated with a similar objective rate:

$$\dot{C}_{ijkl} = \overset{\triangledown}{C}_{ijkl} + w_{ip}C_{pjkl} + w_{jp}C_{ipkl} + w_{kp}C_{ijpl} + w_{lp}C_{ijkp} \qquad (3.26)$$

An alternative formulation results from the use of the Truesdell rate in eqn. (3.23):

$$\overset{\circ}{\sigma} = \underline{C}:d \qquad (3.27)$$

(3.23) and (3.27) are equivalent if one sets

$$\underline{C}_{ijkl} = C_{ijkl} + \sigma_{ij}\delta_{kl} - (\sigma_{ik}\delta_{jl} + \sigma_{il}\delta_{jk} + \sigma_{jk}\delta_{il} + \sigma_{jl}\delta_{ik})/2 \qquad (3.28)$$

The Truesdell stress rate is the forward Piola transformation (eqns. 2.22, 2.25) of the rate of the 2nd Piola-Kirchhoff stress tensor:

$$\overset{\circ}{\sigma} = \phi_{t*}(J^{-1}\dot{S}) \qquad (3.29)$$

Pinsky, Ortiz and Pister (1983) have suggested that the Truesdell rate formulation is the natural one to use (in the current configuration) for hyperelasticity. In this case the constitutive tensor is obtained directly, from the total Lagrangian tensor D, as

$$\underline{C} = \emptyset_{t} * (J^{-1}D).$$

Classical plasticity is described on the current configuration (Hill, 1950). Jaumann Cauchy stress formulations have been widely and successfully used for elastic-plastic behaviour (Wilkins (1964), Maenchen and Sack (1964), Krieg and Key (1976)). With such formulations hyperelastic behaviour (related to the original configuration) may also be described, albeit in a less convenient way, as the constitutive relations need to be pushed forward into the current configuration.

Finally, one problem with this formulation is that d is not integrable (i.e. it is not the rate of any valid strain tensor). Additional strain computations must be done if a total strain measure is required.

3.5.3 UPDATED LAGRANGIAN

In this formulation the model is described on a reference configuration, which is updated at each increment to coincide with the current configuration. From this updated reference, the incremental configuration is described with a total Lagrangian formulation. This method was first proposed by Yaghmai and Popov (1971), and has been widely used since for incremental nonlinear analysis: Osias and Swedlow (1974), Bathe et al. (1975), Nagtegaal and de Jong (1981).

For this description, $F = I$ (identity) and $J = 1$. Hence, eqn. (3.29) implies $\dot{S} = \overset{o}{\sigma}$. It is also easy to see from eqn. (2.19) that $\dot{E} =$ d. In fact this formulation reverts to the Truesdell Cauchy stress rate formulation, eqn. (3.27). This means that the tensor to be used for the tangential stiffness is $\underline{C}$.

3.6 TIME INTEGRATION

Using either Finite Difference or Finite Element Methods for the spatial semidiscretization, the partial differential eqns. of motion (3.1) may be transformed into a system of ordinary differential

equations in time:

$$M\ddot{u} + C\dot{u} + P(u) = R \qquad (3.30)$$

These eqns. can be solved either by modal analysis or by direct integration. Modal analysis methods (e.g. Bathe and Wilson (1976), chpt. 8) perform transformations of eqns. (3.30) which are only valid for linear or quasi-linear systems (i.e. $P(u) = Ku$)

For nonlinear analysis, direct integration (time-marching) methods must be used. For these the time domain is divided into time-steps (Δt), and an incremental analysis is performed for each step.

Time integration procedures may be classified into explicit and implicit. Explicit schemes compute the incremental displacements $u^{t+\Delta t}$ from the equilibrium conditions at time t. Implicit schemes, on the contrary, solve the eqns. of motion (3.30) at $t+h\Delta t > t$, producing an implicit system of eqns. for $u^{t+\Delta t}$.

Two of the most common and representative time-integration schemes, one in either class, are presented below.

3.6.1 CENTRAL DIFFERENCE (EXPLICIT)

Central difference methods are the most widely used explicit schemes for solid mechanics, being the optimal from a very wide class (Key, 1978). The Finite Difference expressions used for velocity and acceleration are

$$\dot{u}^{n+1/2} = (u^{n+1} - u^n)/\Delta t \qquad (3.31a)$$

$$\ddot{u}^n = (\dot{u}^{n+1/2} - \dot{u}^{n-1/2})/\Delta t \qquad (3.31b)$$

Note that each derivative lags the value by half a time-step. Particularizing the equations of motion (3.30) at time n,

$$M\ddot{u}^n + C\dot{u}^n + P(u^n) = R^n \qquad (3.32)$$

Using eqn. (3.31b) and letting $\dot{u}^n = (\dot{u}^{n-1/2} + \dot{u}^{n+1/2})/2$, eqn. (3.32) may be solved, yielding:

$$\dot{u}^{n+1/2} = (M/\Delta t - C/2)^{-1}[M/\Delta t - C/2)\dot{u}^{n-1/2} + R^n - P(u^n)] \tag{3.33}$$

The new displacements u^{n+1} are then found from eqn. (3.31a). If the system has no damping ($C = 0$) and the mass matrix M is diagonal, eqns. (3.33) become uncoupled:

$$\dot{u}^{n+1/2} = \dot{u}^{n-1/2} + M^{-1}[R^n - P(u^n)]\Delta t \tag{3.34}$$

These eqns. can then be solved independently for each degree of freedom I:

$$\dot{u}_I^{n+1/2} = \dot{u}_I^{n-1/2} + \Delta t(R_I^n - P_I^n)/m_I \tag{3.35}$$

The equations also become uncoupled if the damping is assumed to be of the Rayleigh type, as shown in section 4.6.

This uncoupling of the equations of motion is the major advantage of explicit integration procedures. No mass or stiffness matrices need be inverted or even assembled, as all the incremental calculations for each degree of freedom can be done independently at the local level. This not only allows for a simpler architecture in computer codes, but it enables the treatment of non-linearities (be it of Constitutive, Geometric or Boundary type) with virtually no added cost from the linear case. The number of operations per time-step is much smaller than for implicit methods (section 3.6.2), and storage requirements grow only linearly with the size of the problem.

The main disadvantage of the central difference and other explicit methods is that computations are only conditionally stable depending on the time-step size. The time-step must be smaller than a certain critical value for numerical errors not to grow unbounded. This constitutes a major obstacle for certain problems where an excessive number of time-steps makes the analysis too costly.

The stability of the central difference method is considered in section 4.7. The time-step is limited by the Courant criterion, i.e.

the time it takes the stress waves to travel across one element. This limitation is consistent with the local, uncoupled integration of the equations of motion. If the time-step was larger than the Courant critical value, stress waves would travel across an element within one time-step, affecting the surrounding elements. The incremental behaviour of that element would no longer be independent from the rest of the model.

Central difference schemes have been widely used in nonlinear numerical codes, from the early FD hydrocodes of Wilkins(1964) and Maenchen and Sack(1964), to the FE codes of Hallquist (1982a, 1982c), Key (1974), and Belytschko and Tsay(1982). The accuracy and stability of central difference methods has been studied and discussed by various authors (e.g. Belytschko, Holmes and Mullen (1975), Belytschko(1978), Krieg and Key(1973)). The central difference method is considered as the most convenient within the explicit class.

3.6.2. TRAPEZOIDAL RULE (IMPLICIT)

The so-called trapezoidal rule is an example of implicit integration methods. In fact it constitutes a particular case of the Newmark family, probably the most popular of the implicit schemes. A constant average acceleration is assumed for each increment Δt. The difference equations are:

$$\ddot{u}^{n+h} = (\ddot{u}^n + \ddot{u}^{n+1})/2 \qquad (0 \leqslant h < 1)$$
$$\dot{u}^{n+1} = \dot{u}^n + (\ddot{u}^n + \ddot{u}^{n+1})\Delta t/2 \qquad (3.36)$$
$$u^{n+1} = u^n + \dot{u}^n \Delta t + (\ddot{u}^n + \ddot{u}^{n+1})\Delta t^2/4$$

For obtaining u^{n+1} the equations of motion are enforced for time $t+\Delta t$. In an undamped case,

$$M\ddot{u}^{n+1} + P(u^{n+1}) = R^{n+1} \qquad (3.37)$$

Eqn. (3.37) is an implicit relation for u^{n+1}. Substituting the difference expressions (3.36) in (3.37) the following system is obtained:

$$[(4/\Delta t^2)M + K^{n+1}]u^{n+1} = R^{n+1} + M[4/\Delta t^2)u^n + (4/\Delta t)\dot{u}^n + \ddot{u}^n]$$ (3.38)

where K^{n+1} is the secant stiffness matrix ($P^{n+1} = K^{n+1}u^{n+1}$).

For a linear system (K^n = constant) eqns. (3.38) may be solved by inverting the modified stiffness matrix K^*, defined as

$$K^* = (4/\Delta t^2)M + K^{n+1}$$ (3.39)

For nonlinear systems the equations are generally solved by direct elimination techniques, e.g. Newton-Raphson type methods (which require triangularization of K^*).

The trapezoidal rule is unconditionally stable (see e.g. Belytschko and Schoeberle, 1975), the time-step being limited only by accuracy considerations. This is the main advantage of implicit schemes, which makes them more appropriate for problems in which large time-steps can be used. If the time-steps are limited to small values for reasons other than stability (e.g. steep nonlinearities, accuracy, stress-waves) implicit methods lose their advantage.

Another limitation is the large storage required for the matrix coefficients, which restricts severely the size of problem that can be solved in-core. Larger models and 3-D analyses must often resort to out-of-core storage with frequent and slow disk I/O. Because of this problem, alternative equation solving methods based on iterative or relaxation procedures are becoming popular. Classical methods of this type are the Jacobi and Gauss-Seidel procedures, although their effectiveness for Finite Element codes is limited (Belytschko, 1983). More promising for FE topologies are conjugate gradient and quasi-Newton methods. A new and seductive Element-by-Element equation solver has been proposed lately by Hughes, Levit and Winget (1983b); basically it consists of an operator-splitting method that takes advantage of the FE data structure (see also sect. 3.6.3).

Implicit methods are less reliable as to completing the computations without crashing and with the requisite accuracy than explicit methods (Belytschko, 1983).

Nonlinear models are generally more difficult with implicit schemes. Firstly lies the increased cost of the Newton-Raphson iterations. Then is the fact that all boundary conditions, nonlinearities, etc. must be included implicitly in the secant stiffness matrix (K^* in eqn. (3.39)). This greatly complicates the formulation and may restrict the range of constitutive models and boundary conditions that may be used.

3.6.3 OPERATOR SPLIT METHODS

From the discussion in sections 3.6.1 and 3.6.2, it is clear that an operator combining the advantages of explicit methods (uncoupled equations, simple program architecture, no storage of global matrix) with the unconditional stability of implicit methods would be very desirable. Operator split methods attempt to combine such characteristics.

An unconditionally stable explicit procedure was proposed by Trujillo (1972) and received various extensions by Park (1982). This consists in splitting the stiffness K into upper and lower matrices and performing two passes in alternate directions, each pass corresponding to half a time-step. Although this procedure appears to work well for heat conduction (Trujillo, 1975), for structural dynamics the accuracy is poor (Mullen and Belytschko, 1983).

A promising avenue is the use of Element-by-Element methods, which perform a factorization taking advantage of the FE data structure. Such an algorithm has been proposed for solid and structural mechanics by Ortiz, Pinsky and Taylor (1983). In its original form this method was proposed by Hughes, Levit and Winget (1983a) for heat conduction. The same authors (1983b) report unsatisfactory accuracy in structural dynamics, and suggest this technique be used instead as a linear equation solver within an implicit scheme. The approach of Ortiz et al (1983) uses velocities and stresses as unknowns. They perform two passes in alternating directions within a trapezoidal rule to obtain second order accuracy. A question mark still hangs over the accuracy of these methods.

3.7 PRACTICAL CONSIDERATIONS FOR DISCRETE MESHES

A number of undesirable effects can be generated by the nature of the spatial semidiscretization. Unacceptable solutions may be produced by Finite Element meshes even if the elements satisfy the standard convergence criteria (e.g. Zienkiewicz, 1977, chpts. 2&3). Two problems, related to the degree of volumetric constraint, are discussed below. "Locking up" occurs for excessive constraint,while "hourglassing" modes appear if volumetric constraints are too relaxed.

Another problem not discussed here, but to which reference is made in other sections (4.2.3, 7.4.4) is the excessive distortion in Lagrangian meshes for models with very large deformations, which may cause tangling over of the mesh.

3.7.1 "LOCKING-UP" FOR INCOMPRESSIBLE FLOW

Some meshes (in particular constant strain triangles and tetrahedra) give overstiff solutions for incompressible plastic flow. Although this is a well known fact, some authors have continued to use them for convenience (e.g. Johnson, 1976, 1977). The validity of such practice has been strongly questioned (Hallquist, Werne and Wilkins, 1977).

The reason for "locking-up" was shown in a classical paper by Nagtegaal, Parks and Rice (1974) to be an excessive number of volumetric incompressibility constraints in the discrete meshes. According to Nagtegaal, the number of volumetric constraints must not exceed the number of Degrees Of Freedom (DOF) of the model. Ideally the degree of constraint should be the same as in the continuum, with one incompressibility equation per material point ($v_{i,i}=0$). Thus the ideal ratio DOF/constraints equals 2 for plane strain or axisymmetric analyses, and 3 for three-dimensional models. For convergence, the ratio DOF/constraints should tend to a value greater than 1 when the mesh is infinitely refined. Nagtegaal et al (1974) studied a few commonly used elements and found some of them to be unsuitable. Some of their results are presented in table 3.1.
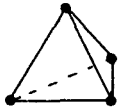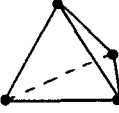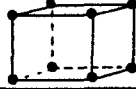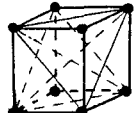
	Constraints / Element	Nodes / Element	DOF / Constraint
PLANE STRAIN			
Constant Strain Triangle (CST)	1	1/2	1
Isoparametric 4-node quadrilateral	3	1	2/3
Mixed Triangles-Quad. (MTQ,MTQC)	1	1	2
AXISYMMETRIC			
Constant Strain Triangle (CST) (exact hoop strain)	3	1/2	1/3
Constant Strain Triangle (CST) (reduced hoop str.)	1	1/2	1
Mixed Triangles-Quad. (MTQ,MTQC) with reduced hoop strains	1	1	2
3-DIMENSIONAL			
Constant Strain Tetrah. (CST),5 per brick, regular lattice	1	1/5	3/5
Constant Strain Tetrah. (CST),6 per brick, regular lattice	1	1/6	3/6
8-node isoparametric brick	7	1	3/7
Mixed Tetrah.-Brick (MTB,MTBC) 5 or 6 Tetrah./Brick	1	1	3

Table 3.1: Ratios of Degrees of Freedom to incompressibility constraints, for infinitely refined 2 and 3-D meshes.

To achieve convergence, the number of volumetric constraints must be relaxed. For this, Nagtegaal et al (1974) proposed a modified variational method which essentially consists of performing a reduced integration on the volumetric stresses. This can be applied only to elements in which full numerical integration comprises more than one quadrature point. A one-point volumetric integration is proposed for 4-node quadrilaterals and 8-node bricks. This method is called "selective" integration, and the elements produced possess the desired number of constraints.   In practice, reduced integration is often extended for convenience to the deviatoric stresses as well(Hallquist,1982b). This excessive relaxation may create additional problems ("Hourglassing") which must be treated appropriately (section 3.7.2). In a Finite Difference context the equivalent to one-point reduced integration is obtained by using contour integral formulae (Wilkins, 1964).

An alternative solution, starting off from the simplest triangles and tetrahedra, is to group several elements together and average the volumetric strains between them. Such a solution is the "Mixed Discretization" (MD) procedure proposed by Marti and Cundall (1982). This refers the deviatoric strains to the basic triangles/tetrahedra and averages the volumetric components within one quadrilateral (2 triangles) or one brick (5/6 tetrahedra) (section 4.2.2). This technique has been employed for the present work. The result of this MD may be interpreted as new, larger elements, which will be termed in the following MTQ (Mixed Triangles-Quadrilateral) and MTB (Mixed Tetrahedra-Brick). These elements have the desired number of constraints (table 3.1).

Johnson (1981) has also used a volumetric averaging procedure for 3-D similar to the proposed MD. For 2-D Johnson (1981) employs meshes of crossed triangles, which were shown by Nagtegaal et al (1974) to be less stiff than ordinary triangle layouts. The behaviour of these crossed layouts is not as good as that of MD, however (see section 5.7).

3.7.2 "HOURGLASSING"

Some commonly used meshes admit certain unopposed deformation modes. These are called "zero-energy" or "hourglassing" modes, because of the similitude with an hourglass pattern. If not dealt with, hourglassing modes quickly grow and dominate the solution. Examples of such meshes are quadrilaterals or bricks, with one-point quadrature in FE, or contour integral formulae in FD. In both cases Hourglassing appears as the price for an excessive reduction in the stress integration. However, anti-hourglassing treatments do exist and may sometimes be preferrable to the excessive cost of selective integration (Goudreau and Hallquist, 1982).

The first anti-hourglassing solutions were reported in the FD hydrocodes (Maenchen and Sack, 1964), consisting of artificial viscosity terms. A similar procedure in 3-D has been used by Wilkins et al.(1975). These techniques involve considerable computation and are not completely independent of rigid body modes. A more rigorous treatment of hourglassing has been followed by Flanagan and Belytschko (1981b), who pursue the idea of the orthogonality of hourglassing modes to the first-order modes, first proposed by Kosloff and Frazier (1978). Flanagan and Belytschko use an additional contribution to the stiffness matrix, called stabilization matrix.

From a more practical viewpoint Goudreau and Hallquist (1982) have considered Flanagan and Belytschko's algorithms to involve an excessive computational cost. Furthermore, exact treatment of hourglassing is not necessary, as hourglassing modes are global modes, and element hourglassing is often a stable kinematic component of a global energy mode. In the DYNA codes Hallquist (1982b) uses an anti-hourglassing viscosity based on Flanagan's orthogonal modes, simplified to produce an operation count 4 to 5 times lower.

Reduced selective integration or "Mixed Discretization" resist the hourglassing modes "naturally" with deviatoric stresses, by-passing the need for any special treatment. A question mark is put by Goudreau and Hallquist (1982) on whether the added cost of these techniques is worthwhile in terms of improved accuracy. Additionally, for some applications like high-pressure shock waves where strength is

not a factor, deviatoric stresses may not be able to restrain hourglassing.

3.8 CONCLUSIONS

Finite Difference and Finite Element methods provide alternative solutions for spatial semidiscretization, with their own independent schools and literature. However, recent trends in Finite Elements avoid the assemblage of global coefficient matrices (e.g. explicit methods or implicit methods with relaxation techniques for equation solving). In these cases FE and FD approaches are conceptually very similar.

Lagrangian, Eulerian or ALE techniques provide alternative descriptions for the mesh, each of them with points in favour and against. Lagrangian meshes are generally preferred for solid mechanics. Various nonlinear formulations are presented, each best suited to a different class of problems. Total Lagrangian formulations are advantageous for hyperelastic-type materials (behaviour described on the original configuration), while Cauchy stress formulations are preferrable for hypoelastic and plastic materials (described on the current configuration). Equivalent algorithms for a given material may generally be found in both formulations, albeit at the expense of costly transformations between current and original configurations.

For time integration, the choice is between implicit and explicit schemes. Both possess very different characteristics as to stability, code architecture and storage requirements. Explicit techniques are well suited for problems dominated by high frequency components (wave propagation), or which are steeply non-linear, and of short duration. Implicit techniques are to be preferred for inertia-dominated models (low frequencies), less non-linear, or of longer duration. The direct elimination techniques used generally for equation solving in implicit methods severely limit the size of problems that can be modelled, specially in 3-D.

The new Element-By-Element techniques proposed recently are promising alternatives. They appear to be most useful as linear

equation solvers within implicit methods. As unconditionally stable explicit time operators, accuracy problems still need to be overcome before they are used in production codes.

Finally, "locking-up" and "hourglassing" are important practical problems related to the spatial semidiscretization, requiring special attention; if not provided for, convergence may not occur in otherwise theoretically "sound" meshes. The method of tackling these problems often conditions strongly the overall approach of the numerical model.

CHAPTER 4

EXPLICIT FINITE DIFFERENCE NUMERICAL MODEL

4.1 INTRODUCTION

    4.1.1 General methodology

4.2 SPATIAL SEMIDISCRETIZATION

    4.2.1 Constant strain triangles and tetrahedra (CST elements)

    4.2.2 Mixed Discretization (MTQ, MTB elements)

    4.2.3 Prevention of negative volumes (MTQC, MTBC elements)

    4.2.4 Mass lumping procedure

4.3 MOMENTUM BALANCE

4.4 CENTRAL DIFFERENCE TIME INTEGRATION

4.5 CONSTITUTIVE MODELS

    4.5.1 Hypoelasticity

    4.5.2 Plasticity; radial return algorithm

    4.5.3 Hardening and uniaxial stress-strain laws

    4.5.4 Objective stress rates

4.6 DAMPING

4.7 STABILITY OF TIME INTEGRATION

4.8 MODELLING OF CONTACTS

    4.8.1 Contact interface laws

    4.8.2 Contact detection algorithm

4.9 HEAT CONDUCTION

4.10 ENERGY COMPUTATIONS

4.11 INPLEMENTATION INTO FORTRAN PROGRAM

4.1 __INTRODUCTION__

Numerical Finite Difference (FD) techniques for the nonlinear analysis of 2 and 3-Dimensional elastic-plastic continua are described here. Explicit central difference interpolations are used both in space and time domains, with triangular/tetrahedral cells for the spatial semidiscretization. No restrictions are placed on the topology of the mesh, which in this aspect is identical to those of Finite Element methods.

The method outlined is a general purpose one and may be applied to both linear and nonlinear, time-marching thermomechanical analysis of continua; however, it will be most advantageous for short duration highly nonlinear problems, such as arise from impact. A great freedom is available for implementation of material constitutive laws. For the present work (mainly in non-cyclic loading of metals) material laws have been restricted to elastic-plastic Von Mises models with kinematic-isotropic hardening.

Material damping is included, permitting the use of dynamic relaxation for quasi-static problems. A numerical contact algorithm models the interface between continua, often present in nonlinear impact calculations. Finally, for generality, thermal effects allowing heat generation/conduction and material dependence on temperature have been included, enabling a fully coupled thermomechanical analysis.

The theory and numerical techniques described below apply in general for 2 and 3-D models. A 2-D code with axisymmetric capability was developed for this thesis, implementing the algorithms described. In general, implementation details for the algorithms are given only for 2-D. Some algorithms (e.g. thermal effects, prevention of negative volumes) have also been implemented by the author in an existing 3-D program (Marti (1981,1983)), (Marti, Goicolea, Kalsi, and Macey (1984)), (Marti, Kalsi, and Last (1984)).

4.1.1 GENERAL METHODOLOGY

Before entering into details of the numerical techniques, it is

useful to describe the philosophy of time-marching explicit calculations. These provide a set of uncoupled discrete equations of motion, which may be solved explicitly without assembling or inverting global stiffness or mass matrices. The program arquitecture is quite different from the usual linear (static or dynamic) or implicit non-linear techniques, allowing a greater generality in the treatment of nonlinearities (large deformations, material behaviour, contacts).

It is assumed that the functional dependence of the displacements on space and time can be separated, giving rise to independent semidiscretizations for both domains. The mesh for the spatial semidiscretization is Lagrangian (sect. 3.4.1), i.e. the grid nodes represent material points and move with them. The time domain is divided linearly into time-steps.

The computational cycle performed to advance the problem in time may be described as follows (fig. 4.12). At a particular instant, coordinates, velocities and accelerations are known. The accelerations are integrated with a central difference scheme for each grid-point, to find the new velocities and displacements. These are then used in spatial difference equations to interpolate the deformation gradients and strains for each cell. Applying the material constitutive equations, strains give rise to stresses, which are then integrated around each grid-point to provide nodal forces. Dividing by the mass (lumped at nodes) the new accelerations may be found. Here the computational cycle is complete and may be recommenced for the next time-step. This process continues until the total time for analysis is reached. Nonlinear boundary constraints giving rise to displacement or force conditions are introduced into the cycle explicitly.

For the thermal analysis the computations advance in parallel and coupled with the mechanical cycle. Influx of heat into a cell from heat sources, heat conduction, or produced by plastic work, gives rise to temperature increments. The gradients of the new temperatures create heat fluxes (calculated from Fourier's conduction law), allowing repetition of the cycle for the next time-step.

A price is paid for the generality and simplicity of explicit algorithms, in that the computations are only conditionally stable,

limiting the size of the time-step to small values. However, the operation count per time-step is much smaller than for implicit methods. The critical time-step may be estimated accurately, and the robustness of the computations does not suffer as a result of the conditional stability. The main implication of the time-step restriction is the large number of computational cycles necessary for medium or long duration analyses, which often become uneconomical.

In explicit calculations, the limiting factor is generally the CPU time, rather than core storage. When constructing the mesh, it must be taken into consideration that the time-step is proportional to the minimum element size. A local refinement of the mesh, even if it only adds a small number of elements, may increase greatly the number of time-steps necessary and hence the computational cost.

Quasi-static models

By their nature, explicit computations are essentially dynamic, relying on numerical integration of the equations of motion with non-zero masses for the time-marching solution. No simplification of the cycle is possible for quasi-static analysis. However, many such problems can still be solved advantageously, using dynamic relaxation (damping out vibrations until a steady-state is reached), or velocity scaling (increasing deformation velocity in a controlled manner).

Dynamic relaxation may be argued to be a more natural approach than the static stiffness equations (3.12), (3.13). As in the physical world, with dynamic relaxation static equilibrium is reached as a limiting steady-state. In general, solution will require a greater computational effort, although if adaptative techniques are used for mass and damping parameters (Underwood, 1983), the difference may be small. One definite advantage explicit relaxation methods have, which may be overwhelming in large 3-D systems, is that they do not need to store any large global coefficient matrices. For non-linear problems, dynamic relaxation requires some care so as not to apply too large load-steps which would cause an irreversible overshoot in the solution. Additionally, if the loads are applied gradually, the amount of relaxation needed after reaching the maximum load is greatly reduced.

Velocity scaling exploits the fact that for sufficiently slow loading, the relaxation process may be ommitted altogether, without excessive errors. This allows modelling a slow, quasi-static process merely by contracting the time-scale. As in dynamic relaxation, loading must be slow enough not to cause overshoots. The errors incurred in this process are in the form of elastic stress waves left travelling in the model. For elastic analyses, velocity scaling will not be appropriate in general, as the intensity of these waves will be important with respect to the overall stresses. For plastic analyses however, the error will merely be in the form of an elastic "noise" superposed on the smoother quasi-static solution (see also sections 6.5.1, 7.3.2.2).

4.2 SPATIAL SEMIDISCRETIZATION

A discrete mesh of triangles (2-D) or tetrahedra (3-D) is affixed on the initial (reference) configuration of the continuum, and particles are followed through time (Lagrangian mesh). The current configuration is a function of the reference configuration and time:

$$x = x(X,t) \tag{4.1}$$

Displacements ($u = x-X$), velocities ($v=\dot{u}$) and accelerations ($a=\ddot{u}$) are defined at the nodes. Deformation gradients F, rates of deformation d, strains E, and stresses σ are referred to the centroid of each cell (fig. 4.1).

The computations related to the discretization fall into two areas: firstly the interpolation of strains and deformation gradients from the nodal displacements, and secondly the integration of stresses around each grid-point to obtain the nodal forces.

Triangles and Tetrahedra are the only element types which provide a one-to-one correlation between the sets of all possible corner movements and deformation gradient tensors. This fact inherently eliminates zero-energy ("hourglassing") deformation modes (unopposed movements of the corner nodes), which occur for other elements such as

quadrilaterals or bricks with reduced integration. It also allows a direct obtention of the gradients from the difference equations without using contour integrals (eqn. 3.4)

However, meshes of constant strain triangles or tetrahedra often "lock-up" when modelling plastic flow, giving solutions which are very overstiff (see sect. 3.7.1). The Mixed Discretization (MD) procedures proposed by Marti and Cundall (1982) are employed here to overcome this problem. The new elements created by Mixed Discretization will be called MTQ (Mixed Triangles-Quadrilateral) and MTB (Mixed Tetrahedra-Brick).

Mixed Discretization is attractive for elastic-plastic calculations because it allows the use of simple elements, which avoid zero-energy modes naturally, without the need for artificial anti-hourglassing terms (see sect. 3.7.2). However, it eliminates an advantage of triangular/tetrahedral meshes, i.e. the impossibility of tangling over due to asymptotically infinite resistance to zero or negative volumes in each cell. This problem need only cause concern for meshes with very large distortions. Nevertheless, for such cases it does constitute a serious drawback, causing the computations to crash unless the mesh is rezoned.

To overcome the problem of tangling over in MD meshes, a new family of corrected elements is proposed in section 4.2.3: corrected MTQ (MTQC) and corrected MTB (MTBC) for 2 and 3-D respectively. These elements recover asymptotically the resistance to zero volumes of the basic CST elements, when one cell in the Mixed Discretization group becomes much smaller than the rest and tends to zero volume. The ability of modelling incompressible flow is maintained, thus providing a more robust alternative to MD.

4.2.1 CONSTANT STRAIN TRIANGLES AND TETRAHEDRA (CST ELEMENTS)

Constant strain triangles and tetrahedra (CST) may be used directly as such for elastic analyses, or as the basic ingredient for MD (sect. 4.2.2) or corrected MD (sect. 4.2.3) meshes.

interpolation of deformation gradients

Velocity gradients are interpolated at the centroid of the cell from direct use of difference equations. Nodes are numbered N=0,1,2 (triangle) or N=0,1,2,3 (tetrahedron) (fig. 4.1). Node 0 is taken as an arbitrary reference point. The difference equations take the form:

$$v_i^N - v_i^0 = v_{i,j}(x_j^N - x_j^0) \qquad (4.2)$$

where superscripts refer to nodes and subscripts refer to components. Using the notation ( )IJ=( )I-( )J, (4.1) may be written as follows:

$$v_i^{N0} = v_{i,j}x_j^{N0} \qquad (4.3)$$

This may be put into matrix form and inverted, to obtain

$$[v_{i,j}] = [VR(i,N)][XR(N,j)]^{-1} \qquad (4.4)$$

where the notation $VR(i,N)=v_i^{N0}$, $XR(N,j)=x_j^{N0}$ has been used. All matrices in eqn. (4.4) are 2x2 for 2-D or 3x3 for 3-D.

The rate of deformation and spin rate tensors may be obtained as:

$$d_{ij} = (v_{i,j} + v_{j,i})/2$$
$$(4.5)$$
$$w_{ij} = (v_{i,j} - v_{j,i})/2$$

For 2-D additional considerations must be made to determine the out-of-plane components. Assuming axis no. 3 pointing out of the plane, these conditions are:

- Plane strain, $d_{33}=0$;

- Plane stress, $\sigma_{33}=0$; this is a stress condition which must be used together with the stress-strain law to obtain the appropriate rate of deformation (eqns. 4.41, 4.42);

- Axisymmetric (axis 2 of symmetry), $d_{33} = v_1/x_1$ at each point in the continuum; this condition may be relaxed by enforcing it only at the
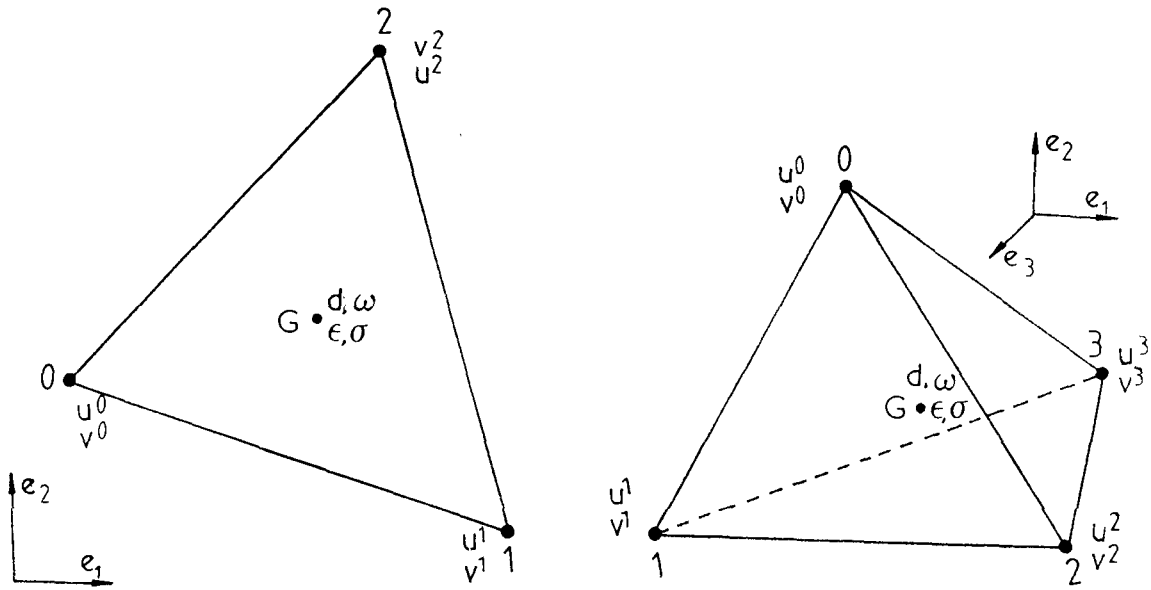
Figure 4.1: Triangular and tetrahedral cells
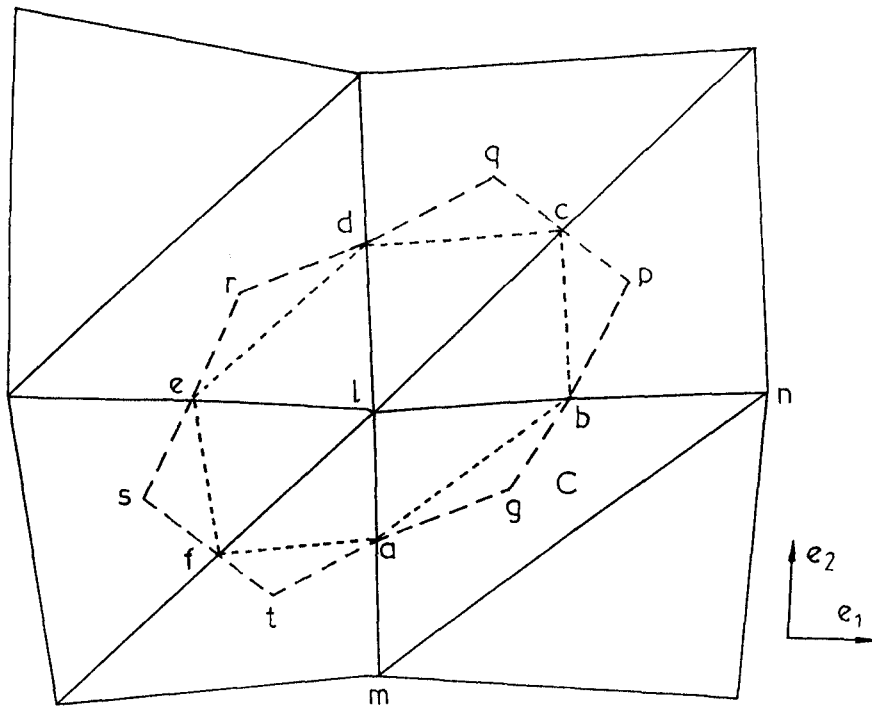
Figure 4.2: Path for stress integral around node 1

triangle centroid,

$$d_{33} = \frac{(v_1^0 + v_1^1 + v_1^2)/3}{(x_1^0 + x_1^1 + x_1^2)/3} \tag{4.6}$$

Generalized natural strain increments are defined as

$$\Delta\epsilon_{ij} = d_{ij}\Delta t \tag{4.7}$$

where Δt is the computational time-step. These increments may be decomposed into:

- Volumetric part, $\Delta\epsilon_v = \Delta\epsilon_{kk}$
- Deviatoric part, $\Delta e_{ij} = \Delta\epsilon_{ij} - \delta_{ij}\Delta\epsilon_{kk}/3 \tag{4.8}$

Integration of stresses to obtain nodal forces

The internal force applied at each node 1 may be obtained by integrating the stresses in a closed surface containing the node, $S(1)$:

$$P_i^{(1)} = \int_{S(1)} \sigma_{ij}n_j dS \tag{4.9}$$

where n_j is the (unit) outward normal to $S(1)$. $S(1)$ is constructed in 2-D (fig. 4.2) by forming a polygon joining the centroids of the triangles and centres of the sides sharing node 1, agbpcqdresfta. In fact, this polygon is only a cross-section of surface $S^{(1)}$; for plane strain and plane stress $S^{(1)}$ is a slab of thickness t, while for axisymmetric models it is the surface of revolution generated rotating the polygon around the axis of symmetry. A similar surface may be constructed in 3-D from a polyhedron with corners in centroids of tetrahedra, centroids of faces and centres of edges.

The contribution of each cell to the nodal forces is detailed below for 2-D. The notation of fig. 4.2 will be followed for node and cell numbers. Different formulations are necessary for plane strain or stress and axisymmetric models.

Plane strain or plane stress

From eqn. (4.9) the contribution of cell C to the force at 1 is obtained as follows:

$$P_i^{(1)C} = t \int_{agb} \sigma_{ij} n_j ds \qquad (4.10)$$

The thickness t is constant (=1) for plane strain but may vary for plane stress. Considering Gauss' theorem, the integral in eqn. (4.10) may be expressed as follows:

$$\int_{agb} \sigma_{ij} n_j ds = \int_{agba} \sigma_{ij} n_j ds + \int_{ab} \sigma_{ij} n_j ds = \int_{A_{agba}} \sigma_{ij,j} dA + \int_{ab} \sigma_{ij} n_j ds \qquad (4.11)$$

where A_{agba} is the plane area enclosed by agba. As the divergence of a constant field is null, the integral over this area is zero. The nodal force becomes:

$$P_i^{(1)C} = t \, \sigma_{ij}^C \int_{ab} n_j ds \qquad (4.12)$$

or explicitly in matrix form:

$$\lfloor P_1^{(1)C}, \; P_2^{(1)C} \rfloor = \frac{t}{2} \lfloor x_2^{nm}, \; x_1^{mn} \rfloor \begin{pmatrix} \sigma_{11} & \sigma_{12} \\ \sigma_{12} & \sigma_{22} \end{pmatrix} \qquad (4.13)$$

Axisymmetric

Cylindrical coordinates are used for describing axisymmetric models (x_1 radial coordinate, x_2 axial coordinate). The divergence of a constant vector is no longer zero as it was for Cartesian coordinates:

$$div \lfloor \sigma_{i1} \; \sigma_{i2} \; \sigma_{i3} \rfloor = \sigma_{i1,1} + \sigma_{i3,3} + \sigma_{i2,2}/x_1 + \sigma_{i1}/x_1 = \sigma_{i1}/x_1 \qquad (4.14)$$

The contribution of a cell C to the integral in eqn. (4.9) becomes

$$\int_{S_{agba}} \sigma_{ij} n_j dS + \int_{S_{ab}} \sigma_{ij} n_j dS = \int_{A_{agba}} (\sigma_{i1}/x_1) 2\pi x_1 dA + \int_{ab} \sigma_{ij} 2\pi x_1 n_j dS =$$

(4.15)

$$= (\pi/6) A^C \sigma_{i1} + 2\pi x_1^h \sigma_{ij} |ab| n_j^{ab}$$

where: S_{agba}, S_{ab} denote surfaces of revolution generated by agba & ab

A^C total Cell area

$A_{agba} = A^C/6$, area enclosed by triangle agba

$|ab|$, n^{ab} are the length and unit normal of segment ab

In addition to the terms from eqn. (4.15), radial forces are produced by the hoop stresses σ_{33}. These forces are not included in (4.15), as the integrals cover the complete 2 toroid where opposite radial components cancel out (fig. 4.3). However, if one considers only a sector of angle φ :

$$P_1^{(1)} = \int_0^{\varphi} P_3^{(1)} d = \varphi P_3^{(1)} = \varphi \int_{A^{(1)}} \sigma_{33} dA$$

and the contribution of cell C for the complete 2 is:

$$P_1^{(1)C} = \frac{1}{3} A^C \sigma_{33} 2\pi = \frac{2\pi}{3} \sigma_{33} A^C$$

(4.16)

which added to (4.15) gives the total nodal force contributions. In matrix form,

$$\lfloor P_1^{(1)C} \quad P_2^{(1)C} \rfloor = \frac{\pi}{2} (2x_1^l + x_1^m + x_1^n) \lfloor x_2^{nm} \quad x_1^{mn} \rfloor \begin{pmatrix} \sigma_{11} & \sigma_{12} \\ \sigma_{12} & \sigma_{22} \end{pmatrix} +$$

$$+ \frac{\pi}{6} A^C \lfloor \sigma_{11} \quad \sigma_{12} \rfloor + \frac{2\pi}{3} A^C \lfloor \sigma_{33} \quad 0 \rfloor$$

(4.17)

4.2.2 MIXED DISCRETIZATION (MTQ, MTB ELEMENTS)

Mixed discretization procedures are described in this section. This techniques avoid the excessive stiffness otherwise associated with constant strain triangles or tetrahedra for incompressible flow (see sect. 3.7.1).

According to Nagtegaal, Parks and Rice (1974), for accurate modelling of incompressible plastic flow, the ratio between the number of Degrees Of Freedom (DOF) in the mesh and the number of constraints imposed by the incompressibility condition must be > 1. For Constant Strain Triangles, The ratio DOF/constraints for infinitely refined plane strain and axisymmetric meshes is equal to 1 (considering for the axisymmetric case that the radially varying hoop stresses are reduced to the value at the element centroid (eqn. 4.6), otherwise the ratio would be 1/3) (table 3.1). For tetrahedra forming bricks in a regular lattice, the ratio is either 3/5 or 3/6 depending on whether each brick is composed of 5 or 6 tetrahedra (table 3.1).

Nagtegaal et al. (1974) suggested a modified variational principle to improve meshes which would otherwise be unsuitable. The idea behind this modification is to make sure dilatation is governed by fewer parameters than for conventional elements. Starting from elements with more than one integration point, this is achieved by averaging the volumetric strains within each element (effectively performing a reduced integration on them). Based on the same principle, Marti and Cundall (1982) have proposed Mixed Discretization (MD) procedures valid for FE or FD meshes with lower order elements (one integration point), in which volumetric strains are averaged for groups of several elements.

The ideal value for the ratio DOF/constraints is that of the continuum, in which for each material point there is one volumetric equation and N (no. of space dimensions) DOF. Using MD these ideal ratios are achieved if averaging is performed within the following MD groups (table 3.1):

- 2 Triangles in one Quadrilateral for 2-D (MTQ elements);
- 5 or 6 Tetrahedra in one Brick for 3-D (MTB elements).

If C_i (i=1 to M) stands for the individual cells and E for the total element (MTQ or MTB), the Mixed Discretization procedure consists simply of substituting the volumetric strains in each cell by the volume-weighed average of the group:
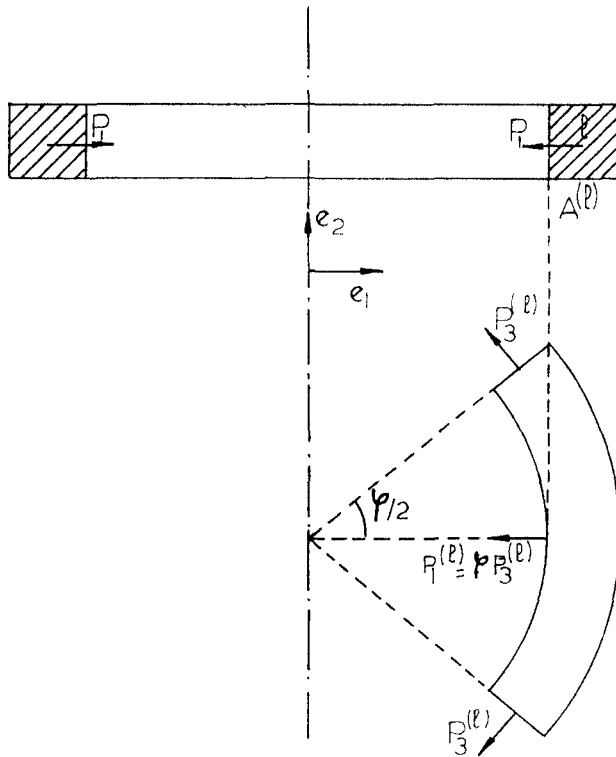
Figure 4.3: Radial forces from Hoop stresses (axisymmetric model)
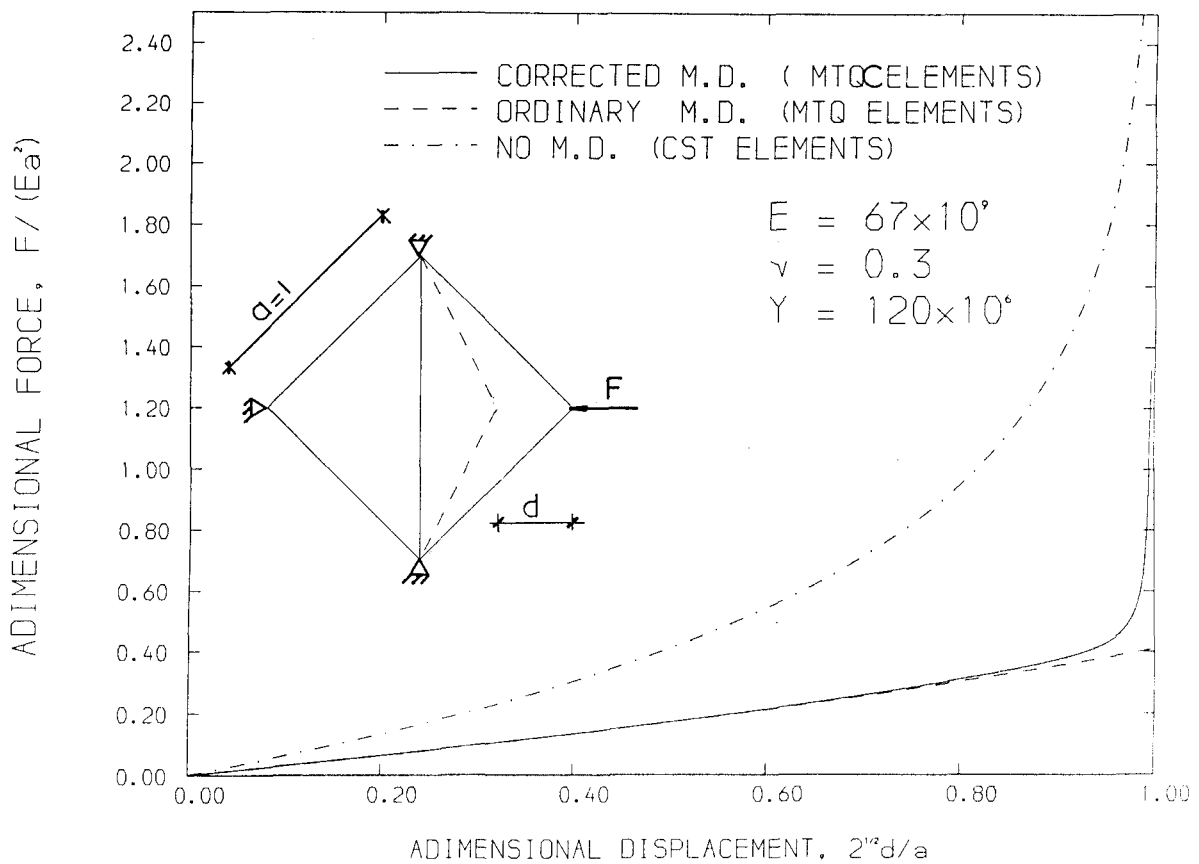
Figure 4.4: RESISTANCE TO ZERO-VOLUME FOR DIFFERENT ELEMENT TYPES

$$\Delta\epsilon_V^{Ci} := \Delta\epsilon_V^E = \left(\sum_{i=1}^{M}\Delta\epsilon_V^{Ci}V^{Ci}\right)/\sum_{i=1}^{M}V^{Ci} \qquad (4.18)$$

where V^{Ci} are the volumes of the individual cells. M=2 for 2-D and M=5 or 6 for 3-D. For axisymmetric models, the average in eqn. (4.18) is area-weighed instead, in order to avoid problems near the axis of symmetry.

Apart from having the ideal number of volumetric constraints, MTQ or MTB elements will produce non-zero strains and stresses in the component cells for any set of corner movements. No zero-energy hourglassing may occur, as it is opposed by deviatoric stresses.

Validation examples for MD procedures in simple plasticity problems are provided in sections 5.4.1 and 5.4.2.

4.2.3 PREVENTION OF NEGATIVE VOLUMES (MTQC, MTBC ELEMENTS)

One important advantage of CST elements is that no tangling over may occur without ocassioning negative volumes in the basic cells (Johnson, 1976). A hypoelastic material will generate resisting forces that grow towards infinite as the volume tends to zero. This advantage is lost by MD, which accepts zero volume in one cell without generating infinite resisting pressures, as long as the whole MD group has a non-zero volume. This may be seen letting the volume of one cell C_j tend to zero:

if $V^{Cj} \longrightarrow 0$

CST: $\Delta P = K\,\Delta\epsilon_V^{Cj} = K(\Delta V^{Cj}/V^{Cj}) \longrightarrow -\infty$

MD : $\Delta P = K\,\Delta\epsilon_V = K\left(\Delta\epsilon_V^{Cj}V^{Cj} + \underbrace{\sum_{i\neq j}\Delta\epsilon_V^{Ci}V^{Ci}}\right)/V^E \longrightarrow K\left(\underbrace{\sum_{i\neq j}\Delta\epsilon_V^{Ci}V^{Ci}}\right)/V^E$

(finite)

This fact has a number of undesirable side-effects. Large reductions in volume are usually associated with large distortions in

shape, causing considerable numerical errors as the element interpolations become ill-conditioned. On the other hand, the critical time-step will be reduced, increasing the costs greatly. Finally, if negative volumes occur from tangling over in the mesh, the calculations will crash. It must be noted that these problems occur only for special cases with highly distorted Lagrangian meshes. However they do detract seriously from the robustness of MD procedures for general applications.

Johnson (1981) has recognized this problem, but his solution has been an inconsistent use of averaging procedures. For certain critical portions of the calculations, averaging is switched off, in order not to incur in overlapping. No explanation is given by Johnson for the inevitable loss of accuracy, except the convenience of the analyst.

A consistent solution is proposed here using a Mixed Discretization mesh that recovers the resistance to negative volumes of CST elements, when for an individual cell the volume tends to zero, $V^{Cj} \to 0$. This takes the shape of a correction to the averaged volumetric strain increment $(\Delta \epsilon_V)$ from eqn. (4.18):

$$\Delta \epsilon_V^{Ci} := \Delta \epsilon_V^E + \alpha \min(\Delta \epsilon_V^{Cj}, 0)[V^E/(MV^{Ci}) - 1] \qquad (4.19a)$$

where M is the number of cells in the MD group, and α is an empirical coefficient ($\alpha = 0.01$ is the recommended default value). This correction only operates when volumetric strain increments in the smallest cell of the group are compressive (i.e. cell volume is being decreased).

It can be seen easily that this correction (eqn. 4.19) conserves the volume weighed average, thus maintaining the consistency of the computations. Calling the new average $(\Delta \epsilon_V^E)^*$:

$$(\Delta \epsilon_V^E)^* = (\sum \Delta \epsilon_V^{Ci} V^{Ci})/V^E = \Delta \epsilon_V^E + \alpha \min(\Delta \epsilon_V^{Cj}, 0)(1/V^E) \sum [(V^E V^{Ci})/(MV^{Ci}) - V^{Ci}] \qquad (4.19b)$$

where the second term on the right hand side is null, as $V^E = \sum V^{Ci}$.

On the other hand, when the cell volume tends to zero the volumetric strain increment grows asymptotically, producing an

infinite resistance to tangling over

$$\text{for } V^{Cj} \longrightarrow 0, \quad \Delta\epsilon_V^{Cj} := \Delta\epsilon_V^E + \alpha \min(\Delta\epsilon_V^{Cj}, 0)[V^E/(MV^{Cj})-1] \longrightarrow -\infty \quad (4.20)$$

For axisymmetric problems, again the correction formula must be area weighed. In order to preserve the volume-weighed average (eqn. 4.19b) the axisymmetric correction takes the form

$$\Delta\epsilon_V^{Ci} := \Delta\epsilon_V^E + \alpha \min(\Delta\epsilon_V^{Cj}, 0)[A^E/(MA^{Ci})-1]r^E/r^{Ci} \quad (4.21)$$

where A^{Ci}, A^E are areas of the individual cells and complete element r^{Ci}, r^E are the radial coordinates of their centroids.

The new elements created by this correction against negative volumes in MD procedures will be called:

-   MTQC (MTQ corrected) for 2-D;
-   MTBC (MTB corrected) for 3-D.

A simple test with a quadrangle, in which one of the component triangles tends to zero volume, was done to verify the behaviour of these elements (fig. 4.4). For Constant Strain Triangles (CST), the resisting force grows towards infinity when a node tries to cross over the opposite side. MTQ and MTQC elements display a softer response, both being nearly identical up to 90% reduction in volume. For further reductions, the resistance of MTQC elements shoots up steeply towards infinity, while MTQ allows crossing over (negative volume).

This important result means that the new proposed elements are capable of accurately modelling incompressible plastic flow, even for situations with very large distortions, but recover the desirable resistance of CST meshes to overlapping. Further results using MTQC elements are presented in sections 5.4, 5.7, and 7.3.4.4 which confirm this point.

4.2.4 MASS LUMPING PROCEDURE

The mass in the discrete model is lumped at the grid-points, by integrating the continuum mass over a volume surrounding each node. For a Lagrangian mesh, nodal masses need only be computed once, at the beginning of the calculations. Two conditions must be met by the mass lumping procedure: firstly the centre of gravity must be preserved for dynamic calculations, and secondly the volume of integration, for consistency, must correspond to the surface used when integrating the stresses (fig. 4.2).

The contribution of a cell C to the mass of node 1 is (fig. 4.2):

- Plane stress or plane strain

$$\rho V_{albg} = \rho t A_{albg} = \rho t A_{lmn}/3 \qquad (4.22)$$
(1/3 of the mass to each node)

- Axisymmetric

$$\rho V_{albg} = \rho \int_{A_{albg}} 2\pi r dA = \rho(\pi/54)A_{lmn}(22r_l + 7r_m + 7r_n) \qquad (4.23)$$

For 3-D, 1/4th of the mass of every tetrahedron is lumped at each of its nodes.

4.3 MOMENTUM BALANCE

Having integrated the stresses (eqn. 4.9) and obtained the nodal masses (eqns. 4.22, 4.23), balance of momentum is applied locally, using the integral form of the principle (eqn. 2.28). Note that the corresponding field equation (Cauchy's eqn. of motion, (2.29)) requires a stronger differentiability, which is not satisfied at the element interfaces.

Integrating over a small surface $S^{(1)}$ around each node 1,

$$\ddot{u}^{(1)} = [\int_{S^{(1)}} \sigma \, ndS + M^{(1)}f + R^{(1)}]/M^{(1)} \qquad (4.24)$$

where: $R^{(1)}$ are intensive forces applied on node 1
$M^{(1)}$ is the mass lumped at 1.

4.4 CENTRAL DIFFERENCE TIME INTEGRATION

The accelerations are integrated in time with a centred scheme to provide new values for velocities and displacements:

$$\dot{u}^{n+1/2} = \dot{u}^{n-1/2} + \ddot{u}^{n}\Delta t \qquad (4.25)$$

$$u^{n+1} = u^{n} + \dot{u}^{n+1/2}\Delta t \qquad (4.26)$$

Note that all the variables representing rates or increments are defined at mid-step. The central difference equations (4.25, 4.26) together with the discretized momentum balance eqns. (4.24), form an uncoupled system, which may be solved independently for each node in the mesh.

The numerical dispersion (frequency distortion errors) associated with a lumped mass idealization and a central difference scheme are of different signs (Key, 1978), which makes this combination a natural choice for explicit models.

4.5 CONSTITUTIVE MODELS

Explicit schemes allow a great generality in the constitutive laws that can be modelled. In principle, any law that can be expressed explicitly in the following rate form is acceptable:

$$\overset{\circ}{\sigma} = C(E,d,\sigma,K,T) \qquad (4.27)$$

where: $\overset{\circ}{\sigma}$ represents an objective stress rate (section 2.5.1)

K is a set of material parameters

T is the temperature

E is Green's strain tensor

d is the rate of deformation tensor.

For the present work, the constitutive laws considered are elastic-plastic models with Von Mises yield criterion. A hypoelastic prediction is computed first, and then corrected back to the yield surface if the yield condition is exceeded (radial return). For a more

complete study of constitutive laws in explicit Finite Diference Lagrangian codes, see Herrmann and Bertholf (1983).

4.5.1 HYPOELASTICITY

The basic (predictor) constitutive behaviour is a hypoelastic law of the type:

$$\overset{\circ}{\sigma}_{ij} = \lambda d_{kk}\delta_{ij} + 2Gd_{ij} - \alpha(3\lambda+2G)\dot{T}\delta_{ij} \qquad (4.28)$$

where λ,G are Lame's elastic constants

T is the temperature rate

α is the coefficient of thermal expansion

Hypoelastic stresses are computed always as predictors, being later corrected for other types of behaviour if needed. All stress and deformation measures used in eqn. (4.28) refer to the current configuration; it produces a linear relation between true stress and natural strain in a uniaxial test. For large strains (4.28) does not derive from an elastic potential (hyperelastic). For small strains, both concepts are equivalent.

4.5.2 PLASTICITY; RADIAL RETURN ALGORITHM

The plastic yield criterion is a stress condition, defining a yield surface in stress space. The yield criterion depends on the history of deformation, through the plastic hardening parameters, Q:

$$F(\sigma,Q) = 0 \qquad (4.29)$$

The trial stress from the hypoelastic prediction (eqn. 4.28),

$$\sigma_E^{n+1} = \sigma^n + \overset{\circ}{\sigma}_E^{n+1/2}\Delta t \qquad (4.30)$$

is tested with the yield criterion, eqn.(4.29). If $F(\sigma_E^{n+1})<0$ no correction is necessary:

$$\sigma^{n+1} = \sigma_E^{n+1} \qquad (4.31)$$

If $F(\sigma_E^{n+1}) > 0$ the stresses are returned normally to the yield surface (fig. 4.5):

$$\sigma^{n+1} = \sigma_E^{n+1} - (\beta/3)\frac{\partial F}{\partial \sigma} \qquad (4.32)$$

$$\Delta\sigma^{n+1/2} = \sigma^{n+1} - \sigma^n$$

where β is a scalar factor, used for convenience of presentation. The new stresses must satisfy $F(\sigma^{n+1}) = 0$.

This radial return method is due to Wilkins (1964). Other (more sophisticated) methods for calculating the stress update exist, such as the tangent stiffness radial return (e.g. Krieg and Key, 1976). A variation to the radial return method, applying the consistency condition to the end state rather than in a differential sense has also been proposed by Krieg and Key (1976). Recently, Ortiz and Simo (1985) have proposed more general "return mapping algorithms", for arbitrary plastic models and non-constant tangent elasticity tensors. Results obtained here (e.g. sect. 5.6) indicate that for the small explicit steps used, even in highly non-linear calculations, the performance of the simplest radial return method is acceptable.

The rate of deformation tensor is composed of elastic and plastic parts:

$$\mathbf{d} = \mathbf{d}^e + \mathbf{d}^p \qquad (4.33)$$

The elastic component may be expressed as

$$d_{ij}^E = \frac{1}{2G}\overset{\circ}{s}_{ij} + \frac{1}{E}\lfloor \dot{\sigma}_{kk}\delta_{ij} + 9K\dot{T}\alpha \rfloor \qquad (4.34)$$

where s_{ij} are the deviatoric stresses (eqn. 2.59), and $K = \lambda + 2G/3$.

In the following, it will be assumed that the yield surface is a Von Mises cylinder, with no dependence on hydrostatic stresses. The plastic correction (4.32) takes place in the deviatoric hyperplane (σ_{kk} = constant), as $\frac{\partial F}{\partial \sigma} = \frac{\partial F}{\partial s}$. Hence, the volumetric stress-strain behaviour is purely elastic:
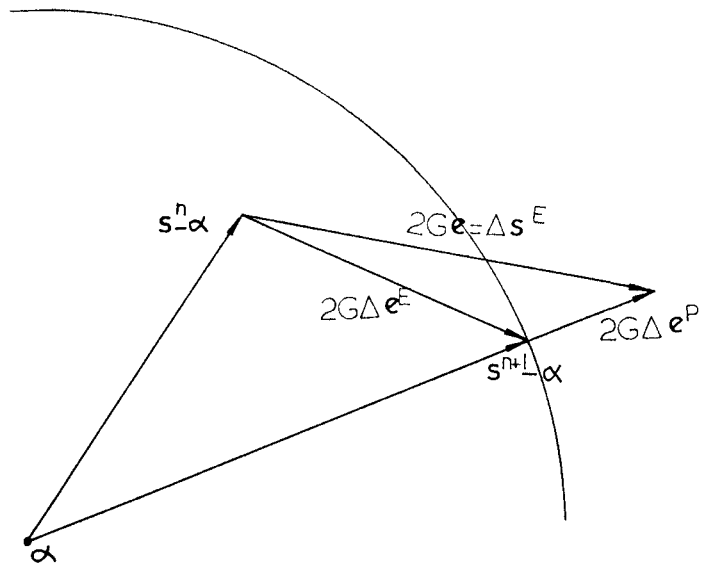
Figure 4.5: Radial return plastic stress correction

$$\dot{\sigma}_{kk} = \dot{\sigma}^E_{kk} = 3K(d_{kk} - 3\dot{T}\alpha) \qquad (4.35)$$

The rate of deformation may be expressed inverting eqn. (4.28):

$$d_{ij} = \frac{1}{2G}\dot{s}^E_{ij} + \frac{1}{E}(\dot{\sigma}_{kk} + 9K\dot{T}\alpha)\delta_{ij} \qquad (4.36)$$

The plastic rate of deformation is derived combining eqns. (4.32), (4.33), (4.34) and (4.36):

$$\mathbf{d}^P = \mathbf{d} - \mathbf{d}^E = \frac{1}{2G}(\dot{\mathbf{s}}^E - \dot{\mathbf{s}}) = \frac{\beta/3}{2G}\frac{\partial F}{\partial \sigma} \qquad (4.37)$$

Hence the return algorithm (eqs. 4.30 - 4.32) implicitly defines a normality rule for the plastic flow (associativity).

In particular, for a Von Mises yield criterion with kinematic-isotropic hardening of the type

$$F = (3/2)(s_{ij} - \alpha_{ij})(s_{ij} - \alpha_{ij}) - Y^2 \qquad (4.38)$$

if the plastic condition is reached ($F(\sigma^{n+1}_E) > 0$), the deviatoric stresses are simply scaled back along the radius of the Von Mises circle (fig. 4.5):

$$s^{n+1}_{ij} - \alpha_{ij} = ((s^{n+1}_{ij})^E - \alpha_{ij})/(1+\beta) \qquad (4.39)$$

and if the hardening is purely isotropic ($\alpha_{ij}=0$):

$$s^{n+1}_{ij} = (s^{n+1}_{ij})^E/(1+\beta) \qquad (4.40)$$

The plane stress condition $\sigma_{33}=0$ requires special treatment in the elastic-plastic algorithm. If the material behaves elastically, plane stress is enforced implicitly by setting (in terms of the incremental strains, eqns. (4.7), (4.8)):

$$\Delta\epsilon_{33} = -\frac{\nu}{1-\nu}(\Delta\epsilon_{11} + \Delta\epsilon_{22}) \qquad (4.41)$$

If plastic deformations occur within the step, an exact one-step

algorithm enforcing the plane stress condition is not possible (as the plastic correction is stress-dependent). It may be achieved applying the following corrections after the radial return (eqn. 4.32) is performed:

$$\dot{\sigma}_m := -\dot{s}_{33}$$

$$\Delta\epsilon_v := \Delta\sigma_m/(\lambda+2G/3) \tag{4.42}$$

$$\Delta e_{ij} := \Delta e_{ij} + (1/3)(\Delta\epsilon_v^0 - \Delta\epsilon_v)\delta_{ij}$$

where: $\dot{\sigma}_m = (1/3)\,\dot{\sigma}_{kk}$, mean stress

$\Delta\epsilon_v^0$ = predicted volumetric strain

This correction implies a very slight volumetric non-associativity,

$$\sigma_m^{n+1} = (\sigma_m^{n+1})^E/(1+\beta) \tag{4.43}$$

which has no effect for deviatoric plasticity criteria (e.g. Von Mises).

4.5.3 HARDENING AND UNIAXIAL STRESS-STRAIN LAWS

Plastic strains give rise to material hardening. For a kinematic-isotropic Von Mises model (eq. 4.38) the hardening is composed of a kinematic translation (α_{ij}) and an isotropic expansion (Y) of the yield surface:

$$\overset{\circ}{\alpha} = \frac{2}{3} h_\alpha \, \mathbf{d}^p$$

$$\Delta Y = h_Y \Delta\epsilon^p \tag{4.44}$$

where $\Delta\epsilon^p = \sqrt{\dfrac{2}{3}\Delta e_{ij}^p \Delta e_{ij}^p}$ (effective plastic strain increment)

h_α and h_Y are the kinematic and isotropic moduli respectively

The plastic hardening modulus in uniaxial tension is

$$h' = h_\alpha + h_\gamma \qquad (4.45)$$

If $h_\alpha = 0$, hardening is purely isotropic; if $h_\gamma = 0$, it is purely kinematic.

Uniaxial stress-strain laws may be defined as the true axial stress - natural axial strain curves in uniaxial tension tests (sect. 6.2):

$$\sigma = f(\epsilon) \qquad (4.46)$$

where the notation $\sigma = \sigma_{11}$, $\epsilon = \epsilon_{11}$ has been used. Decomposing the differential strain increment into elastic and plastic components,

$$d\epsilon = d\epsilon^E + d\epsilon^P = d\sigma(1/E + 1/h') \qquad (4.47)$$

the total stress-strain modulus may be expressed as

$$h = \frac{d\sigma}{d\epsilon} = \frac{1}{1/E + 1/h'} \qquad (4.48)$$

Uniaxial stress-strain laws are convenient for specifying isotropic material behaviour. A few examples of laws used within this work are given in figure 4.6.

The yield condition may depend also on the strain-rates and the temperature, which provide additional sources of hardening (or softening, as the case may be):

$$Y = Y_0(\epsilon^P) f_R(\dot{\epsilon}^P) f_T(T) \qquad (4.49)$$

Functions f_R (strain-rate dependence) and f_T (temperature dependence) may be defined as piecewise linear laws. A useful analytical form for f_R is (Bodner and Symonds, 1960):

$$f_R(\dot{\epsilon}^P) = 1 + (\dot{\epsilon}^P/B)^m \qquad (4.50)$$

where m and B are material constants. Eqn. (4.50) is equivalent to a
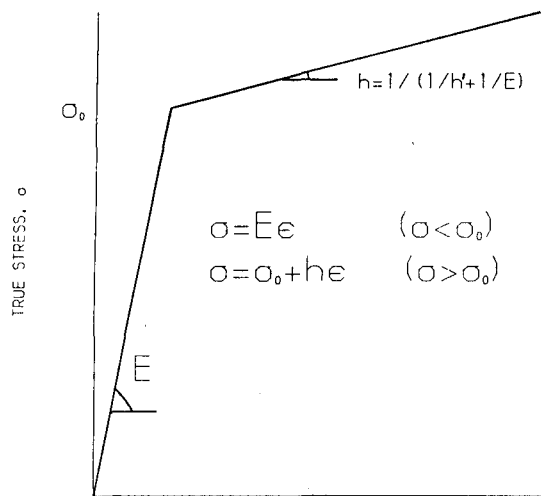
A) BILINEAR ELASTIC-PLASTIC

$$\sigma = E\epsilon \qquad (\sigma < \sigma_0)$$
$$\sigma = \sigma_0 + h\epsilon \qquad (\sigma > \sigma_0)$$
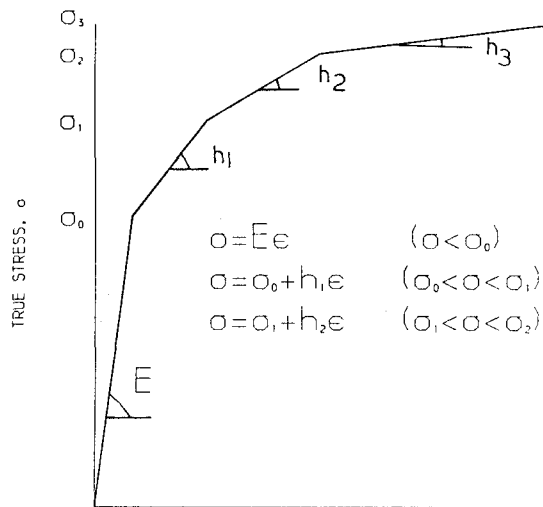
B) PIECEWISE LINEAR ELASTIC-PLASTIC

$$\sigma = E\epsilon \qquad (\sigma < \sigma_0)$$
$$\sigma = \sigma_0 + h_1\epsilon \qquad (\sigma_0 < \sigma < \sigma_1)$$
$$\sigma = \sigma_1 + h_2\epsilon \qquad (\sigma_1 < \sigma < \sigma_2)$$
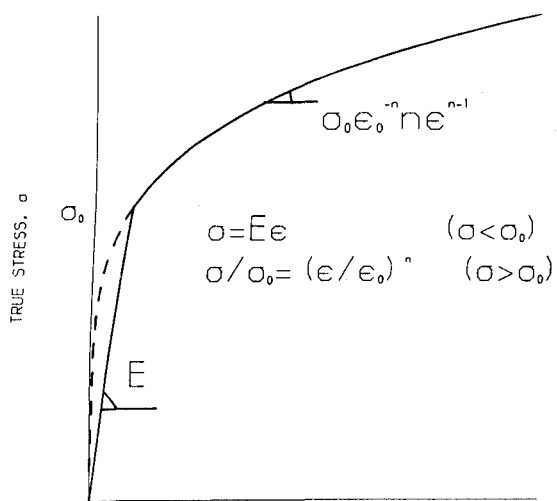
C) POWER LAW ELASTIC-PLASTIC

$$\sigma = E\epsilon \qquad (\sigma < \sigma_0)$$
$$\sigma/\sigma_0 = (\epsilon/\epsilon_0)^n \qquad (\sigma > \sigma_0)$$

Figure 4.6: Uniaxial stress-strain laws implemented in numerical model

$(A_{min} = $ min. Area of any element)

$t_1 = 0.8 \sqrt{A_{min}}$

NODE-SIDE

NODE-NODE

$t_2 = 0.1 \sqrt{A_{min}}$

NODE-NODE

Figure 4.7: Node to node and node to side contacts - regions and normals

viscoplastic idealization such as suggested by Perzyna (1963) or Owen and Hinton (1980):

$$\epsilon^P = \gamma < (F/F_0 - 1)^N > \frac{\partial F}{\partial \sigma} \tag{4.51}$$

where: F_0 and F are the static and dynamic yield conditions resp.;

$<A> = A$ for $A > 0$,

$<A> = 0$ for $A < 0$.

Equivalence between eqns. (4.50) and (4.51) is achieved by assigning the values

$$m = 1/N$$

$$B = \gamma \sqrt{(2/3) \frac{\partial F}{\partial \sigma} : \frac{\partial F}{\partial \sigma}}$$

4.5.4 OBJECTIVE STRESS RATES

Rate-type constitutive equations (4.27) need to be formulated in terms of objective stress rates (section 2.5.1). Jaumann and Truesdell objective rates have been implemented incrementally in the following way:

Jaumann rate of Cauchy stress

$$\overset{\triangledown}{\sigma}_{ij}^{n+1/2} = \overset{\bullet}{\sigma}_{ij}^{n+1/2} + \sigma_{ip}^{n+1} w_{pj}^{n+1/2} + \sigma_{jp}^{n+1} w_{pi}^{n+1/2} \tag{4.52}$$

Truesdell rate of Cauchy stress

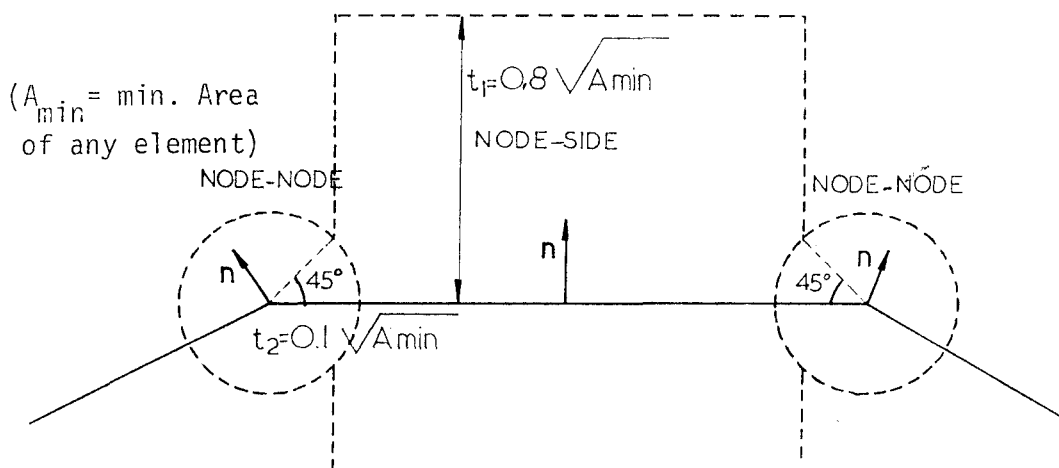$$\overset{\triangle}{\sigma}_{ij}^{n+1/2} = \overset{\bullet}{\sigma}_{ij}^{n+1/2} - \sigma_{ip}^{n+1} v_{j,p}^{n+1/2} - \sigma_{jp}^{n+1} v_{i,p}^{n+1/2} + \sigma_{ij}^{n+1} v_{p,p}^{n+1/2}$$

$$= \overset{\triangledown}{\sigma}_{ij}^{n+1/2} - \sigma_{ip}^{n+1} d_{pj}^{n+1/2} - \sigma_{jp}^{n+1} d_{pi}^{n+1/2} - \sigma_{ij}^{n+1} d_{pp}^{n+1/2} \tag{4.53}$$

Other vectors or tensors (e.g. α, eqn. 4.44) linked to the material frame must also be corrected for rigid body rotations. For a vector T, a corotational rate equivalent to eqn. (4.52) is defined by

$$\overset{\triangledown}{T}_i^{n+1/2} = \overset{\bullet}{T}_i^{n+1/2} - w_{ip}^{n+1/2} T_p^n \tag{4.54}$$

Note that there is half a step lag for the values of stresses in eqns. (4.52) - (4.54). For explicit integration in which steps are very small errors introduced by this will not be important (sect. 5.6). For larger implicit steps, more rigorous algorithms have been proposed by Hughes and Winget (1980), Pinsky, Ortiz and Pister (1983), and Rubinstein and Atluri (1983).

Jaumann's rate is the most commonly used formulation, being a natural choice for removing rigid body rotations (Prager, 1961). Some inconsistencies may arise however in large deformation simple shear with kinematic hardening (Nagtegaal and de Jong (1982), Dafalias (1983), Lee and Mallett (1983)). On the other hand Truesdell's rate is the forward Piola transformation of the rate of 2nd Piola-kirchoff stress and provides a "canonical" form for hyperelastic rate equations (Pinsky, Ortiz and Pister, 1983).

Both Truesdell and Jaumann rates can be made equivalent by appropriate definition of the constitutive tensor (eqn. 3.28). The classical elastic-plastic relations (Prandtl-Reuss eqns. (2.64)) are expressed in terms of true stress and true strain (Hill, 1950). The assumption is made here, as by Hibbit, Marcal and Rice (1970), that the Prandtl-Reuss equations are referred to Jaumann rates of stresses.

4.6 DAMPING

The semidiscrete equations of motion (4.24) may be assembled in matrix form for the complete model, and generalized to include viscous damping:

$$M\ddot{u} + C\dot{u} + P = R \qquad (4.55)$$

where M is the diagonal mass matrix, C is the damping matrix, and P, R represent internal and external forces respectively.

A useful form for the damping matrix is the so-called Rayleigh

damping:

$$C = AM + BK_t \qquad (4.56)$$

where: K_t is the tangent stiffness matrix, $K_t = dP/du$
       A, B are the mass and stiffness damping coefficients.

Rayleigh damping allows eqns. (4.55) to remain uncoupled, and therefore is easily implemented in an explicit code. Mass damping is integrated into the time-marching scheme (eqns. (4.25), (4.26)) by the following operator:

$$\dot{u}^{n+1/2} = [\dot{u}^{n-1/2}(1-A\Delta t/2) + M^{-1}(R^n - P^n)\Delta t]/(1+A\Delta t/2) \qquad (4.57)$$

which implies a modification of the time-integration eqn. (4.25). Stiffness damping is considered by adding viscous force terms to the internal forces:

$$P^{*n} = P^n + B\dot{u}^n dP^n/du \qquad (4.58)$$

approximated in finite difference form by

$$P^{*n} = P^n + B\Delta P^{n+1/2}/\Delta t$$

Stiffness damping is considered by substituting P^n in eqn. (4.57) by P^{*n}.

The amount of damping provided by (4.56) is a function of the frequency. If the system of eqns. (4.55) is put in modal form (assuming tangent linear behaviour and small disturbances), one equation of the following type is obtained per mode:

$$\ddot{x} + (A+B\,\omega^2)\dot{x} + \omega^2 x = r \qquad (4.58)$$

where x is the modal amplitude and ω the frequency of vibration. The amount of damping for each frequency ω is given by

$$\beta = (A/\omega + B\omega)/2 \qquad (4.59)$$

where $\beta = 1$ corresponds to the critical damping. From eqn. (4.59) it may be seen that the effect of mass damping is small for high frequencies, where stiffness damping is important, and viceversa. Mass damping may be likened to dashpots connecting each degree of freedom to ground, and stiffness damping to dashpots between connected nodes.

4.7 STABILITY OF TIME INTEGRATION

Fourier methods (e.g. Richtmeyer and Morton, 1967) may be used for studying the stability of linear systems and small perturbation tangent behaviour in nonlinear systems. The differential modal eqns. (4.58) may be rewritten as

$$\ddot{x} + 2\beta\omega\dot{x} + \omega^2 x = 0 \qquad (4.60)$$

from which the external forcing function (r) has been dropped. The harmonic solution to this equation is

$$x^n = e^{\gamma n \Delta t} = \lambda^n \qquad (4.61)$$

where γ, λ are complex numbers (note the superscript on λ is an exponent). Substituting eqn. (4.61) within central difference eqns. (4.25 - 4.26) one obtains

$$\ddot{x}^n = (x^{n+1} - 2x^n + x^{n-1})/\Delta t^2 = \lambda^{n-1}(\lambda^2 - 2\lambda + 1)/\Delta t^2$$

$$\dot{x}^n = (x^{n+1} - x^{n-1})/2\Delta t = \lambda^{n-1}(\lambda^2 - 1)/2\Delta t \qquad (4.62)$$

which with eqn. (4.60) yield

$$\lambda^2(1 + \Delta t \omega \beta) + \lambda(\omega^2 \Delta t^2 - 2) + (1 - \Delta t \omega \beta) = 0 \qquad (4.63)$$

for stability, the solution λ to this equation must be complex and of modulus not greater than 1. These conditions impose

$$\beta \geqslant 0$$

$$\Delta t < \frac{2}{\omega}\sqrt{1 - \beta^2} \qquad (4.64)$$

The second condition must be satisfied for all the frequencies present in the model. As damping is usually small, a sufficient condition will be

$$\Delta t < \frac{2\sqrt{1-\beta^2}}{\omega_{max}} \qquad (4.65)$$

Damping has an adverse effect on stability, although stiffness and mass damping behave differently in this respect. Considering that the condition (4.65) applies for the highest frequency of the model, from eqn. (4.59) it may be seen that mass damping will virtually have no effect, while stiffness damping may be very detrimental.

For undamped motion ($\beta = 0$) the critical time-step reduces to

$$\Delta t < 2/\omega_{max} \qquad (4.65)$$

An upper bound expression for the critical time-step is given by the Courant criterion (Courant, Friedrichs and Lewy, 1928), which limits the time-step to the interval necessary for the stress-waves to travel across one element,

$$\Delta t < h_{min}/c \qquad (4.66)$$

where h_{min} is the minimum element dimension, and c the maximum stress-wave velocity. For an elastic-plastic material the fastest stress waves are the compressional or "P" waves, for which $c = \sqrt{(\lambda+2G)/\rho}$.

4.8 MODELLING OF CONTACTS

Contact between different boundaries of one or more continua is frequent in impact modelling and imposes special nonlinear boundary conditions. Two main aspects are involved in contact modelling: the contact interface laws and the detection of interacting surfaces.

4.8.1 CONTACT INTERFACE LAWS

A penalty method is used for the contact laws, consisting of placing interface springs between "intruding" nodes and "target" surfaces. Forces generated by these springs will act on both sides of the interface. For complete symmetry of the logic, both sides of the interface may be taken in turn as "intruding" sides. The interface laws are

- Normal force: $F_C^N = K^N d^N$

$$(4.68)$$

- Shear force: $F_C^S = \min(K^S d^S, F_C^N \mu)$

where K^N, K^S are the normal and shear stiffness values

d^N, d^S are the normal and shear penetrations

μ is the coefficient of friction

The shear law defines a kinematic slip circle of radius $F_C^N \mu / K^S$. Note that the penetration d is a vector linked to the Lagrangian frame and therefore must be updated with a corotational formulation (eqn. 4.54).

An important detail of the formulation is the value used for the contact stiffness. Marti (1983) uses a constant user-defined value for the whole model, which should be of similar magnitude to the element stiffness. This method is simple and appropriate for uniform 3-D meshes, but problems will arise for non-uniform or axisymmetric models. Hallquist (1982) computes a different stiffness for each contact, proportional to that of the target element.

In this work, the contact stiffness varies for each contact, using a simple but effective method. The stiffness is calculated for each contact as

$$K = kM^I / \Delta t_C^2 \qquad (4.69)$$

where M^I is the mass of the intruding node

Δt_C is the critical time-step for the model (eqn. 4.66)

k is a coefficient normally defaulted to 0.1 (Larger values may

cause instabilities if a corresponding reduction is not used for the computational time-step)

This form for the contact stiffness ensures a value below the maximum element stiffness in the model (thus not compromising stability) and above the stiffness of the element in contact (thus avoiding unacceptable penetrations):

- maximum element stiffness - $K^{max} = (1/4)V_{cr}(\lambda+2G)/h^2_{min}$
- contact stiffness - $K_C = 2kV_{cr}(\lambda+2G)/h^2_{min}$
- interface (target) element stiffness - $K^T = (1/4)V^T(\lambda+2G)/h^2_{min}$

where V_{cr} is the volume of the element giving the critical time-step, and V^T that of the interface target element.

This derivation of the contact stiffness also produces a uniform "push-back" recovery action along the contact interface, which is important specially for axisymmetric models, where the element stiffnesses and masses are radius dependent. This may be shown by considering the accelerations at the intruding side (a^I) and target side (a^T) for a given penetration d:

$$a^I = F_C/M^I = Kd/\Delta t_c^2$$

$$a^T = F_C/M^T = (Kd/\Delta t_c^2)(M^I/M^T)$$

(4.70)

Assuming the mesh is uniform on both sides of the interface $(M^I/M^T=1)$, for symmetric (double) contacts the recovery of the penetration in one time-step will be

$$d_R = 2(1/2)(a^I + a^T)\Delta t^2 = K\eta^2 d \qquad (4.71)$$

where $\Delta t = \eta \Delta t_c$ is the computational time-step $(\eta < 1)$. The mesh can be non-uniform along the contact interface, but should generally not be too different accross it $(M^T \sim M^I)$. The frequency of the contact spring connecting M^T and M^I will be proportional to

$$(K/\Delta t_c^2) M^I/M^T$$

Large ratios M^I/M^T will require reductions in the computational time-step.

For high velocity impact in which large contact pressures are produced, the contact stiffness may have to be scaled up by changing the default value of k in eqn. (4.69), in order to avoid unacceptably large penetrations. This would again require a corresponding reduction of the computational time-step.

Application of eqns. (4.68) requires definition of a normal to the contact. For this purpose, contacts are classified as node-node or node-side (fig. 4.7). For node-side contacts, the normal is directly that of the target side. For node-node contacts, the normal is computed by averaging those from the two adjoining sides.

Finally lies the question of distributing the contact force on target and intruding surfaces. On the intruding surface the sole recipient is always the intruding node, but for the target side force distribution depends on whether contact is of node-node or node-side type. For node-node contacts the interface force is assigned entirely to the target node. For node-side contacts the interface force is distributed to the two nodes in the target side, in inverse proportion to their distance to the intruding node.

A flowchart of the computations for determining the normals, penetration and contact forces is given in figure 4.8.

4.8.2 CONTACT DETECTION ALGORITHM

Detection of new contacts and book-keeping for the lists of active contacts must be performed in an efficient and reliable way to provide robust models for impact and sliding. In the present 2-D model a contact is established and kept if the intruding node either

a) penetrates the target side (*non-zero interaction force*)
b) projects on the target side without penetrating, lying in either of the node-side or node-node areas (fig 4.7) (zero interaction force)

START

NODE – NODE?

Intruding Node: P
Target Node: A
Normal & Tangential
vectors: **n, t**
(average adjoining sides)

Intruding Node: P
Target Nodes: A,B
Normal & Tangential
vectors: **n, t**

ERROR
STOP

CONTACT
SLIDING?

Old
contact side?

Old vectors: t_0, n_0

Old vectors: t_0, n_0

COMMON CELL?

New
contact NODE–
SIDE ?

NEW
CONTACT SIDE?

C = common Cell
avge. vectors:
$n_{av}=n_C$, $t_{av}=t_C$

C = new Cell
avge. vectors:
$n_{av}=n$, $t_{av}=t$

C = old Cell
avge. vectors:
$n_{av}=n_C$, $t_{av}=t_C$

C = new Cell
avge. vectors:
$n_{av} = \dfrac{n_0+ n}{n_0+ n}$

C = new cell
avge., old vectors:
$n_{av}=n_0=n$
$t_{av}=t_0=t$

RETURN

BREAK
CONTACT

Normal penetration
$d_n = -AP \cdot n$

Compute w_{ij}^C, $v_{i,j}^C$
$\Delta d_i^I = (-d_n^O n_j^O + d_s^O t_j^O)w_{ij}^C \Delta t$
$\Delta d_i^{II} = [v_i^P - (v_i^A + v_{i,j}^C(x_j^P - x_j^A))] \Delta t$
$d_s = d_s^O + (\Delta d_i^I + \Delta d_i^{II})t_i^{av}$

$d_s = 0$

$d_n > -t_2$?

$d_n = \max(0, d_n)$

$F_n = K_n d_n$
$F_s = \min(\mu_C F_n, K_s d_s)$
$d_s = \min(d_s, F_s/K_s)$

new contact ?
$d_n^{old} < 0$

distribute forces
$r^A = AP \cdot AB/(AB \cdot AB)$
$F^A = -F \ r^A$
$F^B = -F(1-r^A)$

$F = F_s t + F_n n$

NODE – NODE?

Apply force to P:
$F^P = F$

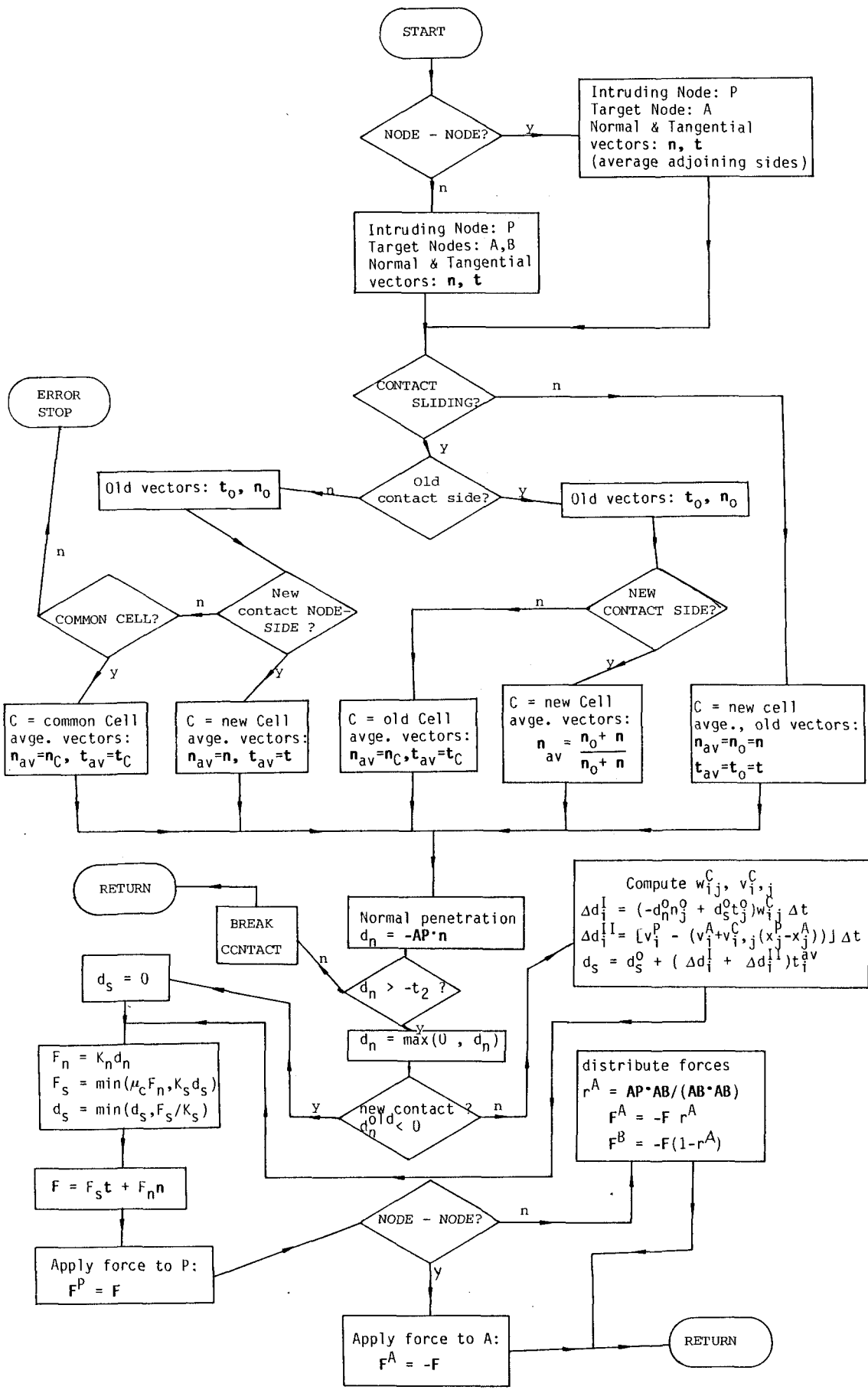Apply force to A:
$F^A = -F$

RETURN

FIGURE 4.8: SUBROUTINE CONFOR – CALCULATION OF CONTACT PENETRATION AND INTERFACE FORCES
(FLOWCHART)

A completely general capability for automatic detection of new contacts (i.e. any node of any external surface with any other surface) would generally carry an excessive computional overhead. Two intermediate procedures have been implemented here for the detection of contacts:

- New interactions near an existing contact will be detected automatically, by checking in every step the neighbours to all existing contacts. Element adjacency lists are kept in the program memory for this purpose. All contacts within one interface area will be picked up by giving just one seed contact. A contact search algorithm has been included which finds the correct target side from an incorrect guess.

- For Automatic detection of new contacts, areas that may touch at an unknown instant may be earmarked by specifying lists of nodes, which will be checked against each other for contact at each time-step. In fact, these areas may encompass the whole external boundary of the bodies involved, if the location of contacts is totally unpredictable beforehand, although this will normally carry a large overhead in the computational costs.

Sliding of existing contact areas is achieved by checking, prior to relinquishing a non-active contact, if the intruding node has slid to any of the neighbouring target sides.

Flow-charts for the contact calculations with the search and the book-keeping logic are given in figures 4.9 and 4.10.

4.9 HEAT CONDUCTION

Heat flow rates accross the continuum are computed from Fourier's law:

$$h_i^{n+1/2} = KT_{,i}^n \qquad (4.72)$$

where h_i is the rate of heat flow in direction i per unit normal surface, K the conductivity, and T the temperature. An explicit Euler
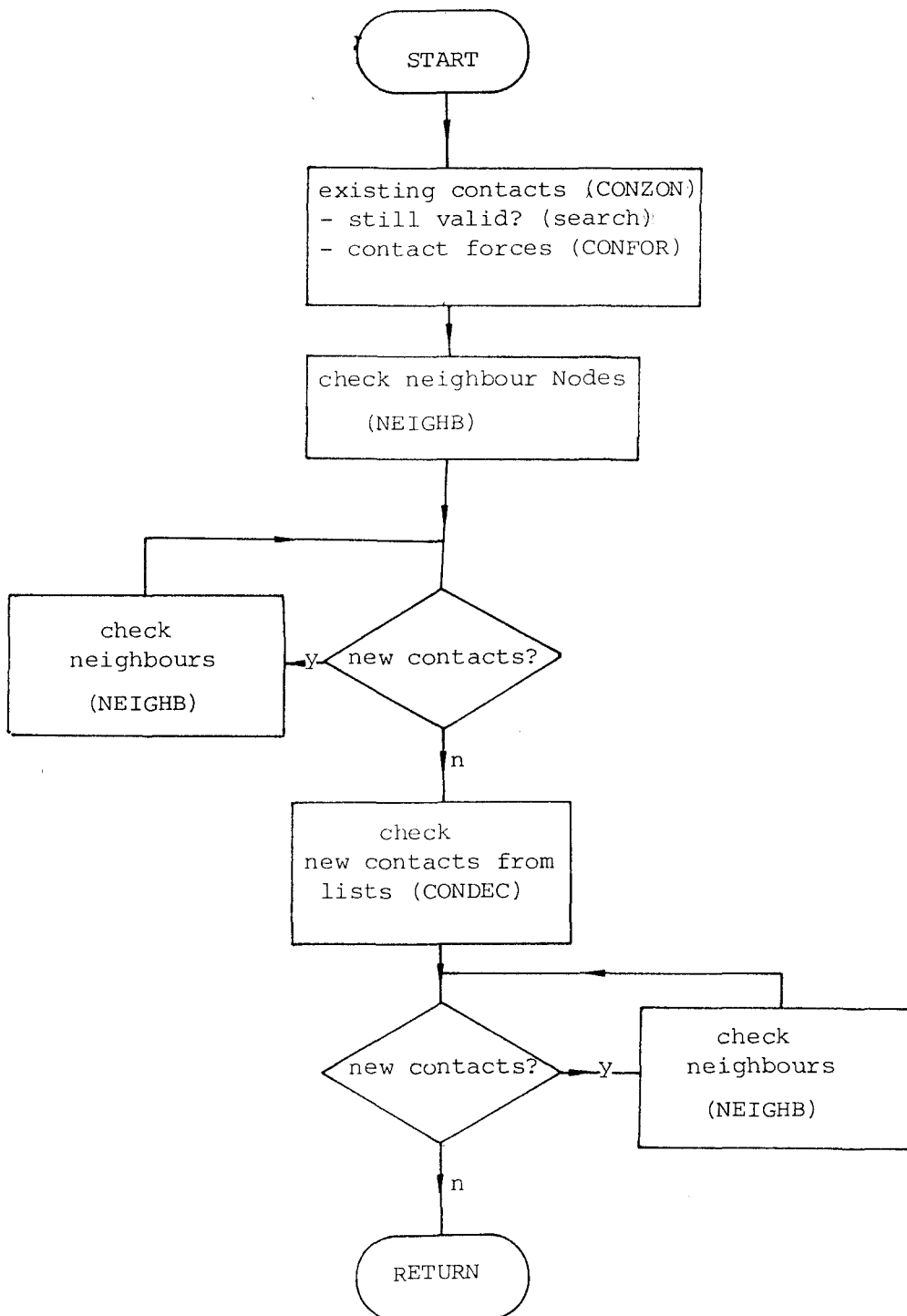
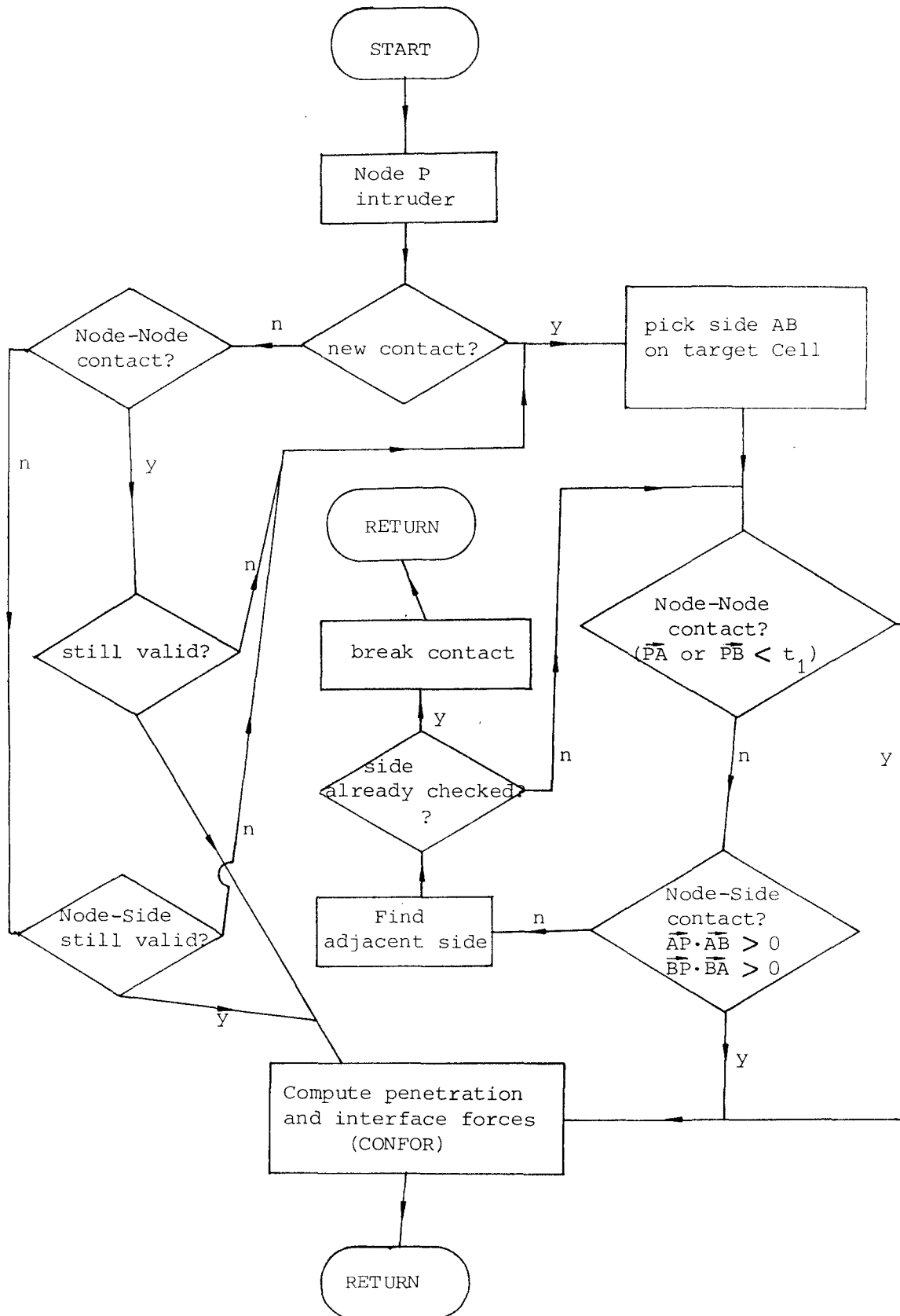Figure 4.9: Subroutine CONTAC, driver for Contact calculations
(Flowchart)

START

Node P
intruder

Node-Node
contact? ←n— new contact? —y→ pick side AB
on target Cell

Node-Node
contact?
$(\overline{PA}$ or $\overline{PB} < t_1)$

still valid?

RETURN

break contact

Node-Side
still valid?

side
already checked?
?

Find
adjacent side ←n— Node-Side
contact?
$\overline{AP} \cdot \overline{AB} > 0$
$\overline{BP} \cdot \overline{BA} > 0$

Compute penetration
and interface forces
(CONFOR)

RETURN

Figure 4.10: CONZON subroutine - check and search for contacts
(Flowchart)

forward integration scheme is implied in eqn. (4.72).

For a small region the rate of heat inflow into it may be found by integrating over its surface S,

$$H^{n+1/2} = -\int_S KT^n_{,i} \, n_i \, dS \qquad (4.73)$$

which may be particularized for a triangular or tetrahedral cell as a sum over the cell faces:

$$H = (1/m)\sum_{j=1}^{m} K^j S^j (T^j - T)/(d^j - d) \qquad (4.74)$$

where m = no. of sides (3 triangle, 4 tetrahedron)

K^j, S^j are the conductivity and surface of side j

d^j, T^j are the height of and temperature at the cell adjoining j

d, T are the height and temperature at the current cell.

For boundary faces, the contribution to the sum in eqn. (4.74) is calculated according to the appropriate boundary condition:

- Dirichlet $\quad T^e = Const., \quad H^j = mK(T^e - T)S^j/d \qquad (4.75)$

- Neumann $\quad h^e = Const., \quad H^j = h^e S^j \qquad (4.76)$

- Mixed $\quad T^e/C_T + h^e/C_h = 1, \quad H^j = mKS^j(C_T - T)/(d + KmC_T/C_h) \qquad (4.77)$

Other sources of heat such as plastic work must be considered when formulating the energy balance (eqn. 2.32), to compute the temperature increments in each cell:

$$\Delta T = [(H\Delta t + \xi \, \sigma : \Delta \epsilon^P V^C)/\rho V^C + \Delta Q]/C_p \qquad (4.78)$$

where: ξ defines the amount of plastic work transformed to heat, (defaulted to 0.95)

V^C is the cell volume

ρ is the mass density

ΔQ is heat generated from other sources per unit mass

C_p is the specific heat

For an Euler forward time integration scheme (eqn. 4.72), computations are conditionally stable. For a rectangular mesh, the critical time-step for stability is (Richtmyer and Morton, 1967):

$$\Delta t_c = (1/2)(1/\Delta x^2 + 1/\Delta y^2) \, / \, (K/\rho C_p) \qquad (4.79a)$$

For triangular and tetrahedral meshes, empirical results obtained in this work suggest the following critical time-steps.

- Triangles: $\Delta t_c = (1/8)h_{min}^2 \, / \, (K/\rho C_p)$ (4.79b)
- Tetrahedra: $\Delta t_c = (1/12)h_{min}^2 \, / \, (K/\rho C_p)$ (4.79c)

4.10 ENERGY COMPUTATIONS

Explicit schemes such as central difference are only conditionally stable. In a linear system, an instability is readily detected, as it will cause overflow in the computations within a few cycles. Unfortunately, this is not the case generally for non-linear materials. Instabilities are associated with spurious release of energy. Plastic materials may absorb the spurious energy through plastic deformation, whereby instabilities could go unnoticed even though large errors may be present. An energy balance check (as recommended by Belytschko (1978, 1983)) has been implemented in order to detect "arrested" instabilities.

At every instant, Energy balance dictates

$$W_{Int} + U_{Kin} - W_{Ext} = 0 \qquad (4.80)$$

For checking eqn. (4.80), W_{Int} (internal energy), U_{Kin} (kinetic energy) and W_{Ext} (external energy) are followed during the computations. The algorithms for these energy computations are given below. Note that some energy components are computed incrementally,

$$W^{n+1} = W^n + \Delta W^{n+1/2}$$

while for others the total value W^n is recomputed at each step.

Internal Energy

Internal energy is composed of continuum energy (I), damping energy (II), and energy in the contacts (III):

$$W_{int} = W_I + W_{II} + W_{III} \tag{4.81}$$

- Continuum energy is computed incrementally as

$$\Delta W_I^{n+1/2} = (\Delta t/2) \int (\sigma^n + \sigma^{n+1}){:}d^{n+1/2}dV = (1/2)\sum_{N=1}^{NUMNOD} \Delta u_N^{n+1/2}(P_N^n + P_N^{n+1}) \tag{4.82}$$

Where **P** are the nodal forces, obtained by integrating the continuum stresses (eqn. 4.9). For elastic-plastic materials the continuum energy may be decomposed into elastic and plastic components:

$$W_I = W_{El} + W_{Pl}$$

$$\Delta W_{Pl}^{n+1/2} = (\Delta t/2) \int (\sigma^n + \sigma^{n+1}){:}(d^P)^{n+1/2}dV$$

$$\Delta W_{El}^{n+1/2} = (\Delta t/2) \int (\sigma^n + \sigma^{n+1}){:}(d^E)^{n+1/2}dV \tag{4.83}$$

For an isotropic elastic Von Mises model the expression for the plastic work may be simplified to

$$\Delta W_{Pl}^{n+1/2} = (\Delta t/2) \int (\sigma_{eq}^n + \sigma_{eq}^{n+1}) \, \dot{\epsilon}^P dV \tag{4.84}$$

where $\sigma_{eq} = \sqrt{(3/2)s{:}s}$ (Von Mises equivalent stress).

- Damping energy increments are computed as

$$\Delta W_{II}^{n+1/2} = (1/2)\sum_{N=1}^{NUMNOD} \Delta u_N^{n+1/2}[AM_N u_N^{n+1/2} + (P_N^{n+1} - P_N^n)B/2\Delta t] \tag{4.85}$$

- Energy at contacts consists of potential energy stored plus

dissipated frictional energy:

$$W_{III}^n = (1/2) \sum_{J=1}^{NUMCON} [K_N^J (d_N^J)^2 + K_S^J (d_S^J)^2] + W_{Fri}^n \qquad (4.86)$$

$$\Delta W_{Fri}^n = F_N^n (d_{So}^n - d_S^n)$$

where $d_{So}^n - d_S^n$ represents the slip (predicted minus corrected shear displacement). Subscript N here indicates Normal (penetration or stiffness)

Kinetic energy

$$U_{Kin}^n = (1/8) \sum_{N=1}^{NUMNOD} (\dot{u}_N^{n+1/2} + \dot{u}_N^{n-1/2})^2 M_N \qquad (4.87)$$

External work

$$\Delta W_{Ext}^{n+1/2} = (1/2) \sum_{N=1}^{NUMNOD} \Delta u_N (F_N^n + F_N^{n+1}) \qquad (4.88)$$

For computations carried out on a CRAY-1S with around 10^5 time-steps and 500 cells, the errors in matching energy balance (eqn. 4.80) have normally been lower than $0.005\% W_{Ext}$. The same computations on a VAX11/785 have had errors lower than $0.15\% W_{Ext}$.

4.11 IMPLEMENTATION INTO FORTRAN PROGRAM

The algorithms described in this chapter have been implemented into a Fortran77 computer program (Goicolea, 1985a). The program contains some additional facilities not described here, such as rod elements (e.g. for modelling bolts, reinforced or prestressed concrete). Some effort was taken to make the program user-friendly, allowing a flexible structure for the input, free format command interpretation, some mesh generation facilities, and sensible defaults for non-specified parameters. User-friendliness was important for two reasons:

- The program has been used as a production code for non-linear and impact engineering analyses (e.g. Principia Mechanica Ltd.(1983), Dostal, Phelan and Trbojevic (1985))

- Extensive application of the program has been done within this thesis (Chapters 5,6,7).

A restart facility is available, which permits the computations to be recommenced from predetermined "saved" instants. It also allows recovery from a system crash or forced halt.

Output files with histories of monitored variables, deformed geometries, and stress/strain components for contour plotting are produced. These files can be input to post-processors such as PR2DPL (Goicolea, 1985b), CURVA (Goicolea, 1985c) and PRISM (Principia Mechanica Ltd., 1984). PRISM can also act as a pre-processor generating meshes.

Program development was done initially on a CDC7600 and later on a CRAY-1S of the University of London. Minor parts of the code have been vectorized for the CRAY, but a more thorough effort in vectorization was not considered necessary for the present research work. As it is, the performance is about 15000 cellsXcycle per CPU second. On a CDC7600 the program will run approximately 50% slower, on a PRIME750 40 times slower, and on a VAX11/785 20 times slower.

Definition of the problem, time-cycle computations, and redefinition may be specified in a flexible way within certain rules (e.g. material properties and mesh must be defined before the time-cycle computations). A typical problem sequence is indicated in fig. 4.11. The flow-chart for the time-cycle computations is given in fig. 4.12.
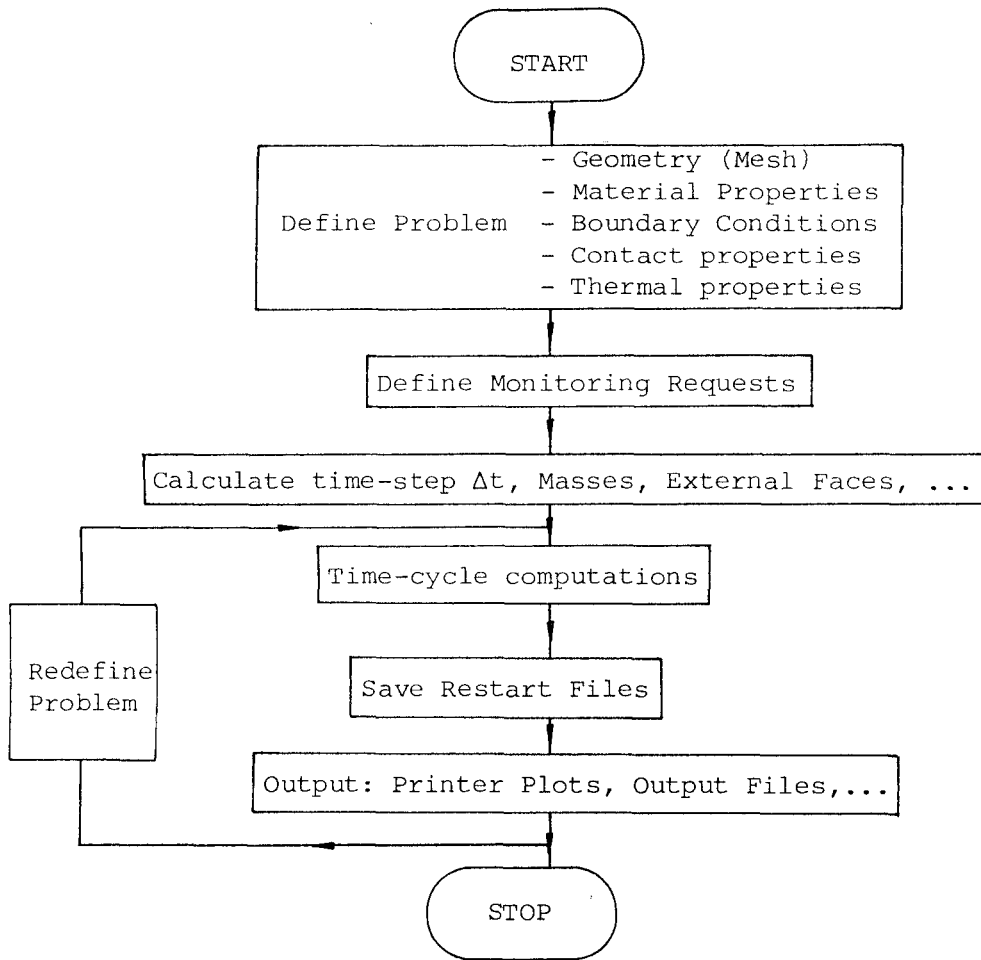
```
                    ╭─────────────╮
                    │    START    │
                    ╰─────────────╯
                           │
                           ▼
        ┌──────────────────────────────────────────┐
        │                   - Geometry (Mesh)        │
        │                   - Material Properties    │
        │  Define Problem   - Boundary Conditions    │
        │                   - Contact properties     │
        │                   - Thermal properties     │
        └──────────────────────────────────────────┘
                           │
                           ▼
           ┌──────────────────────────────┐
           │  Define Monitoring Requests  │
           └──────────────────────────────┘
                           │
                           ▼
    ┌──────────────────────────────────────────────────────┐
    │ Calculate time-step Δt, Masses, External Faces, ...   │
    └──────────────────────────────────────────────────────┘
                           │
              ┌────────────▼──────────────┐
              │  Time-cycle computations  │
              └───────────────────────────┘
                           │
  ┌──────────┐             ▼
  │ Redefine │   ┌────────────────────────┐
  │ Problem  │   │   Save Restart Files   │
  │          │   └────────────────────────┘
  └──────────┘             │
                           ▼
        ┌──────────────────────────────────────────────┐
        │ Output: Printer Plots, Output Files,...       │
        └──────────────────────────────────────────────┘
                           │
                           ▼
                    ╭─────────────╮
                    │    STOP     │
                    ╰─────────────╯
```

Figure 4.11: Typical sequence for explicit numerical modelling job
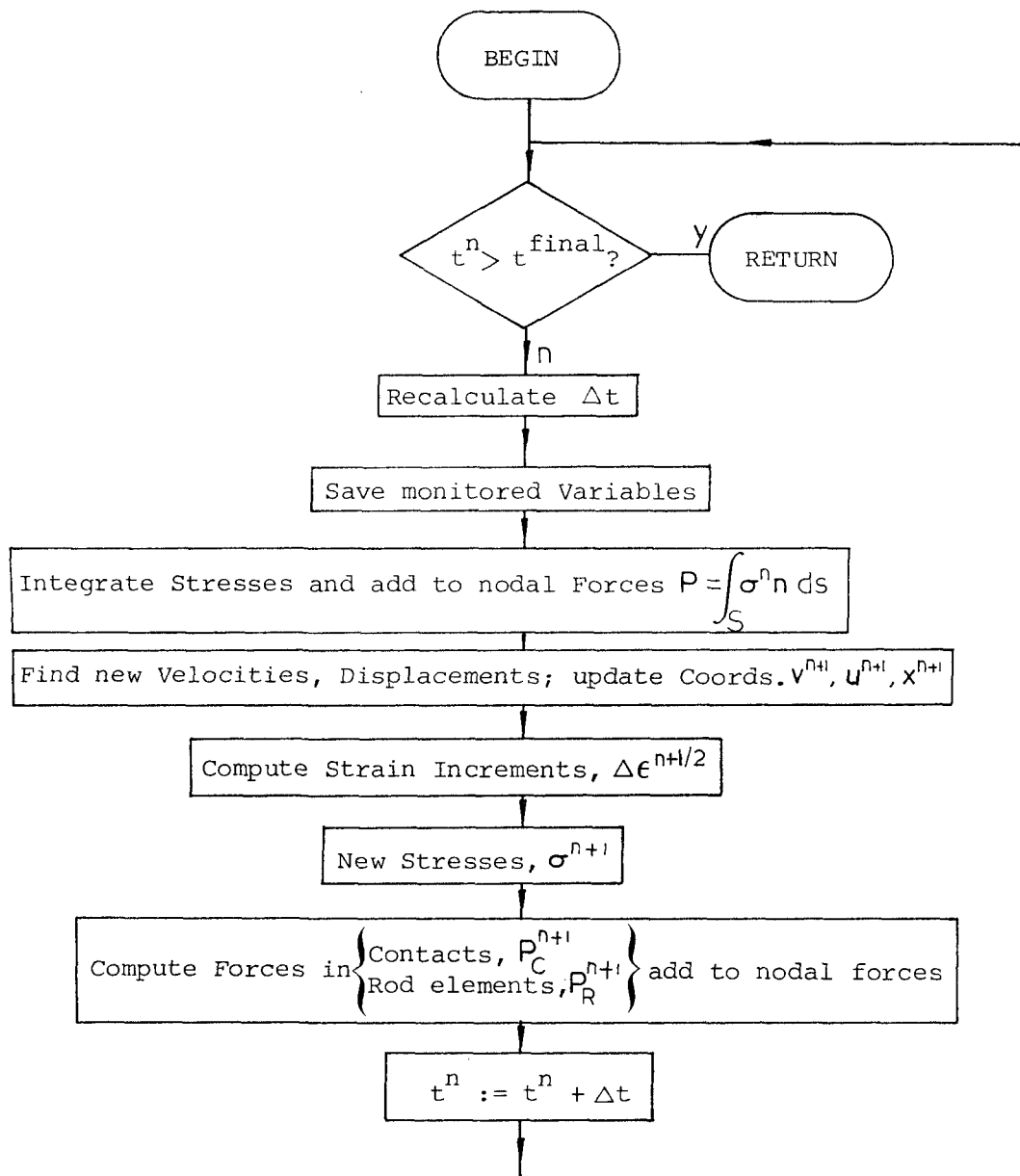
Figure 4.12: Flowchart for explicit computational cycle

CHAPTER 5

BENCHMARKS AND VALIDATION EXAMPLES

5.1 INTRODUCTION

5.2 WAVE PROPAGATION

    5.2.1 Elastic waves in bars

    5.2.2 Elastic-Plastic waves

    5.2.3 Elastic waves in cone

5.3 VIBRATION OF A CANTILEVER

5.4 STATIC ELASTIC-PLASTIC PROBLEMS

    5.4.1 Punch test

    5.4.2 Elastic-Plastic sphere under internal pressure

5.5 HEAT CONDUCTION

    5.5.1 Coupled thermomechanical analysis

    5.5.2 Temperature redistribution in a slab

5.6 LARGE STRAINS AND ROTATIONS

5.7 IMPACT OF CYLINDER

5.8 CONCLUSIONS

5.1 <u>INTRODUCTION</u>

The purpose of this chapter is to present a number of representative benchmark tests, validating the Finite Difference techniques used in this work. Most of the tests have been chosen with available analytical solutions to compare with, but for some the comparison can only be done with other numerical results reported in the literature.

The features tested concern primarily the Elastic-Plastic mechanical behaviour of continua. This includes mainly dynamic tests (both wave-propagation and inertia-dominated types), although some quasi-static problems are also solved using dynamic relaxation. A simple heat conduction test provides a check for the thermal capabilities.

No tests are presented for thermo-mechanical coupled problems, as further application work on the topic was not done for this thesis. This leaves some scope for further work on the matter.

5.2 <u>WAVE PROPAGATION</u>

A few examples of wave propagation problems are given here. The first three concern the propagation of waves along a bar in response to the sudden application of a body force. An example of the transmission of waves in an Elastic-Plastic material with hardening is given next. Finally, the behaviour of stress waves in a conical bar is examined with an illustrative example.

5.2.1 ELASTIC WAVES IN BARS

Three problems are presented in this section concerning the propagation of elastic waves in bars. The bar dimensions are in all cases 1mx1mx20m, and the common mesh utilized in the analyses consists of 20 quadrilaterals of 1mx1m (fig. 5.1) (each quadrilateral is composed of 2 triangles). The material properties are as follows:

$\rho = 2000 \ Kg/m^3$

$E = 13.2 \times 10^8 Pa$

$\nu = 0.31$

1m x 1m x 20m

gravity
force
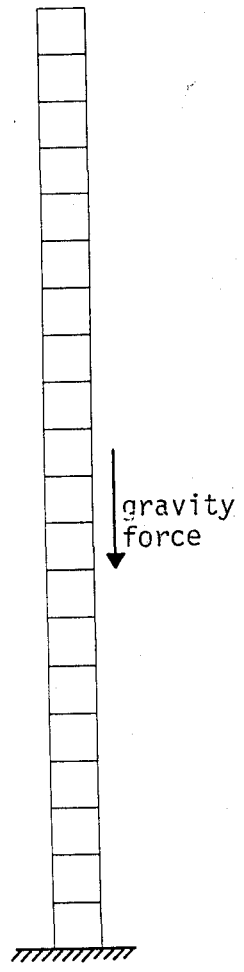
Figure 5.1: Mesh used for models of wave propagation in bars
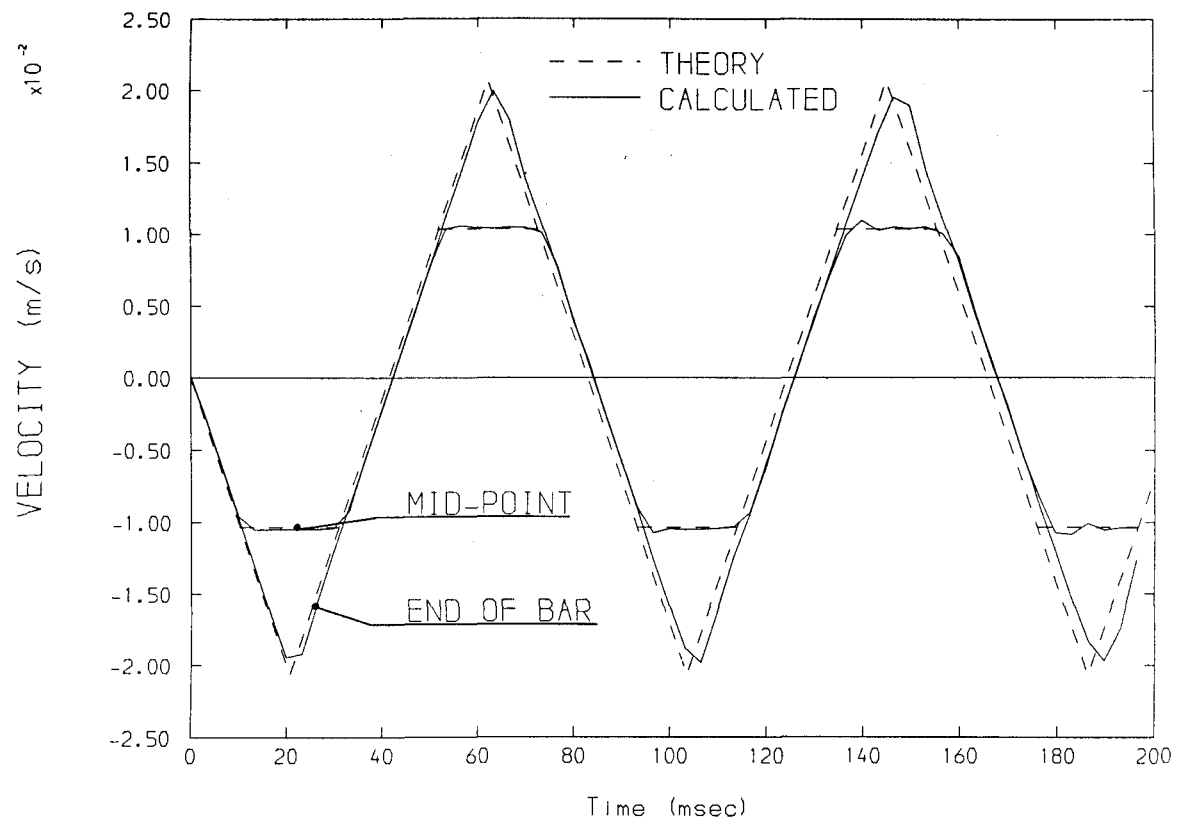
Figure 5.2: CONSTRAINED LONGITUDINAL ELASTIC WAVES IN BAR

Density $\qquad$ $\rho = 2000$ Kg/m^3

Elastic modulus $\qquad$ E = 1320 MPa

Poisson's ratio $\qquad$ $\nu = 0.31$

The bars are initially at rest, stress-free and fixed at one end. A body force (gravity) of unit value is then applied suddenly. This creates a wave pattern as the pulse rebounds and travels back and forth along the bar. The period of this wave is

$$T = 4L/c \qquad\qquad (5.1)$$

where L is the length of the bar and c the velocity of propagation. The maximum point velocity attained should be

$$v = gL/c \qquad\qquad (5.2)$$

where g is the gravity force applied.

Constrained P-waves

If the nodes are constrained to move only parallel to the axis of the bar and in plane strain, the velocity of propagation is that of a plane compressional wave in an infinite medium:

$$c_p = \sqrt{(\lambda + 2G)/\rho} \qquad\qquad (5.3)$$
$$= 966.2 \text{ m/s}$$

Theoretical and numerical results showing the velocity histories at the free tip and mid-point of the bar are presented in fig. 5.2.

Unconstrained P-waves

In this case the bar is allowed to expand laterally, being modelled in plane stress. The wave velocity is that of a one-dimensional bar,

$$c_0 = \sqrt{E/\rho} \qquad\qquad (5.4)$$
$$= 811.5 \text{ m/s}$$

The resulting velocity histories are given in fig. 5.3

Shear waves

The body force will now be normal to the axis of the bar. To prevent bending from developing, the nodes are constrained in the longitudinal direction; this way, the distortion is resisted only by shear stresses. The velocity of wave propagation is:

$$c_S = \sqrt{G/\rho}$$
$$= 500 \text{ m/s}$$

(5.5)

Results for this case are given in figure 5.4.

5.2.2 ELASTIC-PLASTIC WAVES

Let an unconstrained rod of Elastic-Plastic material, with linear strain-hardening, impinge normally upon a rigid flat anvil, giving rise to a stress higher than the yield value Y. An Elastic and a Plastic wave are originated and propagate simultaneously through the material. the theoretical solution to this problem has been discussed by Johnson (1972).

The bar is again of dimensions 1mx1mx20m, and the same mesh from fig. 5.1 is used. The remaining parameters are:

Elastic modulus	$E = 6400$ Pa
Yield stress	$Y = 40$ Pa
Mass density	$\rho = 1$ Kg/m^3
Elastic-Plastic modulus	$H = 640$ Pa
Impact velocity	$v = 1$ m/s

The elastic wave will travel at a speed of

$$c_0 = \sqrt{E/\rho} = 80 \text{ m/s}$$

while the Plastic wave lags behind with a velocity of
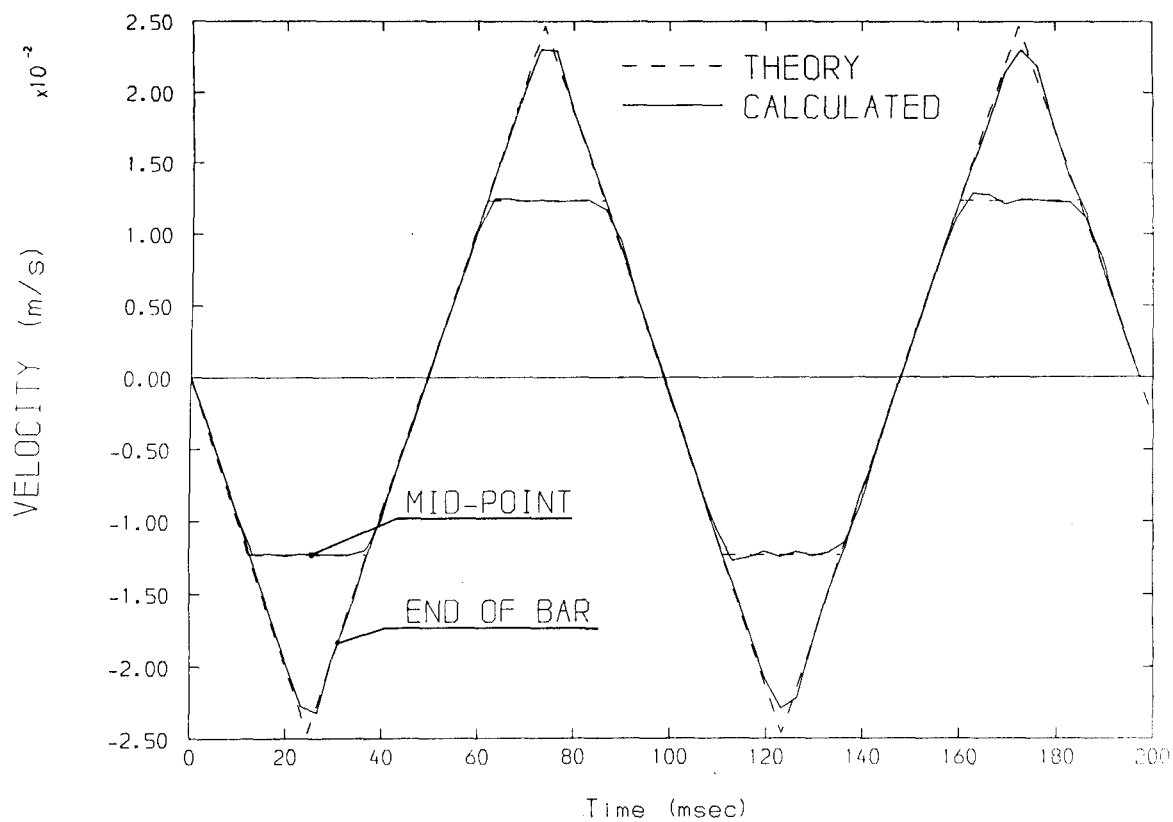
Figure 5.3: UNCONSTRAINED LONGITUDINAL ELASTIC WAVES IN BAR
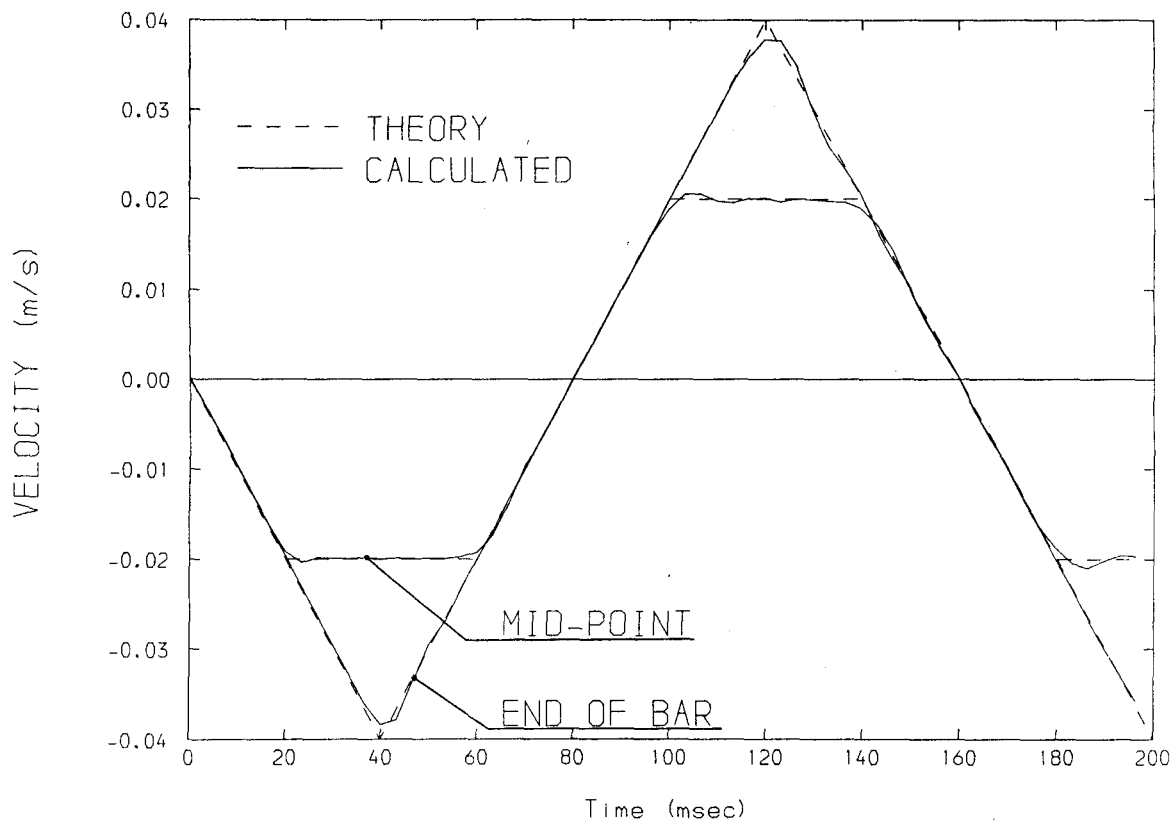
Figure 5.4: ELASTIC SHEAR WAVES IN COLUMN

$$c_1 = \sqrt{H/\rho} = 25.3 \text{ m/s}$$

The Elastic wave is reflected from the free end as an unloading wave. As it returns along the bar it will meet the oncoming plastic front at a certain instant t_1, at a point defined by its distance from the impacting end, x_1:

$$t_1 = 2L/(c_0 + c_1) = 0.38s$$

$$x_1 = (2c_1/c_0)/(1 + c_1/c_0) = 9.61m$$

From this point elastic waves are reflected back into each part of the bar; these waves continue to travel and rebound succesively. The plastic strains extend only to the region $x < x_1$.

In the calculations, appreciable plastic strains occurred only for the first 10m of the bar, as predicted. A time history of stress at a distance x=4.67m is shown in fig. 5.5. This point sees the passage of the elastic front, and then the plastic front. After that, elastic rebounds create further fronts.

5.2.3 ELASTIC WAVES IN CONE

Experiments on conically-tapered Hopkinson bars show that compressive stress-waves create a tension tail, which makes the bar move backwards as the time-piece is thrown off. Landon and Quinney (1923) first analyzed this phenomenon, assuming an exponential form for the applied pressure pulse, typical of an explosive charge. Kolsky (1953) has presented the theoretical analysis in a revised form. The pulse is given by a displacement law of the form

$$u = (A/r)\exp[(-r - c_0 t)/B] - (A/r) \qquad (5.6)$$

where r is the distance from the apex of the cone and t the time. t=0 corresponds to the arrival of the head of the pulse at the apex, t being negative whilst the pulse is travelling towards the apex. Eqn. (5.6) holds for negative values of t, where $r > |c_0 t|$. For $r < |c_0 t|$ the displacement is zero. B is the characteristic length of the pulse,
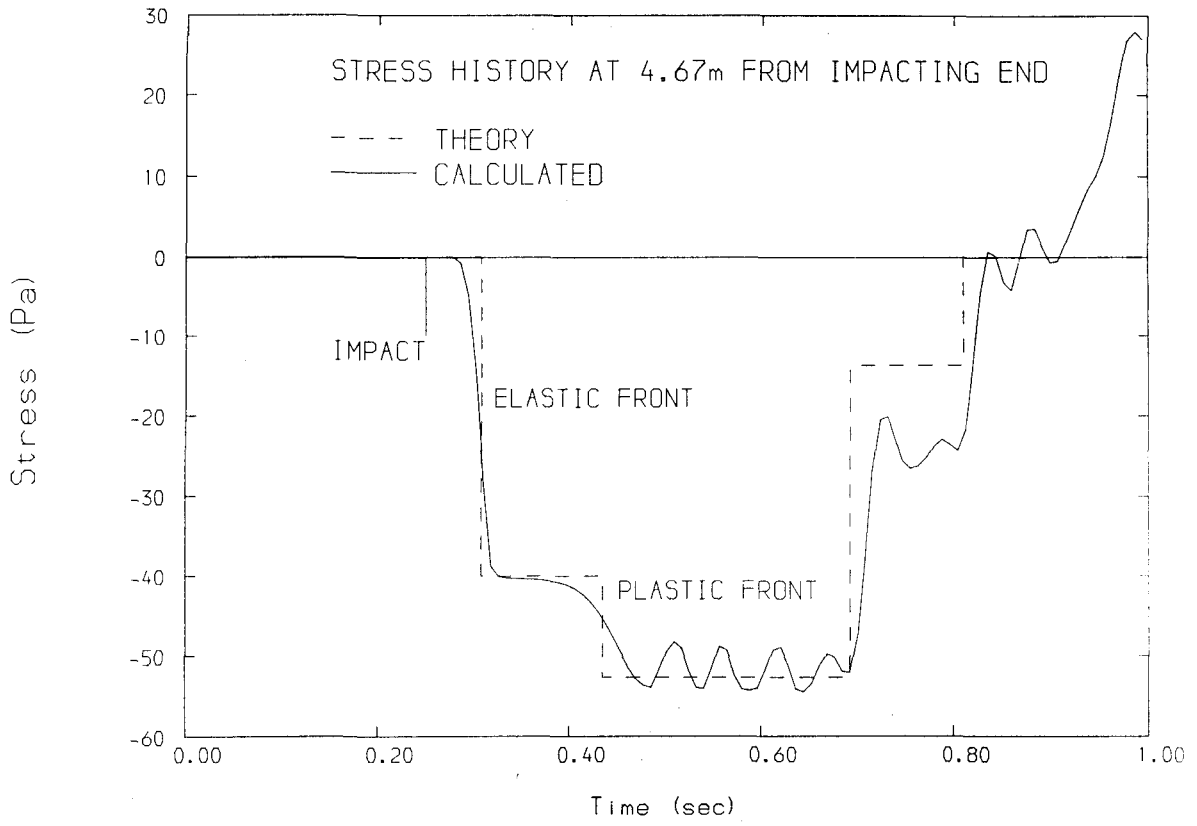
Figure 5.5: ELASTIC-PLASTIC WAVES IN BAR

while A defines the amplitude. c_0 is the bar wave velocity (eqn. (5.4)).

The stress associated with this pulse is:

$$\sigma = -(AE/Br)\exp[(-r-c_0t)/B] + (AE/r^2)[1-\exp[(-r-c_0t)/B]] \quad (5.7)$$

The right-hand side of eqn. (5.7) consists of two opposing sign terms, the first always negative (compressive front) and the second positive (tension tail). The following may be noted:

- the peak compressive stress increases as the wave approaches the apex (proportional to $-AE/Br$);

- the length of the compressive portion decreases correspondingly;

- a tension tail is left, which sufficiently behind the head of the pulse approaches AE/r^2 in magnitude.

A conical bar of end radii 6mm and 60mm, and length 2000mm, was modelled numerically with a graded mesh of 4x150 quadrilaterals (fig. 5.6). Material properties were typical of Aluminium ($E=67$Gpa, $\rho=2700$Kg/m^3, $c_0=4981$m/s). The pulse input was given as a velocity history at the wide end, derived from eqn. (5.6). Amplitude of the pulse was $A=1.3382\times10^{-4}$m^2, and the length $B=0.300$m.

The numerical results compare well with the analytical stress profiles (fig. 5.6). Predictably, the extremely sharp peak at the wave front is blunted somewhat, and some dispersion is introduced behind it. Part of this is attributable to the surface waves produced in the axisymmetric model.

5.3 VIBRATION OF A CANTILEVER

The motion of a vibrating cantilever is a problem that may be readily checked with elastic beam theory. A mesh of 4x21 quadrilaterals is used to model a vertical cantilever clamped at the top end (fig. 5.7a). It is set in motion by giving the bottom right
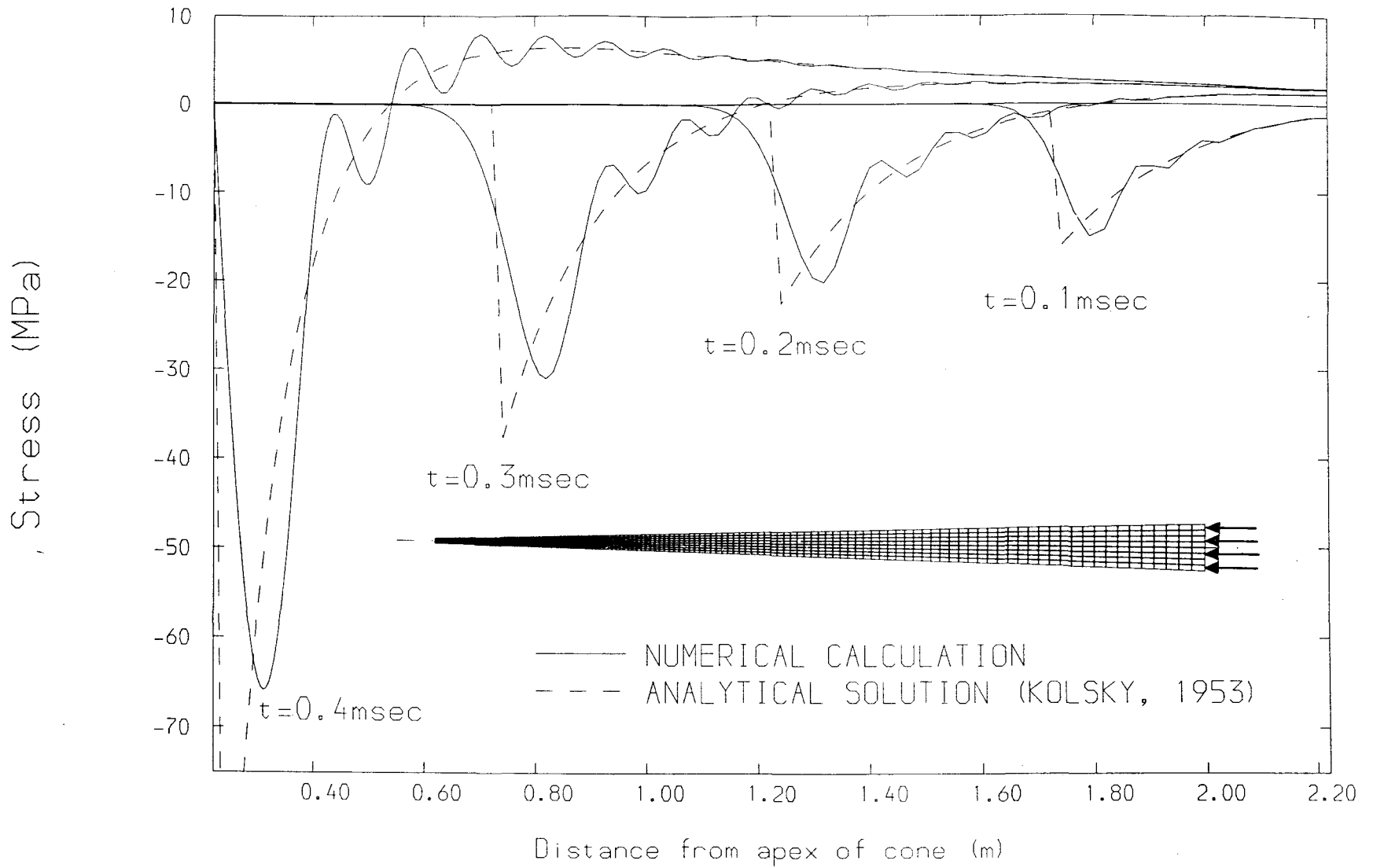
Figure 5.6: PROPAGATION OF STRESS WAVE ALONG CONICAL BAR

The figure shows stress (MPa) on the vertical axis versus distance from apex of cone (m) on the horizontal axis.

- Vertical axis: Stress (MPa), ranging from -70 to 10
- Horizontal axis: Distance from apex of cone (m), ranging from 0.40 to 2.20

Curves labeled:
- t=0.1msec
- t=0.2msec
- t=0.3msec
- t=0.4msec

Legend:
- —— NUMERICAL CALCULATION
- – – – ANALYTICAL SOLUTION (KOLSKY, 1953)
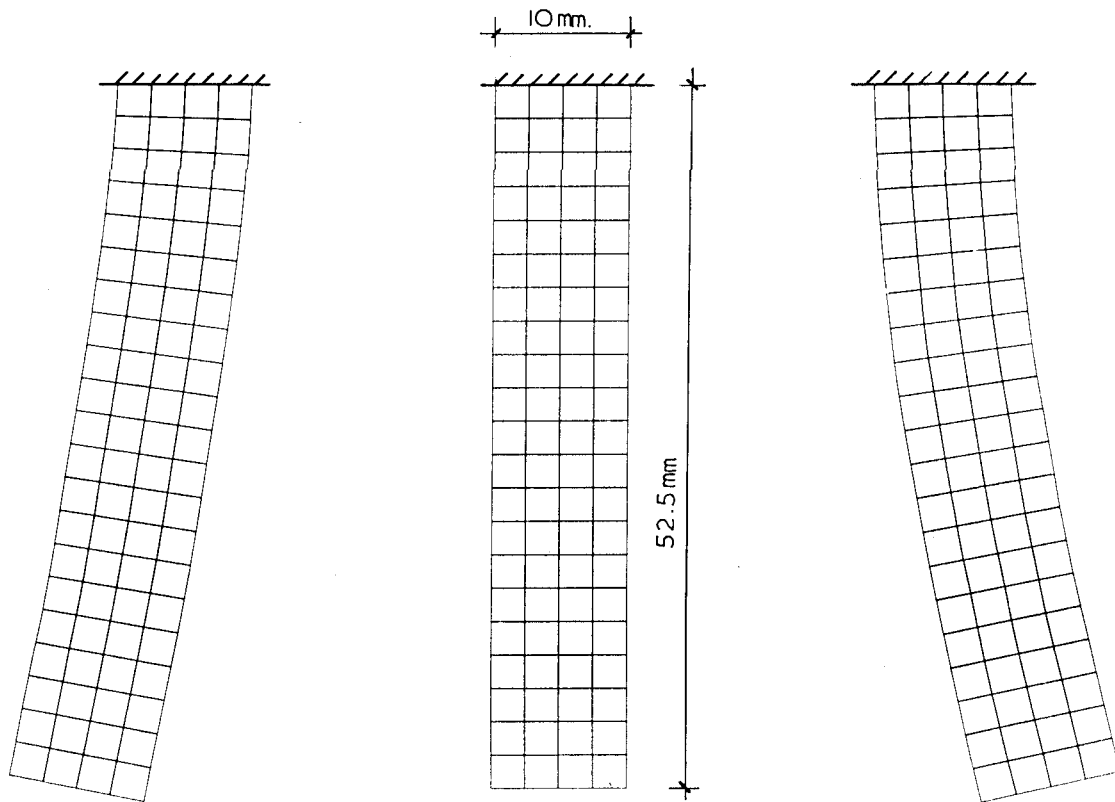
B) PEAK LEFT DEFLECTION   A) UNDEFORMED MESH   C) PEAK RIGHT DEFLECTION

Figure 5.7: ELASTIC VIBRATION OF CANTILEVER (DISPLACEMENTS X10)

hand node a velocity of 10m/s during 0.05ms. It is then left to vibrate during 1ms. Material properties are

Density ρ = 7720 Kg/m^3

Elastic modulus   E = 213.4 GPa

Poisson's ratio ν = 0.311

Figures 5.7b and 5.7c show the maximum positive and negative displacements, exagerated 10 times. Displacement histories of points at the tip and middle of the beam (fig. 5.8a) show the dominance of the flexural fundamental mode of vibration in the response. This is also notable in the frequency spectrum at the tip, shown in fig. 5.8b, where the first three (theoretical) natural frequencies of a flexion-only beam are shown as well for comparison. For the first frequency, the coincidence with the theoretical value is remarkable. Some discrepancy exists for the second and third modes. This is expected from the fact that the theoretical frequencies do not take into account shear or finite deformation effects. This problem has been analyzed previously by Wilkins (1969) with substantially the same results as here.

5.4 STATIC ELASTIC-PLASTIC PROBLEMS

Two classical problems of static plasticity are solved in this section. As discussed in section 4.1, the explicit Finite Difference code lacks the ability to perform static analysis directly. The static solutions are reached through dynamic relaxation. The vibrations are damped out with the use of viscous damping, and the forces (or displacements) are applied gradually. Some "overshoot" in the solutions is unavoidable for plastic materials, although it can be minimized by proper use of damping and slow loading rates.

5.4.1 PUNCH TEST

The case of a semi-infinite body indented by a frictionless, flat rigid punch, under conditions of plane strain, was solved originally by Prandtl (1920), using shear line theory. The plastic collapse
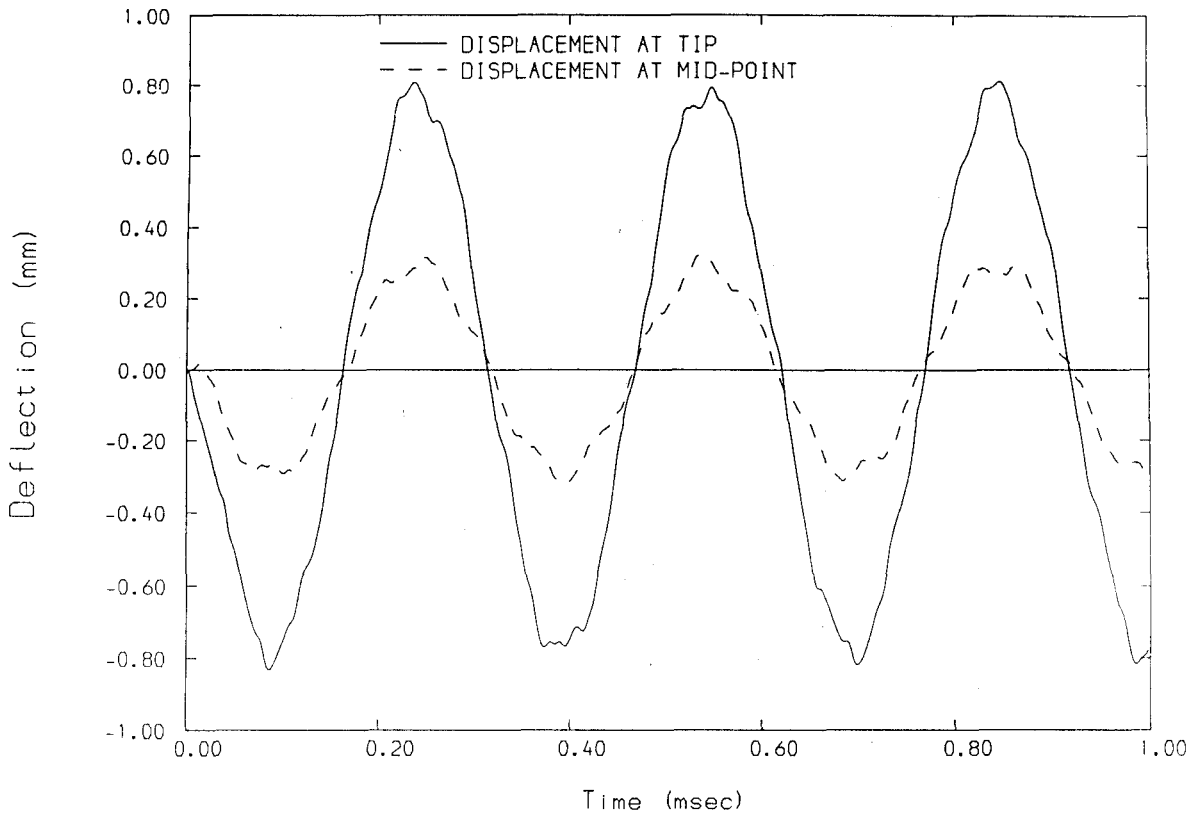
Figure 5.8a: ELASTIC VIBRATION OF CANTILEVER - DISPLACEMENT HISTORIES
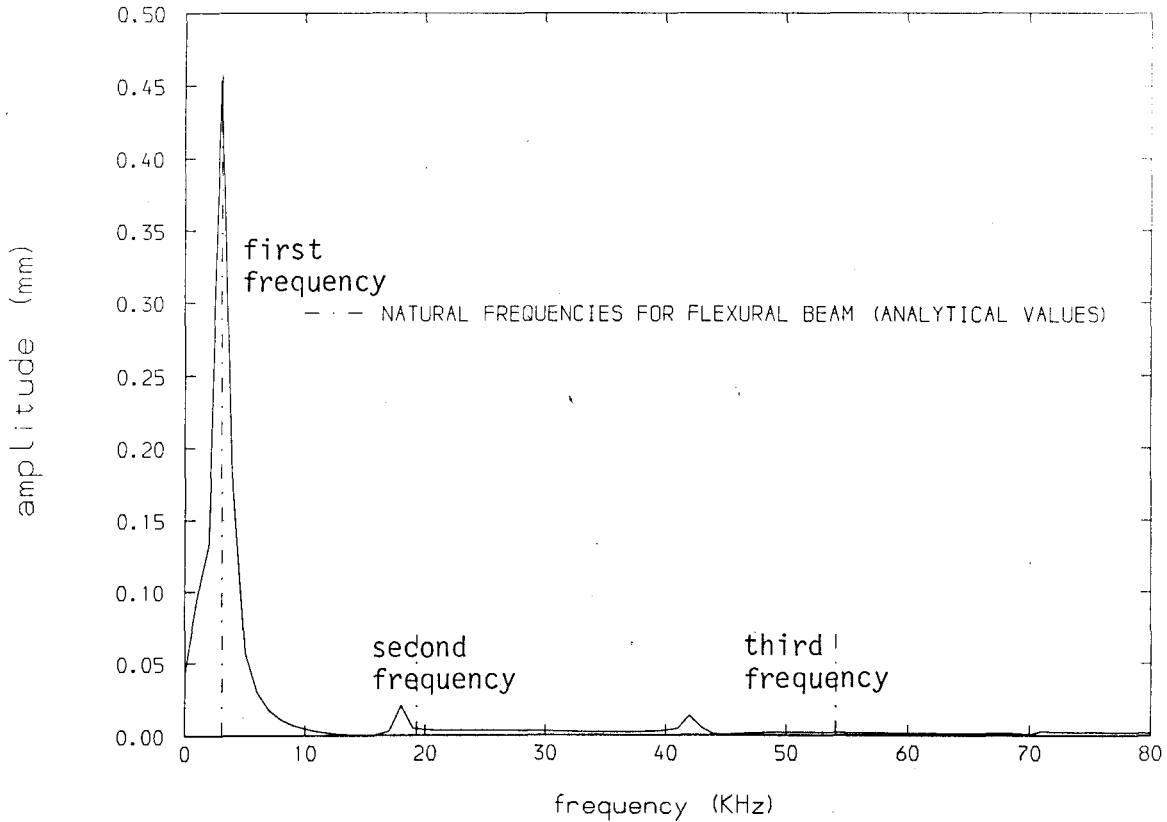
Figure 5.8b: ELASTIC VIBRATION OF CANTILEVER - FREQUENCY CONTENT

pressure is constant and equal to

$$p = \lfloor (2+\pi)/\sqrt{3} \rfloor \; Y = 2.97Y \qquad\qquad (5.8)$$

Numerically, the half-space is discretized rather crudely (fig. 5.9), modelling only a finite rectangular portion, with displacements at the boundary constrained in both directions. Prescribed velocities are given to the nodes under the die. The material properties are

      Elastic modulus E = 100 Pa

      Poisson's ratio ν = 0.3

      Yield stress Y = 0.01 Pa

For this problem, a mesh of constant strain triangles does not give a satisfactory result. Not only does it overestimate the collapse pressure, but the load grows monotonically, failing to achieve a limit value (fig. 5.9), in direct contravention of the limit theorems of plasticity. The reason for this is the inadequacy of these meshes to model incompressible plastic flow, as discussed in section 3.7.1.

The Mixed Discretization procedures advocated here (sections 4.2.2, 4.2.3) do provide a satisfactory solution (fig. 5.9). The slight overestimation is due to the coarseness of the mesh and the total constraint at the boundaries. This problem was solved using the CMTQ quadrilaterals proposed in section 4.2.3, thus proving that the modifications introduced in these to prevent negative volumes do not stiffen these elements up for ordinary situations with small or moderate strains.

To achieve the solution, a relaxation process was used. Mass density (fictitious) was taken as 0.1 Kg/m^3, and full Rayleigh damping was used, with 1% of critical damping at 1 Hz. The relaxation process was followed for 10 seconds (458 steps). The prescribed velocities at the die were applied gradually during the first second.
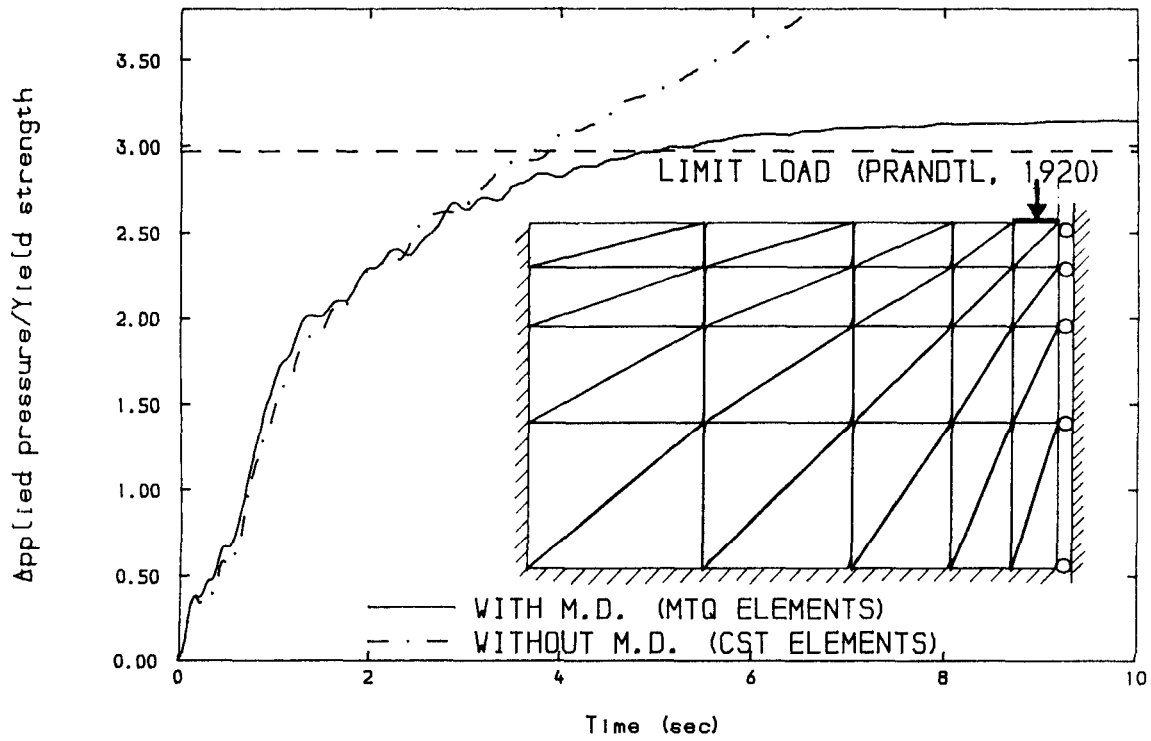
Figure 5.9: PUNCH TEST IN PERFECTLY PLASTIC, PLANE STRAIN HALF-SPACE

5.4.2 ELASTIC-PLASTIC SPHERE UNDER INTERNAL PRESSURE

When a thick-walled spherical vessel is subjected to growing internal pressure, a plastic zone starts to develop from the interior. There is a range of pressures for which contained plastic flow is achieved, defining a plastic zone and an elastic outer zone. The theoretical solution (e.g. Hill, 1950) defines the radius c of the plastic zone from $\int y \ 99$

$$p = 2YLn(c/a) + (2Y/3)(1-c^3/b^3) \tag{5.9}$$

where p is the pressure, a the internal radius, and b the external radius.

The stresses in the elastic zone (c<r<b) are given by

$$\sigma_r = -(b3/r3-1)2Yc3/3b^3 = -\frac{2Yc^3}{3b^3}\left(\frac{b^3}{r^3}-1\right)$$

$$\sigma_\theta = (b3/2r3+1)2Yc3/3b^3 = \frac{2Yc^3}{3b^3}\left(\frac{b^3}{2r^3}+1\right) \tag{5.10}$$

and in the plastic zone (a<r<c) by

$$\sigma_r = -2YLn(c/r) - 2Y(1-c^3/b^3)/3$$

$$\sigma_\theta = Y + \sigma_r \tag{5.11}$$

Numerically this problem was solved discretizing a 30 deg. axisymmetric sector, with a mesh of 10x8 CMTQ quadrilaterals (fig. 5.10a). The material parameters were

Elastic modulus	E = 1
Poisson's ratio	$v = 0.2$
.Yield strength	$Y = 0.83588 \times 10^{-3}$
Density	$\rho = 1$

With a=1, b=2 and an applied pressure of $p=10^{-3}$, the plastic zone extends to c=1.5 exactly (eqn. 5.9). The calculated profiles of radial and hoop stresses (fig. 5.10b) show an excellent agreement with theory. Only a small difference is present in the peak of the
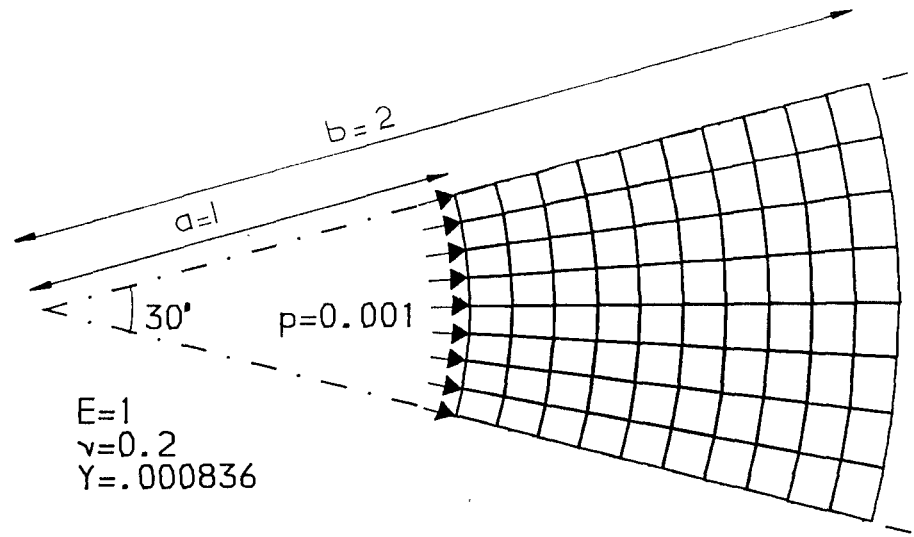
A) MESH USED AND MODEL PARAMETERS
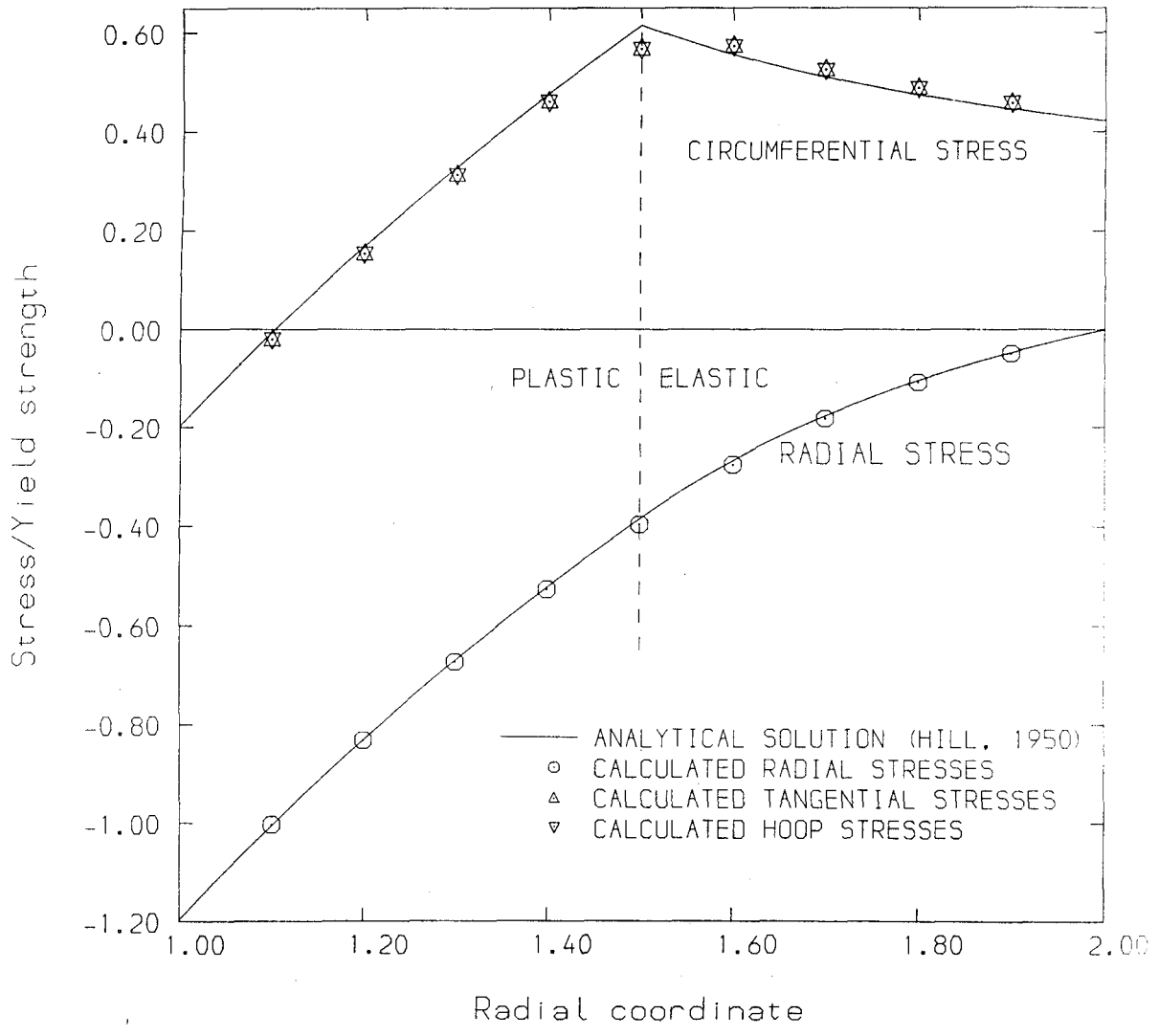
B) STRESS DISTRIBUTION ACROSS THE RADIUS

FIGURE 5.10: ELASTIC-PLASTIC SPHERE UNDER INTERNAL PRESSURE

circumferential stresses at the plastic boundary, due to the crudeness of the mesh and the stepwise representation of stresses in the model (constant strain elements). As a check, calculated circumferential stresses in the sphere are provided in both in-plane and out-of-plane directions, showing excellent agreement.

To achieve the solution, a dynamic relaxation process was followed for 40s, with mass damping 50% of critical at 0.08 Hz. (782 steps). The load was increased gradually to its final value in the first 30s.

5.5 HEAT CONDUCTION

The numerical procedures described in chapter 4 have the capability of performing purely mechanical, purely thermal, or simultaneous coupled thermo-mechanical calculations.

5.5.1 COUPLED THERMOMECHANICAL ANALYSIS

The complexity of the mathematical description of general coupled thermomechanical systems, in which the heat is generated by plastic flow, accounts for the fact that analytical solutions are not readily available in this field. As on the other hand thermomechanical applications were not intended for this work, no validation example is presented here as such.

However, the mathematical model for thermomechanical coupling has been derived and implemented by the author, both in the 2-D program developed for this thesis, and in an existing 3-D program (Marti, 1981, 1983). A 3-D application of this work has been published elsewhere.(Marti, Goicolea, Kalsi and Macey, 1984), which concerns the extrusion of an aluminium disk with an irregular die. Very severe plastic distortions are achieved in the process, producing increases in temperature.

5.5.2 TEMPERATURE REDISTRIBUTION IN A SLAB
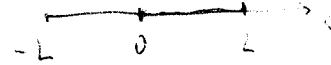
A thermal-only analysis is performed for an infinite slab, initially at a uniform temperature T=1, and cooled down by keeping the ends x=-L and x=L at T=0. The problem parameters are

half thickness	L = 20
Conductivity	K = 1
Density	ρ = 1
specific heat	C_p = 1

Calculated temperature profiles for various times are compared with theoretical values in fig. 5.11, showing excellent agreement. A time-step of 56.25ms was used for the analysis, with a mesh of 40 triangles. The theoretical solution was obtained by Fourier series analysis (e.g. Carslaw and Jaeger (1947), p83).

5.6 LARGE STRAINS AND ROTATIONS

A Quadrilateral subjected simultaneously to a finite rigid rotation and a simple axial extension (i.e. lateral movement constrained) is considered here. The purpose of this example is principally to check the objectivity of the integration algorithm.

The material behaviour is described by a hypoelastic law (eqn. 4.28), involving the Jaumann rate of Cauchy stress:

$$\overset{\triangledown}{\sigma} = \mathbf{C}:\mathbf{d} \tag{5.12}$$

Calling $\theta(t)$ the rigid rotation at time t, and $\lambda(t)$ the axial stretch ratio (L(t)/L) in the rotated coordinate frame, the two normal stress components may be obtained analytically by integrating eqn. (5.12):

$$\begin{Bmatrix} \sigma_{11} \\ \sigma_{12} \end{Bmatrix} = \begin{pmatrix} \cos^2\theta & \sin^2\theta \\ \sin^2\theta & \cos^2\theta \end{pmatrix} \begin{Bmatrix} 1 \\ \frac{\nu}{1-\nu} \end{Bmatrix} E(1-\nu)\text{Ln}\lambda / [(1+\nu)(1-2\nu)] \tag{5.13}$$
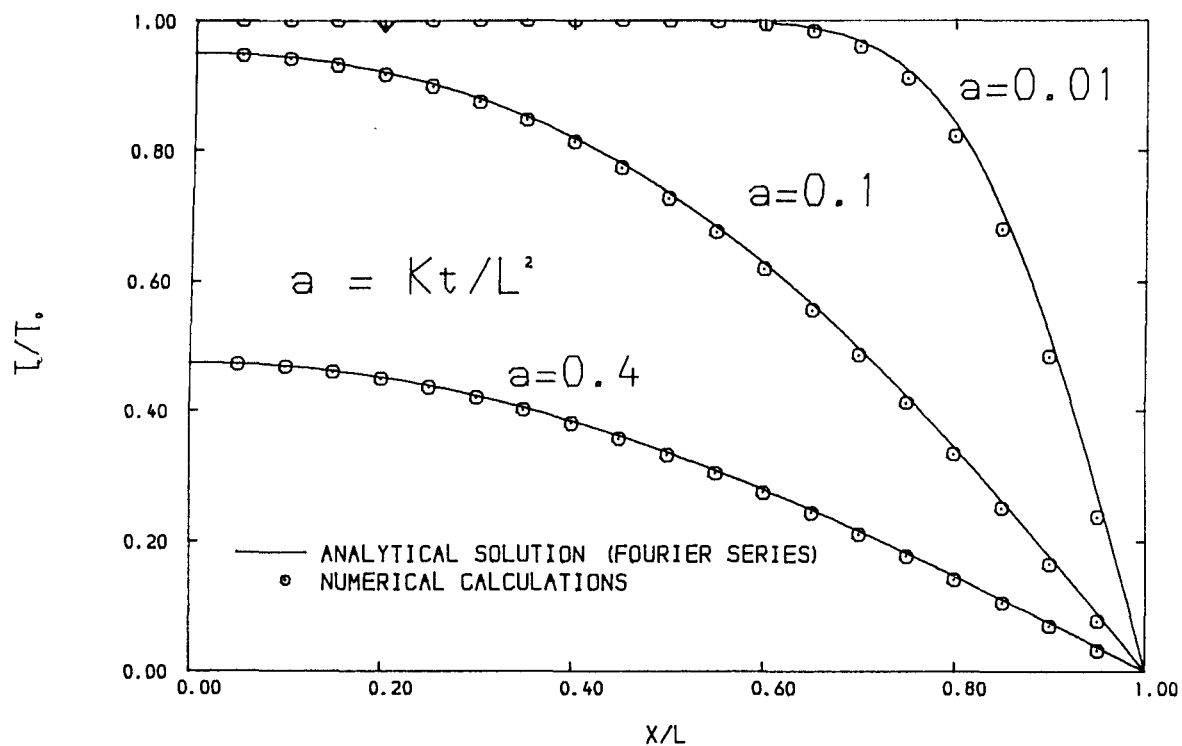
Figure 5.11: HEAT CONDUCTION IN SLAB – TRANSIENT TEMPERATURE PROFILES
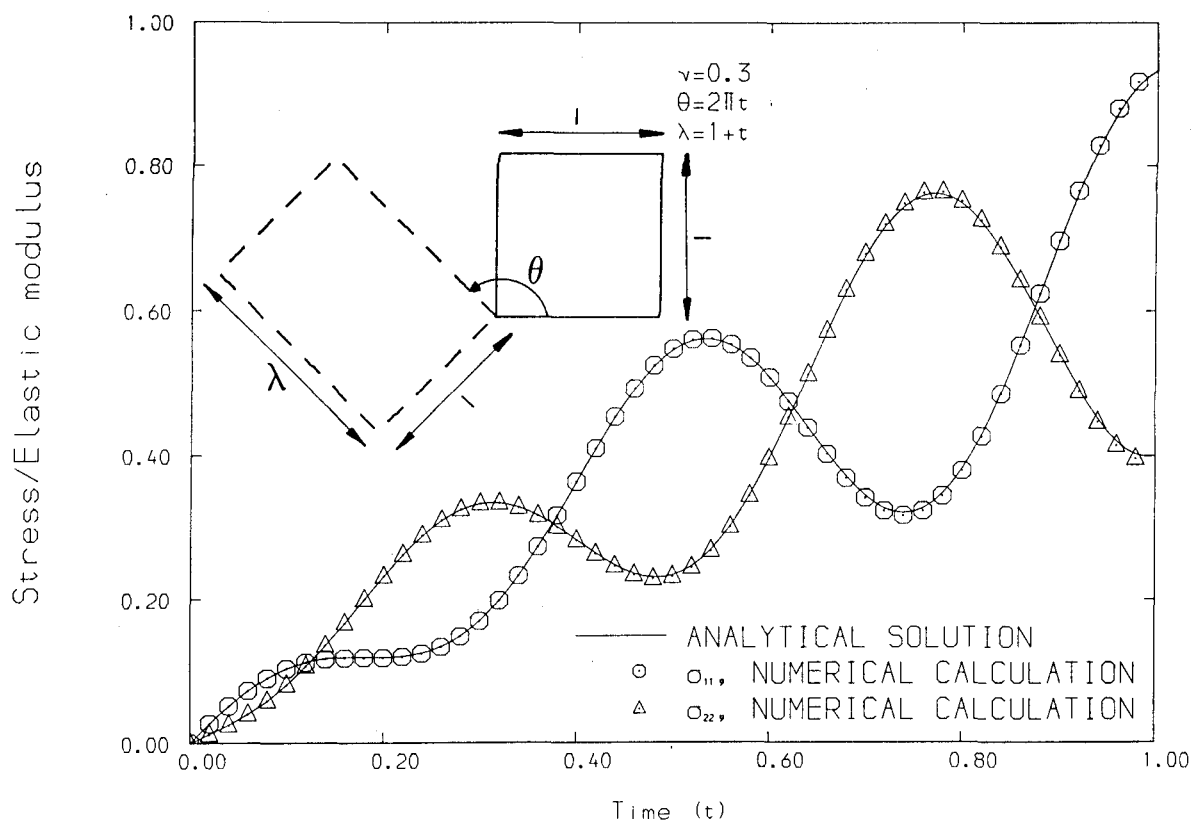

Figure 5.12: HOMOGENEOUS FINITE SIMPLE EXTENSION AND ROTATION

A full 360 deg. rotation with a final stretch ratio of 2 was performed (fig. 5.12), the numerical results agreeing closely with theory. A large number of time-steps - 1824 - was used for the calculation, which could have been reduced without affecting significantly the accuracy of the results. However, this is a realistic situation for explicit calculations, where time-steps must be very small for reasons of stability. The simple Jaumann rate algorithm (eqn. 4.52) provides excellent results, without needing the more rigorous procedures necessary for larger implicit steps (Hughes and Winget (1980), Pinsky, Ortiz and Pister (1983)).

5.7 IMPACT OF CYLINDER

The impact of a solid cylinder against a rigid stonewall is a problem in which the final shape is sensitive to the plastic properties of the material. Wilkins and Guinan (1973) used tests and numerical analyses of such impacts to calibrate the plastic material behaviour. Here, the impact of a copper cylinder is described. This problem has been analyzed by Hallquist with NIKE2D (1979), DYNA2D (1982a) and DYNA3D (1982c), and by Johnson (1981).

Impact velocity is 227m/s. A simple Elastic-Plastic Von Mises idealization with linear isotropic hardening is used for the material. The dimensions and material parameters are given in figure 5.13a.

The mesh comprised 50x5 CMTQ quadrilaterals and was severely distorted as a result of the impact (figs. 5.13b, 5.13c). The first part of the deformation (40 microsec.) ocassions a flattening of the impact end into an elephant's foot. The latter part (till 80 microsec.) produces a barreling upwards of the bar, as the bottom part has become very hardened by then. The cylinder starts to rebound after 79 microsec. (velocity histories in fig. 5.14), in agreement with Hallquist's results. Note that for this problem the nodes at the impacting end were fixed in the axial direction. Although a stonewall boundary condition (permitting separation) would have been more realistic, the outer edges tending to lift slightly, this simpler idealization was adopted for compatibility with Hallquist's results.
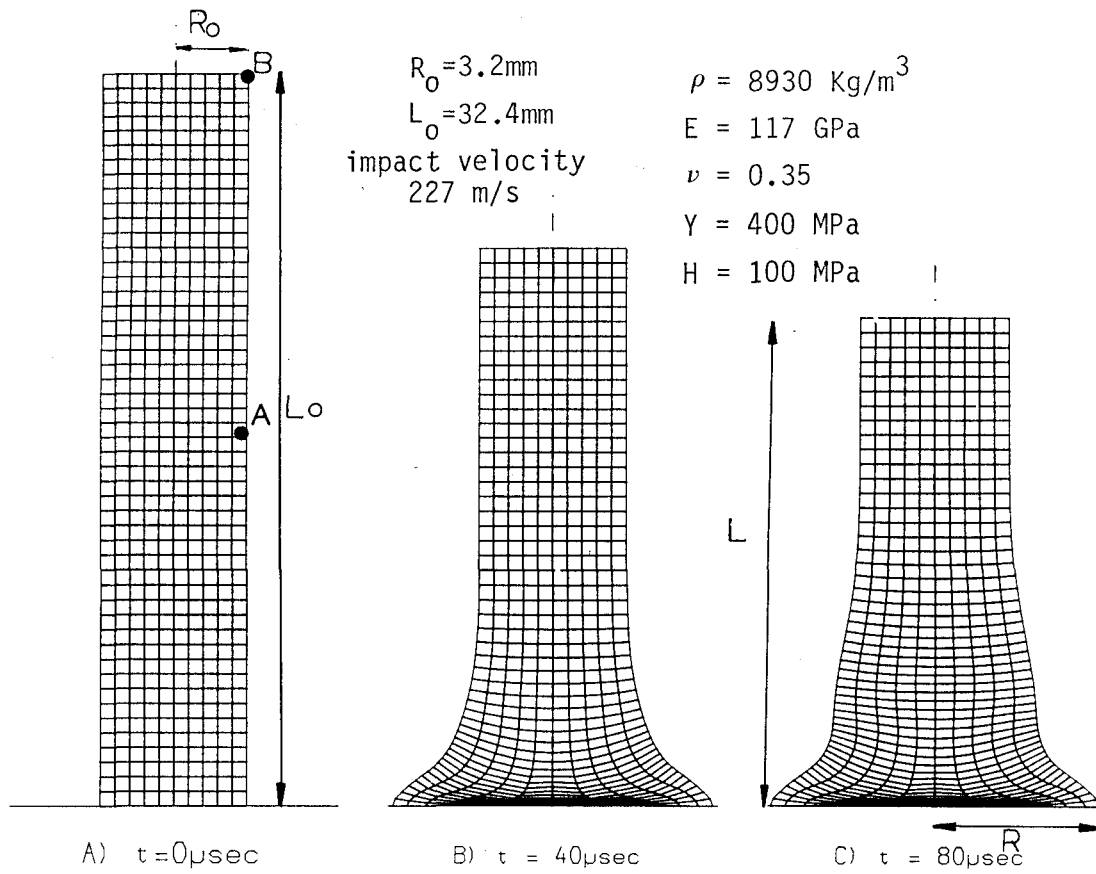
R_o=3.2mm
L_o=32.4mm
impact velocity
227 m/s

ρ = 8930 Kg/m^3
E = 117 GPa
ν = 0.35
Y = 400 MPa
H = 100 MPa

A) t=0μsec   B) t = 40μsec   C) t = 80μsec

Figure 5.13: IMPACT OF CYLINDER - UNDEFORMED AND DEFORMED VIEWS
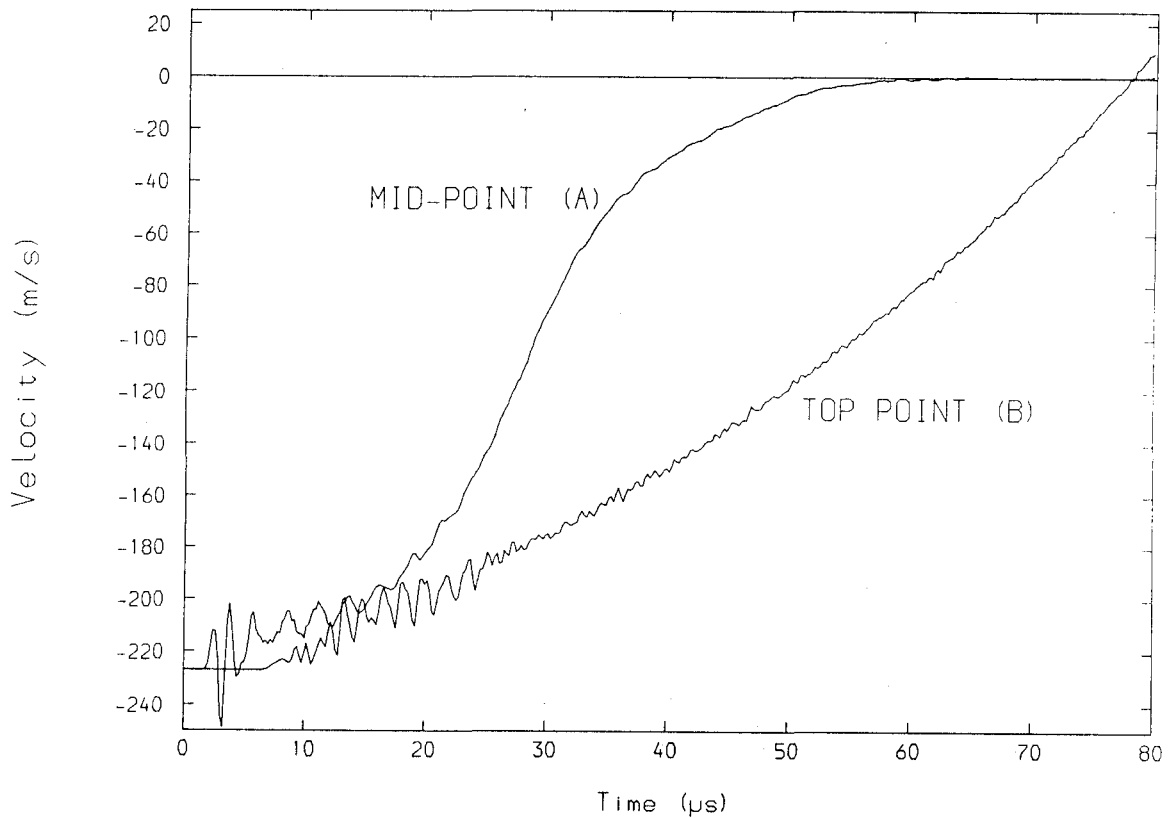

MID-POINT (A)

TOP POINT (B)

Figure 5.14: IMPACT OF CYLINDER - VELOCITY HISTORIES

Results from various calculations are presented in table 5.1, giving the deformed length, bottom radius, and maximum effective plastic strain (achieved always at the bottom centreline cell). The results obtained here using CMTQ or MTQ elements compare well with Hallquist's results. Mesh distortion, although large, is quite uniform, and MTQ elements behave well here. As predictable, the response of CST elements is poor. Also presented in table 5.1 are results from Johnson (1981); two different types of crossed triangle layouts are seen to provide better results than CST elements, but still not as good as the Mixed Discretization used here (specially as to maximum plastic strain).

	Hallquist(1982a,1982c)			This work			Johnson(1981)		
	DYNA2D	DYNA3D	NIKE2D	CMTQ	MTQ	CST	X1	X2	CST
L	21.47	21.47	21.47	21.45	21.44	21.13	21.61	21.61	21.12
R	7.127	7.034	7.068	7.068	7.155	6.061	7.136	7.040	6.016
ϵ_p^{max}	3.05	2.96	2.97	2.90	2.94	1.63	2.38	2.70	1.34

Table 5.1: Comparison of results from various calculations for impact of cylinder (see fig. 5.13)

5.8 CONCLUSIONS

The capacity of the proposed explicit Finite Difference algorithms for modelling Elastic-Plastic material behaviour in plane and axisymmetric models has been validated, with a series of static and dynamic benchmark tests. Special attention has been given to the wave propagation and finite deformation capabilities.

CHAPTER 6

TENSION TESTS ON ALUMINIUM BARS

6.1 INTRODUCTION

    6.1.1 Constitutive idealization

    6.1.2 Tension tests - a review

6.2 THEORETICAL INTERPRETATION OF TENSION TESTS

    6.2.1 Strain distribution at minimum neck section

    6.2.2 Stress distribution

6.3 TENSION TESTS

    6.3.1 Specimens and material

    6.3.2 Programme

    6.3.3 Procedure

    6.3.4 Results

    6.3.5 Microhardness measurements

6.4 MATERIAL HARDENING LAW

6.5 NUMERICAL CALCULATIONS FOR TENSION TESTS

    6.5.1 Model

    6.5.2 Analysis

    6.5.3 Results

6.6 CONCLUSIONS

6.1 __INTRODUCTION__

Experimental and numerical studies of tension tests with necking in bars are reported in this chapter. The aim is to derive constitutive laws for the aluminium material used in the tube crumpling analyses (chapter 7). Stress-strain laws valid for up to 1.5 strain are necessary for these analyses.

6 tension tests were carried out on HE30 annealed aluminium bars. In these tests, after an initial stage of uniform extension, an instability occurs, causing deformations to become localized in a neck with very large strains. Reductions in cross-sectional area of $A/A_0 = 0.26$ (fig. 6.1), corresponding to a uniaxial strain of 1.35, were achieved before fracture.

The stress and strain fields around the neck are markedly non-uniform. Theoretical analyses of these distributions with some empirical basis have been proposed by Bridgman (1952) and Davidenkov and Spiridinova (1946). These semi-empirical distributions were used here to provide a first interpretation of the test results, obtaining tentative hardening laws for the material.

The tension tests were then modelled with the explicit numerical techniques proposed in this thesis (chapter 4). Calculations were performed successfully up to the large neck strains observed in experiment. the stress/strain distributions obtained in the calculations confirmed in general the validity of Bridgman's and Davidenkov's solutions. Load and average stress evolution curves fitted closely the experimental results. With the hardening laws obtained using Bridgman's semi-empirical interpretation as a first guess, the computations allowed a further adjustment of the parameters to provide a better fit with experiment.

The following terminology is employed in this chapter:

- True (average) stress, P/A, axial load divided by current cross-section of bar;
- Natural (or logarithmic) strain, $Ln(L/L_0)$, logarithm of current over initial length;

Initial area of cross-sect.

$$A_o = \pi D_o^2/4$$

Deformed cross-section area at neck

$$A = \pi D^2/4$$

Figure 6.1: schematic view of neck region in tensile bar

Figure 6.2: geometry of tension test specimen

- Effective plastic strain, ϵ_p (eqn. 2.60b)
- Von Mises equivalent (or effective) stress,

$$\sigma_{eq} = \sqrt{(3/2)\mathbf{s}:\mathbf{s}} \qquad (6.1)$$

where $\mathbf{s}$ is the deviatoric Cauchy stress tensor, eqn. (2.59).

6.1.1 CONSTITUTIVE IDEALIZATION

Elastic-Plastic theory has been very successful in describing the deformation of metals and provides a good framework on which to build models of material behaviour. A Von Mises yield criterion with isotropic hardening and associative plastic flow provides a simple and robust model for non-cyclic loading, giving acceptable answers for most cases. With this choice of constitutive model, reliable data for the elastic properties may be obtained from the supplier, handbooks, or simple tests. The material parameters will be complete with the hardening law $Y(\epsilon_p)$, which relates the yield strength of the material, Y, to a scalar measure of the plastic strain, the effective plastic strain ϵ_p.

The flow stress Y is defined by the value at yield of the Von Mises equivalent stress:

$$Y = \sigma_{eq} \qquad (6.2)$$

In some special cases, a simple isotropic Von Mises model may not represent the material satisfactorily. Specialized calculations for well defined local stress states may require careful consideration and/or matching of the loading condition for the test in which the constitutive data were derived (e.g. pure tension, pure shear, combined loadings).

If in such a problem plasticity is confined to a particular local stress state, a determination of the yield and flow parameters for that state within an isotropic plasticity idealization may suffice and give satisfactory results. In a general situation more sophisticated plasticity idealizations (e.g. Mroz (1967,1972), Ortiz and Popov

(1983)) will be needed, determining the constitutive data by numerous tests for each stress orientation, at each level of hardening. This process requires extensive and difficult experimental work, as well as research to assess the appropriateness of constitutive idealizations. Moreover, for large strain analysis, the effort involved would be greatly increased and complicated, with uncertain results.

In the Concertina tube collapse mechanism, large plastic strains are produced under a variety of stress states. For a global modelling of this phenomenon an isotropic Von Mises idealization is a simple and reliable idealization, which produces satisfactory results. Additionally, with this choice of model the constitutive data can be determined easily from direct measurements in simple tension tests.

Due to the quasi-static nature of the problem to be modelled, material rate effects do not need to be included. Fracture of the material is not necessary in the model either, as the annealing process to which the Aluminium was subjected increased the ductility sufficiently to remove fracture from the range of relevant phenomena.

6.1.2 TENSION TESTS - A REVIEW

Tension tests have been widely used for determining mechanical properties of metallic materials. Standard specifications exist for carrying out these tests : ASTM E8-82, ASTM E646-78, BS18. The material behaviour can be easily obtained from these standard test procedures when strains are small or moderate, in which case the deformations in the tensile specimen may be assumed uniform (Over the cross-section and along the bar). Such is not the case, however, when strains become large: the specimen necks and deformations become highly localized, creating as a result non-uniform stress and strain distributions.

In a test to derive the mechanical properties of a material discrete measurements are taken of forces and displacements, producing average values for stresses and strains. If the stress and strain fields can be assumed uniform, these average measurements provide directly the data for the elementary constitutive laws. However, all

means of producing large plastic deformations involve highly complex non-uniform stress distributions. Appropriate large strain test procedures include torsion tests on tubes or cylinders, compression tests on cylinders (in which results must be corrected for barrelling and friction), and tension tests on cylindrical bars or flat plates. Tension tests on cylindrical bars were chosen here for the simplicity in measurements and suitability of available equipment.

The analysis and interpretation of the necking deformation in tension tests is a solid mechanics problem which has attracted some interest. Bridgman (1944, 1945, 1952) and Davidenkov and Spiridinova (1946) were the first to study this problem in some depth. They presented analytical interpretations based on some experimentally confirmed assumptions, which provide stress/strain distributions valid in the minimum section of the neck. The main assumption in both Bridgman's and Davidenkov's work is that the radial strains are constant across the minimum neck section. This fact was corroborated experimentally by Davidenkov (1946) measuring the average grain sizes at different positions and orientations in the neck section. Bridgman silver-soldered cores of various diameters into hollow specimens, obtaining a similar confirmation. Experimental evidence to this effect has been obtained here from microhardness tests and is presented further down in section 6.3.5.

Bridgman's and Davidenkov's early work in the interpretation of tension tests has represented the state of the art for many years. Not until recently have minor extensions to their analytical work been produced (Kaplan (1973), Jones (1979)).

On another front, the development of digital computers has enabled tension tests to be interpreted in a more general form through the use of numerical models. The first general numerical solution was obtained by Wilkins (1968) with an early version of his HEMP finite difference hydrocode, but received limited publicity. Further work along this line has been reported by Wilkins (1978), Wilkins et al (1980), employing tension tests to obtain material idealizations for perforation analyses and ductile fracture test models. Wilkins carried out computer calculations to corroborate certain assumptions and gain additional information on constitutive parameters. However, in the

interpretation of the tension tests Wilkins does not consider the effect of the non-uniformity of axial stresses in the neck. He acknowledges the error, using his simple interpretation to establish a first crude guess for the material parameters, which are then corrected on the basis of the results of numerical calculations.

Norris et al. (1978) have also used HEMP to simulate tension tests. They followed essentially the same method as Wilkins, performing iterative computer analyses to obtain universal flow stress curves from the tension test data. They reported triaxial tensions at the specimen axis higher than those predicted by Bridgman (1952).

A Kantorovich numerical approach assuming global polynomial displacement functions has been proposed by Chen (1971). He used an early large strain formulation which contains some deficiencies such as lack of correction for rigid body rotations. The global displacement functions failed to represent adequately the boundary conditions. A similar large strain formulation was used by Needleman (1972) within a Finite Element context. As Norris (1978), Needleman found Bridgman's (1952) solution to underpredict the triaxial tensions in the specimen.

The work presented here uses both theoretical stress/strain distributions and numerical calculations for the interpretation of tension tests. Analytical results and empirical correlations due to Bridgman (1952) are first used to provide an initial guess for a universal flow stress curve from simple tension test data. This material law is then fed into the computational model, and by comparing the results with experiment, the parameters are adjusted more finely. The interpretation based on Bridgman's semi-empirical results provided with little effort very reasonable guesses for the material laws, and only minor changes were suggested by the computational results. On the other hand, the stress/strain distributions obtained in the calculations confirm broadly Bridgman's (1952) and Davidenkov's (1946) assumptions.

Although the numerical approach used by Wilkins (1978) is broadly similar to the present one (both employ explicit finite difference codes) neither he nor Norris et al.(1978) used any interpretation of

the tension test data fed into the computer model; the stress was merely averaged across the neck section. Adjustment of material stress-strain law parameters was achieved by iterative computer analyses. Here it was found that the difference between the direct average data (fig. 6.4) and the material uniaxial stress-strain law (fig. 6.7) was considerable for the reductions in area sustained (20% difference for $A/A_0=0.26$). An accurate initial guess could be obtained using a simple semi-empirical interpretation, thus saving considerable computer resources.

6.2 THEORETICAL INTERPRETATION OF TENSION TESTS

Tensile tests on cylindrical bars have been used extensively to study the mechanical behaviour of metals. For brittle or low ductility metals the strain and stress fields are approximately uniform throughout the test, with small reductions in area. Fracture occurs before departing from this uniform state. Uniformity is also the case for a more ductile material, when only the determination of the elastic constants or the yield point is sought.

Ductile metals can sustain large plastic strains before fracture. The reduction in cross-sectional area is important, and the original area (A_0) and gauge length (L_0) no longer provide a valid basis on which to measure stresses and strains. In a **first phase** of moderate reductions in area, deformations remain uniform; true (Cauchy) stresses and natural (logarithmic) strains provide a good description of the material behaviour. For a uniaxial tensile test they are defined thus:

$$\sigma_{zz} = P/A \qquad\qquad (6.3)$$

$$\epsilon_{zz} = \int_{L_0}^{L} dL/L = Ln(L/L_0) \qquad\qquad (6.4)$$

where: σ_{zz} is the true axial stress

           P is the applied axial load

           A is the current cross-sectional area

           ϵ_{zz} is the natural axial strain

           L_0 is the original gauge length

L is the current gauge length

The natural strain keeps a cumulative record of the straining in each direction at a point in the material, referred at every instant to the current configuration. This description is very convenient for the tensile test, for as long as deformations remain uniform, the axial stress coincides with the Von Mises equivalent stress, and the natural axial strain equals the effective plastic strain:

$$\sigma_{eq} = \sigma_{zz}$$
$$\epsilon_p = \epsilon_{zz}$$

(6.5)

A proof of this last assertion is given further down in section 6.2.1.

A **second phase** in the tensile test begins when the specimen starts to neck. At this moment the material hardening no longer compensates for the reduction in area, occasioning a decrease in the total axial load. The material tries to harden enough to match the applied load, producing localized deformations in a small neck region, to which subsequent plastic flow is confined; the rest of the specimen unloads elastically. A non-uniform state of stresses and strains exists, and formulae (6.4) alone no longer provide a valid description of the test.   (6.3)

6.2.1 STRAIN DISTRIBUTION AT MINIMUM NECK SECTION

From the assumptions of axial symmetry and uniformity of radial strains, and considering the symmetry condition across the plane of the minimum neck section, the rate of deformation components (see sect. 2.2.3) may be expressed as follows:

$$d_{rr} = \frac{\partial \dot{u}_r}{\partial r} = \dot{D}/D$$

$$d_{\theta\theta} = \frac{1}{r}\frac{\partial \dot{u}}{\partial \theta} + \frac{\dot{u}_r}{r} = 0 + \dot{D}/D = d_{rr}$$

(6.6)

$$d_{r\theta} = d_{\theta z} = d_{rz} = 0$$

where: r, θ, z stand for radial, circumferential and axial directions respectively

d_{ij} are the physical components of the rate of deformation.
u_i are the displacement components
D is the diameter
superposed dots represent material time derivatives as usual

From (6.6) it may be seeen that uniformity of d_{rr} implies $d_{rr} = d_{\theta\theta}$ as well. This fact was checked independently by Davidenkov(1946) measuring grain sizes in both radial and circumferential directions.

In the necking phase elastic strains are negligible so it may be assumed the deformation is produced entirely by plastic flow. The incompressibility characteristic of plasticity in metals permits the derivation of the axial rate of deformation component:

$$d_{zz} = -2d_{rr} = -2\dot{D}/D \tag{6.7}$$

From eqns. (2.60b), (6.6) and (6.7) the effective plastic strain may be expressed as

$$\epsilon_p = \int_{Do}^{D} -2(\dot{D}/D)dt = -2Ln(D/D_o) = \epsilon_{zz} \tag{6.8}$$

where D_o is the original diameter of the bar.

Thus ϵ_p and consequently the yield strength Y are constant across the minimum neck section.

This result has been corroborated experimentally here with the help of microhardness measurements, taken on sections of the deformed tensile specimens (sect. 6.3.5).

6.2.2 STRESS DISTRIBUTION

From the Levy-Mises plastic flow rule,

$$s_{ij} = \lambda d_{ij}p \tag{6.9}$$

where λ is an arbitrary positive scalar. Considering eqn. (6.6) one may then write:

$$\sigma_{rr} = \sigma_{\theta\theta} \qquad (6.10)$$

This equation was derived independently by Nadai(1946) from solely theoretical considerations of a Von Mises yield surface and a minimum force principle. Considering the constancy of Y across the section, one may also write:

$$\sigma_{zz} - \sigma_{rr} = Y \qquad (6.11)$$

which is valid for all points in the section. This stress distribution may be interpreted as a uniform axial tension of value Y superposed to a varying hydrostatic stress of value σ_{rr}. The hydrostatic stress, due to the free boundary condition, vanishes on the outer edge. In the interior the sign is tensile due to the concavity of the curvature, and from the symmetry condition around the axis, a maximum value must be reached on it. Equation (6.11) implies then that $\sigma_{zz} > Y$ throughout the section; hence the average value must also be greater, $\bar{\sigma}_{zz} > Y$. This explains the difference reported by Wilkins et al.(1980) in their calculations with HEMP, where for an axial strain of 0.52, $\bar{\sigma}_{zz} = 460$ MPa while Y = 430 MPa .

From the general equilibrium equations

$$\sigma_{ij,j} = 0 \qquad (6.12)$$

Bridgman(1952) and Davidenkov(1946) derived the distribution of axial stresses, depending on the radial coordinate r and on the radius of curvature of the longitudinal principal stress line, ρ :

$$\sigma_{zz} = Y(1 + \int_{r}^{D/2} \frac{dr}{\rho}) \qquad (6.13)$$

Bridgman(1952) proposes the following formula for the radius of curvature ρ depending on the radial coordinate :

$$\rho = (D2/4 + DR - r2)/2r \qquad (6.14)$$

where R is the geometrical radius of curvature at the root of the neck. Substituting in eqn. (6.13) and integrating to find the average stress:

$$\sigma_{zz} = Y(1 + Ln[(D^2/4+DR-r^2)/DR])$$

$$\qquad (6.15)$$

$$\bar{\sigma}_{zz} = Y(1 + 4R/D)Ln(1 + D/4R)$$

This last equation gives the value of the material strength Y from the measured average axial stress σ_{zz}. It depends on the possibility of measuring R, the radius of curvature. This can be a little bit cumbersome in a test where multiple measurements are to be taken. Bridgman(1952) produced an empirical correlation from multiple observations for different sorts of steel and other metals that expresses D/R as a function of the reduction of area A/A_0 (or what is the same, the axial natural strain ϵ_{zz}) :

$$D/2R = \sqrt{LnA_0/A - 0.1} = \sqrt{\epsilon_{zz} - 0.1} \qquad (6.16)$$

This result allows the correction factor $\bar{\sigma}_{zz}/Y$ to be expressed directly as a function of the axial strains:

$$\bar{\sigma}_{zz}/Y = [1 + 2\sqrt{\epsilon_{zz}-0.1}]Ln[1 + \sqrt{\epsilon_{zz}-0.1}/2] \qquad (6.17)$$

This formula may be applied only for $\epsilon_{zz} > 0.1$. For $\epsilon_{zz} < 0.1$ the deformation is assumed uniform, and no correction is needed.

6.3 TENSION TESTS

6.3.1 SPECIMENS AND MATERIAL

The material used in the tests was HE30 (BS1474) Aluminium alloy, with the following composition : 0.1% Cu, 0.4-1.5% Mg, 0.6-1.3% Si, 0.6% Fe, 0.4-1.0% Mn, 0.1%Zn, 0.5%Cr, 0.2% others, and the rest Aluminium. This material comes in extruded cylindrical form.

Mechanical properties in the as-received condition were obtained from the manufacturers:

0.1% proof stress	239 - 270 MPa
density	2700 Kg/m^3
Young's modulus, E	67000 MPa
Poisson's ratio, ν	0.3
Ultimate tensile strength	278-293 MPa
Elongation on 2 in	7 - 10%

This material was cut and machined to form specimens of the geometry described in figure 6.2 . A slight taper was given in order to control the necking position, the smallest diameter being located at the mid-section.

The composition and treatment of HE30 Aluminium is identical to the HT30 Aluminium tube material employed in the tube crumpling tests. The only difference lies in the forming processes (extrusion or drawing). As a result, mechanical properties for both materials are very similar. The small difference was assumed to vanish in the annealing process to which both specimen types were subjected (sect. 7.3.2.1).

6.3.2 **PROGRAMME**

The specimens were annealed at 350oC prior to testing. Six tests in all were performed with the following annealing times:

Test	Annealing time, hours
CT1	5
CT2	7
CT3	none
CT4	3
CT5	5
CT6	5

After annealing, all specimens were oven cooled.

6.3.3 PROCEDURE

The tests were carried out using an INSTRON Model 1195 machine, with a 100kN load cell. The specimens were secured with transversal 12.9 mm diameter steel pins to a fixed crosshead at one end and a moving crosshead at the opposite end. The load was applied with stroke control, at crosshead velocities of between 0.5 and 1.0 mm/min , up to specimen fracture. Frequent measurements of the neck diameter were taken with a Vernier caliper (precision ± 0.05 mm).

6.3.4 RESULTS

The results of the tests are summarized in figures 6.3 and 6.4. Figure 6.3 shows the axial load against the axial strain ϵ_{zz} at the minimum neck section. In all the tests a peak value of the load is reached when the necking instability arises. All specimens show fairly close results except CT3, which was not annealed. CT3 shows an earlier onset of necking, at around $\epsilon_{zz}=0.07$, and much higher levels of loads, with peak value 57kN. This corresponds to a strength of 285MPa referred to the original cross-sectional area, in accordance with the manufacturer's specifications (sect. 6.3.1). The non-annealed CT3 test showed also considerably less ductility (max. natural strain $\epsilon_{zz}=0.70$).

Results for the remaining tests all lie within a narrow band; peak loads range between 21 and 25kN, onset of necking between $\epsilon_{zz}=0.15 - 0.20$, and maximum strains before fracture between $\epsilon_{zz}=1.15 - 1.25$. Differences in annealing time clearly did not influence the behaviour beyond experimental uncertainty. For instance, specimens CT5 and CT6 were annealed for longer time (5 hrs) than CT4 (3 hrs), yet they yield results which are slightly closer to the non annealed CT3. These differences must be attributed to experimental scatter. The annealing process may be assumed complete for all specimens except CT3.
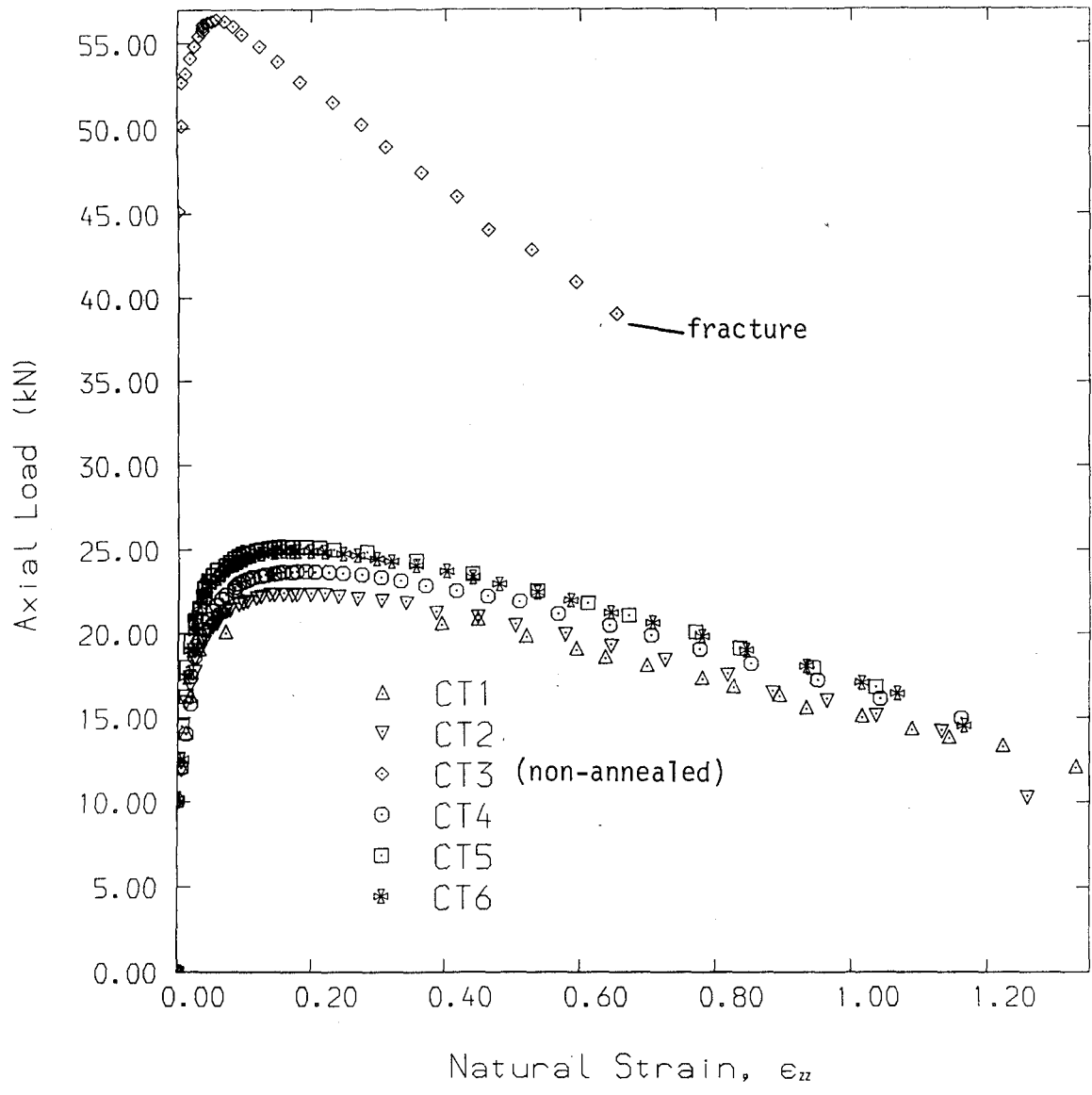
Figure 6.3: TENSION TESTS - AXIAL LOAD VS. STRAIN

In figure 6.4 the average axial stress at the neck is plotted against the axial strain for the annealed specimens. Although the total load drops after the onset of necking due to the geometrical reduction in area, it may be seen that at the elementary level the material does not cease to harden.

Fracture occurred with ductile cup-and-cone geometries for all the annealed specimens. A representative picture of one of the fractured specimens is given in figure 6.5 . For the non-annealed specimen CT3 fracture was more brittle and occurred earlier with a bang, producing a much less well developed neck (fig. 6.6).

Judging from these results it was concluded that completion of the annealing process was reached for CT1, CT2, CT4, CT5 and CT6 specimens. The mechanical properties derived from each of the tests may be averaged in order to obtain representative properties for annealed HE30 aluminium alloy.

6.3.5 MICROHARDNESS MEASUREMENTS

The necked bars were employed to study the distribution of plastic strains across transversal sections. This was done through microhardness measurements performed in a section normal to the axis of one of the tensile specimens after fracture. This section was the nearest to the fracture zone which did not show visible voids or change to its structure from the fracture. After polishing, microhardness indentations were performed at several locations along two normal radii. Further details of the microhardness testing procedure and equipment are given in section 7.3.1.3.1. The results are shown in table 6.1; they show no significant variation of the hardness accross the section.
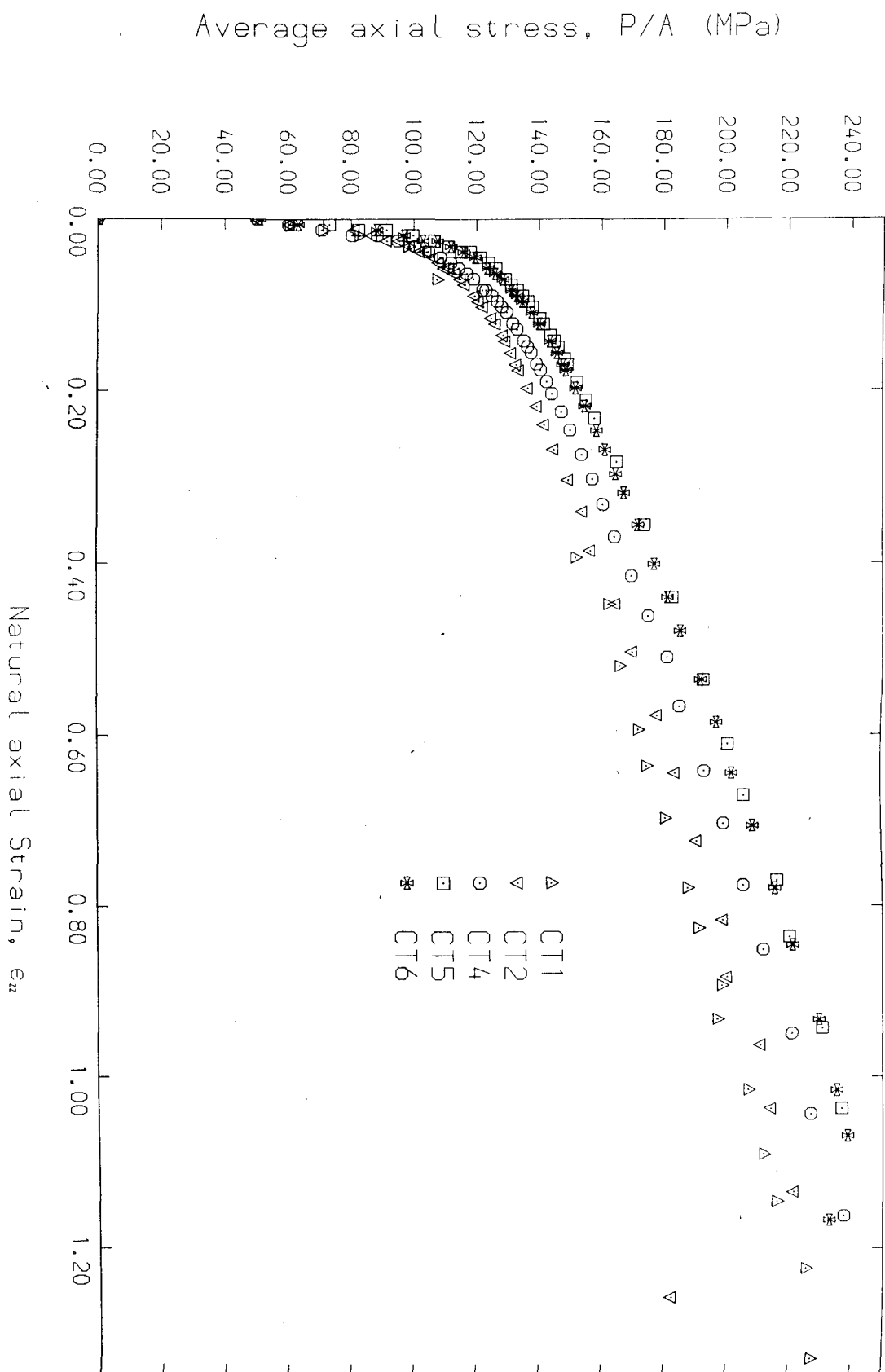
Figure 6.4: TENSION TESTS - AVERAGE STRESS vs. STRAIN AT NECK
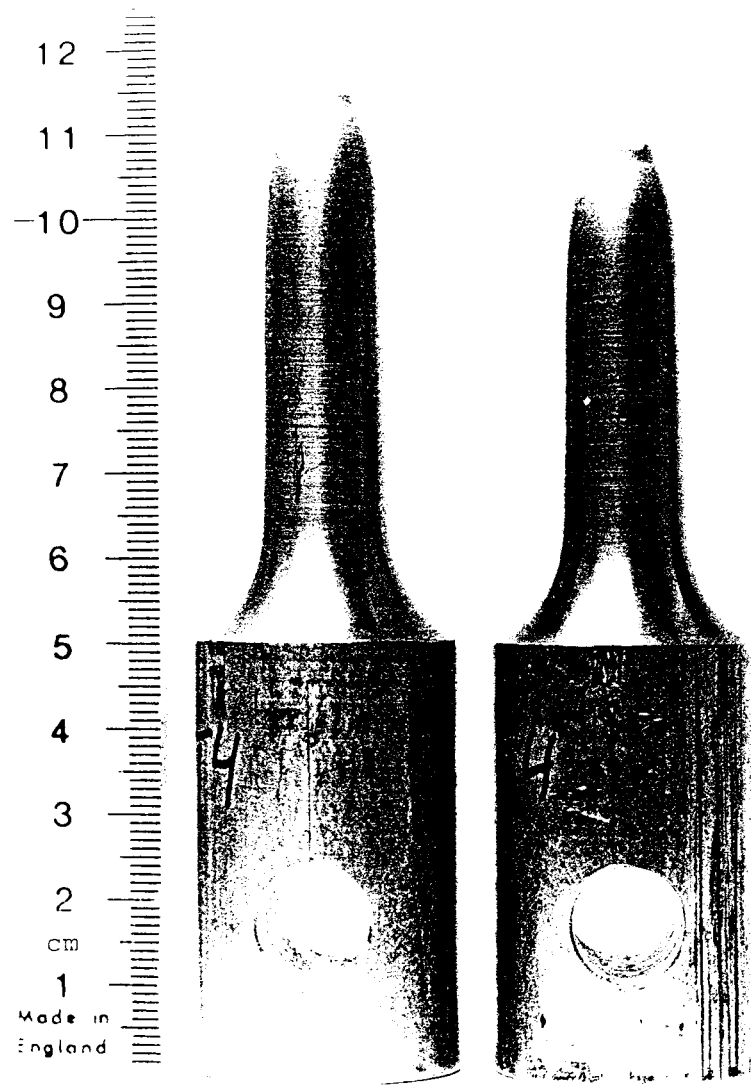
Figure 6.5: CT4 tensile specimen after fracture
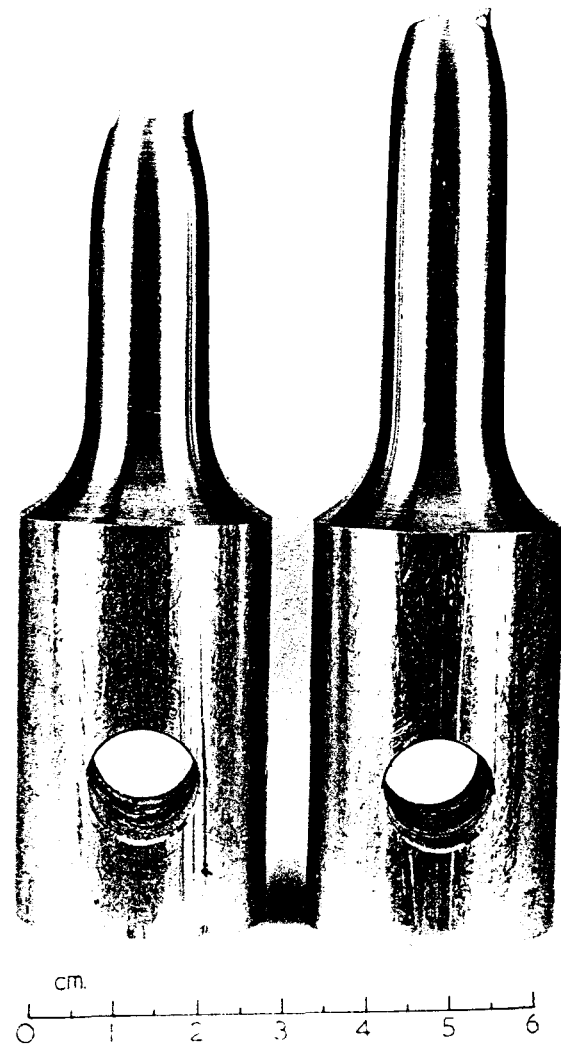
Figure 6.6: CT3 tensile specimen after fracture (non-annealed)

Point	Indentation Diagonal (Microns)	Microhardness $H_m(Kg/mm2)$
1	53	64
2	53	64
3	54	63
4	52	66
5	52	66
6	53	64
7	53	65
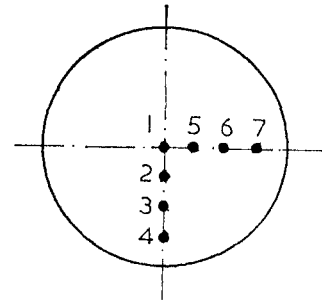
Current diameter

D = 9.2mm

Original diameter

D_o = 15.9mm

Microhardness load

P = 99g

$\epsilon_{zz} = -2Ln(D/Do) = 1.11$

Table 6.1: Microhardness measurementes in neck section of tensile specimen CT4.

From simple considerations of plasticity theory (Hill(1950), p.254), the hardness value H can be related linearly to the material strength Y, itself function of the plastic strain ϵ_p:

$$H = CY(\epsilon_p)$$

C being a constant whose value lies between 2.5 and 3.0 . Hence these microhardness results support the assumption of constancy of Y and ϵ_p across the minimum neck section (sect. 6.2.1).

6.4 MATERIAL HARDENING LAW

For aluminium power laws of the type

$$\sigma = A \epsilon^n \tag{6.18}$$

where: σ uniaxial true stress

ϵ uniaxial natural strain

A,n material constants

fit the material behaviour very well. The parameters A,n have a physical interpretation: A equals the stress for unit strain, and it can be shown that n corresponds to the strain at the peak load in a tensile test.

Given the equivalence between the uniaxial stress and equivalent stress pointed out in eqn. (6.5), a convenient and general form of expressing the material behaviour is

$$Y = A(\epsilon_{zz})^n = A(\epsilon_p + Y/E)^n \simeq A \epsilon_p^n \qquad (6.19)$$

Y/E represents the elastic part of the strains; these are usually very small compared to the plastic part, ϵ_p.

The average axial stress data presented in figure 6.4 were corrected with formula (6.17) to obtain the values for the material strength, Y. A power law $Y = A(\epsilon_{zz})^n$ was then fitted to the data from each test, by performing a linear regression in the logarithmic values (table 6.2). The parameters A,n so obtained for each test were averaged yielding mean values of A=181.7 MPa, n=0.182; these parameters provide a reasonable first estimate for the material hardening law.

Test	A (MPa)	n
CT1	169.1	0.190
CT2	172.5	0.177
CT4	184.7	0.196
CT5	191.5	0.170
CT6	190.6	0.178
Average	181.7	0.182

Power law
$Y = A \epsilon^n$

Table 6.2: Results of power law fits to tension test results

The results of this average fit, together with the equivalent stress - strain data derived from experiment, are plotted in figure 6.7 . Comparing with the average axial stresses in figure 6.4 the influence of the correction formula (6.17) is patent, lowering considerably the stress values for the larger strains. For a unit strain, the average axial stress is approximately 215 MPa, while the equivalent stress is lowered to 182 MPa , a reduction of 18%.

Although the "average" power law obtained represents a good overall fit, it can be seen in figure 6.7 that some discrepancies still exist in the region of low strains ($\epsilon_{zz} < 0.2$), while the fit is very good for the higher strains. It can also be seen that the discontinuous application of the correction formula (6.17) from $\epsilon_{zz} > 0.1$ has produced a discontinuity in the slope of the stress - strain data.

It is reasonable to suspect that the critical region for application of the correction formula (6.17) is in the low strain region, before the necking or when the neck curvature is small. It is here that the empirical relationship (6.16) between the neck curvature and the axial strain may be more in error. This relationship has a bias towards steel, which usually necks earlier than aluminium. Greater confidence can be placed in eqn. (6.16) for the higher strains, where the necking is well developed.

Consequently two additional curve fits to the corrected experimental data have been tried. These maintain roughly the same stress values for the higher strains, but differ slightly from the average curve fit for the lower strain region. A simple way for this variation is, maintaining the power law approach, to keep the same value for parameter A (which represents the stress for unit strain), and vary the exponent n. Two additional values of n were tried :

$$n_1 = 0.159 \text{ which gives a curve in the middle of the stress}$$
band, for $\epsilon_{zz} < 0.2$

$$n_2 = 0.133 \text{ which gives a curve near the top of the stress}$$
band, for $\epsilon_{zz} < 0.2$

It appears that n_1 should give the best fit, but this will be
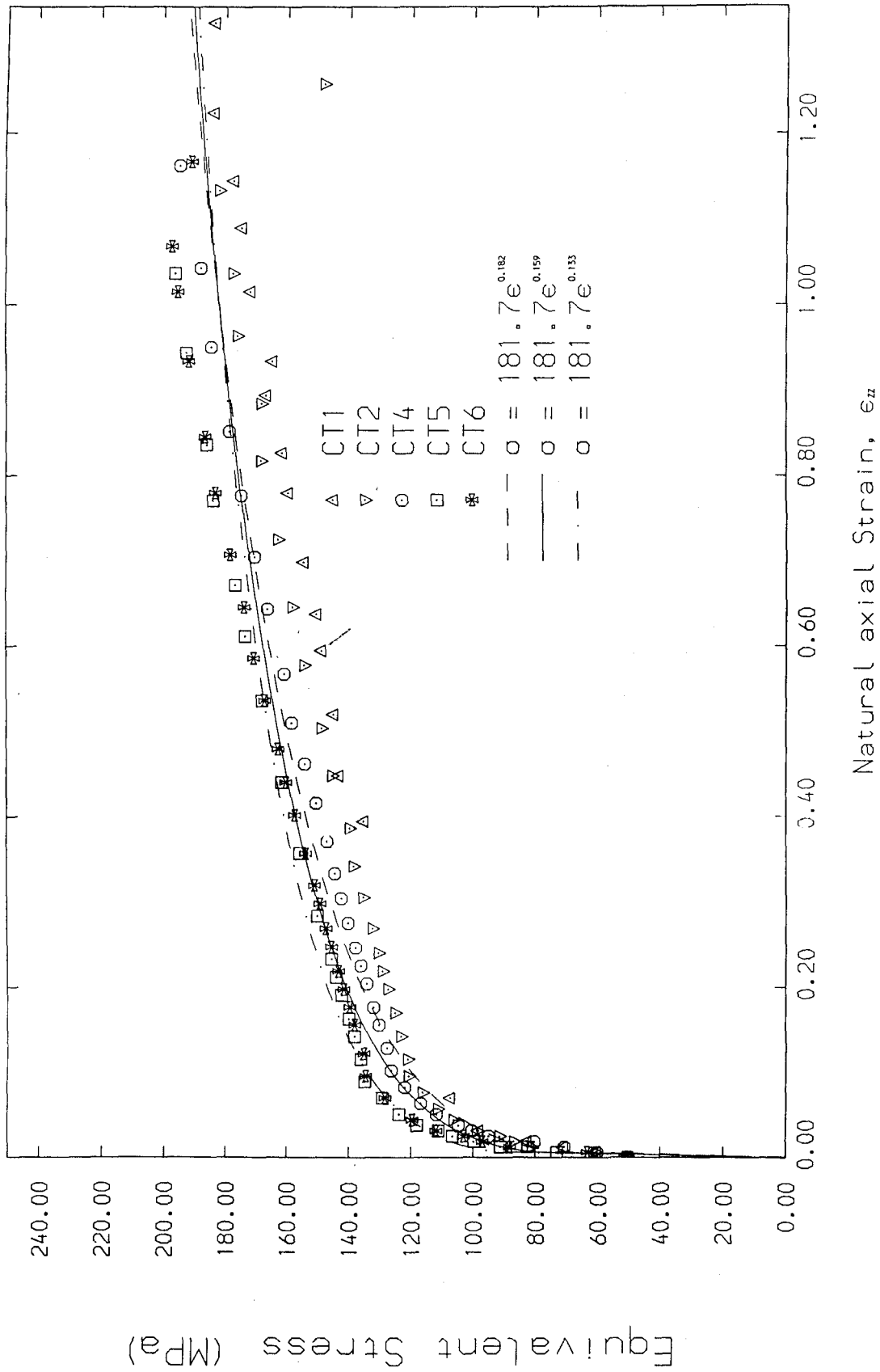
Figure 6.7: TENSION TESTS – EQUIVALENT STRESS VS STRAIN, POWER LAW FITS

decided from the results of numerical calculations using the three suggested curve fits, and their comparison with experimental observation.

6.5 NUMERICAL CALCULATIONS FOR TENSION TESTS

The tension tests were simulated numerically. From the results of the calculations it was possible to decide on the power law parameters that provide the best fit for the experimental results. Additionally, the calculations provided a check for the validity of the assumptions that were made in the interpretation of the tensile test for the stress and strain distributions. Finally this exercise was useful as a validation of the Explicit Finite Difference model proposed in this thesis (chapter 4), when applied to large scale non-linear computations for practical engineering problems.

6.5.1 MODEL

The calculations were performed using axisymmetric analysis, with a 2-D discretization in the r-z plane (fig. 6.8). The symmetry condition around the plane of the minimum cross-section (z=0) allowed a further reduction to a quarter of the r-z section. The mesh consisted of 875 triangular cells, grouped into 438 MTQ elements (see sect. 4.2.2) and 390 nodes. The model did not comprise the end fixings as they lie far from the area of interest and it was considered that they behave in practice as rigid load-transmitting devices. Only the central tapered portion of half-length 37.5 mm was modelled. Shear-free boundary conditions were assumed at the top and bottom ends of the specimen modelled. The mesh becomes progressively finer near the neck region, which is the area of interest, and where the stress and strain gradients will be steepest. Additionally, a high r:z aspect ratio was given to the elements in this area in order to avoid excessively distorted shapes when the neck is elongated in the axial direction.
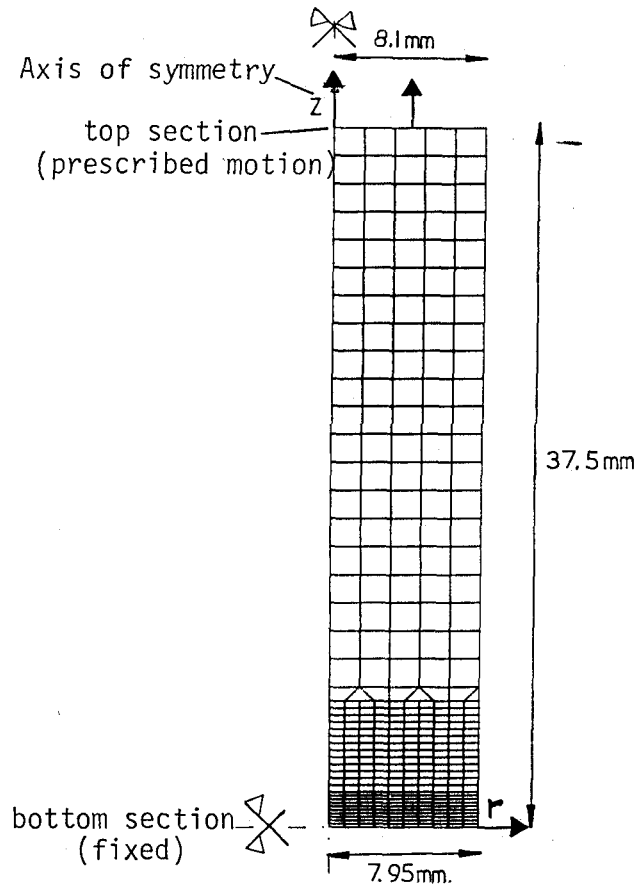
Figure 6.8: MESH USED FOR TENSION TEST CALCULATIONS
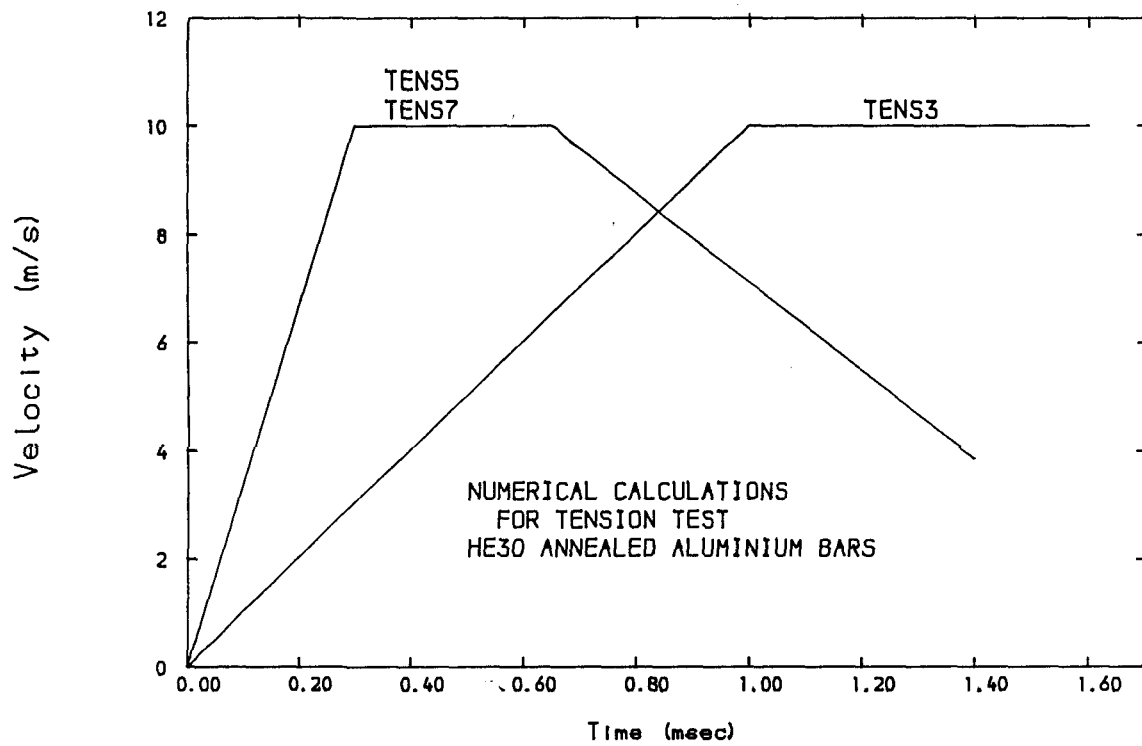
Figure 6.9: HISTORIES OF VELOCITY APPLIED AT END OF NUMERICAL MODEL

6.5.2 ANALYSIS

The tests were performed under quasi-static conditions at speeds of between 0.5 - 1.0 mm/min. The numerical algorithm used solves the equations of continuum mechanics in time with an explicit time-marching scheme; this leaves no option for static analysis, as calculations represent always a full dynamic model. As the computational time-step is limited for numerical stability to a small value (sect. 4.7), it would be too expensive in computer time to perform the dynamic analysis in real time.

To be able to perform the calculations velocity scaling was introduced (see sections 4.1, 5.4). The velocity of deformation was increased in order to bring down the number of computational cycles necessary for the analysis, from the 2×10^{10} that would be needed if the real velocity of deformation were to be used, to around 4×10^4.

Velocity scaling usually works well for quasi-static problems, as long as the deformation is applied slowly enough so as to let the stress-waves travel back and forth along the model several times, allowing redistribution of stresses. In other words, the model must not depart too much from the static equilibrium which must be simulated at each step in time. Two ways of quantifying this departure from equilibrium are:

- Ensuring that the load histories at opposite ends of the specimen are approximately equal (the out of balance forces must be small when compared to the total forces);

- Checking that the kinetic energy is small compared to the overall energy involved in the deformation process.

Three calculations are reported here, for each of the power law curve fits for the material constitutive behaviour suggested in section 6.4 (eqn. 6.18):

$$Y = A \epsilon^n$$

Analysis	A (MPa)	n
TENS3	181.7	0.182
TENS5	181.7	0.159
TENS7	181.7	0.133

In the calculations the typical axial velocity was 10 m/s and total times of analysis were between 1.25 msec and 1.6 msec.

The neck section was kept fixed in its plane while a prescribed velocity was applied to the upper end (fig. 6.8). The histories of applied velocities are given in figure 6.9 . Ramps were introduced to avoid sudden changes causing alterations to the equilibrium. Considering the stress-wave propagation velocity in Aluminium of 6000 m/s and an initial length of 37.5 mm , the largest stress-wave period is (initially) 0.0125 msec . Thus the number of stress-wave periods in the calculations, or in other words, the number of times the stress waves travelled back and forth redistributing stresses, is between 100 and 128. We shall see later (sect. 6.5.3) that the departure from equilibrium in the force histories this amount of velocity scaling ocassioned was small.

The importance of this cost-cutting compromise will be clear by mentioning that CPU time for each of the calculations in a CRAY-1S was between 30 and 45 minutes. This represents considerable computer resources. In a model without velocity scaling the costs would be 5×10^5 times higher (tens of years CPU time), way beyond the feasible range with the current development in digital computers.

6.5.3 RESULTS

The average stres versus strain results (fig. 6.10) lie precisely where it was presumed from the choice of curve fits done in section 6.4 . In all three cases for the large strain region ($\epsilon_{zz} > 0.2$) the fit is very good, in the middle of the experimental band. For the low strain region ($\epsilon_{zz} < 0.2$) the results from TENS3 are in the lower part of the band, TENS5 in the middle, and TENS7 in the upper part.
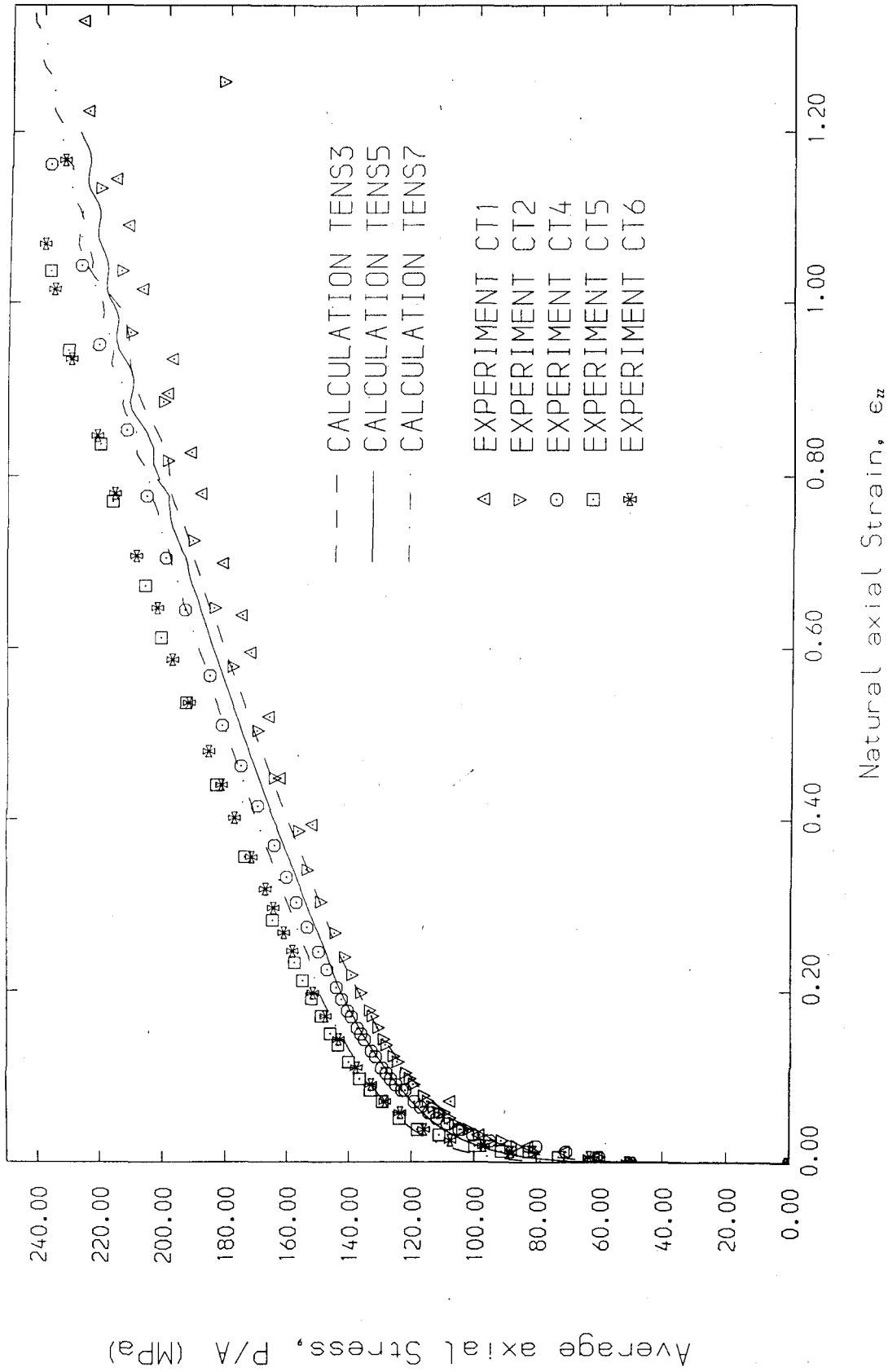
Figure 6.10: TENSION TEST CALCULATIONS – AVERAGE STRESS vs. STRAIN AT NECK
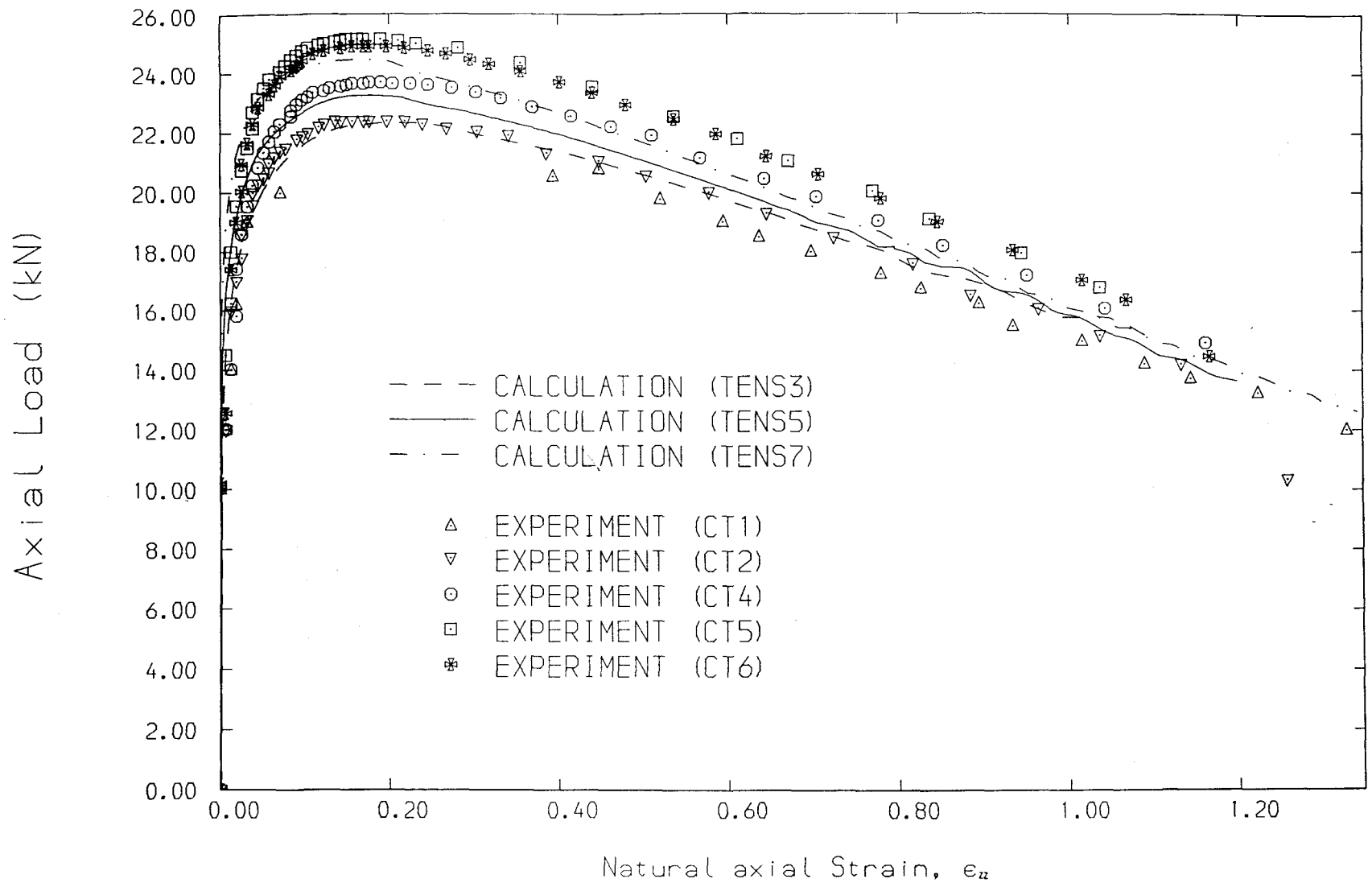
Figure 6.11: TENSION TEST CALCULATIONS - LOAD VS. STRAIN AT NECK

The figure plots Axial Load (kN) versus Natural axial Strain, ϵ_{zz}.

Legend:
- – – – CALCULATION (TENS3)
- ——— CALCULATION (TENS5)
- – · – CALCULATION (TENS7)

- △ EXPERIMENT (CT1)
- ▽ EXPERIMENT (CT2)
- ⊙ EXPERIMENT (CT4)
- ⊡ EXPERIMENT (CT5)
- ✳ EXPERIMENT (CT6)

This suggests that the curve fit used for TENS5 is the most appropriate, as had been anticipated. Hence, the hardening law for the HE30 aluminium material will be taken as:

$$Y = 181.7 \, \epsilon^{0.159} \; (MPa) \qquad\qquad (6.20)$$

A view of the deformed mesh for TENS5 with all symmetries plotted is given in figure 6.12. At this point the axial strain at the neck was $\epsilon_{zz} = 1.22$.

The curves presented in figures 6.10 and 6.11 were taken from the calculated time-histories, after averaging the load between top and bottom of the model, and having applied a numerical filter with a centred moving average technique, to facilitate the visualization and interpretation. The exact time-histories obtained in the calculations for top and bottom loads are given in figure 6.13 . It can be seen that a state of static equilibrium existed for most of the analysis, the two load histories being approximately equal. At about 1.1 msec however, some oscillations occur in the histories creating certain departure from static equilibrium. These oscillations have approximately the period of the longitudinal stress waves travelling along the specimen:

$$T = 2 \, \frac{L}{c} = 2 \, \frac{45 \times 10^{-3} m}{6000 \; m/s} = 0.015 \; msec$$

L being the current length of the specimen and c the velocity of stress waves. It can be appreciated that only a small number of stress-wave periods occur in an interval of time at which large variations in the neck size (see figure 6.14) and material behaviour take place. The model does not have time to digest these changes quickly enough and the information is transmitted in jumps originating the consequent elastic oscillations. It is interesting to note the larger amplitude of the oscillations at the top end, which is unloading elastically, than at the neck, where the plasticity of the material behaviour dampens out the oscillations. At no moment however do the oscillations in load depart from the equilibrium value by more than 10%, and the expected trend of the load curve is maintained.

For details of
initial geometry
see Figure 6.8
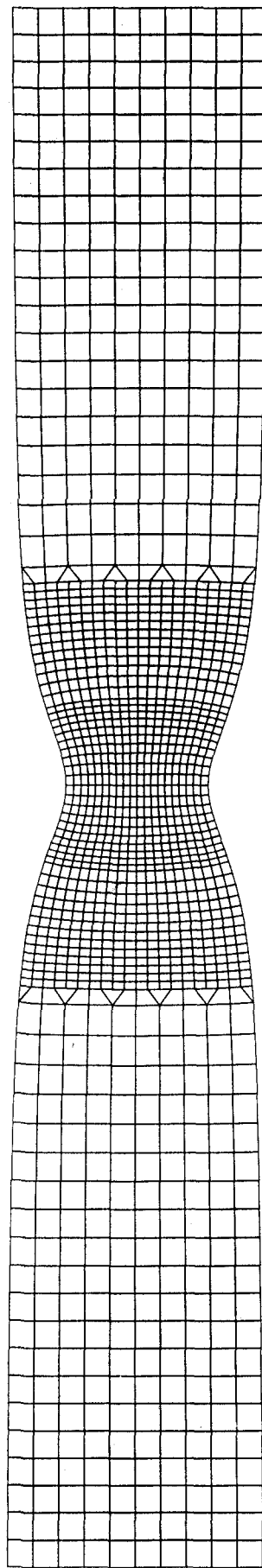
strain at neck
$\epsilon = 1.22$

Figure 6.12: DEFORMED MESH FOR $A/A_0=0.29$
HE30 ANNEALED ALUMINIUM BAR - TENSION TEST CALCULATION (TENS5)
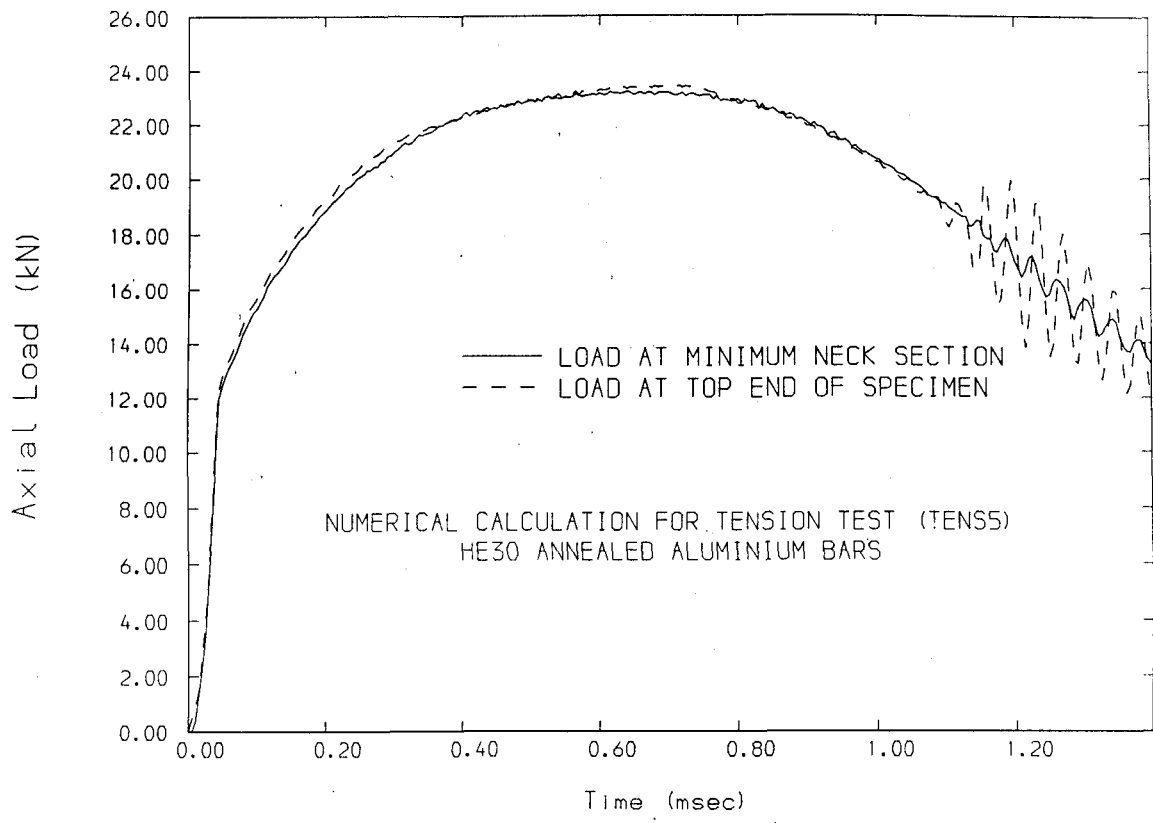
Figure 6.13: CALCULATED LOAD HISTORIES WITHOUT FILTERING
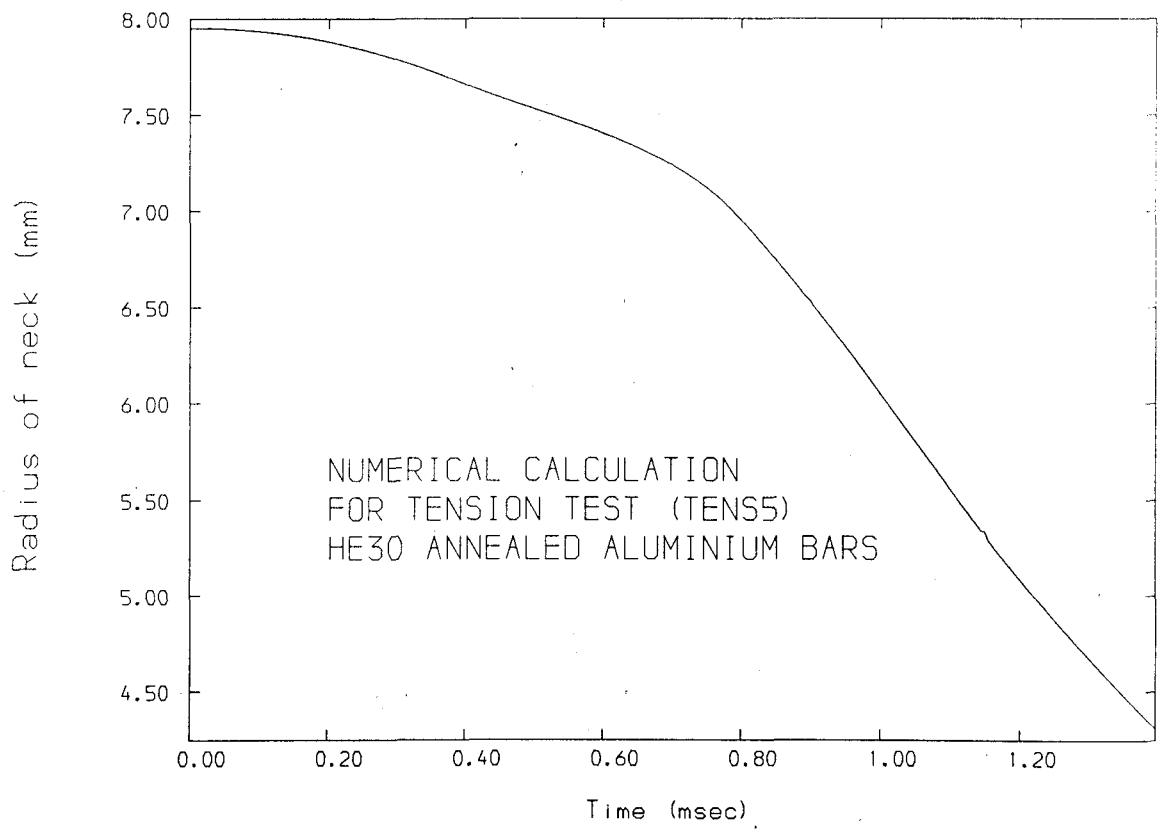
Figure 6.14: HISTORY OF NECK RADIUS

For figures 6.10 and 6.11 the load histories were averaged and filtered, removing oscillations of frequencies higher than 50000 Hz, which corresponds roughly to the stress-wave period. In this way the overall trend of the results can be seen more clearly, without unwanted numerical oscillations, due mainly to the compromise made in the velocity scaling.

Some contour plots of different stress components for the neck region are presented in figure 6.15; the following observations may be made about these:

a) The radial (fig. 6.15b) and hoop (fig. 6.15c) stresses are approximately equal in the neck region, tending to zero at the outside edge, and reaching maximum values near the axis of about 60 MPa;

b) The axial stress (fig. 6.15d) is clearly non-uniform across the neck section, decreasing from approx. 270 Mpa in the axis to 200 MPa on the outside;

c) The yield strength Y (eqn. 6.2) is roughly uniform across the neck section (fig. 6.15a), with an approximate value of 189 MPa;

d) The axial strain at the minimum section is $\epsilon_{zz} = 1.22$, which from eqn. (6.20) corresponds to a flow stress of

$$Y = 181.7 \times 1.22^{0.159} = 188 \text{ MPa}$$

and an average axial stress (from eqn. (6.17)) of

$$\sigma_{zz} = Y(1+2/\sqrt{1.12})Ln(1+\sqrt{1.12}/2) = 1.23Y = 231 \text{ Mpa}$$

These values correspond very closely to those expressed above in c) and b) respectively.

The yield strength contours for the complete specimen are plotted in figure 6.16, showing the much lower levels of strain-hardening which occurred in the upper part of the model. This hardening happenned in the first stage of uniform deformation of the specimen; after the necking that region has been unloading elastically.
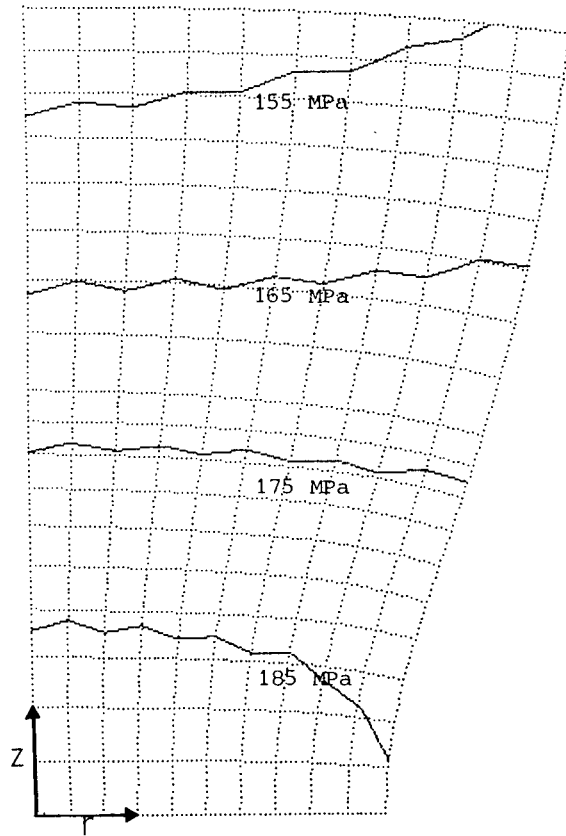
a) Yield Strength Y
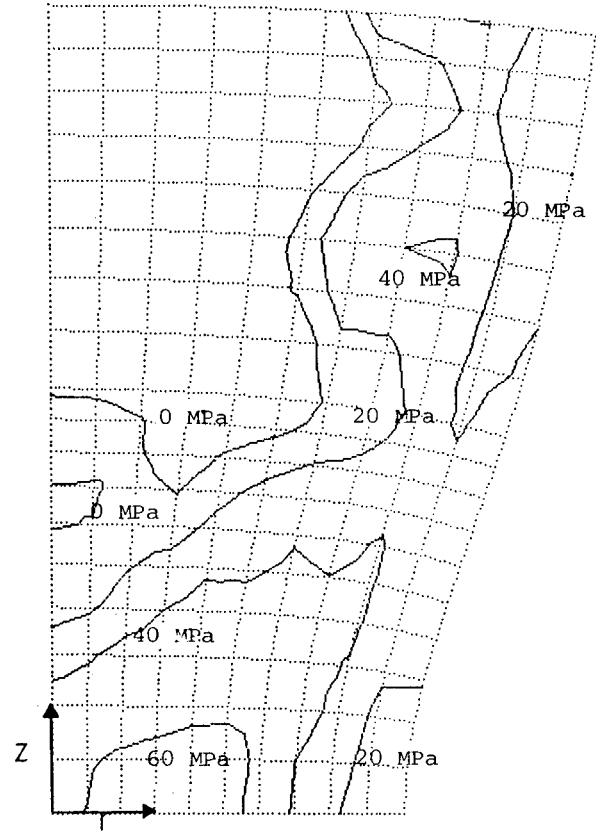
b) Radial Stress σ_{rr}
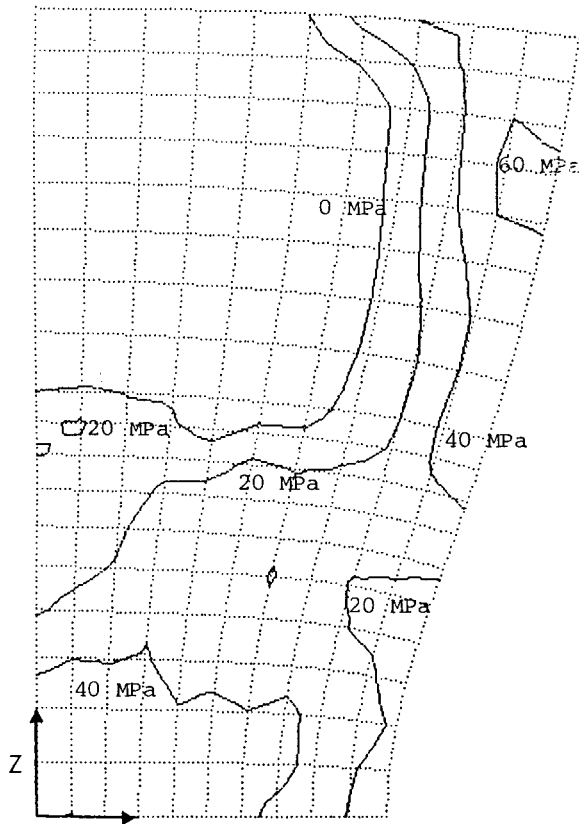
c) Circumferential Stress $\sigma_{\theta\theta}$
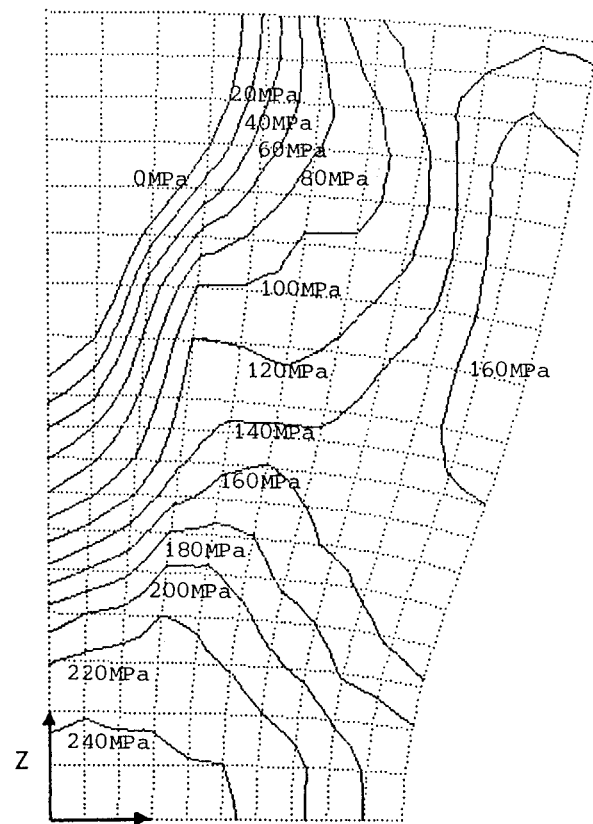
d) Axial Stress σ_{zz}

Figure 6.15: Tension test calculations - Stress contours in neck region
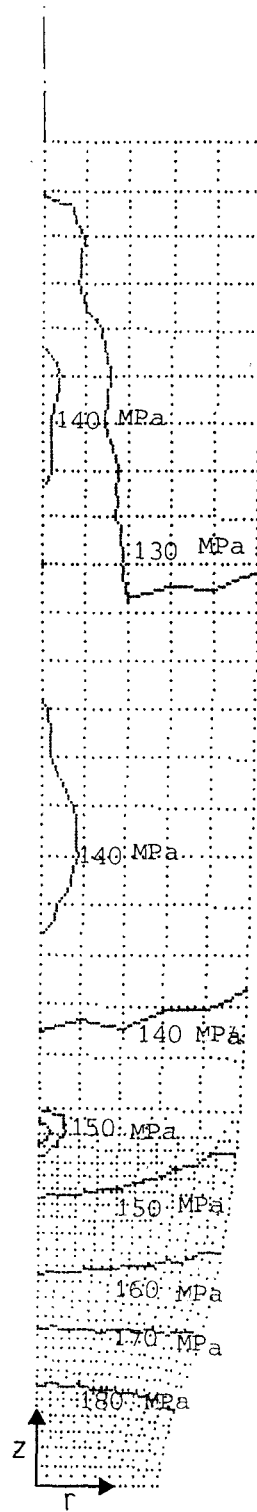
Figure 6.16: Tension test calculations - yield strength (Y) contours
(general view)

All these results match very closely the theoretical interpretation of the tensile test detailed in 6.2, suggesting the general validity of that interpretation and of the numerical model.

6.6 **CONCLUSIONS**

1.   Tension tests on cylindrical bars constitute a simple and reliable means of obtaining material stress/strain data at large strains, when viewed as a 3-D plasticity problem.

2.   The interplay between the theory (sect. 6.2) and numerical analysis (sect. 6.5), coupled with experimental fact (sect. 6.3), allowed a simple and representative constitutive law for the HE30 Aluminium to be established (eqns. 6.18, 6.20), for use in future large strain plasticity analyses (chapter 7). This constitutive law assumes Von Mises plasticity with power law isotropic hardening.

3.   Excellent agreement was achieved between numerical predictions, experimental fact, and theoretical understanding, of the behaviour of a plastically deforming necked cylindrical bar (sections 6.3.5, 6.5.3, figs. 6.10, 6.11, 6.15). The semi-empirical theories of Bridgman (1952) and Davidenkov and Spiridinova (1946) were broadly confirmed by the numerical results.

CHAPTER 7

CONCERTINA TUBE COLLAPSE ANALYSIS

7.1 INTRODUCTION

7.1.1 Scope

7.2 OVERVIEW OF ENERGY DISSIPATING DEVICES

7.2.1 Definition and criteria

7.2.2 Types of energy dissipating devices

7.2.3 Tubes as energy absorbers

   7.2.3.1 Lateral compression

   7.2.3.2 Axisymmetric axial crumpling

   7.2.3.3 Diamond-fold axial crumpling

   7.2.3.4 Tube inversion

7.2.4 Methods of analysis

7.3 QUASI-STATIC CONCERTINA TUBE COLLAPSE MECHANISMS

7.3.1 Related experimental work

   7.3.1.1 Experimental Programme and method

   7.3.1.2 Typical experimental results

   7.3.1.3 Microhardness tests

      7.3.1.3.1 Equipment and procedure

      7.3.1.3.2 Derivation of material strength, Y

7.3.2 Numerical model

   7.3.2.1 Discretization and material

   7.3.2.2 Velocity scaling

   7.3.2.3 Interpretation of output

7.3.3 Results from numerical calculations and experiment

   7.3.3.1 Tube geometry A: ID=19.05mm, t=1.64mm, L=50.8mm

   7.3.3.2 Tube geometry B: ID=19.05mm, t=1.17mm, L=50.8mm

.

7.1 **INTRODUCTION**

The numerical methods described in chapter 4 are applied here to the analysis of tube collapse mechanisms, with a view to studying their performance as energy dissipating devices.

In accordance with the characteristics of the computer program, the attention was restricted to mechanisms which could be studied through axisymmetric or 2-dimensional models. In particular, most of the work relates to axial collapse of tubes through axisymmetric sequential folding. This mode of collapse plays an important role in energy dissipation and its numerical modelling poses some interesting challenges. For example:

a) Large strains (with values higher than 1.3) and gross deformations (complete crumpling of tube walls) need a careful and consistent mathematical treatment (chapter 2);

b) The need to provide constitutive laws valid for large strains (chapter 6);

c) Contacts with the platens and between folds make necessary a general logic for interaction between continua;

d) Dynamic analysis is necessary, as energy dissipation occurs mainly in impact situations, where stress-wave propagation or inertia effects are often important;

e) Lastly, a robust numerical algorithm is necessary which accomodates the solution to the above problems and works well in practice for real, engineering scale problems (chapter 4).

7.1.1 **SCOPE**

This chapter relates to the following:

1- Firstly a general overview of energy dissipation, and the role of tubes in it, is presented. This is followed by a description of some

experimental work on tube collapse; most of this work was carried out by Ghani (1982), and it will be used to compare with the numerical predictions for axisymmetric tube crumpling that follow.

2- Results from numerical calculations of quasi-static axial collapse are given for 4 different tube geometries (table 7.3). Over 20 computer analyses (table 7.4) were performed in order to assess the applicability of the method, and evaluate the influence of various modelling choices. Optimal models were then selected for the final analyses. The results are compared with experimental data.

3- In the medium velocity range, a full-scale model of the impact of a thin-walled vessel at 176 m/s was performed. This problem tested the performance of the computer code for large scale engineering computations, involving several thousand degrees of freedom and over a hundred thousand time-steps. The results compared well with available experimental data. The crushing force obtained was found to be considerably larger than for low-velocity collapse.

7.2 OVERVIEW OF ENERGY DISSIPATING DEVICES

Energy dissipating devices are reviewed briefly in this section. The intention is to introduce practical projections for the numerical applications presented later. The importance of the various tube collapse mechanisms is highlighted.

7.2.1 DEFINITION AND CRITERIA

Energy dissipating devices are mechanisms which can dissipate the kinetic energy from the impact of colliding bodies in an irreversible manner.

Elastic, recoverable systems are therefore excluded from this definition. Usually, energy is dissipated through plastic work, being converted into heat eventually. To fulfill their function without excessive deceleration and consequent damage, energy absorbers must provide a reasonably constant operating force over as long a stroke as

possible. This must occur in a controlled (i.e. without catastrophic failure) and reliable way.

Ideally energy absorbers should be made of low cost and widely available components, with high values for the following parameters:

- Specific energy, i.e. Energy dissipated / Mass of device

- Stroke efficiency, i.e. Absorbing length / Total length

- Energy dissipating density,i.e. Energy dissipated / Volume of device.

7.2.2 TYPES OF ENERGY DISSIPATING DEVICES

Some of the main types of energy absorbers are summarized below, concentrating on destructive (one shot) devices, mainly of metallic materials. No attempt is made to provide a comprehensive review of the topic. Excellent reviews have been given by Johnson and Reid (1978) and Ghani (1982).

Schematically one may classify the various mechanisms according to their mode of behaviour, as follows.

a) Extension. Steel rods or cables under tension have been used extensively in pipe-whip restraint systems (e.g. Hernalsteen and Leblois, 1976). A disadvantage is that tensile deformations tend to become localized in necks and may produce overall failure.

b) Compression. For instance the crushing of lightweight cellular bodies or of soft copper bumpers (Hernalsteen and Leblois, 1976).

c) Bending. Beams and plates may dissipate energy through rotation in plastic hinges. Laterally crushed tubes or assemblies thereof provide some very useful devices (Thomas, Reid and Johnson (1976), Shrive, Andrews and England (1984)).

d) Compression and bending. Systems in which bending modes are

produced as a result of a structural compression may be included here. These comprise some of the most efficient energy absorbers, such as the axial crumpling of circular tubes (axisymmetric or diamond modes) and tube inversion. Tubes with non-circular sections have been used advantageously by Kukkola (1976). Honeycomb panels provide also a very popular and reliable mechanism (McFarland, 1963).

e) Cyclic bending, Here one may include systems such as the rolling torus of Johnson, Reid and Singh (1975). These tend to be associated with lighter operating loads.

7.2.3 TUBES AS ENERGY ABSORBERS

Tubes have a particular interest as energy absorbers, because of all the existing devices they present the widest range of possible uses; These include some of the most efficient and reliable energy dissipation mechanisms.

Tubes are simple structures and therefore cheap and widely available. Additionally, the basic structure of many moving vehicles and aircraft is a tube, which will double up in function as an energy absorber in the event of a collision.

The main tube collapse mechanisms are reviewed below. Some simple classical analytical formulae for collapse loads are included where pertinent.

7.2.3.1 LATERAL COMPRESSION

Tubes crushed laterally provide a very reliable energy absorber in which the plastic deformation is concentrated around localized hinges. DeRuntz and Hodge (1963) studied experimentally and theoretically their behaviour, deriving a formula for the collapse load based on a rigid-plastic, thin shell model:

$$P = \frac{(4\sqrt{3}) \ Y \ t_0^2}{D\sqrt{1-(\delta/D)^2}} \qquad (7.1)$$

where δ is the displacement, t_0 and D the thickness and Diameter of the tube respectively, and Y the Yield stress for a perfectly plastic material model. Due to the absence of material hardening in (7.1) some discrepancies with experiments were notable; Reid and Reddy (1978) have proposed more recently solutions in which linear strain hardening is considered, achieving better results.

7.2.3.2 AXISYMMETRIC AXIAL CRUMPLING

When subjected to axial compression, tubes may buckle in an axisymmetric fashion, forming concertina-type folds which pile up sequentially on top of each other (Figure 7.1a).

This collapse mode constitutes a very efficient energy absorber, by reason of the gross plastic deformations which occur in a large proportion of the tube. The sequential nature of the folding process accounts for a reasonably constant operating force over a long stroke. For given tube dimensions this mechanism is reproducible and very reliable (Ghani, 1982).

Alexander (1960) first derived an approximate solution for this mechanism from rigid-plastic thin shell assumptions. The average collapse load and fold length according to this theory are

$$P = 6t_0 Y\sqrt{Dt_0} \qquad (7.2)$$

$$h = \sqrt{\frac{\pi}{2\sqrt{3}} Dt_0} \qquad (7.3)$$

Alexander's formulae, however simple, give sensible predictions in general; they are often referred to (e.g. Johnson, 1972) and continue to be used today by many workers (e.g. Hurley, 1983, Mamalis and Johnson, 1983). However, eqn. (7.2) assumes a perfectly plastic material (no hardening); for good predictions care must be taken to use a value for Y representative of the actual average strain-

hardening of the material. Experimental and numerical studies carried out here show effective plastic strains accross the fold sections of the crumpled tube between 0.3 and 1.3 (section 7.3.3). This suggests an appropriate average value of 0.8 strain to be used for obtaining the value of Y.

Numerical analyses of these mechanisms are undertaken in sections 7.3 and 7.4, constituting the core of this chapter.

7.2.3.3 DIAMOND FOLD AXIAL CRUMPLING

When subjected to axial compression, another possible collapse mechanism is the formation of non-axisymmetric folds in a diamond pattern, accompanied by a change in cross section of the tube (figure 7.1b). This mechanism is also reliable and efficient as an energy absorber, although the specific energy is slightly lower than for the concertina mode (Ghani, 1982).

Diamond fold crumpling was studied by Pugsley and Macaulay (1960), who proposed formulae based on rigid-plastic analysis. Further study has been made by Johnson, Soden and Al-Hassani (1977) who assumed 'inextensional collapse modes'. Thornton and Magee (1977) have also used these devices as energy absorbers; they prepared the tubes previously by making 3 circumferential indentations at one end, in order to avoid the initial peak load and trigger smoothly a 3-lobe diamond pattern.

7.2.3.4 TUBE INVERSION

Tube inversion modes may be achieved either by pushing a tube axially against a radiused die or by preforming and clamping appropriately one end. Inversion may be external or internal. Plastic deformations extend to virtually the complete length of tube, as each section is first bent, and then straightened out. An efficient energy absorber with a nearly flat load response is thereby obtained.

Guist and Marble (1966) have considered inversion tubes for

impact absorption in landing of aircraft and space vehicles; they proposed a simple rigid-plastic equation for the collapse load:

$$P = \pi t_0 Y \sqrt{8 D t_0}$$ (7.4)

Al-Hassani, Johnson and Lowe (1972) have presented a detailed study of these devices, developing further the analysis to include power-law strain-hardening, achieving thus a better match to experimental results.

7.3 QUASI-STATIC CONCERTINA TUBE COLLAPSE ANALYSIS

7.3.1 RELATED EXPERIMENTAL WORK

A description is given here of the experimental work on quasi-static collapse of Aluminium tubes to which reference will be made in the following sections, where the experimental results will be compared with numerical predictions. Most of the experimental data mentioned here are derived from work done by Ghani (1982) who undertook an extensive programme of study and classification of collapse modes, spanning 189 different tube geometries. A good synopsis of these tests and their results has been given by Andrews, England and Ghani (1983).

In addition to Ghani's work, 5 extra tubes have been crumpled for this investigation in order to provide additional experimental data which were needed (Table 7.1). This was done with the same material and under identical conditions as Ghani (1982).

Finally, in order to provide data for the stress distributions around the fold hinges, some crumpled tubes were cut and microhardness tests performed on the wall sections. The microhardness data were calibrated and correlated to the material strength Y.

Geometry			Collapse mechanism
t_o(mm)	L(mm)	OD(mm)	
1.27	50.8	38.1	Concertina, 3 1/2 folds
1.28	88.9	38.1	Concertina, 6 folds
1.67	50.8	38.1	Concertina, 3 folds
1.65	50.8	38.1	Concertina, 3 folds
1.67	88.9	38.1	Concertina, 5 folds

Table 7.1: Additional tests for axial collapse of tubes
(HT30 annealed aluminium)

7.3.1.1 EXPERIMENTAL PROGRAMME AND METHOD

The tests were performed on HT30 (BS1471) Aluminium alloy tubing. This material has identical composition and similar mechanical properties as the HE30 alloy used for the bar tension tests reported in chapter 6. The as-received mechanical properties of HT30 are as follow:

0.1% proof stress	228 -243 MPa
density	2700 Kg/m^3
Young's modulus, E	67000 MPa
Poisson's ratio	0.3
Ultimate tensile strength	304 MPa
Elongation on 2 in.	7 - 9%

The slight variation in mechanical properties from those of HE30 is due to the different cold-forming processes: HT30 tubes are formed by drawing, while HE30 bars are extruded.

The specimens were annealed prior to testing at a temperature of 350o C for times ranging between 3 and 7 hours, depending on wall thickness; all specimens were oven cooled.

The tubes were crumpled under stroke control using an Instron Model 1195 press, with a 100 kN load cell. The few specimens which required larger loads were tested with a Losenhausen press. Deformation rate was approximately 5 mm/min. Undeformed tube lengths

ranged between 6.35 and 533.4 mm.

7.3.1.2 TYPICAL EXPERIMENTAL RESULTS

The collapse modes obtained by Ghani (1982) may be grouped into the following broad categories:

- Concertina (49 tubes); Axisymmetric, sequential folding starting at one end of tube
- Diamond (5 tubes); Non-axisymmetric but sequential folding accompanying a change in cross section shape
- Mixed concertina-diamond (44 tubes); starting as concertina and changing over to the diamond mode after some folds
- Euler (31 tubes); buckling of tube as a strut
- Various crushing modes (60 tubes); simultaneous collapse of the whole tube due to crushing, tilting, 2-lobe diamond, or simultaneous concertina failure.

Figure 7.1 shows a selection of test results, featuring an example of each of the collapse modes mentioned above. According to the length/diameter and wall thickness/diameter ratios of the undeformed tubes, a classification chart was drawn up (figure 7.2). This diagram indicates distinct regions in which a certain collapse mode can be expected.

Curves indicating the variation of axial load with axial shortening of the tubes were plotted directly for all the tests. From the analysis of these curves, the energy absorption characteristics were obtained for the various modes of collapse.

Using the collapse mode regions defined in figure 7.2, tube geometries can be selected for which one may expect concertina sequential failure. The 5 extra tubes (table 7.1) tested for this investigation were selected with such characteristics; they all collapsed in concertina mode as expected. A typical result together with the corresponding load-compression curve is shown in figure 7.3.
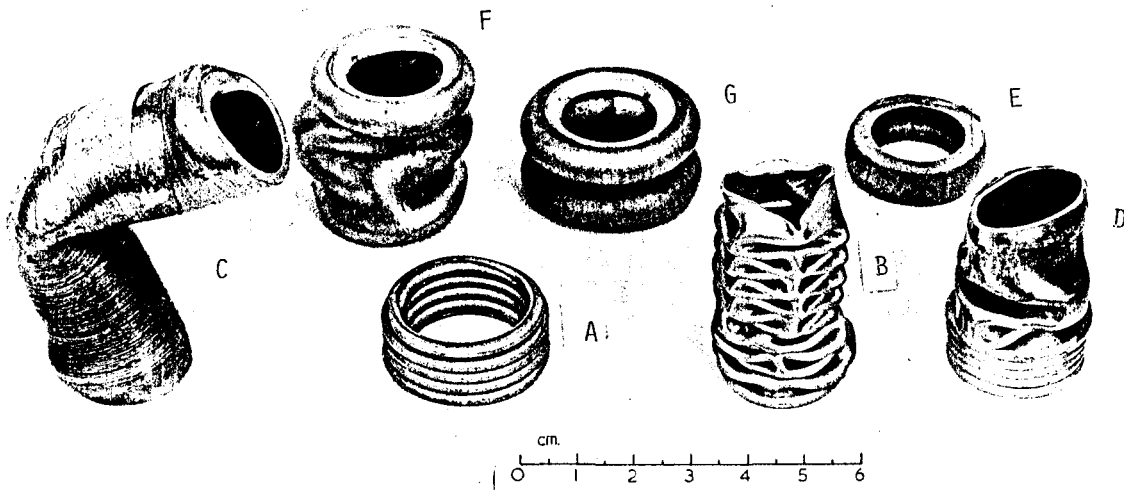
FIGURE 7.1:COLLAPSE MODES FOR ALUMINIUM TUBES UNDER AXIAL COMPRESSION (GHANI, 1982)
A - Concertina, B - 3 lobe diamond, C - Euler buckling, D - Mixed Concertina-
Diamond, E - Crushing, F - 2 lobe diamond crushing, G - simultaneous concertina
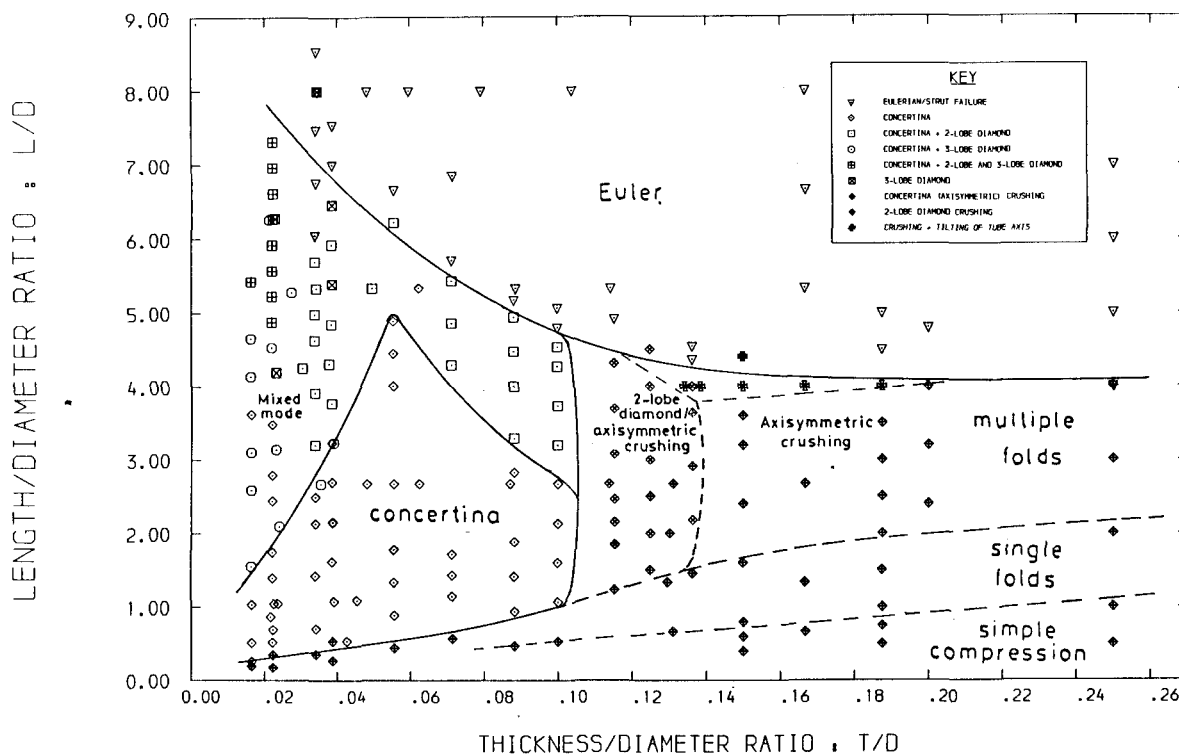
FIGURE 7.2: CLASSIFICATION CHART OF AXIAL COLLAPSE MODES IN CIRCULAR TUBES
(FROM GHANI, 1982)

A) view of crumpled tube
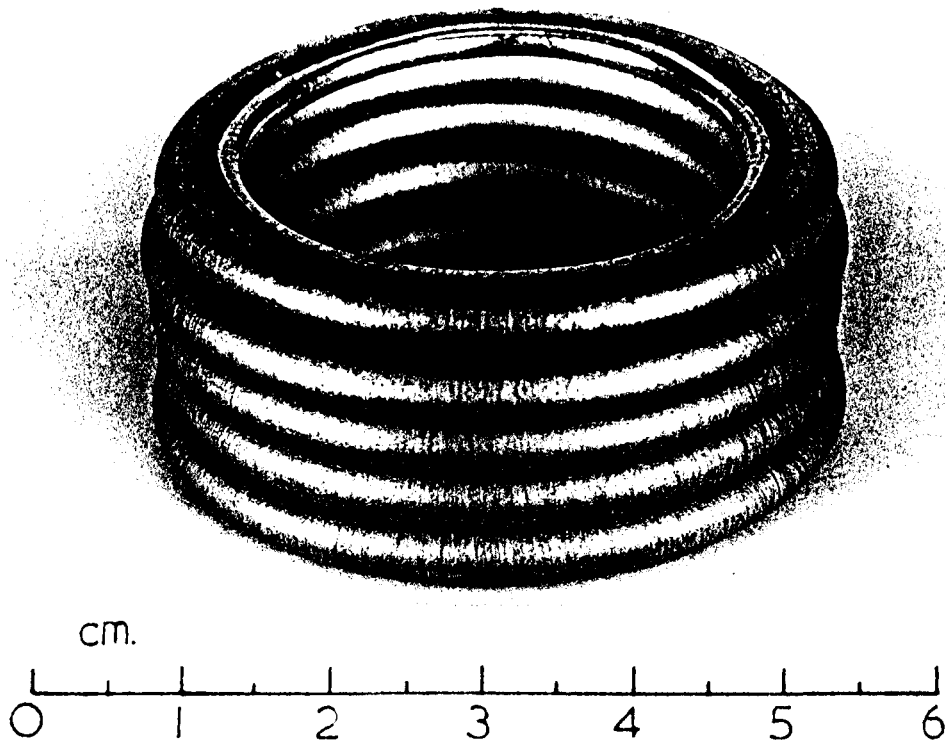
OD=38.1mm, t_o =1.67mm, L=88.9mm TUBE
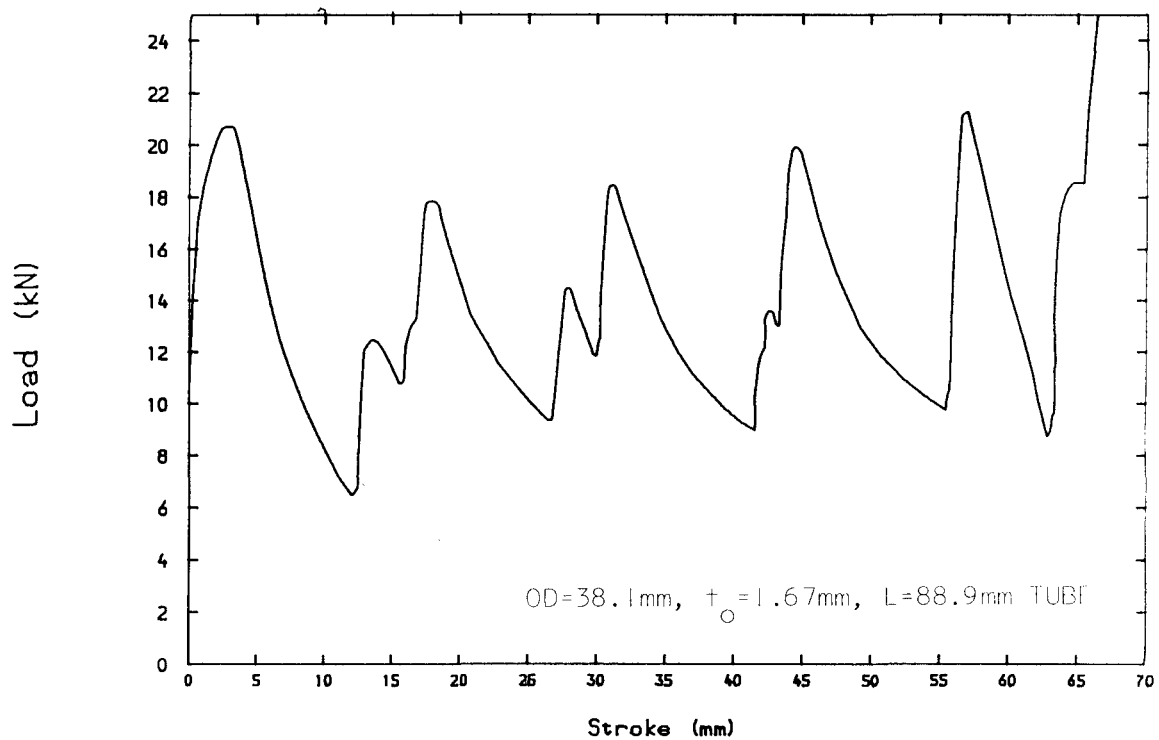
B) LOAD – COMPRESSION CURVE

Figure 7.3: Typical results of quasi-static tube crumpling experiment with HT30 annealed aluminium alloy (Concertina mode of collapse)

7.3.1.3 **MICROHARDNESS TESTS**

Longitudinal sections of some tubes have been cut and microhardness tests performed on them, in order to derive strain and stress distributions which could be checked against numerical predictions.

7.3.1.3.1 Equipment and procedure

A Reichert microhardness tester was used for these tests. It consists in essence of a 1360 apex angle square pyrammid diamond indentor, which can be pressed against the specimen with a specified load, and then moved out of the way for measuring with a microscope lens the size of the impression.

The microhardness H_m is defined as the mean pressure exerted on the surface of the indentor. Simple geometrical considerations permit the expression of H_m (Kg/mm2) as a function of the applied load P (g) and the indentation diagonal, d (microns):

$$H_m = 1854.4 \ P/d \tag{7.5}$$

Although there is geometrical similitude between indentations of different sizes, and contrary to what happens for (macro)hardness (VPN) at higher loads, the microhardness is not independent of the load applied. Hence an arbitrary constant load of 99 g was selected for all the measurements.

The surfaces of the specimens were lapped prior to testing, in order to obtain smooth, flat surfaces in which the microscopic indentation measurements could be taken with sufficient precision.

Three crumpled tube specimens were selected for testing. The original dimensions of these tubes were

- ID = 19.05mm, t_o = 1.64mm, L = 50.8mm (geometry A, sect. 7.3.3.1);
- ID = 19.05mm, t_o = 1.17mm, L = 50.8mm (geometry B, sect. 7.3.3.2);

- OD = 38.1 mm, t_0 = 1.65mm, L = 50.8mm (geometry C, sect. 7.3.3.3).

In each case, the microhardness measurements were done only in an area around one of the folds. The size of the indentation diagonals varied between 50 and 70 microns; a separation of 200 to 300 microns was left between different indentations in order to eliminate cross-influences. Typical results for one of the above tubes are shown in figure 7.4.

7.3.1.3.2 Derivation of material strength, Y

The strain-hardened flow stress Y is related to the hardness. For a perfectly plastic material this relationship is linear (Hill (1950), p260):

$$H = CY \qquad\qquad (7.6)$$

where C is a constant factor depending on the geometry of the indentor and the angle of friction, which normally lies between 2.5 and 3.0. For a smooth, flat die Prandtl's solution (sect. 5.4.1) yields

$$C = (2 + \pi)/\sqrt{3} = 2.97$$

In the event of real materials with strain-hardening, eqn. (7.6) is not true in a strict sense. The plastic distortion around the indentor is non-uniform and different elements harden by different ammounts. Mean equivalent values of Y need to be used in eqn. (7.6); determination of these mean values involves necessarily an approximation and a certain degree of error. Nevertheless for metals which are heavily pre-strained the error will be small, as:

a) the slope of hardening has diminished considerably;
b) the indentation strains are small with relation to the existing strains.

The area around the folds in which microhardness tests were performed has very high strains, in general upwards of 0.5. Calibration data for the derivation of a linear relationship between

A) VIEW OF INDENTATIONS

B) MICROHARDNESS CONTOUR MAP (KG/MM2)
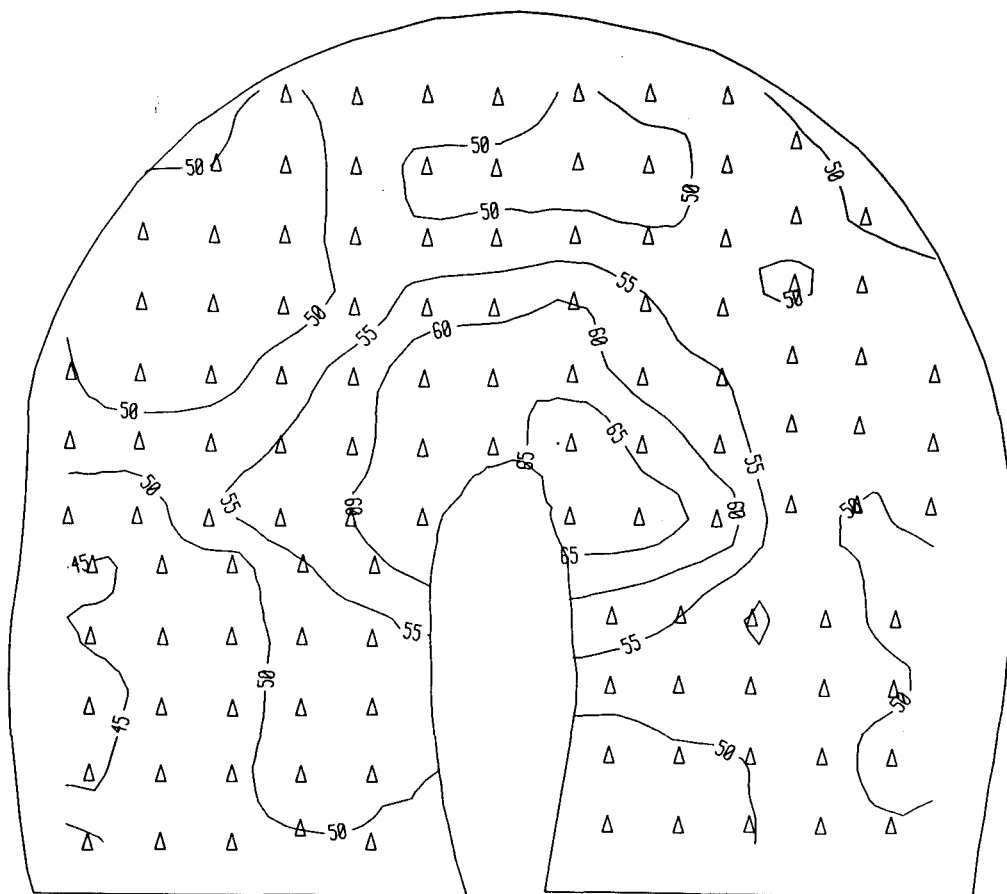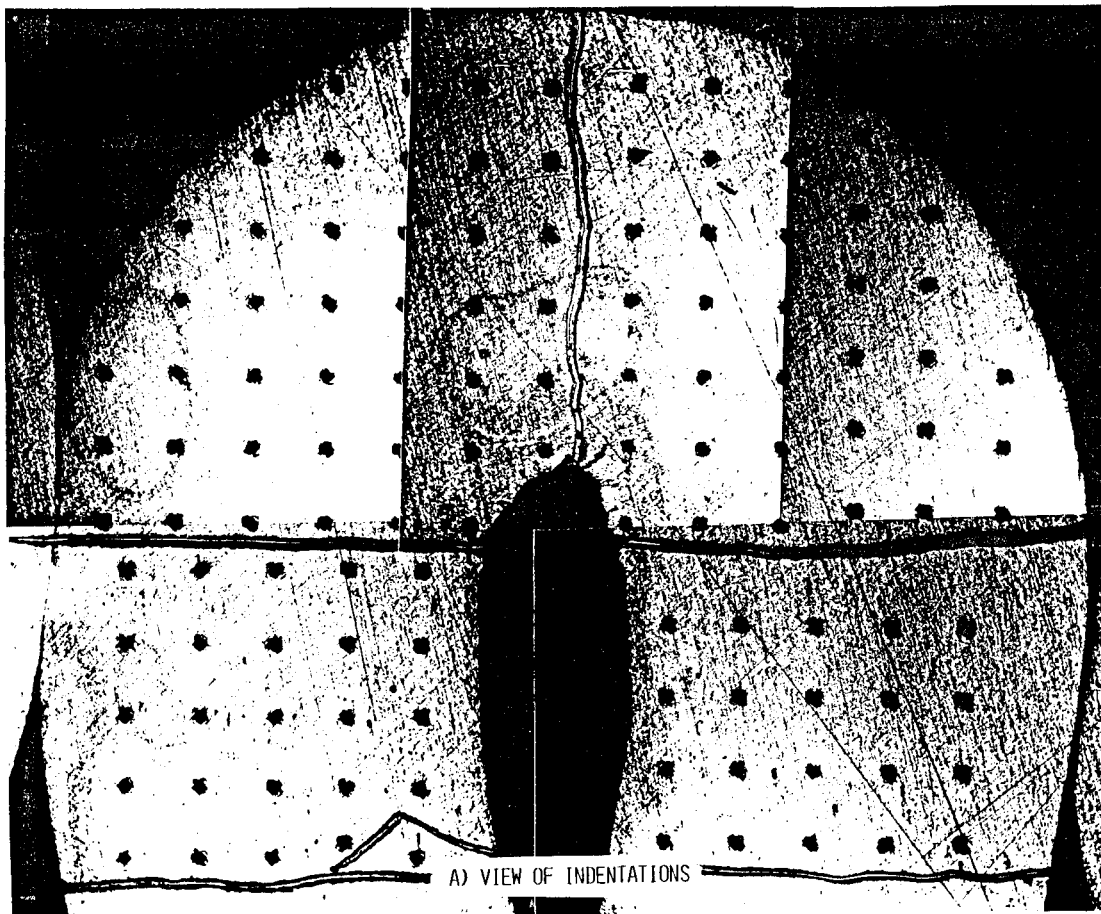
FIGURE 7.4: TYPICAL RESULTS OF MICROHARDNESS TESTS ON CRUMPLED TUBE SECTION
(OD=38.1mm, t_0=1.67mm, L=50.8mm) (TUBE GEOMETRY C)

H_m and Y were obtained from microhardness tests in transversal sections of an annealed HE30 necked tension bars (chapter 6). This relationship is valid as well for HT30, which after annealing has the same mechanical properties as HT30 (see section 7.3.2.1).

For each section of the necked bar the strain can be computed from eqn. (6.8); from the stress-strain relationship of the material, eqn. (6.20), a value for the strength Y was found (table 7.2). A linear regression was then performed through the (H_m,Y) data points (figure 7.5). For the least squares fit the point corresponding to the unstrained material has been disregarded as the region of interest is at high strains. The relationship obtained,

$$Y = -38.5 + 0.35H_m \text{ (MPa)} \qquad (7.7)$$

was then used to derive contour maps of the strain-hardened flow stress Y (figures 7.13, 7.18 and 7.23), which could be compared directly to those obtained from the computational model.

Section	Microhardness(*) H_m(MPa)	Original Diameter D_o(mm)	Deformed Diameter D(mm)	Strain $\epsilon=-2Ln(D/D_o)$	Yield Strength $Y=181.7\epsilon.159$
0	384	31.7	31.7	0.00	59.4(**)
1	493	16.2	15.0	0.15	134.4
2	522	16.2	14.8	0.18	138.3
3	509	16.1	14.3	0.24	144.8
4	540	16.1	14.0	0.28	148.4
5	565	16.0	12.4	0.51	163.2
6	638	16.0	9.2	1.11	184.7

(*) Microhardness values averaged from a minimum of 6 measurements along two perpendicular radiuses of each section
(**) Strength for unstrained material corresponds to initial yield

Table 7.2: Microhardness, strain and stress values on transversal sections of necked HE30 tension bar for calibration of Microhardness-strength relationship
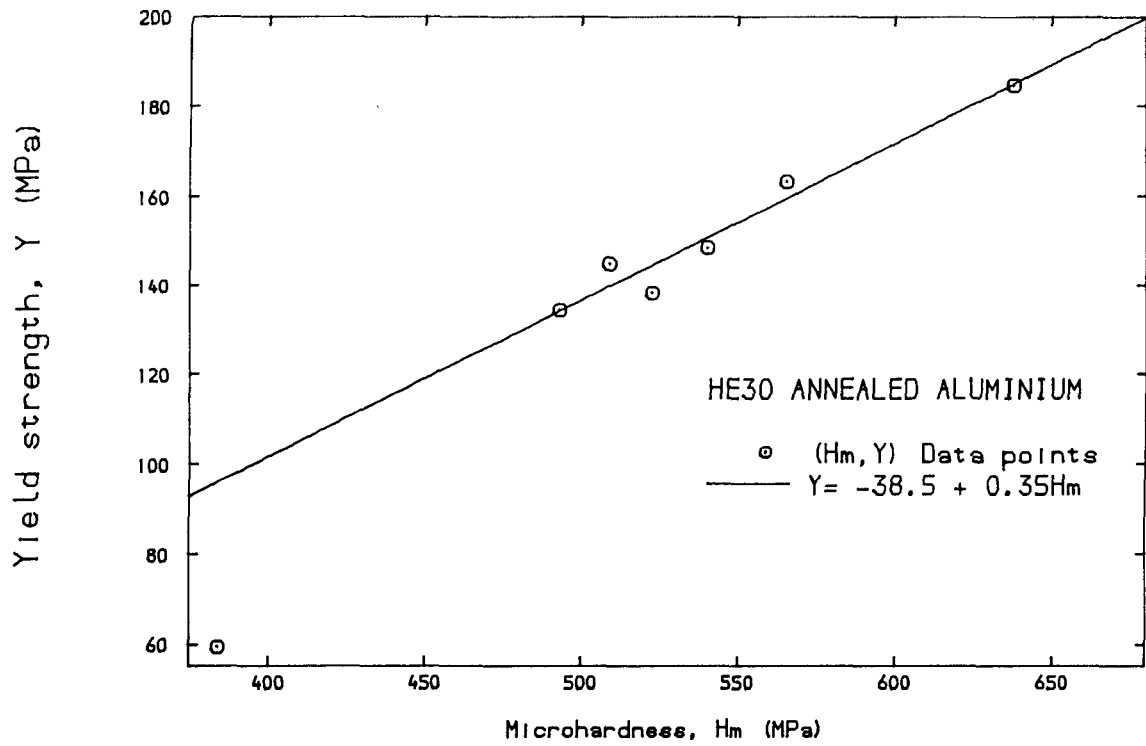
Figure 7.5: YIELD STRENGTH - MICROHARDNESS CORRELATION
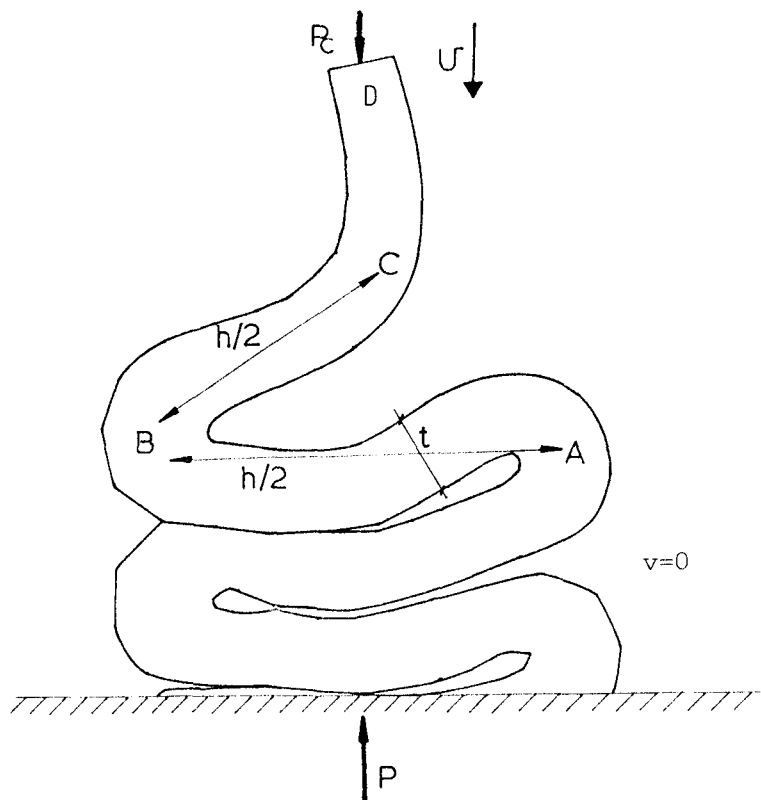
Figure 7.6: Forces involved in dynamic concertina folding;
P=total force, P_c=crushing force, v=crushing velocity

7.3.2 NUMERICAL MODEL

The axial collapse of tubes was simulated using the 2-D numerical code described in chapter 4. Axisymmetric continuum MTQC elements (sect. 4.2.3) were used under an explicit time-marching procedure.

The tubes were crushed between two platens; the bottom one was fixed, while the top platen moved downwards, causing the tube to collapse. The platens, as the rest of the tube, were modelled with axisymmetric continuum elements. Interaction between platens and tube as well as between tube folds themselves was considered through numerical contacts (section 4.8).

In order for the calculations to be meaningful, it must be checked that axisymmetric deformations are to be expected for the particular tube geometry, e.g. by locating the appropriate point in the collapse classification chart (figure 7.2). Non-axisymmetric modes of collapse such as the diamond mode cannot be simulated, as axial symmetry of deformation is imposed by the model. The analyses performed here all corresponded to experimentally observed concertina failures.

Apart from the axial symmetry, no further numerical constraints were imposed upon the model, being completely free to develop its preferred form of collapse (e.g. simultaneous, sequential) as well as the number and length of folds. No geometrical imperfections were introduced to trigger off buckling modes. 'Natural' imperfections were provided by the random numerical roundoff errors.

The axial collapse of tubes is a fairly reliable and repeatable mechanism (e.g. Ghani, 1982), indicating little sensitivity to imperfections. In the numerical model, the imperfections depend on the precision of the floating point arithmetic. A check was done, running the same tube collapse model (TUBE7, see table 7.4), on a CRAY-1S (64-bit floating point words) and on a VAX 11/785 (32-bit floating point words). Results obtained were substantially identical. The deviation from the energy balance condition was larger on the VAX (0.15% error versus 0.005% error on the CRAY), but still within very acceptable

limits.

7.3.2.1 DISCRETIZATION AND MATERIAL

Discretizations with varying fineness were used for the analyses. The meshes employed may be grouped into the following categories:

- Coarse mesh, 3 quadrilateral MTQC elements through the thickness, approximate aspect ratio 2:1 (largest dimension axially);
- Medium mesh, 3 quadrilateral MTQC elements through the thickness, approximate aspect ratio 1:1;
- Fine mesh, 4 quadrilateral MTQC elements through the thickness, approximate aspect ratio 1:1.

The platens were discretized with two CST elements each in all cases. They were assumed infinitely rigid, i.e. no deformations were allowed.

Symmetric contacts (sect. 4.8) were used for the interaction between opposite walls in the tube folds. Each interacting node is included in two simultaneous numerical contacts: firstly as an intruder on the opposite side, and secondly as part of a target side being penetrated by the node opposite. This ensures fully symmetrical behaviour in the interface algorithms.

For the contacts between tube and platens only the tube nodes were considered as intruders; the lack of intermediate nodes in the platens would have prevented otherwise. However, this is not undesirable, as the contact between deformable tube and rigid platen is naturally asymmetric.

For the material model, an elastic-plastic isotropic Von Mises idealization was used. Elastic parameters were

Elastic modulus, E	67000 MPa
Poisson's ratio ν	0.3

Strain-Hardening was considered with the power law obtained in chapter

6 (eqn. 6.20):

$$Y = 181.7 \, \epsilon^{0.159} \quad (MPa)$$

The above hardening law was derived for HE30 annealed Aluminium bars. HE30 and HT30 materials are identical aluminium alloys, except for the fact that HE30 comes in bars (extruded), whereas HT30 comes in tubes (drawn). After being annealed both materials can be assumed to have the same mechanical behaviour.

In effect, differences due to cold-working may be banished in the annealing process. According to Cottrell (1975), "work-hardening is caused by the mutual obstruction of dislocations gliding on interacting systems". The annealing treatment produces recovery and recrystallization processes. The recovery allows dislocations to move out of the slip planes, disentangling and tidying-up the cold-worked structure, while the recrystallization replaces the cold-worked grains by a new set of more perfect grains, giving complete softening. As on the other hand the differences due to cold-working were only minor, it is justified to assume the constitutive laws derived for annealed HE30 valid for HT30 tubes as well.

7.3.2.2 VELOCITY SCALING (see also section 4.1.1)

Explicit time-marching procedures by their nature can only perform dynamic analyses. Quasi-static or slow loading problems could be solved in real time, but usually this becomes too expensive. For reasons of numerical stability the maximum time-step is limited by the Courant criterion, which is independent of the velocity of loading. In quasi-static analyses such as these the calculations need to be speeded up, which may be done by arbitrarily increasing the velocity of deformation in the numerical model; this is called "velocity scaling".

For these calculations the crushing velocity employed was 20 m/s, representing an increase of 5 orders of magnitude from the experimental velocity. It will be seen (section 7.3.4.2) that the overshoots and distortion introduced by this amount of velocity

scaling were small. As there was no strain-rate hardening in the material, the only additional safeguard needed was to ensure that dynamic effects continued to play a small role in the mechanical deformation process. Some criteria to quantify this role were given in section 6.5.1.

The dynamic forces involved in the concertina crumpling may be assessed with the following simple considerations. Figure 7.6 shows a wall section in a tube which is being crumpled with an axial velocity v. The portion of the tube already crumpled (below A) is stationary, the undeformed portion above C moves with velocity v, and the folding portion between A and C is being decelerated from v to 0. This deceleration occurs in a time $(h-2t_0)/v$, h being the fold length and t_0 the wall thickness; the average inertia force necessary is, by virtue of Newton's second law,

$$P_i = \pi D t_0 \rho h v^2/(h-2t_0) \tag{7.8}$$

where D is the mean tube Diameter and ρ is the mass density. Hence the average dynamic forces grow with the square of the crushing velocity, all other factors being constant for a particular tube.

The total force F exerted at the bottom surface equals the force necessary for crumpling felt at D, P_c, plus that necessary for decelerating the fold ABC, P_i:

$$P = P_c + P_i = P_c + \pi D t_0 \rho v^2 h/(h-2t_0) \tag{7.9}$$

The deformation velocity v used in the calculations was chosen so as to produce acceptably small dynamic distortions ($P_i < 5\% P_c$). These dynamic effects are quantified in section 7.3.4.2, where the influence of the velocity scaling is discussed.

7.3.2.3 INTERPRETATION OF OUTPUT

Load-compression curves obtained from numerical analysis needed some post-processing (averaging and filtering) in order to facilitate their interpretation.

Firstly, a representative value of the load was taken as the average between the loads measured at the top and bottom platens at each instant. In a quasi-static situation the difference between both measurements would be negligible. Here, due to the velocity scaling, there were finite, although small, differences between the two end loads.

Secondly, high-frequency oscillations in the load histories arising from stress-wave propagation between the two extremes of the specimen were filtered out, using a centred moving average filter (see below). Again in a true quasi-static model this would not be necessary; for each load increment, the new displacements are those that fulfill static equilibrium. It is assumed that the stress waves have travelled back and forth along the specimen many times, redistributing stresses, and eventually damped out.

The velocity of deformation has been greatly increased here, while the information (stress waves) continues to be transmitted at the same speed. On the other hand, there are steep changes in load due to the buckling instabilities and rapid variations in boundary conditions (contact-impact). Whereas in the real - slow loaded - specimen there is still time for numerous stress waves to transmit these changes smoothly enough, here they are transmitted more abruptly as finite amplitude dynamic pulses, occasioning visible oscillations in the load curves. As long as the amplitude of these oscillations remains small relative to the total loads, their distortive influence is not important, and the underlying trend in the load curves may be recovered by filtering them out.

High frequency filter (centred moving average)

Centred moving average techniques are simple and effective for high frequency filtering. From a given time series x_i, $i=1$ to N, with constant time interval Δt, a new filtered time series is defined as

$$y_i = \frac{1}{2M+1} \sum_{i-M}^{i+M} x_j \qquad M < i < N-M \qquad (7.10)$$

This filter removes frequencies higher than $1/(2M\Delta t)$. The values

of M were chosen so as to remove oscillations occasioned by stress-wave propagation.

7.3.3 RESULTS FROM NUMERICAL CALCULATIONS AND EXPERIMENT

Numerical results are presented here and compared with experiment, for the axial collapse of 4 different tube geometries:

- Tube geometry A, ID=19.05mm, t_0=1.64mm, L=50.8mm;
- Tube geometry B, ID=19.05mm, t_0=1.17mm, L=50.8mm;
- Tube geometry C, OD=38.10mm, t_0=1.65mm, L=50.8mm;
- Tube geometry D, OD=25.40mm, t_0=0.95mm, L=25.4mm.

Other auxiliary calculations were necessary first in order to test the influence of various parameters and choices:

- velocity of deformation;
- mesh refinement;
- friction;
- element type.

Results from these auxiliary calculations are discussed in section 7.3.4. In total over 20 calculations of the complete tube crumpling process for 6 different tube geometries (table 7.4) were carried out successfully.

Mesh refinement was found to have an important effect upon the results (section 7.3.4.3). However, due to the high computer costs involved in these analyses, some of the meshes used could not have the maximum desirable fineness. Two of the models presented below have a "fine" mesh, while the other two have "medium" meshes.

The numerical predictions are presented together with the corresponding experimental results. The tests were described in section 7.3.1.

The computer used for the numerical work was a CRAY-1S of the University of London. Central Processing Unit (CPU) times quoted refer

to this machine.

7.3.3.1 <u>TUBE GEOMETRY A: ID=19.05mm, t_o =1.64mm, L=50.8mm</u>

A "fine" mesh was used for this analysis, comprising 633 nodes and 996 triangular cells (fig. 7.7.a). The calculation proceeded for 95789 time-steps, up to an axial compression of 37.5mm, forming 3 concertina folds: firstly at the bottom end, then at the top, finally in the middle (fig. 7.7b). CPU time for this calculation was 8641 seconds.

In the experiment, the tube collapsed forming 3 concertina folds as well, with a shape very similar to the numerical prediction (figures 7.8, 7.9). Figure 7.10 contains the load-compression curves (numerical and experimental), which show a remarkable agreement. Average collapse loads were 12.2 kN for the calculations and 11.9 kN for the experiment. The succession of peaks and valleys in the load curves is due to the alternancy between axial compression (stiffer peaks) and bending (less stiff valleys) mechanisms. The snapshot views of the mesh at different points included in figure 7.10 confirm this explanation, providing a detailed description of a phenomenon previously observed experimentally in a forcefully more qualitative manner (Ghani, 1982).

The numerical load-compression curve in figure 7.10 was obtained by averaging and filtering the raw data as explained in section 7.3.2.3. To show the effect of this averaging-filtering process, individual load curves obtained directly at the top and bottom platens are presented in figure 7.11. These curves show some small transient imbalances due to the velocity scaling. The underlying quasi-static trend is seen more clearly when this noise is filtered out (fig. 7.10).

The various energy components were monitored (sect. 4.10) during the calculations (fig. 7.12). the energy of deformation in fig. 7.12 comprises plastic work, recoverable elastic energy, and energy dissipated through friction (some 1.4% of the plastic work at the end of the analysis). In order to provide a check for the stability of the

ID =19.05mm

to =1.64mm

HT30 ANNEALED ALUMINIUM
TUBE

(Fine mesh solution)

L =50.8mm

a) Undeformed mesh

Rigid Platens

b) mesh after 37.5mm axial compression
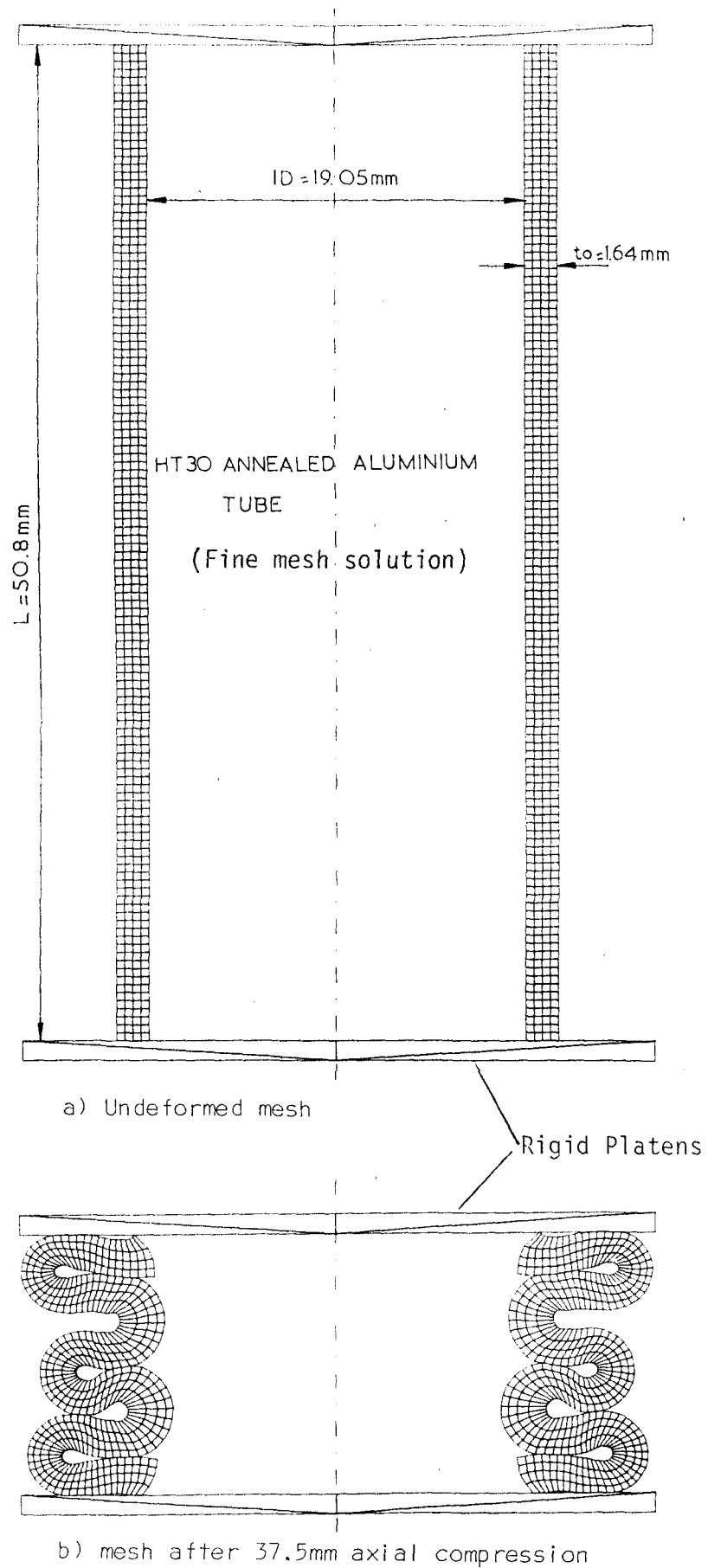
Figure 7.7: Calculations for axial collapse of tube
ID=19.05mm, t_o=1.64mm, L=50.8mm (tube geometry A)

AXIAL COLLAPSE
ID=19.05mm, t_O=1.64mm, L=50.8mm TUBE
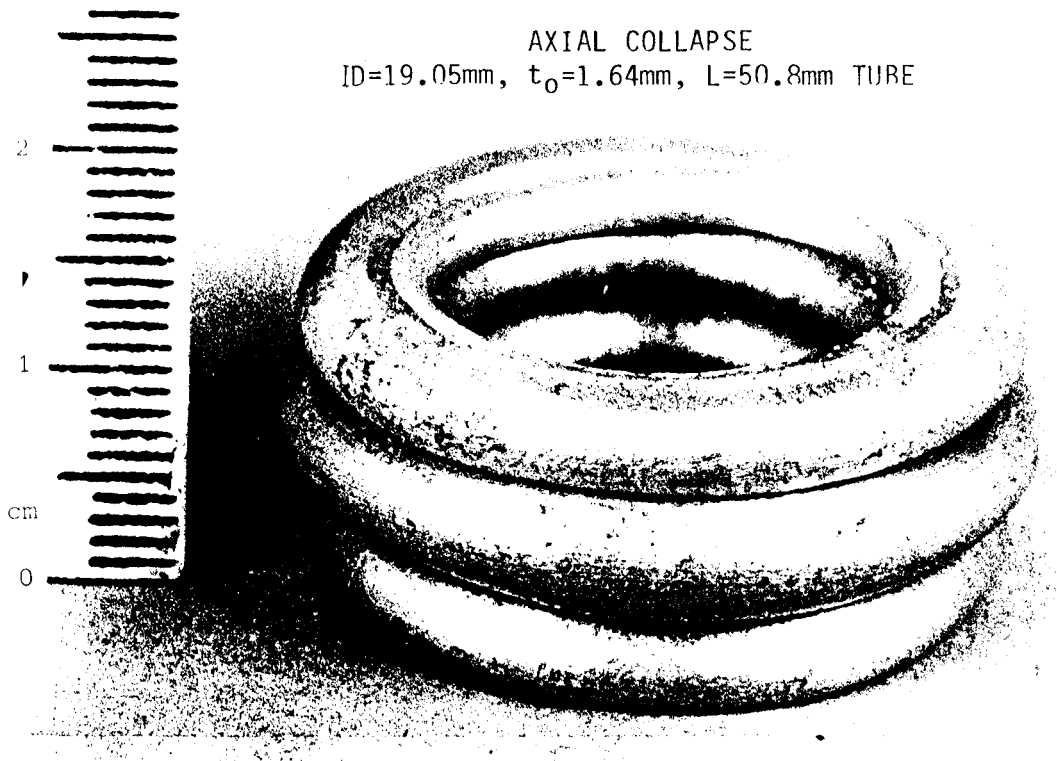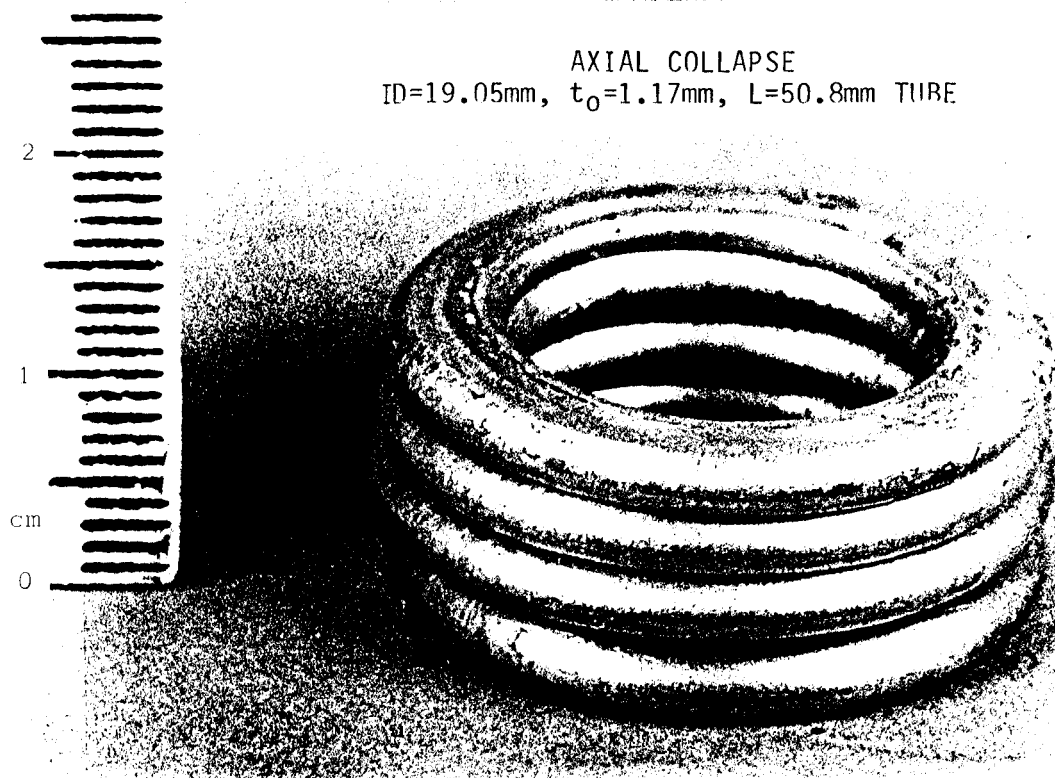

Figure 7.8: View of crumpled tube (geometry A)

AXIAL COLLAPSE
ID=19.05mm, t_O=1.64mm, L=50.8mm TUBE
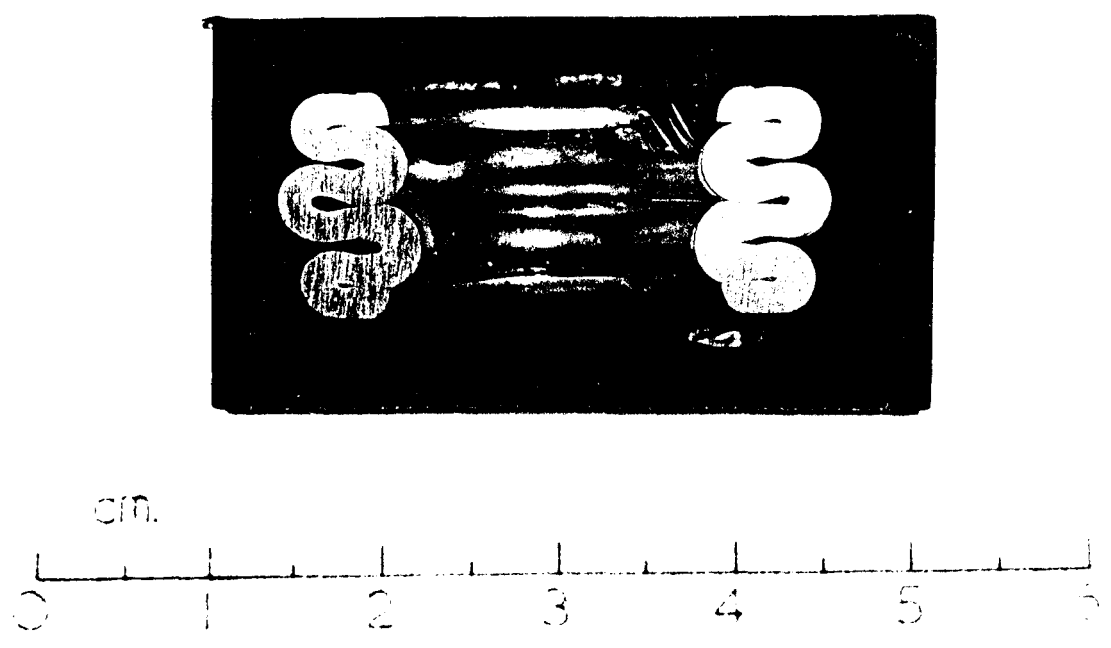
Figure 7.9: Section of crumpled tube (geometry A)
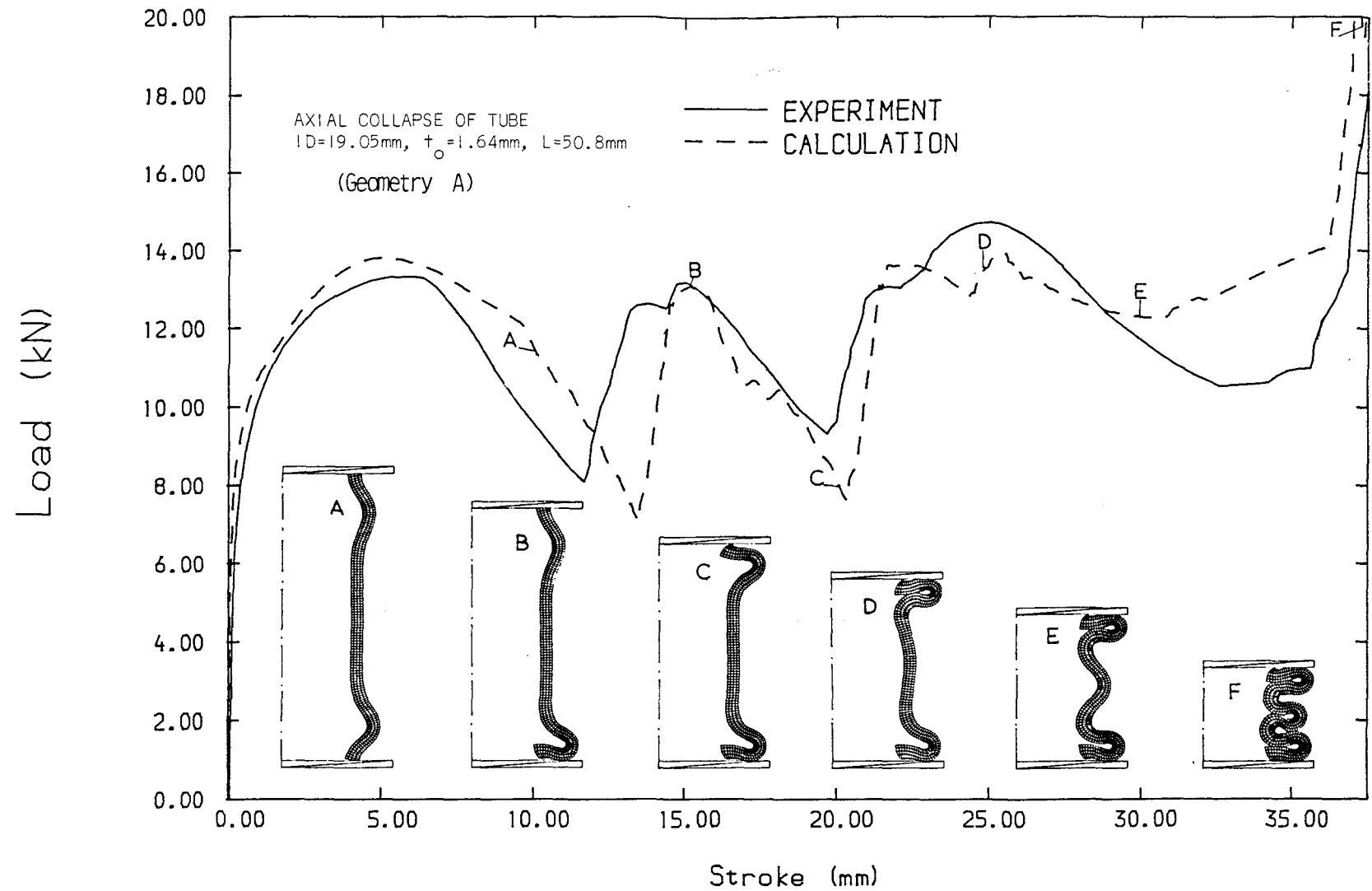
FIGURE 7.10: CALCULATIONS FOR AXIAL COLLAPSE OF TUBE; LOAD - COMPRESSION CURVE
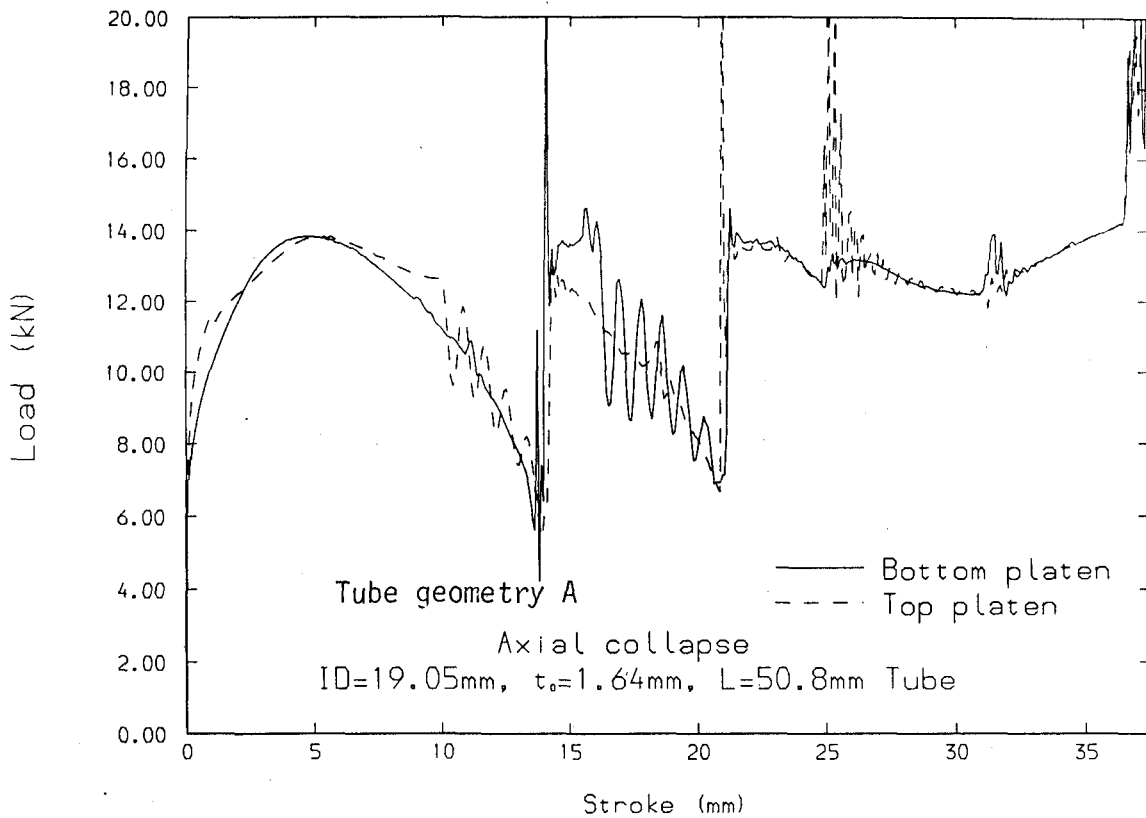
Figure 7.11: INDIVIDUAL LOAD CURVES FOR NUMERICAL MODEL AT BOTH PLATENS
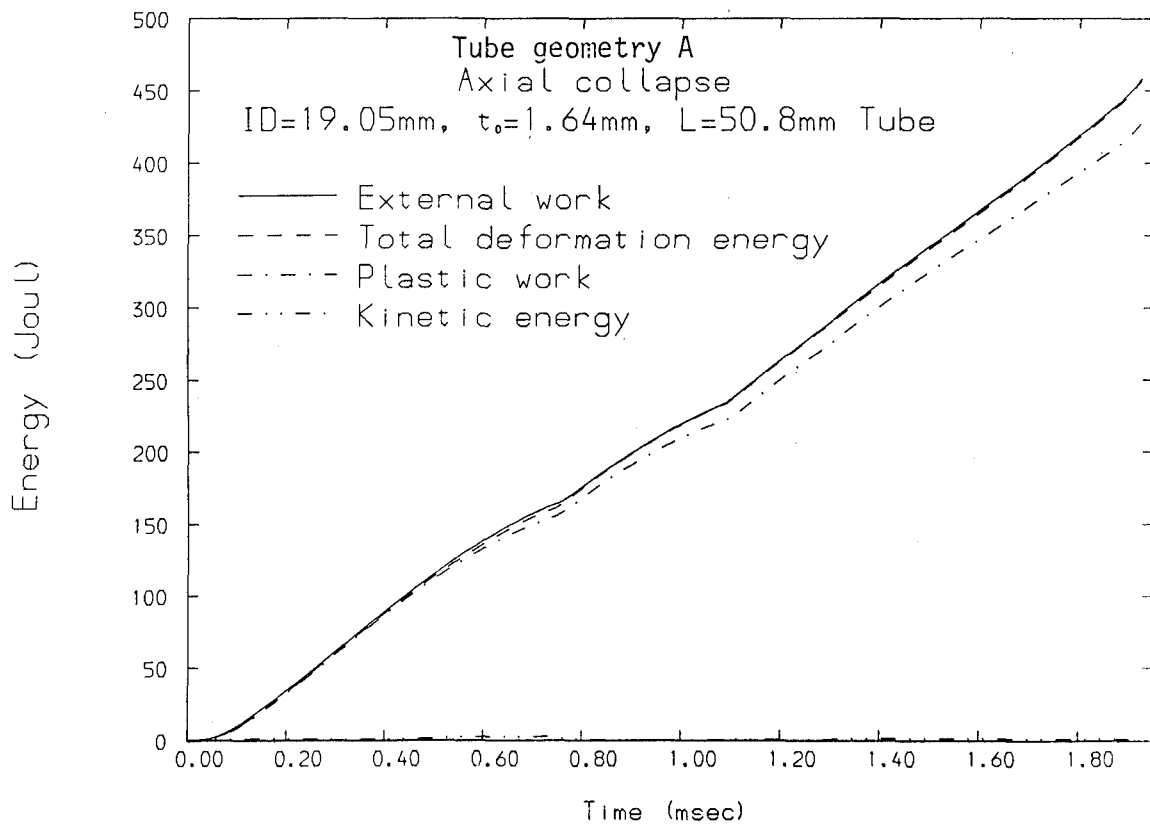
Figure 7.12: ENERGY HISTORIES FOR NUMERICAL MODEL

computations, the work done by the external forces was computed independently and compared to the sum of the deformation and kinetic energies. Within the precision of the figures (5 digits) no difference was perceived between both values, indicating absence of instabilities and soundness of numerical integration algorithms.

Contour maps of the Von Mises flow stress (Y), from the numerical model and experiments, are presented in figure 7.13. The experimental data were derived from microhardness tests, as laid out in section 7.3.1.3. Similar patterns and levels of stress can be observed for both cases, although somewhat steeper gradients and a wider range of values is appreciable for the experiment. This is due on the one hand to the higher curvature for the experimental fold selected, and on the other hand to the relative coarseness of the numerical mesh. Agreement for all these local effects would need an inordinate degree of mesh refinement. Considering the uncertainties of the microhardness measurements and of their correlation to the material strength, Y, this level of agreement was deemed very good.

7.3.3.2 TUBE GEOMETRY B: ID=19.05mm, t_o=1.17mm, L=50.8mm

This problem was discretized with a mesh of medium fineness, comprising 532 nodes and 784 triangular cells (figure 7.14a). 99503 computational time-steps were needed for an axial compression of 40 mm. 3 full concertina folds plus a fourth incomplete fold were formed (figure 7.14b). The order of formation was: bottom, top, second from bottom, second from top. CPU time consumed was 7176 seconds.

In the corresponding experiment 4 full folds were formed in the tube (figures 7.15, 7.16). The discrepancy between experiment and calculation in the fourth fold arose from an overprediction of the fold length in the numerical model. The first 3 folds spanned an excessive tube length, not leaving enough for the natural formation of a fourth fold. The reason for this overprediction is an excess stiffness of the model, caused by the coarseness of the discretization employed. Convergence towards the experimental behaviour was observed from a previous analysis of this same problem with a coarse mesh (section 7.3.4.3). No further refinements of the mesh were performed

x10MPa
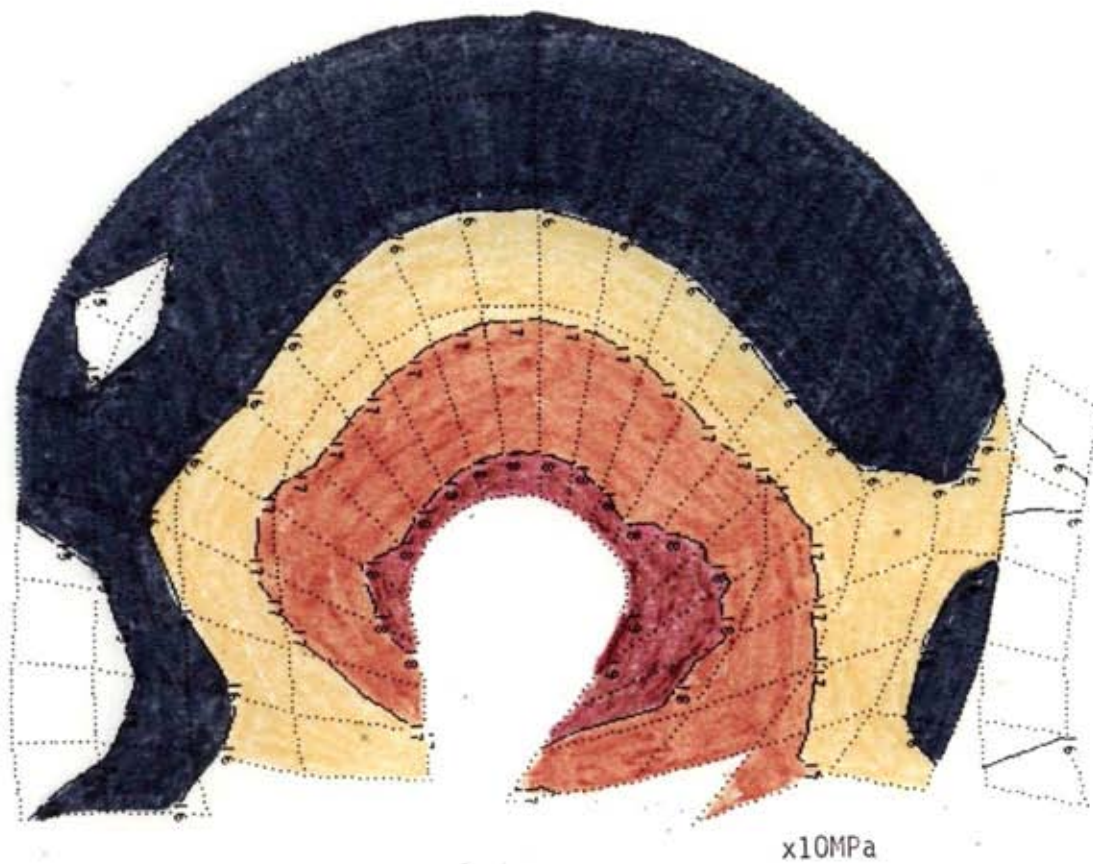
a) from numerical calculations
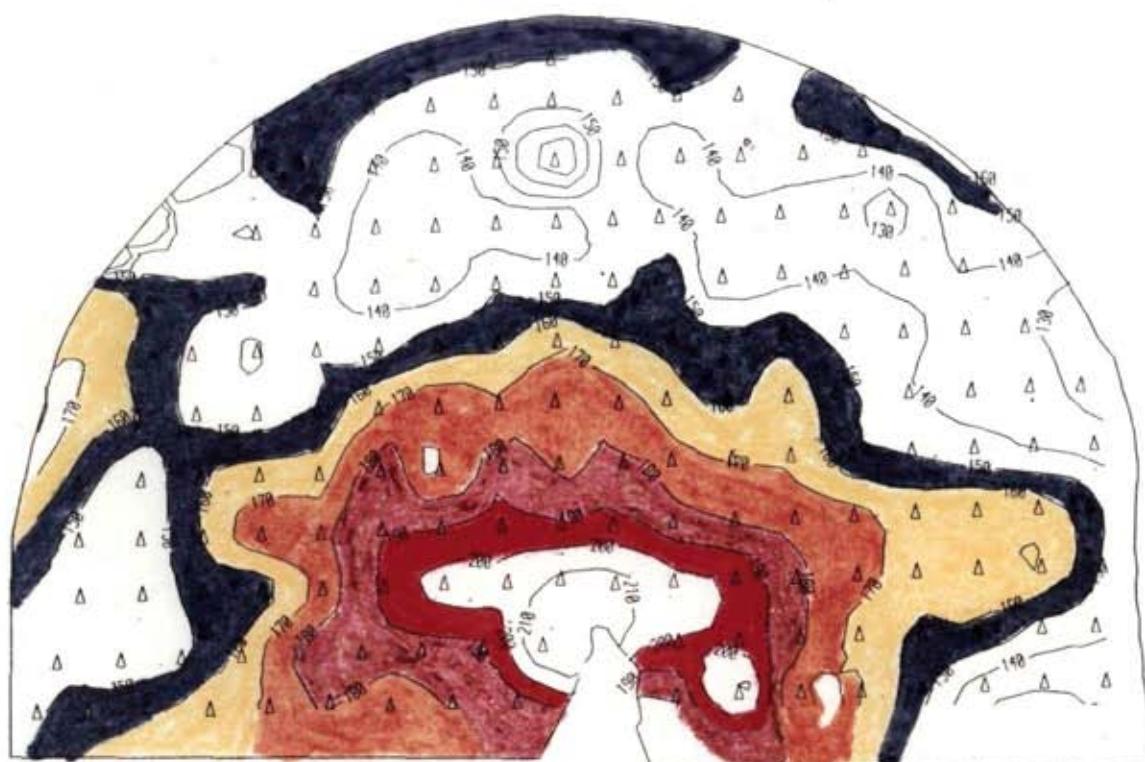
b) from microhardness tests　　　　MPa

Figure 7.13: Contours of yield strength Y in crumpled tube section
(ID=19.05mm, t_o=1.64mm, L=50.8mm Tube) (geometry A)

a) Undeformed mesh

Rigid Platens

b) Mesh after 40mm axial compression
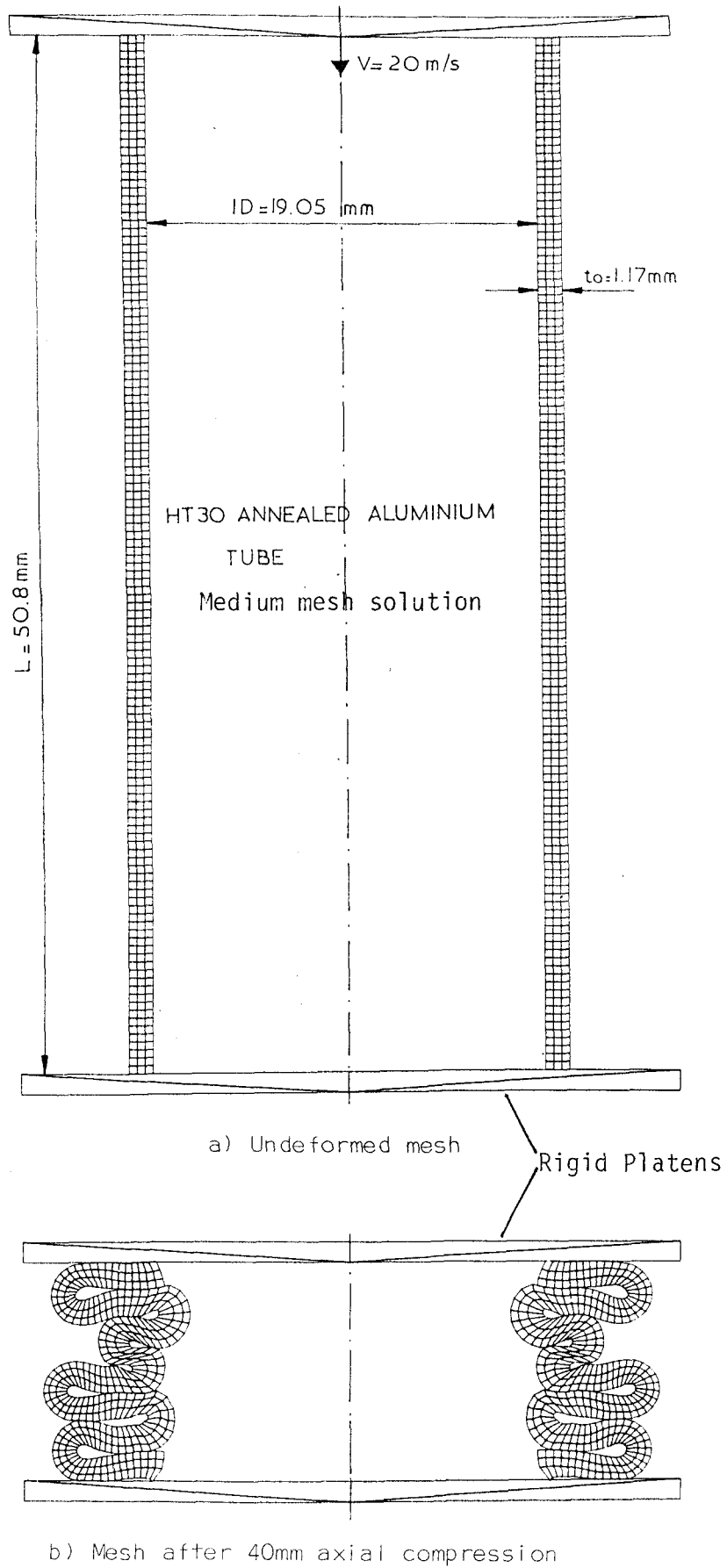
Figure 7.14: Calculations for axial collapse of tube
ID=19.05mm, t_o=1.17mm, L=50.8mm, tube geometry B

AXIAL COLLAPSE
ID=19.05mm, t_0=1.17mm, L=50.8mm TUBE

Figure 7.15: View of crumpled tube (geometry B)

AXIAL COLLAPSE
ID=19.05mm, t_0=1.17mm, L=50.8mm TUBE
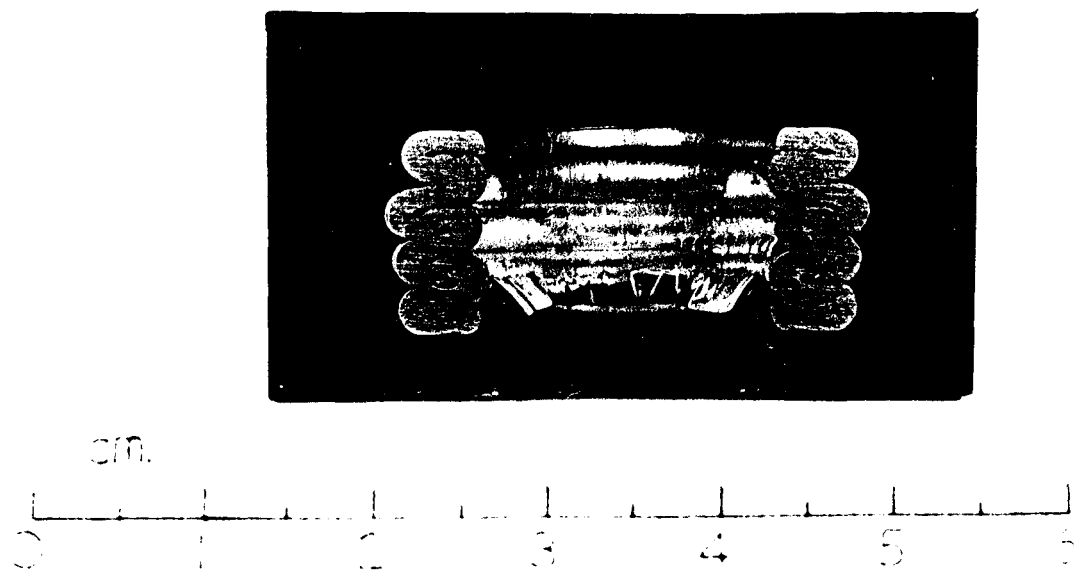
Figure 7.16: Section of crumpled tube (geometry B)

in order to avoid excessive computer costs.

Further insight into the behaviour of the model may be gained from the load-compression curves (figure 7.17). Similar load levels and patterns of rises and falls in the curves were obtained in experiment and calculation. However, the separation between successive peaks is greater for the numerical model, indicating longer folds. For the last fold the length of tube remaining is too short. A very stiff final fold is then formed, with a large degree of shear deformation. Computed load levels become here much greater than experimental ones.

Neither the individual unfiltered load-compression curves for both platens nor the energy balance graph, given for the previous analysis (tube geometry A)in figs. 7.11 and 7.12, are given for this or the following tube analyses (geometries B, C, D). The story told by these graphs is much the same as for tube geometry A.

Numerical and experimental contour maps of Von Mises strength, Y, are given in figure 7.18. As for tube geometry A, similar levels and patterns of stress may be appreciated in both maps. Again, the gradients for the experimental contours are steeper.

7.3.3.3 TUBE GEOMETRY C: OD=38.1mm, t_0=1.65mm, L=50.8mm

A "fine" mesh was used for this analysis, with 633 nodes and 996 triangular cells. The initial and final configurations of the mesh may be seen in figure 7.19. One concertina fold was formed at either end of the tube. As for the previous analysis, the length of the folds was overpredicted, leaving too little tube length left for the proper formation of a third fold in the middle. Although at one point it did seem that a third shorter fold would be formed, eventually this mechanism proved too stiff and the model failed through shear near the top.

The experimental results did not show this behaviour, producing 3 complete folds (figures 7.20 and 7.21). The load-compression curves (figure 7.22) show that, although somewhat translated to the right for the calculations, a great similarity exists between the experimental
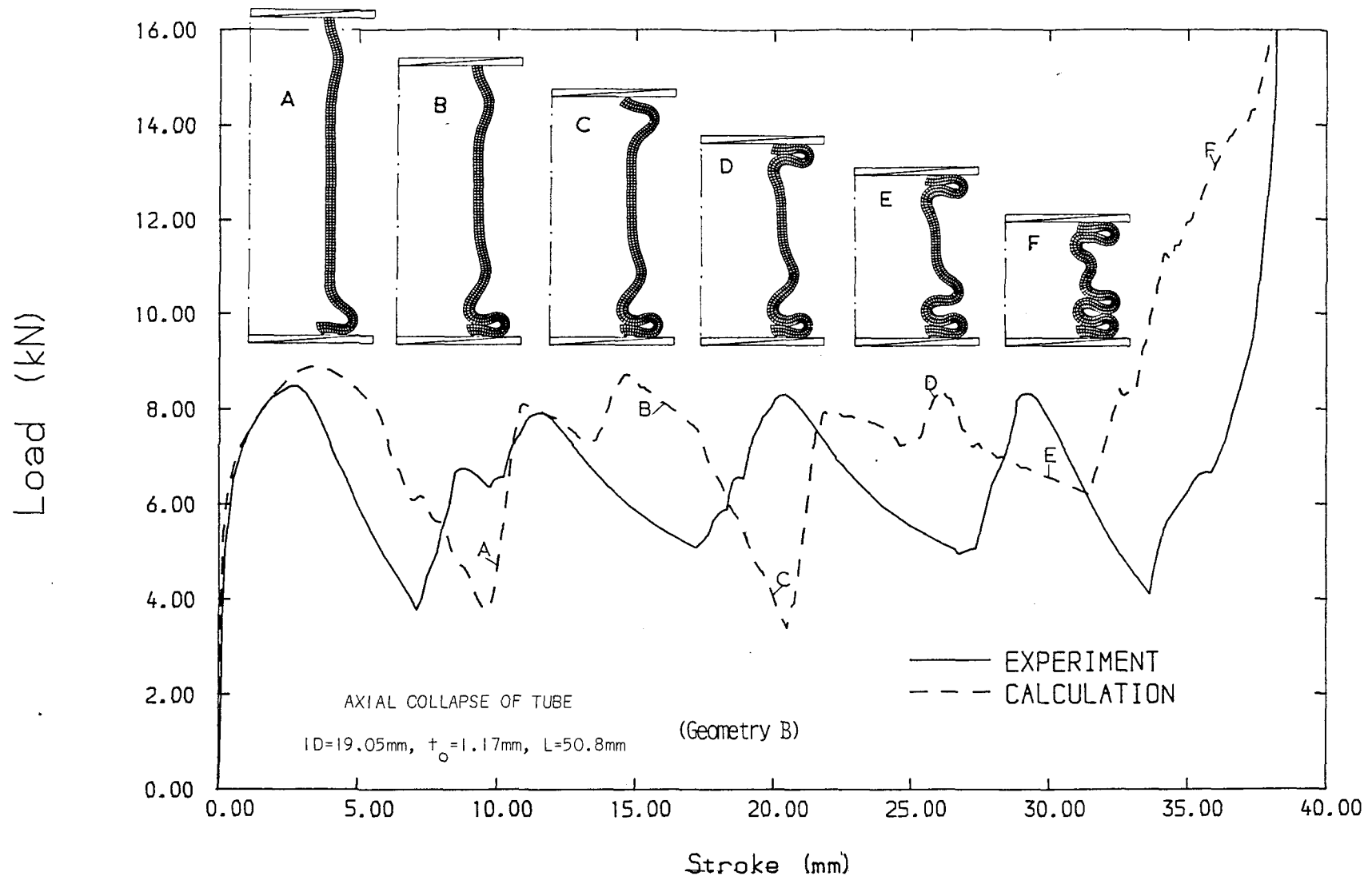
FIGURE 7.17: CALCULATIONS FOR AXIAL COLLAPSE OF TUBE; LOAD - COMPRESSION CURVE

x10MPa

a) from numerical calculations

MPa
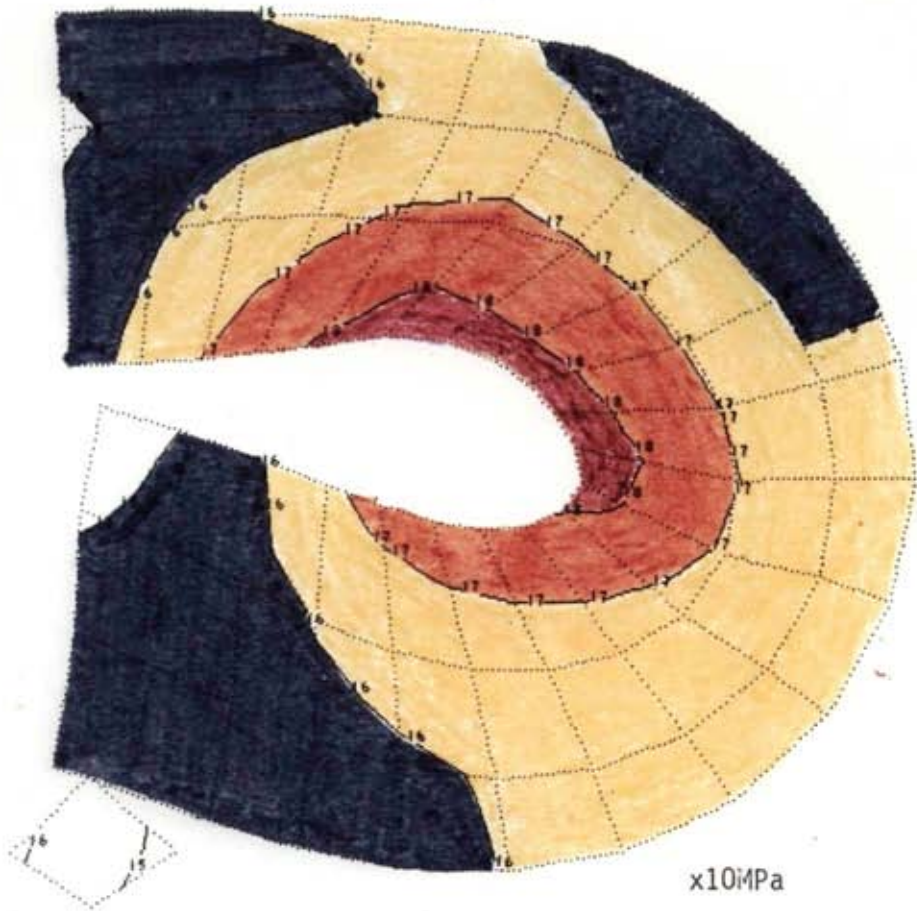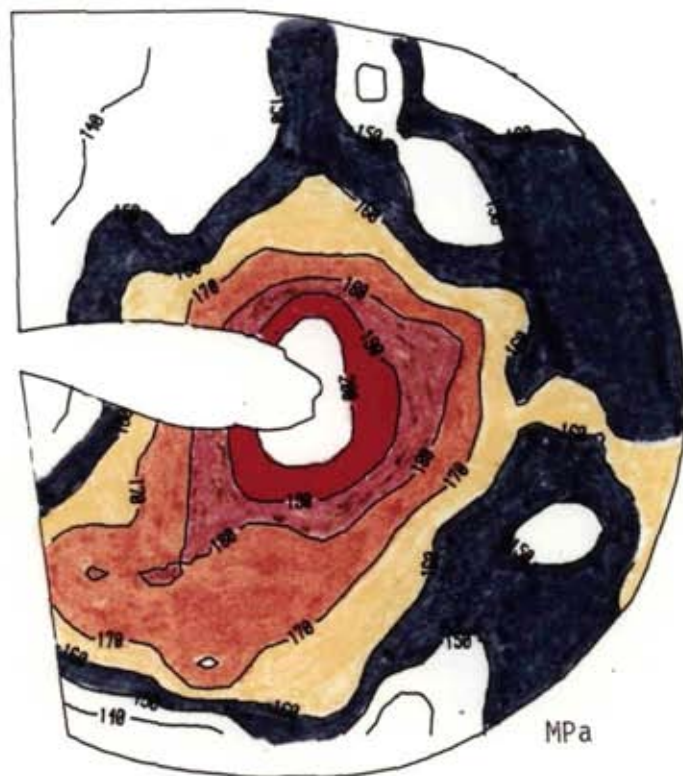
b) from microhardness tests

Figure 7.18: Contours of yield strength in crumpled tube section
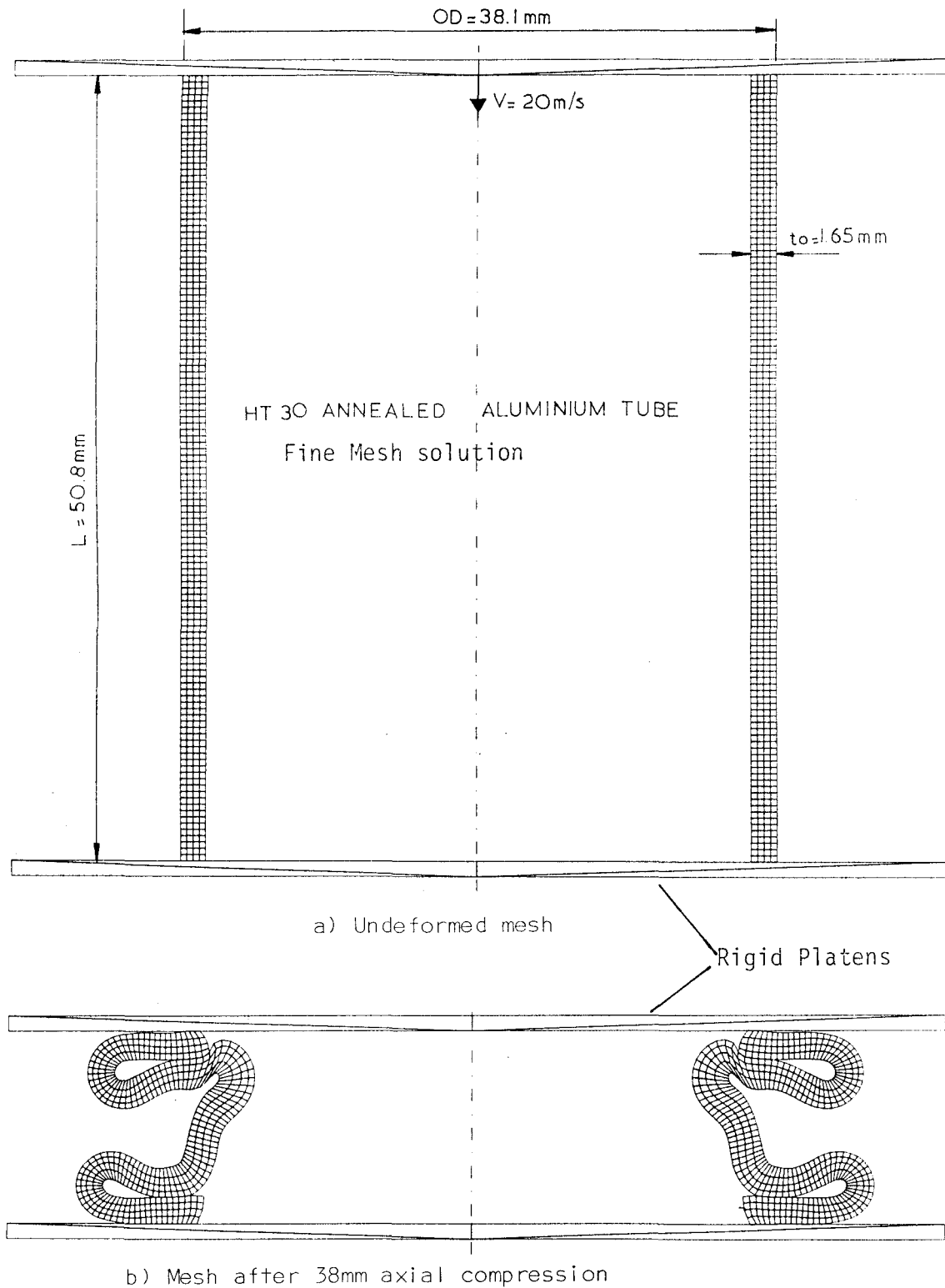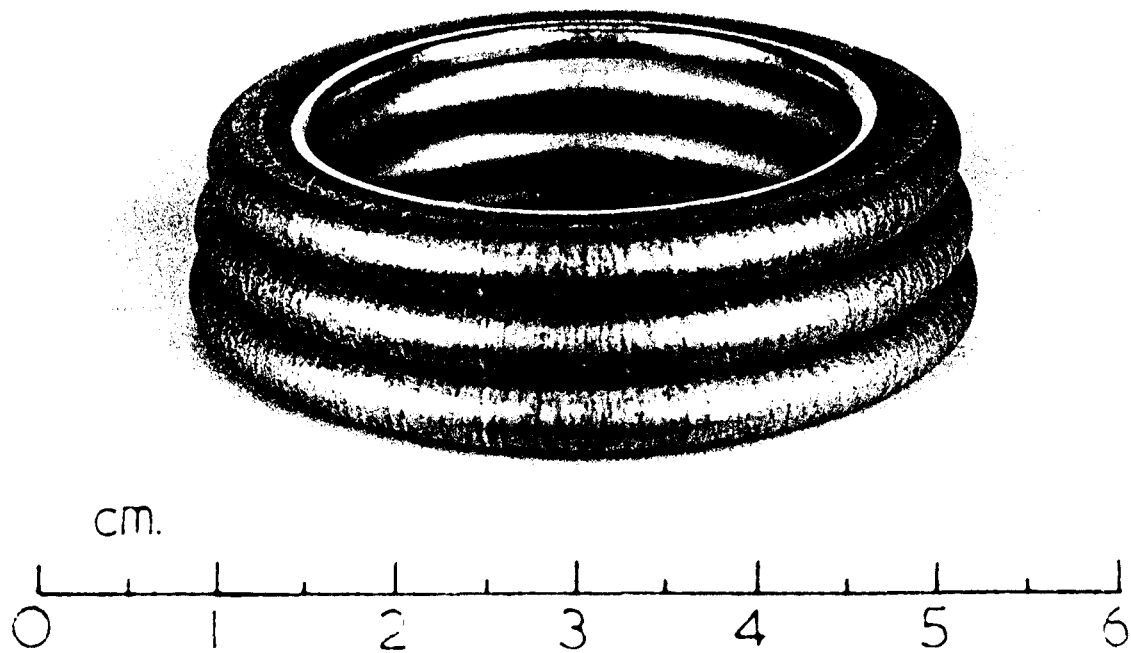(ID=19.05mm, t_o=1.17mm, L=50.8mm Tube) (geometry B)

OD = 38.1 mm

$V = 20$ m/s

$t_o = 1.65$ mm

$L = 50.8$ mm

HT 30 ANNEALED ALUMINIUM TUBE

Fine Mesh solution

a) Undeformed mesh

Rigid Platens

b) Mesh after 38mm axial compression

Figure 7.19: Calculations for axial collapse of tube
OD=38.1mm, t_o=1.65mm, L=50.8mm , tube geometry C

AXIAL COLLAPSE
OD=38.1mm, t_o=1.65mm, L=50.8mm TUBE

cm.

Figure 7.20: View of crumpled tube (geometry C)

AXIAL COLLAPSE
OD=38.1mm, t_o=1.65mm, L=50.8mm TUBE

Figure 7.21: Section of crumpled tube (geometry C)
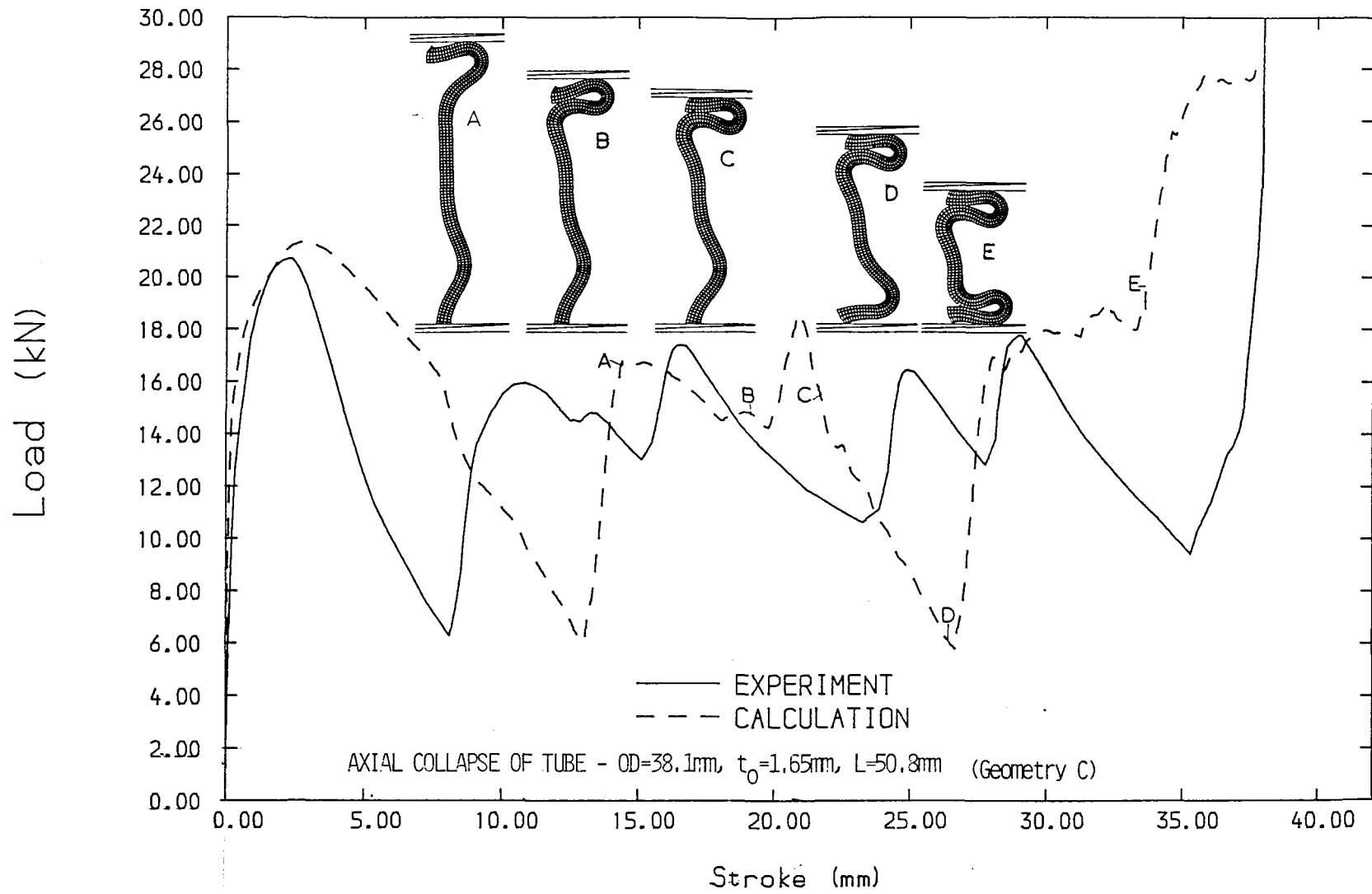
Figure 7.22: CALCULATIONS FOR AXIAL COLLAPSE OF TUBE - LOAD VS COMPRESSION CURVE

and numerical load patterns for the first fold. The deformation process can be clearly understood by examining the snapshot views of the mesh included in figure 7.22. At point A in the figure, after the b ending and sliding of the top edge, contact has been made between the outer wall of the tube and the top platen, occasioning a sharp increase in load. The edge then separates slightly from the top platen leaving only the outer fold surface in contact with the platen. With further compression the fold continues to bend until the bottom part of the fold hits the top edge. This produces a ripple clearly noticeable in both experimental and numerical load curves (B). The bottom part of the fold then pushes the edge up until contact with the top platen is renewed. The load increases steeply for a moment when the tube deforms in axial compression, until the bottom edge starts slipping (C) and bending to form another fold (D). The last fold is ready to be formed at E, but the remaining tube length has become too short. A very high load is necessary, which eventually levels off as shear failure occurs.

The numerical and experimental maps of Von Mises strength (Y), given in figure 7.23, indicate again similar stress distributions around a fold. They also show the same pattern as the two previous analyses.

7.3.3.4 TUBE GEOMETRY D: OD=25.4mm, t_0 =0.95mm, L=25.4mm

The mesh employed for this problem was of medium fineness, with 332 nodes and 484 triangular cells (figure 7.24a). A drawing of the deformed mesh after an axial compression of 20.2 mm is given in figure 7.24b, showing 2 concertina folds. 53554 computational cycles were performed, using 2664 CPU seconds.

the experimental results, shown in figures 7.25 and 7.26, proved again to be slightly less stiff than the computational model. In the experiment, after the first 2 folds, some extra length remained to form another half fold. Load compression curves for experiment and calculations are given in figure 7.27. In a way the comparative behaviour here is the inverse of that reported for the previous two analyses. Here it is in the experiment where a shorter length of tube

x10MPa

a) from numerical calculations

MPa
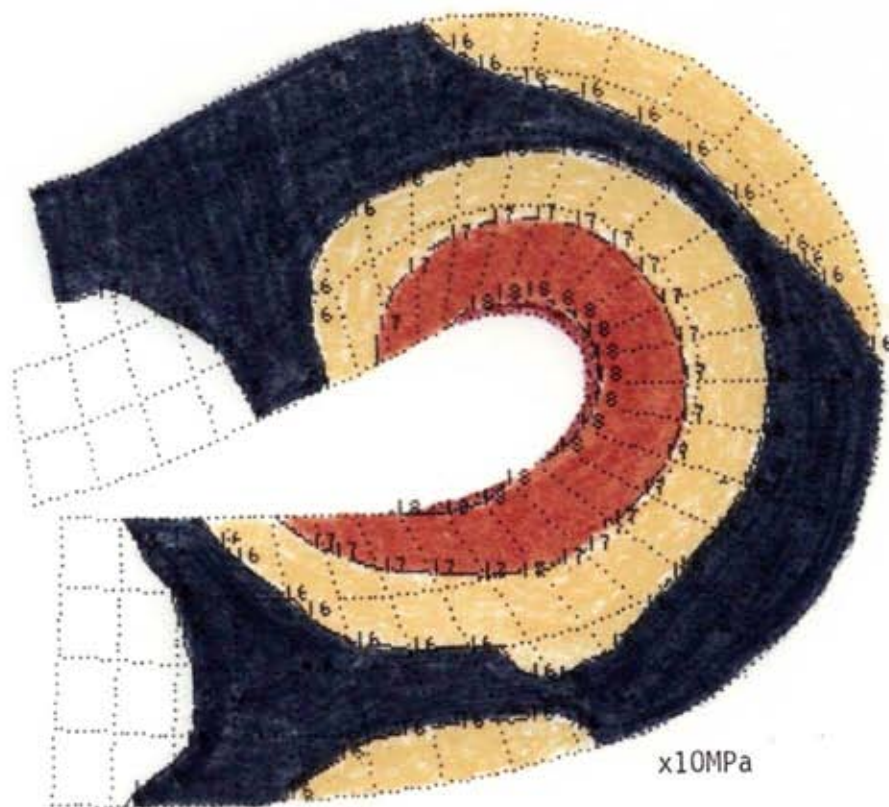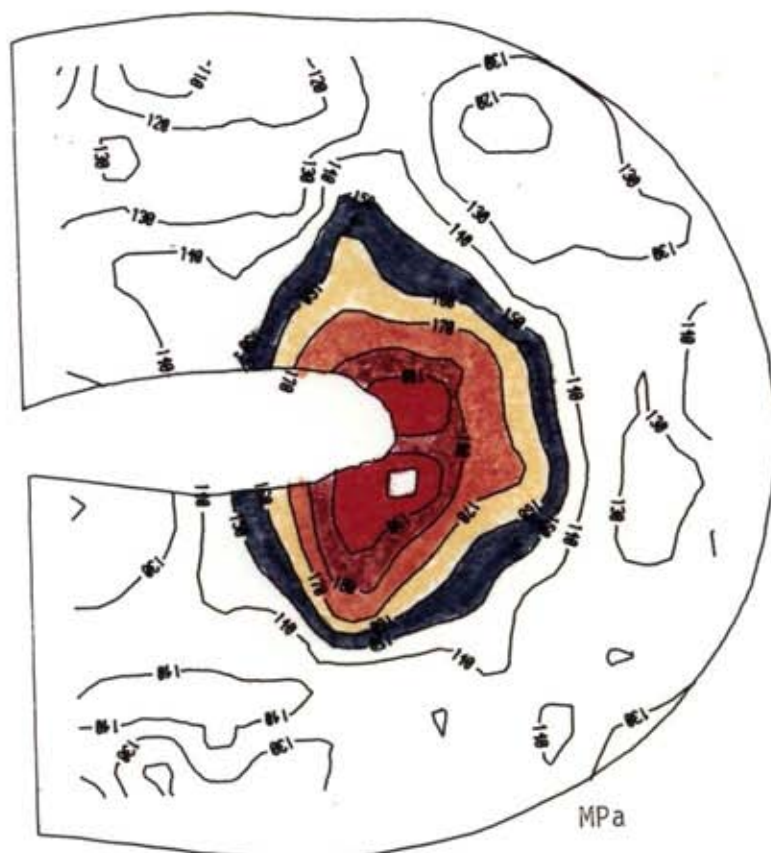
b) from microhardness tests

Figure 7.23: Contours of yield strength Y in crumpled tube section
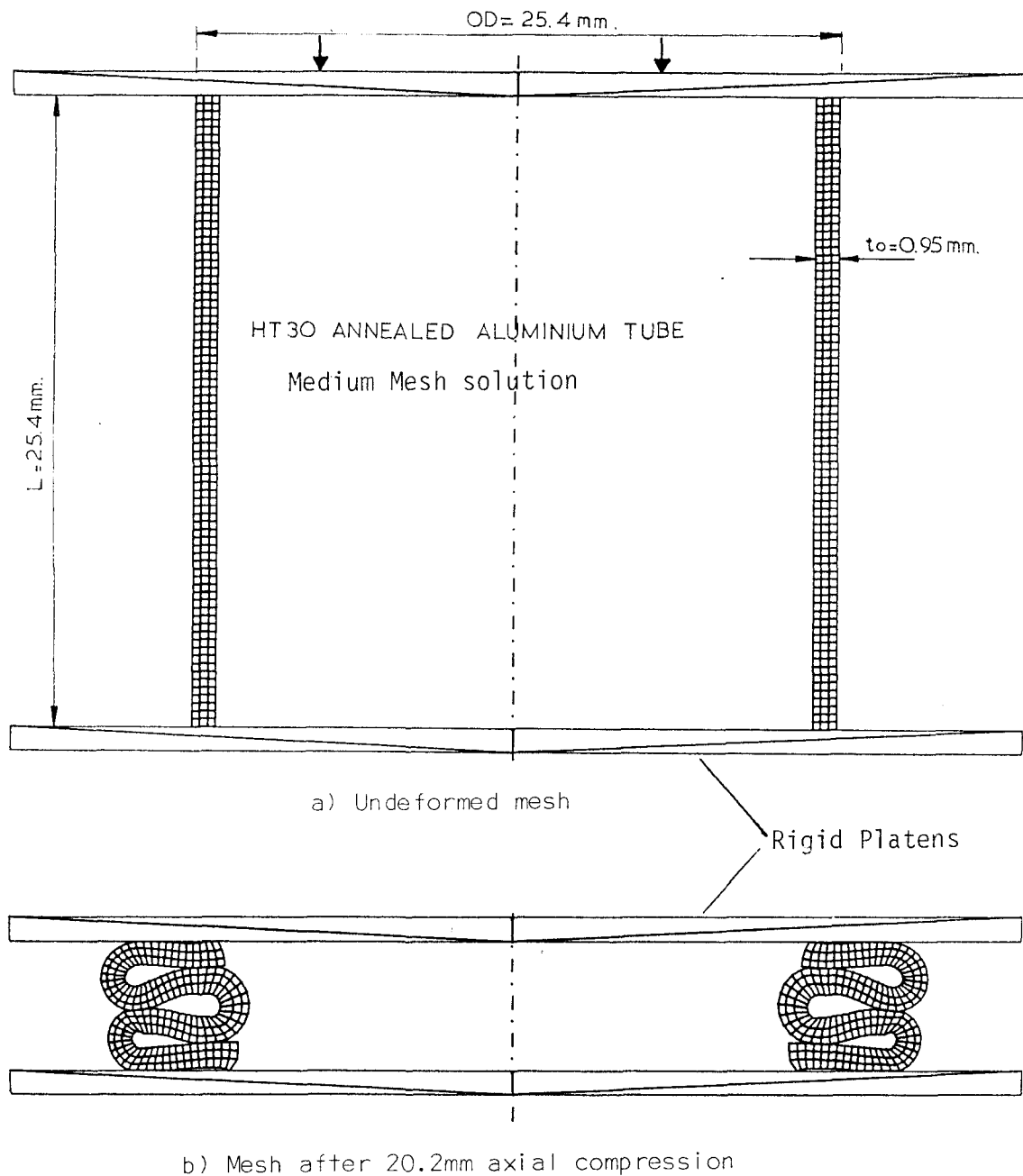(OD=38.1mm, t_o=1.64mm, L=50.8mm Tube) (geometry C)

OD= 25.4 mm.

L = 25.4mm.

to = 0.95 mm.

HT 30 ANNEALED ALUMINIUM TUBE

Medium Mesh solution

a) Undeformed mesh

Rigid Platens

b) Mesh after 20.2mm axial compression

Figure 7.24: Calculations for axial collapse of tube
OD=25.4mm, t_o=0.95mm, L=50.8mm, tube geometry D

AXIAL COLLAPSE
OD=25.4mm, t_0=0.95mm, L=25.4mm TUBE
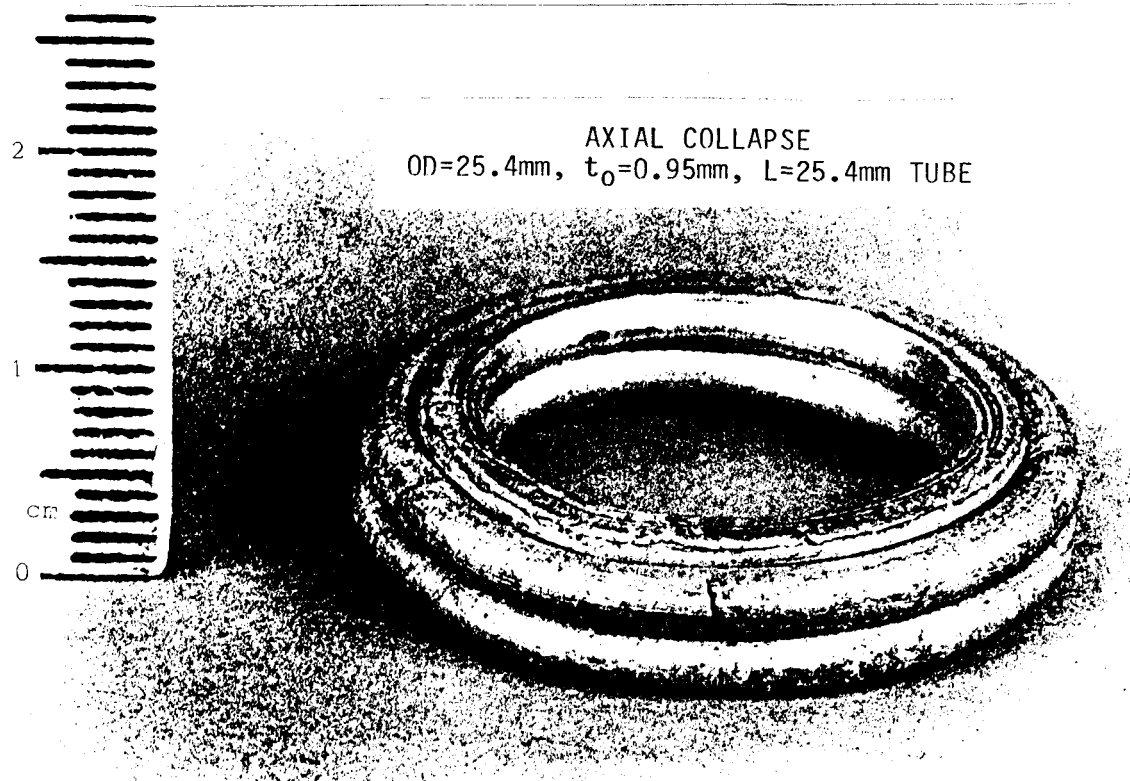
Figure 7.25: View of crumpled tube (geometry D)

AXIAL COLLAPSE
OD=25.4mm, t_0=0.95mm, L=25.4mm TUBE
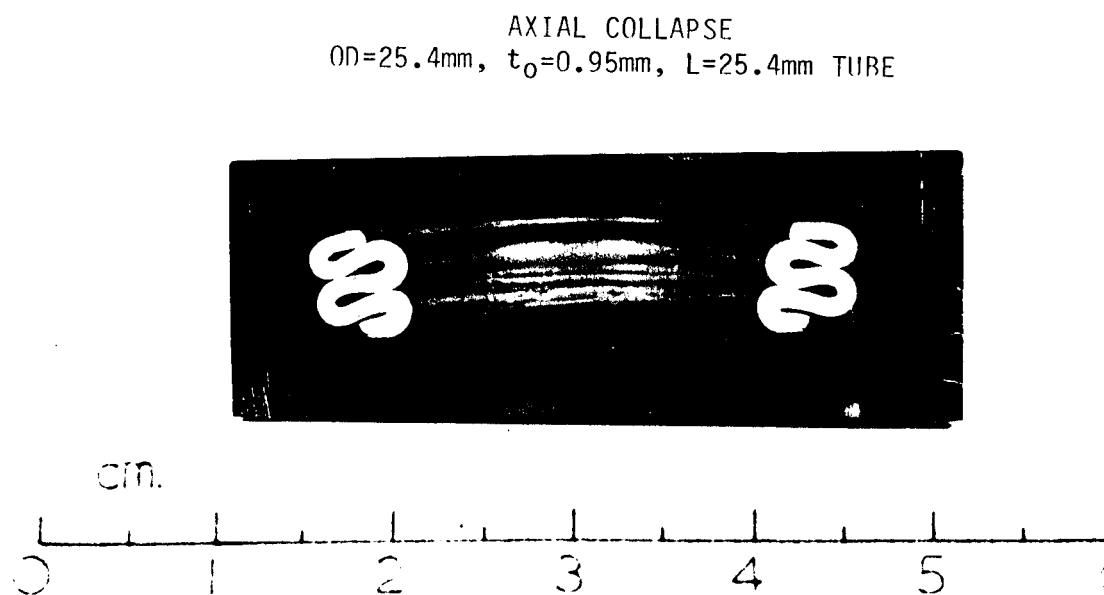
Figure 7.26: Section of crumpled tube (geometry D)
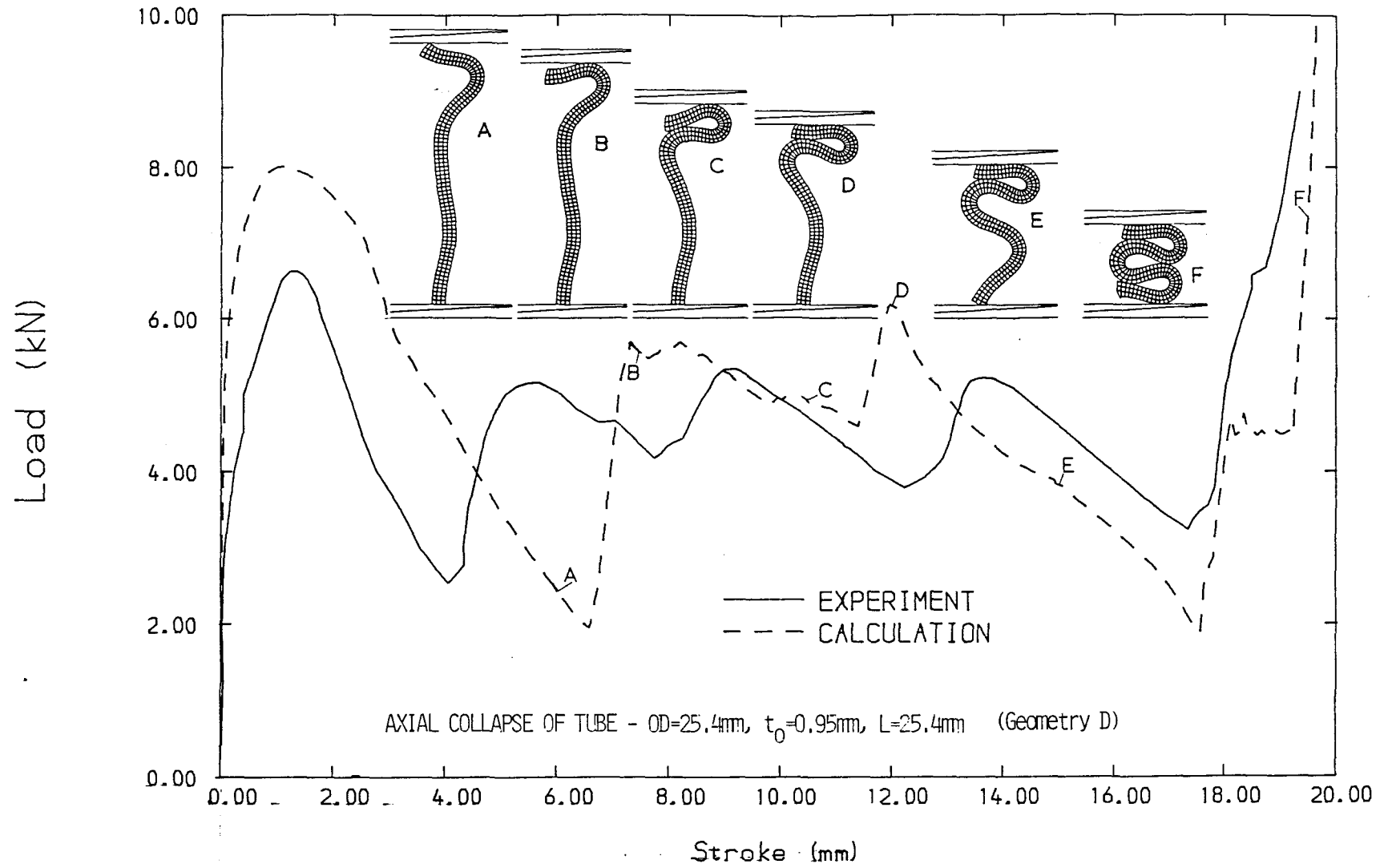
Figure 7.27: calculations for axial collapse of tube; load - compression curve

remains at the end, occasioning stiffer behaviour. The stiffening is not so tragic though, because the extra length occurs at one end; this end eventually slipped towards the outside rounding off its inner edge through friction with the platen. The numerical model does not have enough definition to represent these edge effects. It settles for two slightly longer folds than what would be preferred.

the evolution of the load curves (fig. 7.27) for the first fold show again the same similarities between experiment and calculations as for tube geometry C (sect. 7.3.3.3), and they may be explained in identical fashion (points A,B,C,D,E,F in fig. 7.27).

7.3.4 PARAMETRIC STUDIES IN NUMERICAL ANALYSES

The influence of the following parameters and modelling choices upon calculation results is studied:

- Coefficient of friction for tube-tube and tube-platen contacts;
- Velocity scaling;
- Mesh refinement;
- Element type.

The aim is to obtain numerical feedback, in order to select the characteristics of the models to be employed in the numerical analysis.

Some of the analyses presented here correspond to tube geometries already mentioned in section 7.3.3 (A,B,C,D); there the final analyses were presented. Here the results of preliminary analyses (table 7.4) are considered.

7.3.4.1 INFLUENCE OF FRICTION

A Coulomb law of friction was used in the numerical model (section 4.8.1). The tangential force F_t at the interface is limited by the normal force between the surfaces in contact, F_n, and the coefficient of friction, μ:

$$F_t \leqslant \mu F_n \qquad\qquad (7.11)$$

An experimental determination of the frictional behaviour of the surfaces and materials involved was not attempted within this investigation. In a strict sense, the perfect friction given by the Coulomb law is not applicable for all types of surfaces and arbitrary acting normal pressures (Curnier, 1984). This idealization represents an approximation to the friction phenomenon, consistent with our lack of knowledge and experimental data about it.

The influence of the variation of the coefficient of friction was studied by performing several tube collapse analyses on the same model (Tube geometry E, fig. 7.28). Values for μ ranged between 0.0 (frictionless) and 0.3. The results are summarized in figures 7.29 and 7.30. For comparison, the corresponding experimental results are also included in figure 7.29; the collapse geometry obtained experimentally consisted of 3 1/2 concertina folds.

The collapse of the frictionless model was considerably different from the other models and from the experimental results, producing only two large concertina folds. The other models all produced three folds and load-compression curves similar to each other. The results for $\mu = 0.2$ and $\mu = 0.3$ were particularly close. A tendency for shorter fold lengths is observed as friction decreases. This can be attributed to edge effects, considering that for this particular problem two out of the three folds occur at the tube ends, where the constraint is smaller the less friction between tube and platen.

The reason for the difference between experimental and numerical results is that the numerical model was insufficiently refined in terms of the "coarse" mesh used and velocity scaling (40m/s platen velocity). As will be seen in further sections, more refined models are necessary for good predictions. However, for the parametric studies a large number of computer analyses was necessary, and cost considerations forced compromises in the model refinement.
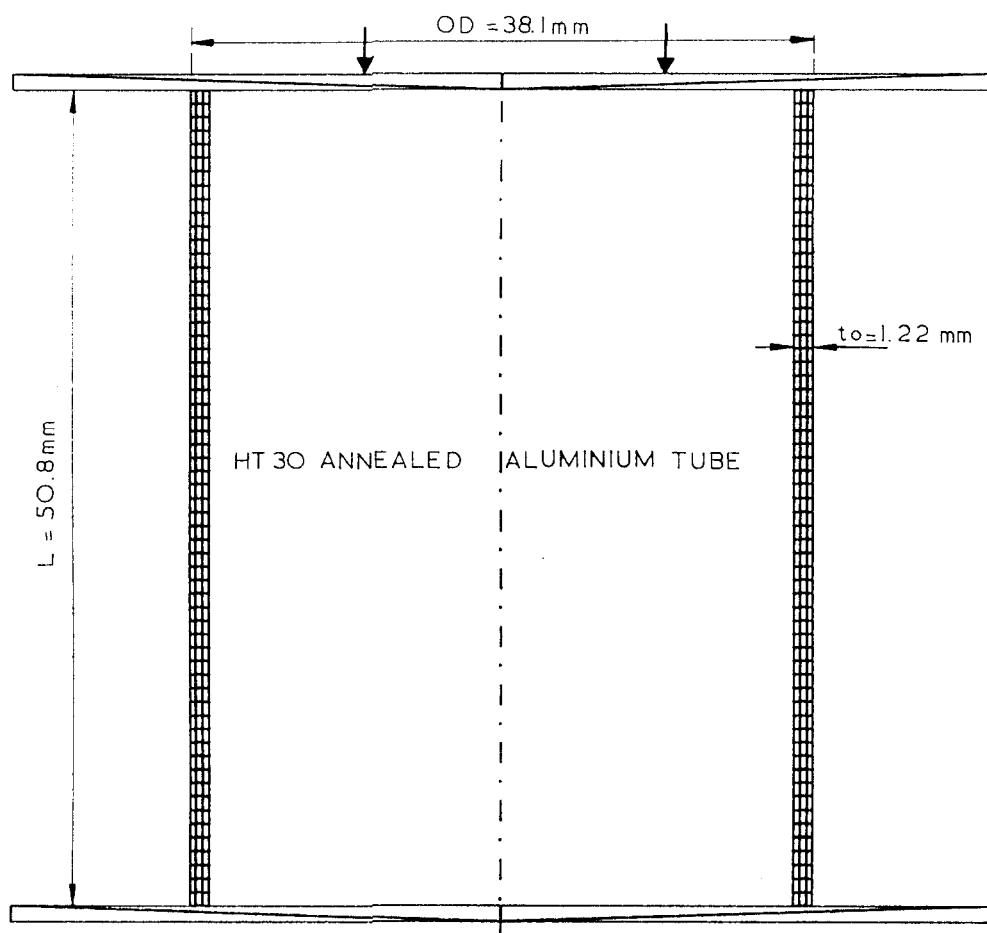
Figure 7.28: Tube model used for friction and velocity scaling
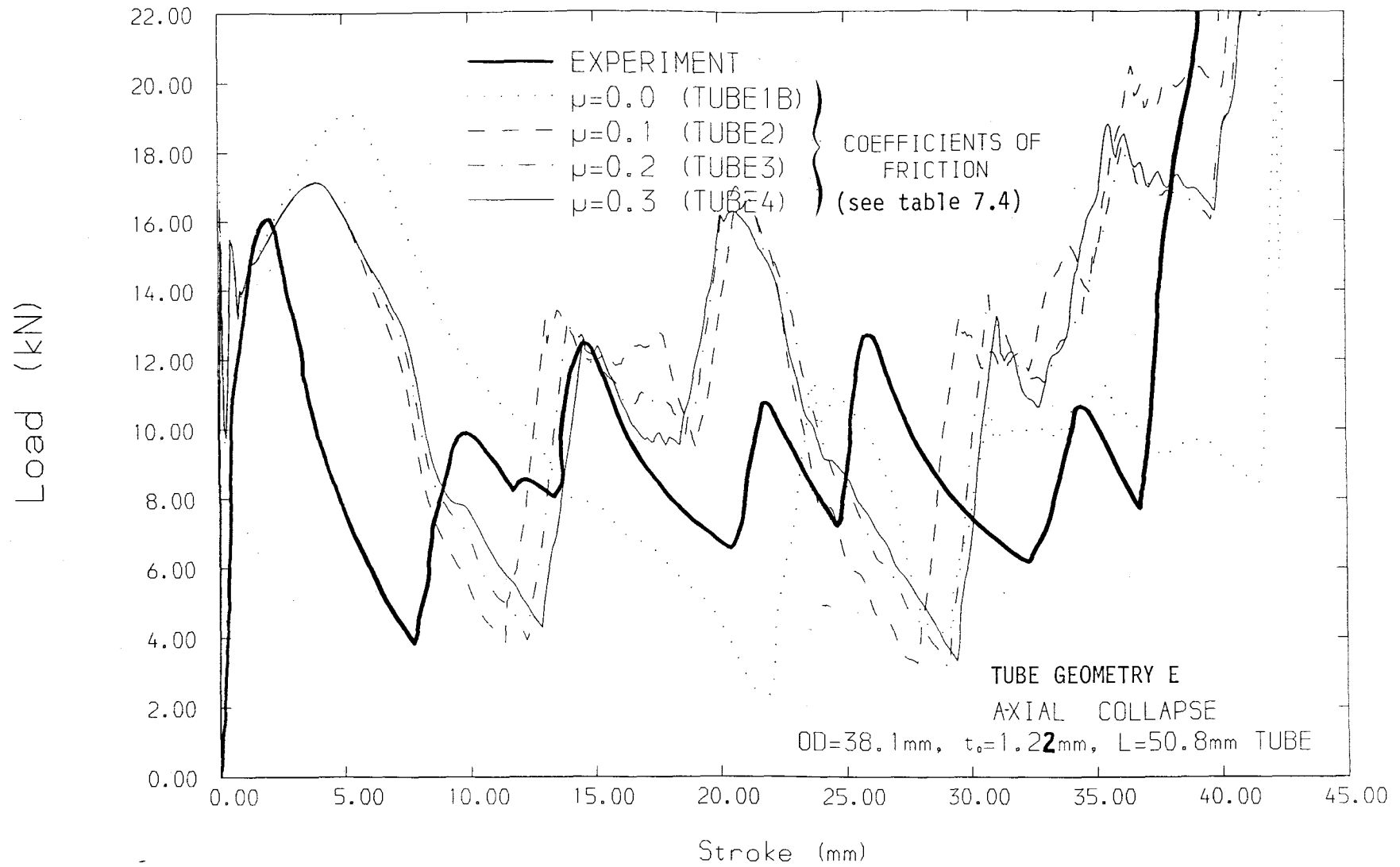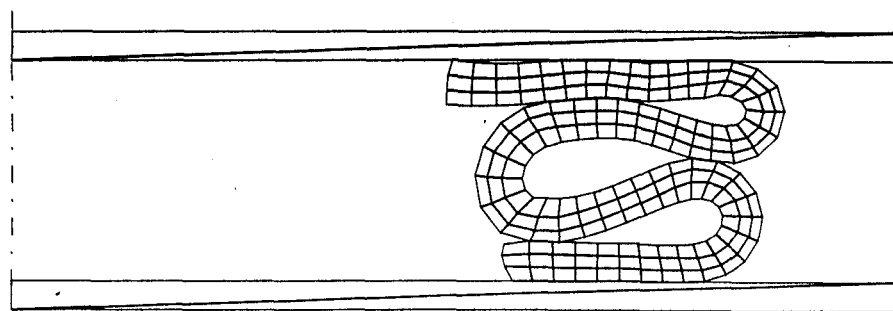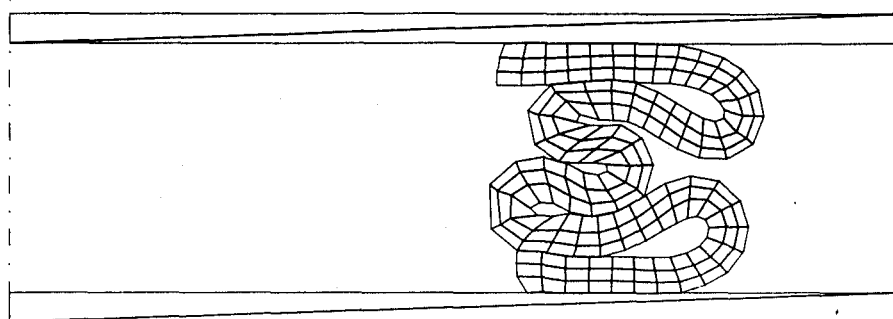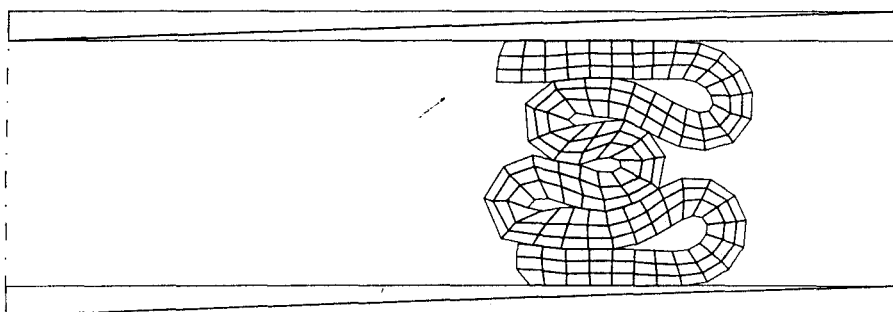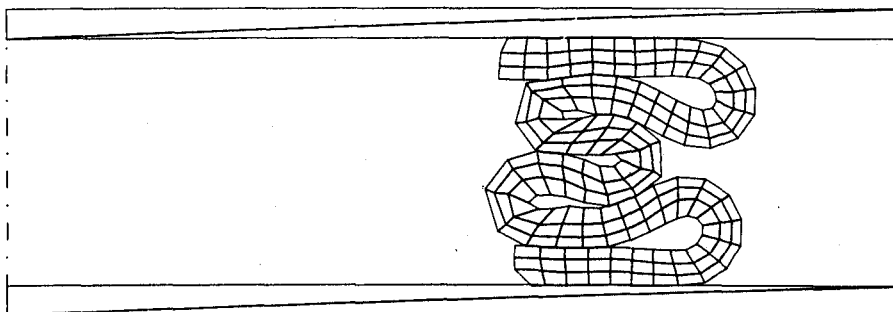parametric analyses

Figure 7.29: INFLUENCE OF FRICTION ON NUMERICAL PREDICTIONS

a) μ=0.0 (TUBE1)

b) μ=0.1 (TUBE2)

c) μ=0.2 (TUBE3)

d) μ=0.3 (TUBE4)

TUBE GEOMETRY E

Figure 7.30: FINAL DEFORMED MESHES FOR DIFFERENT VALUES OF FRICTION (μ)
OD=38.1mm, t_o=1.22mm, L=50.8mm TUBE COLLAPSE ANALYSIS

7.3.4.2 INFLUENCE OF VELOCITY SCALING

The calculations presented in section 7.3.3 all had an axial velocity of deformation of 20 m/s, representing a scaling up of the experimental velocities of five orders of magnitude. Some results are presented here studying the influence of varying the crushing velocity in the model, justifying the choice made for the final analyses in section 7.3.3.

Three analyses were performed with velocities of 10, 20, and 40 m/s on the same model as sect. 7.3.4.1 (tube geometry E, fig. 7.28). The value of the friction coefficient was selected as $\mu = 0.2$. The results are summarized in figures 7.31 and 7.32. A ramp was introduced in the applied velocity history for the beginning of the deformation, the velocity increasing from 0 to its final value in 0.1 msec. This was found to produce a smoother start for the deformation and fewer initial oscillations.

All three analyses produced 3 concertina folds in the tube. The third central fold was slightly shorter for 20 m/s and 10 m/s than for 40 m/s. In the load-compression curves (fig. 7.31), some difference is noticeable when the velocity is decreased from 40 m/s to 20 m/s, but further reduction to 10 m/s produced very little difference. The average collapse loads show a monotonic decrease towards the experimental value, again the results for 20 m/s and 10 m/s being very close.

The criterion proposed in section 7.3.2.2 for evaluating the dynamic forces involved in the wall crumpling, P_i, may be used here. From equation (7.8), the following results were obtained:

$$
\begin{array}{lll}
v=40 \text{ m/s} & P_i=0.737 \text{ kN} & (8.2\% \text{ of } P_c^{expt}) \\
v=20 \text{ m/s} & P_i=0.184 \text{ kN} & (2.0\% \text{ of } P_c^{expt}) \\
v=10 \text{ m/s} & P_i=0.046 \text{ kN} & (0.5\% \text{ of } P_c^{expt})
\end{array}
$$

Judging from these results, a velocity of 20 m/s was selected for the final analyses. The inertia forces introduced by this velocity scaling were small. Only marginal improvements are produced when the velocity is further reduced, while computational costs grow rapidly
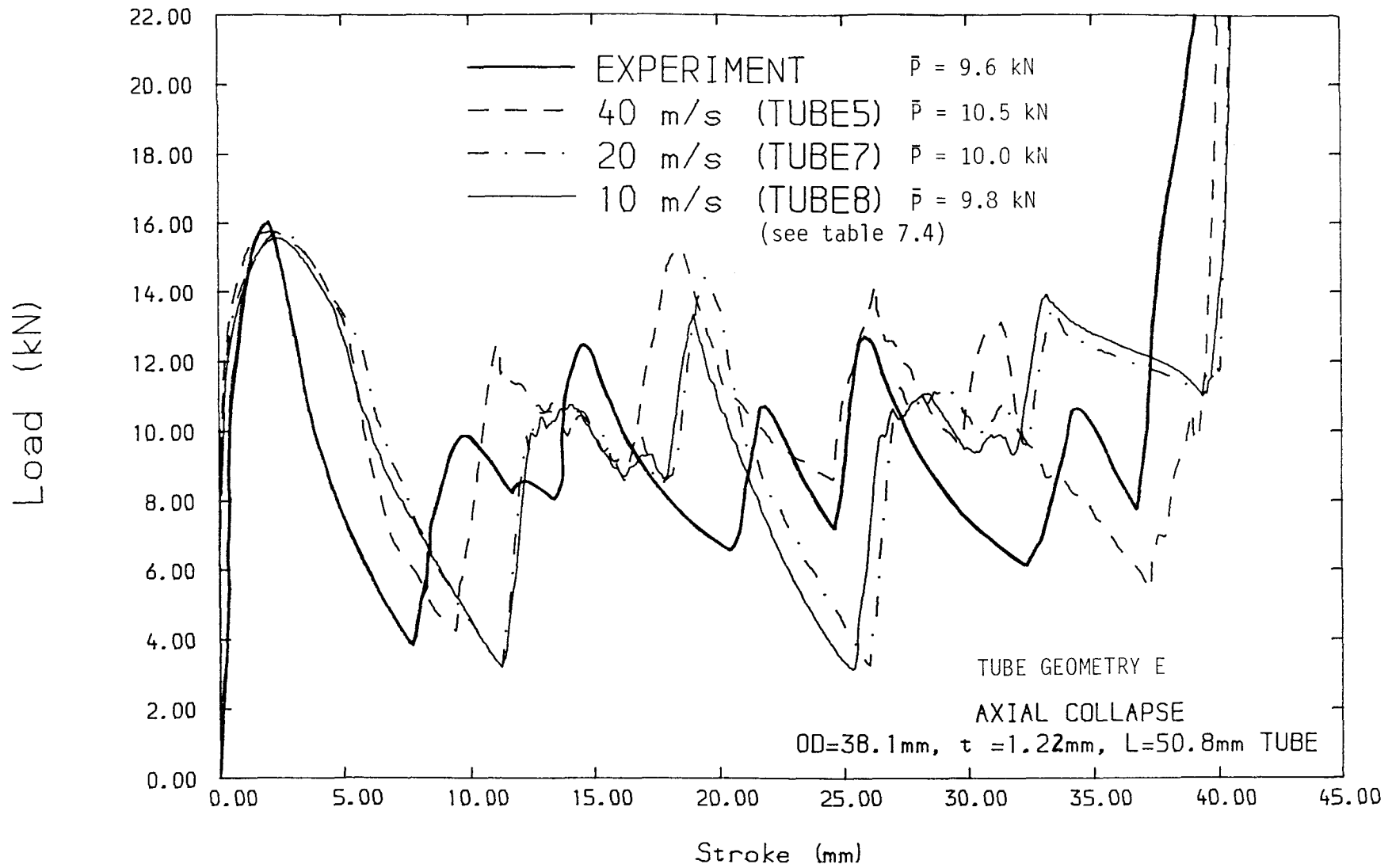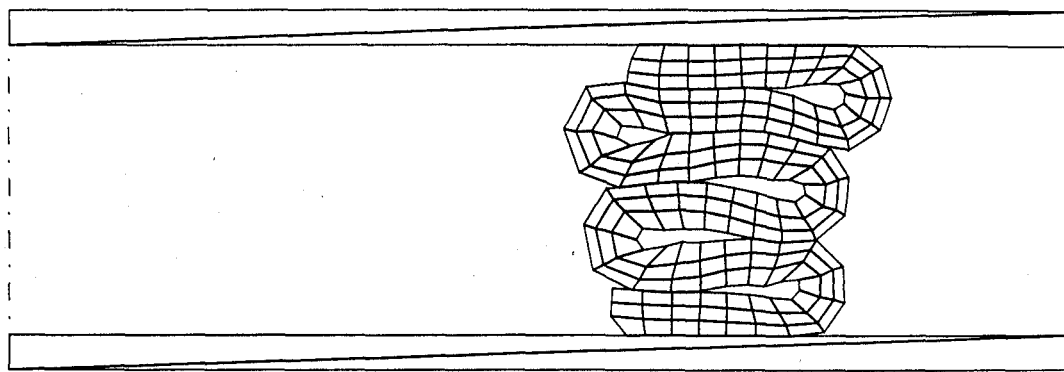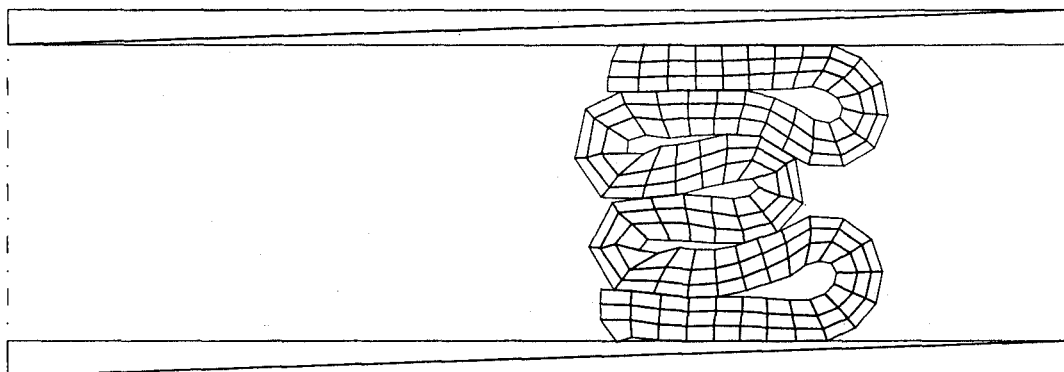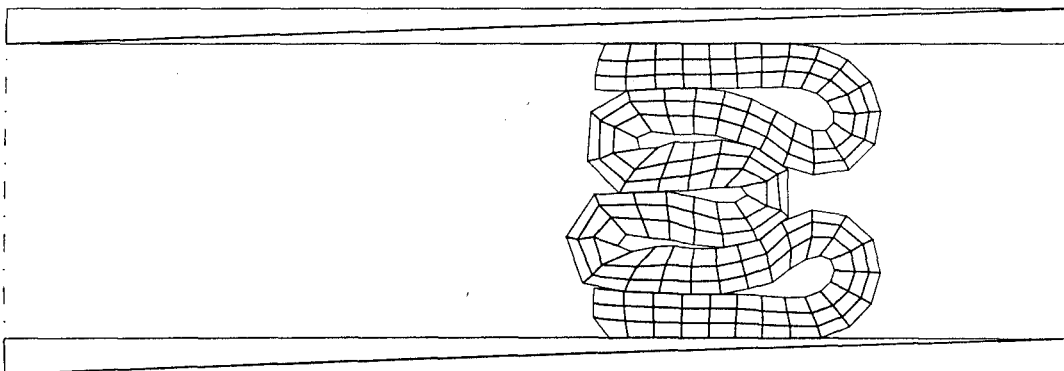
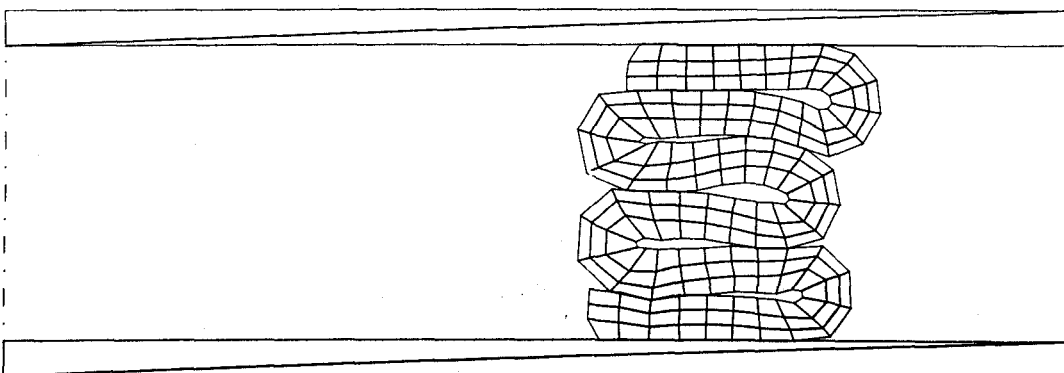Figure 7.31: INFLUENCE OF DEFORMATION VELOCITY ON NUMERICAL PREDICTIONS

a) v=40m/s, MTQC ELEMENTS (TUBE5)

b) v=20m/s, MTQC ELEMENTS (TUBE7)

c) v=10m/s, MTQC ELEMENTS (TUBE8)

d) v=40m/s, MTQ ELEMENTS (TUBE6)

(TUBE GEOMETRY E)

Figure 7.32: FINAL DEFORMED MESHES FOR VARIOUS CRUSHING VELOCITIES AND
ELEMENT TYPES - OD=38.1mm, t_s=1.22mm, L=50.8mm TUBE COLLAPSE

(1758 CPU secs. for 20m/s, 3474 CPU seconds for 10 m/s).

7.3.4.3 INFLUENCE OF MESH REFINEMENT

The influence of mesh refinement in three different cases was studied (tube geometries A, B, and C). These models have already been discussed in section 7.3.3, where results for the more refined meshes considered here were given.

For tube geometry B (fig. 7.14a, sect. 7.3.3.2), two analyses with "coarse" and "medium" meshes were done; some results are presented in figures 7.33 and 7.34. As can be seen, the mesh refinement had a dramatic influence, increasing the number of folds from 3 (coarse mesh) to 4 (medium mesh), more in line with the experimental results. The load-compression curve shows clearly the shorter length of folds for the more refined model. Still the fold length was slightly overpredicted for the medium mesh, the 4th fold being a very short and stiff one which eventually fails by shear. Further refinement of the mesh would probably achieve better results.

For tube geometry A (sect. 7.3.3.1, fig. 7.7a) three different mesh grades were used: "coarse", "medium" and "fine". The results, presented in figures 7.35 and 7.36, are very illustrative; mesh refinement produces a clear and consistent convergence towards the less stiff experimental values. The fold lengths are indicated by the position of the valleys in the load-compression curve; these are consistently shifted towards the left as the mesh is refined, increasing the available length for the last fold. As this last fold grows nearer to its "natural" unconstrained length, the energy - and thereby the force - involved in its formation decreases. A monotonical approximation of the load levels produced in the last fold towards the experimental values is apparent as the mesh is refined.

Lastly, for tube geometry C (sect. 7.3.3.3, fig. 7.19a), "coarse" and "fine" mesh analyses were performed. The results (figs. 7.37,7.38) follow a similar pattern to those outlined for the previous two cases: a decrease in the overpredicted stiffness and fold length with mesh refinement. As for tube geometry B (figs. 7.33, 7.34), the coarse mesh
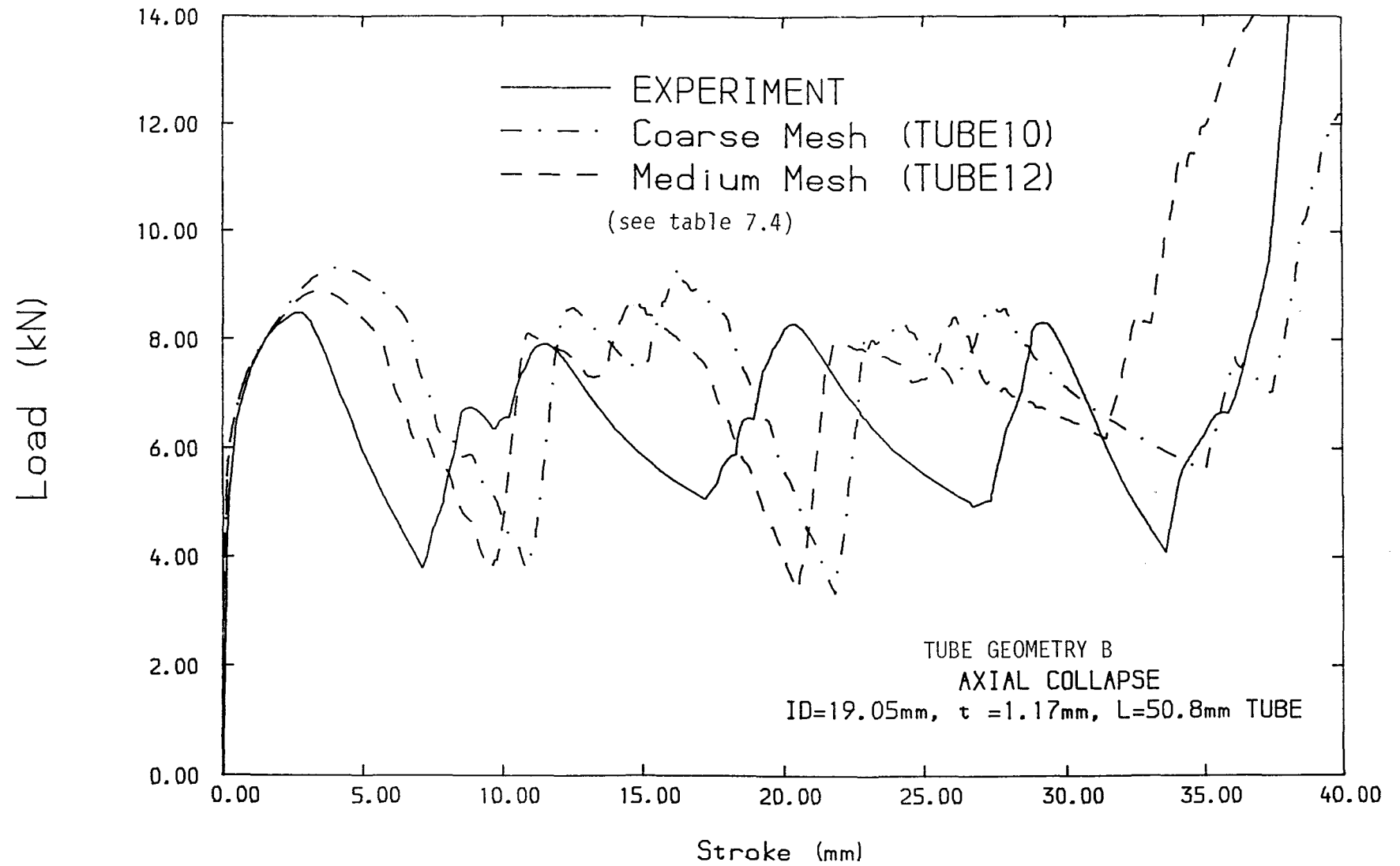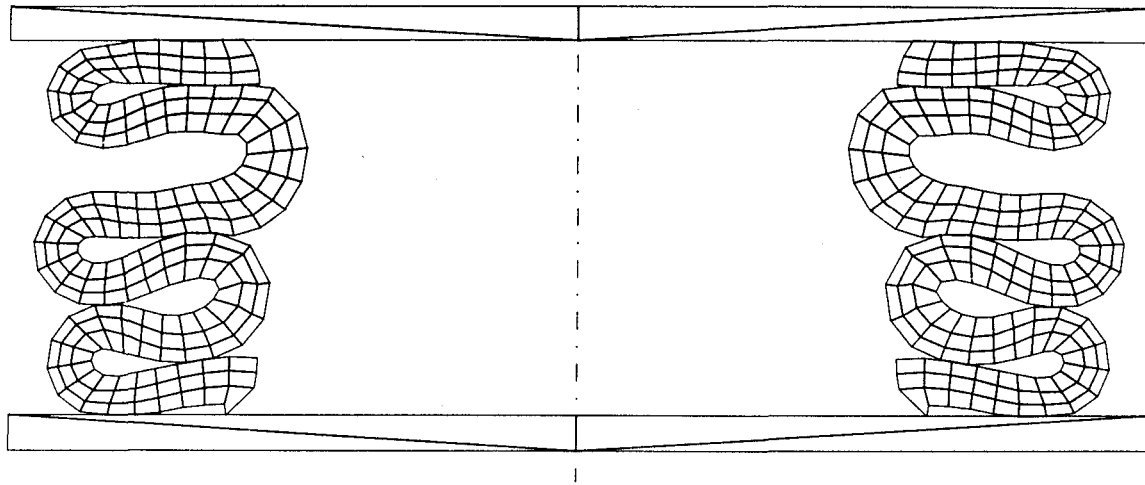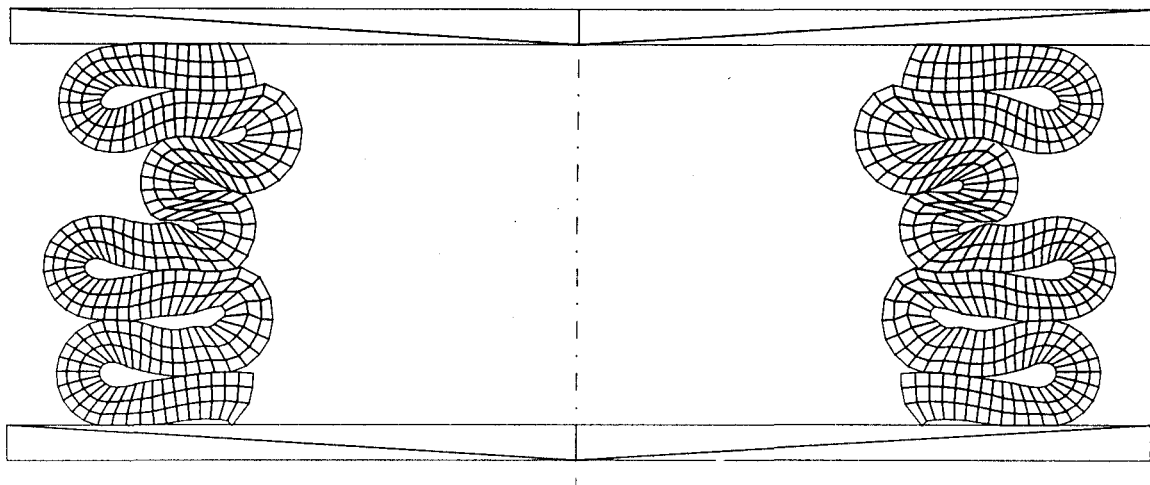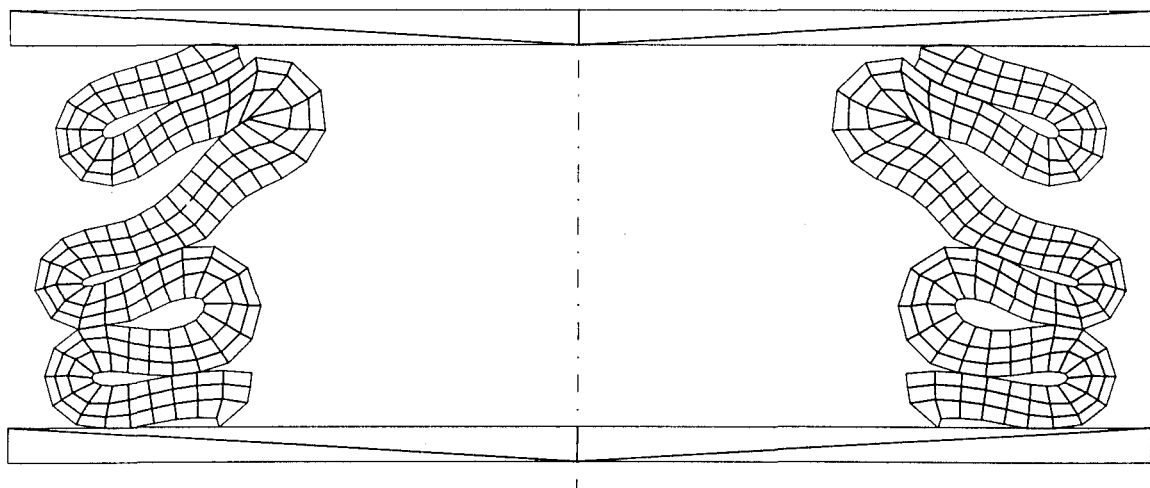
Figure 7.33: INFLUENCE OF MESH REFINEMENT ON NUMERICAL PREDICTIONS (1)

a) COARSE MESH, MTQC ELEMENTS (TUBE10)

b) MEDIUM MESH, MTQC ELEMENTS (TUBE12)

c) COARSE MESH, MTQ ELEMENTS (TUBE11)

Figure 7.34: FINAL DEFORMED VIEWS FOR VARIOUS MESHES AND ELEMENT TYPES
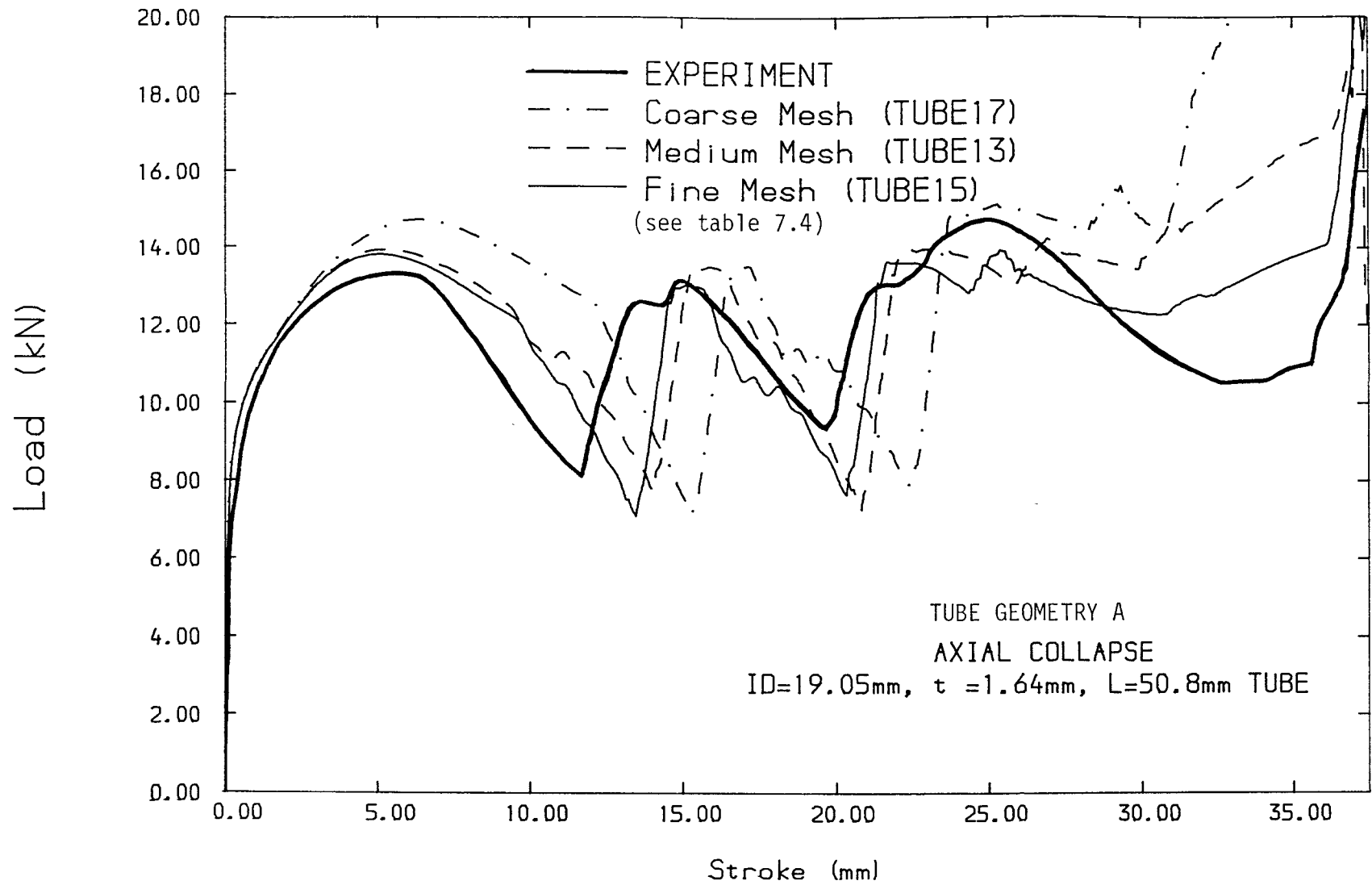ID=19.05mm, t_o=1.17mm, L=50.8mm TUBE (geometry B)

Figure 7.35: INFLUENCE OF MESH REFINEMENT ON NUMERICAL RESULTS (2)

a) COARSE MESH, MTQC ELEMENTS (TUBE17) b) MEDIUM MESH, MTQC ELEMENTS (TUBE13)

c) FINE MESH, MTQC ELEMENTS (TUBE15) d) MEDIUM MESH, MTQ ELEMENTS (TUBE18)

e) MEDIUM MESH, CST ELEMENTS (TUBE16)

Figure 7.36: FINAL DEFORMED VIEWS FOR VARIOUS MESHES AND ELEMENT TYPES
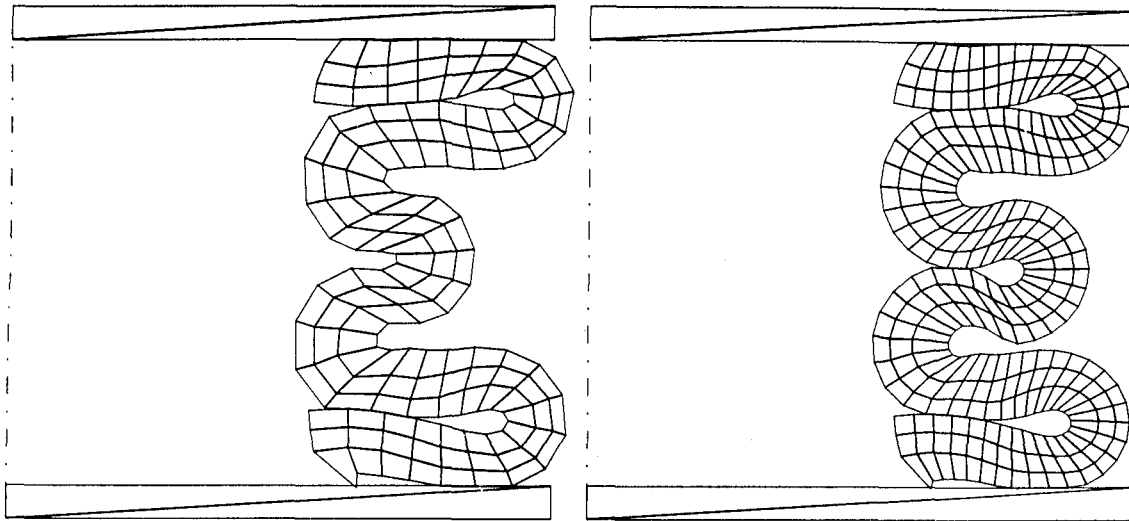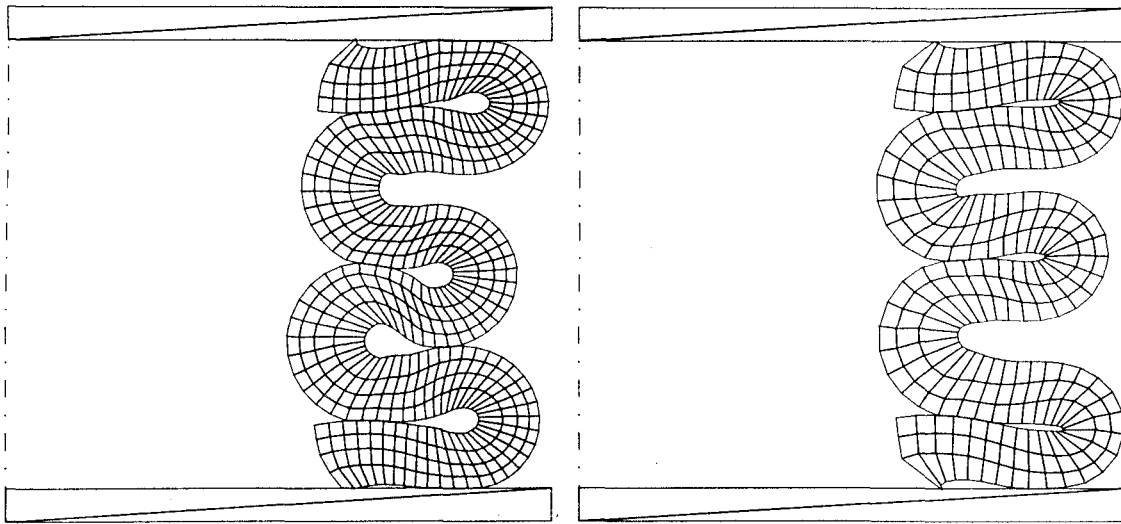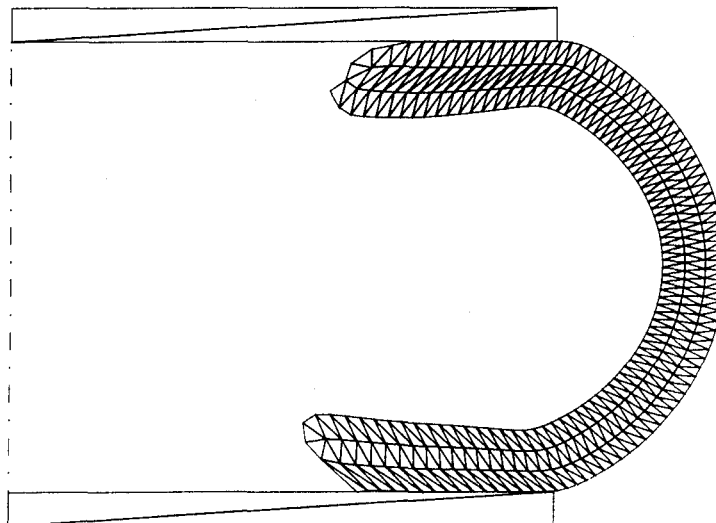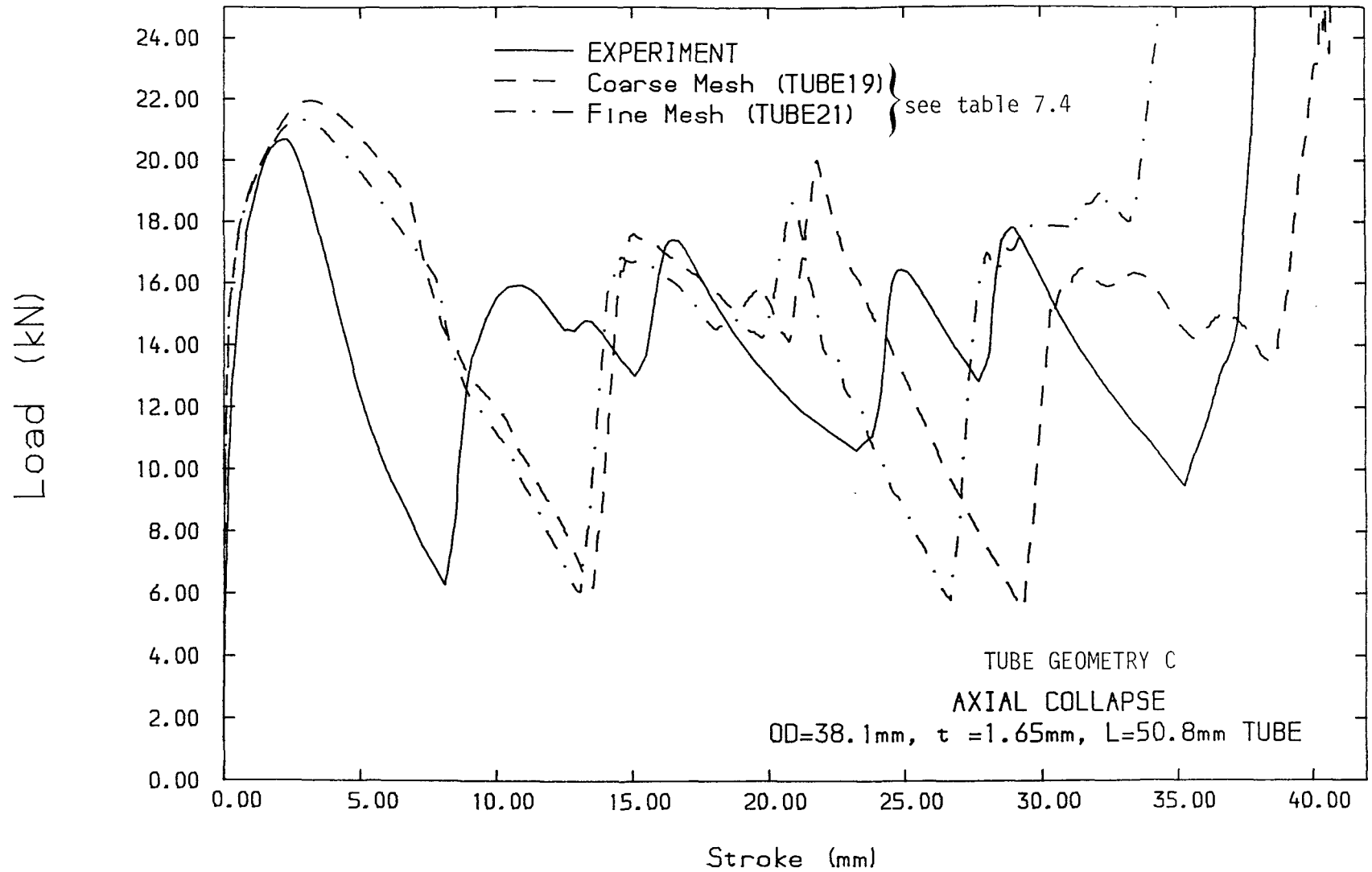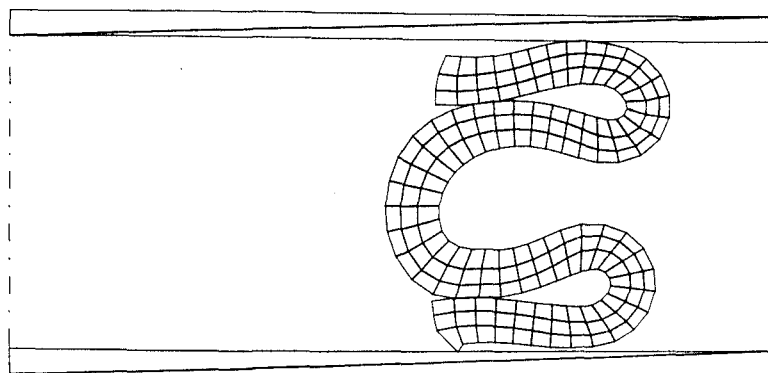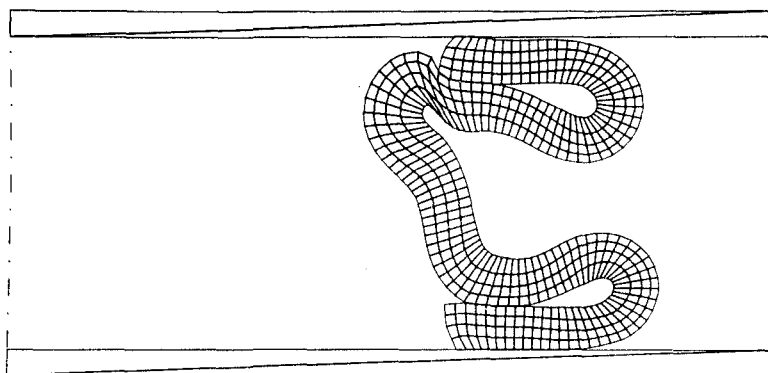D=19.05mm, t_o=1.64mm, L=50.8mm TUBE (geometry A)

Figure 7.37: INFLUENCE OF MESH REFINEMENT ON NUMERICAL PREDICTIONS (3)

a) COARSE MESH (TUBE19)

b) FINE MESH (TUBE21)

Figure 7.38: FINAL DEFORMED VIEWS FOR VARIOUS DEGREES OF
MESH REFINEMENT - OD=38.1mm, t_o=1.65mm, L=50.8mm
(tube geometry C)

model missed one fold altogether. With the fine mesh some more length
was available for the third fold, and its formation was attempted.
However the model was still somewhat overstiff; the length of tube
left over for the third fold was too short, and a shear failure
mechanism was preferred finally.

7.3.4.4 INFLUENCE OF ELEMENT TYPE

All the analyses reported above used the Mixed Triangle-
Quadrilateral with Correction (MTQC) elements, proposed in section
4.2.3. Here an attempt is made to assess the behaviour of these new
elements when compared to the previous Mixed Triangle-Quadrilateral
(MTQ) elements (section 4.2.2) and Constant Strain Triangles (CST)
(sect. 4.2.1).

It was mentioned in section 3.7.1 that CST meshes impose an
excessive number of volumetric constraints and therefore become in
practice artificially stiff for incompressible plastic flow. Mesh
refinement does not solve the problem, failing to converge towards
true solutions. MTQ elements solve this problem by reducing the number
of volumetric constraints, but for very large deformations tangling
over of the mesh can occur, creating unacceptable negative volumes. A
correction to prevent this tangling over was proposed in section 4.2.3
with the MTQC elements.

The convergence of MTQC meshes has been proved in the previous
section 7.3.4.3, where successively finer meshes were shown to
approach monotonically the experimental results. Nevertheless, it
seems inevitable that some stiffening be introduced by MTQC elements.
The aim here is to check, for practical large deformation plastic flow
problems, that this stiffening is small. If so, it will be proved that
MTQC elements retain the advantages of MTQ elements while at the same
time providing a more robust model.

It must be mentioned that all the low velocity tube collapse
problems considered could be analyzed successfully with MTQ meshes.
Although in other cases negative volumes did occur (section 7.4.4), no
problems arose here due to the lack of boundary constraints and the

low deformation velocities.

The "coarse" mesh tube model (tube geometry E, fig. 7.28a) was analyzed with MTQ and MTQC elements. Load-compression curves for both calculations are shown together with the experimental results in figure 7.39, where little difference can be appreciated between the two calculations. The lower value of the minimum loads at the valleys for the MTQ mesh denotes a lower resistance to high curvature bending at folds. This is corroborated by inspection of the deformed shapes (figure 7.32a, 7.32d)

The same comparison as above was done for tube geometry B (fig. 7.14a). Results for coarse meshes with MTQ and MTQC elements are presented in figures 7.40, 7.34a and 7.34c. It was seen in the previous section 7.3.4.3 that the MTQC coarse mesh failed to develop the fourth fold which was observed in experiment. A slightly better behaviour in this respect was obtained from the MTQ coarse mesh. For the first three folds the length is very slightly shorter than for the MTQC mesh. Some extra length is left over after the first three folds, but still too short for the fourth fold, evantually failing in a high curvature hinge. The improvement however is far from that obtained with a finer mesh (fig. 7.12b) where a fourth fold was formed. Again softer bending behaviour is appreciated for MTQ.

Finally the effect of different element types was studied for tube geometry A (fig. 7.7a). Calculations were carried out with CST, MTQ, and MTQC medium meshes, the results being shown in figures 7.41, 7.36b, 7.36d, and 7.36e. The great overstiffness of the CST mesh is immmediately apparent. The model is completely unable to represent the concertina mechanism and buckles into one large fold (fig. 7.36e) with substantially higher loads (fig. 7.41). For the Mixed discretizations MTQ and MTQC, no advantage is apparent for MTQ as to fold lengths in this case. An excessively soft behaviour in high curvature bending is exhibited by MTQ elements.

One practical disadvantage of MTQ over MTQC elements is that, even without developing negative volumes, some triangular cells may become very small in size. As it is cell size which governs the computational time-step, this means increased cost of analysis. In

Figure 7.39: INFLUENCE OF ELEMENT TYPE ON NUMERICAL PREDICTIONS (1)

The figure shows a plot of Load (kN) versus Stroke (mm) with the following legend:
- EXPERIMENT
- MTQC elements (TUBE5)
- MTQ elements (TUBE6)
- (SEE TABLE 7.4)
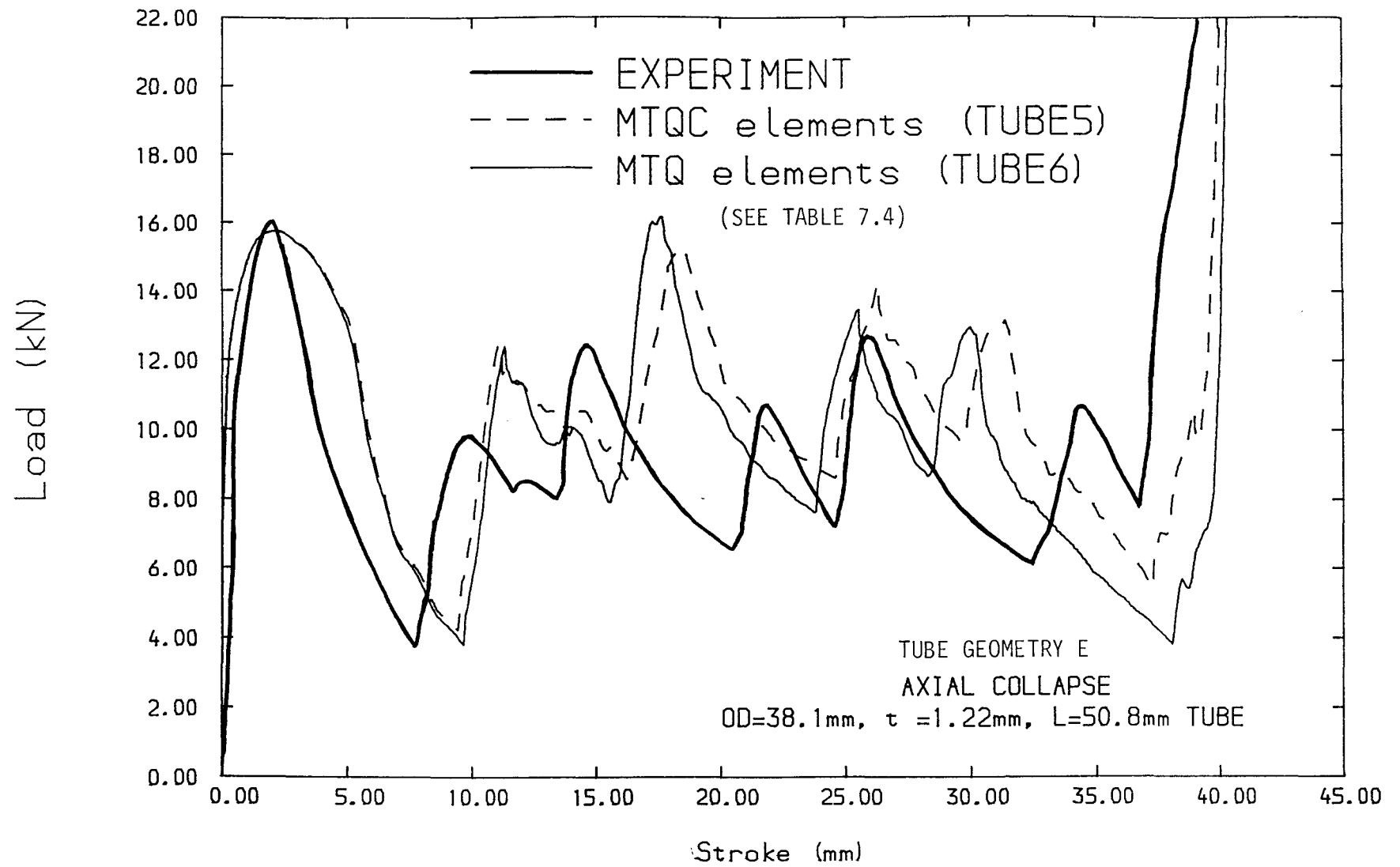
TUBE GEOMETRY E
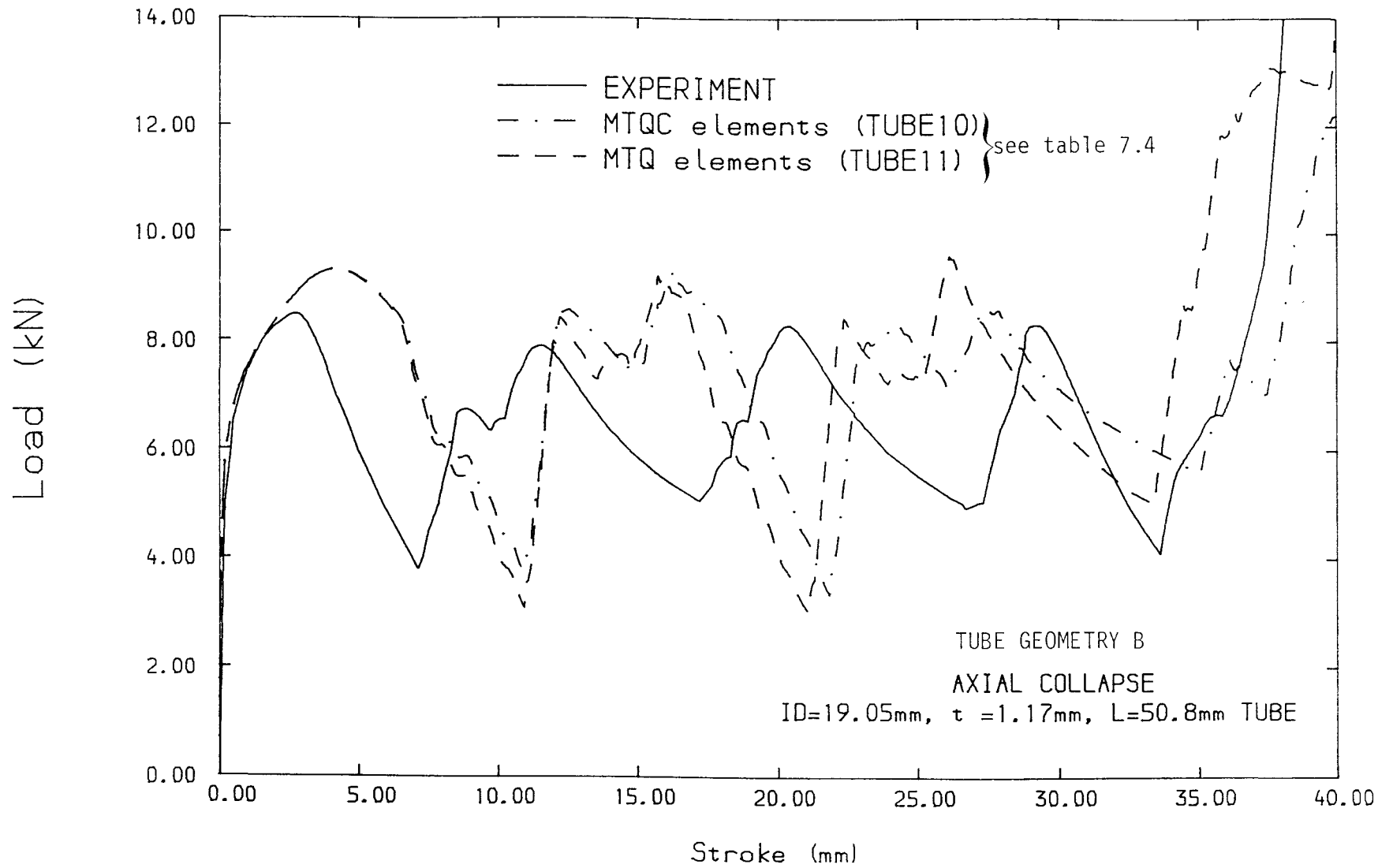AXIAL COLLAPSE
OD=38.1mm, t =1.22mm, L=50.8mm TUBE

Figure 7.40: INFLUENCE OF ELEMENT TYPE ON NUMERICAL PREDICTIONS (2)
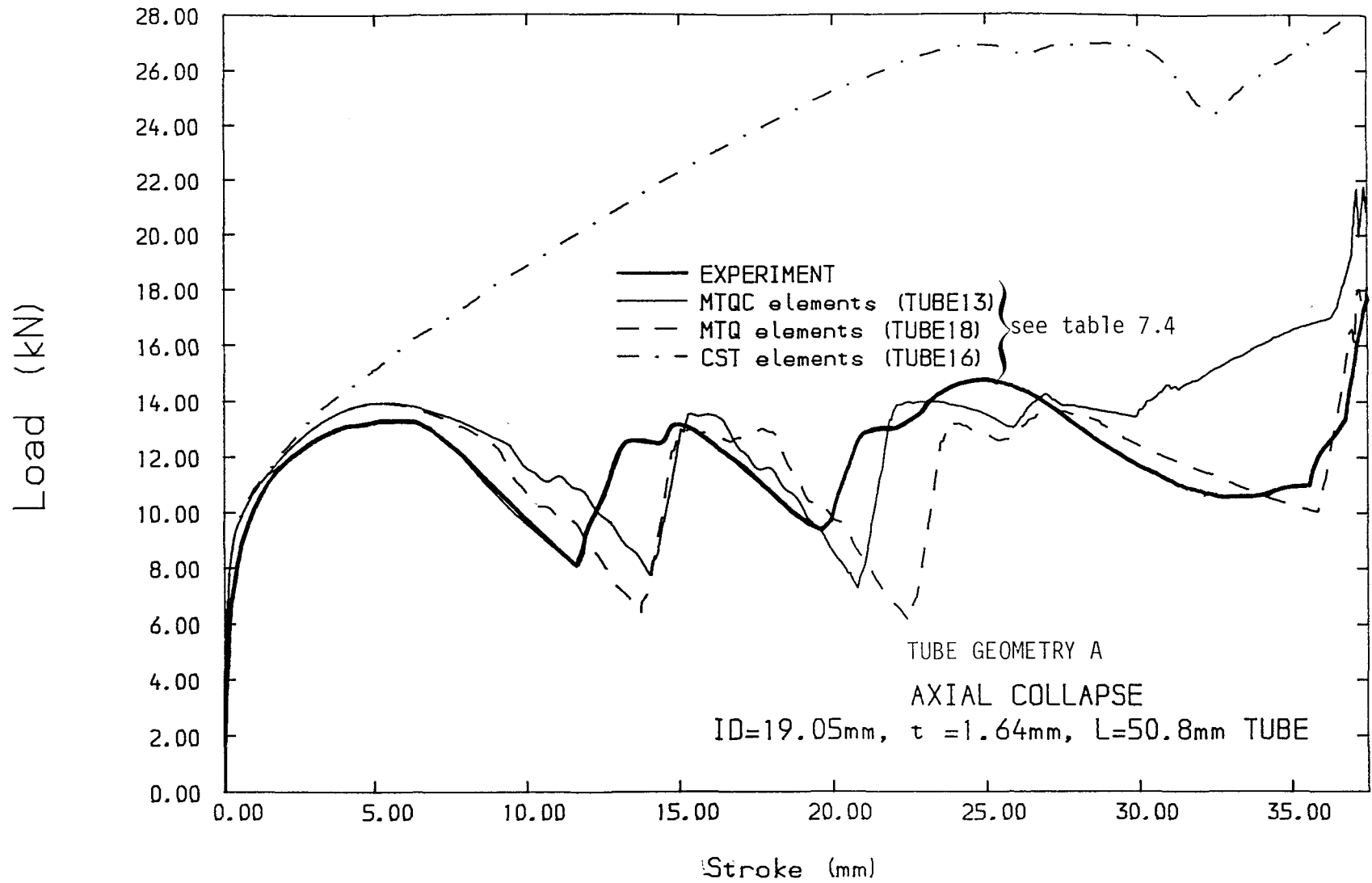
Figure 7.41: INFLUENCE OF ELEMENT TYPE ON NUMERICAL PREDICTIONS (3)

general it was found that refining MTQC meshes was a more consistent, robust and cheaper method of improving the results than using softer MTQ meshes. This is clearly exemplified in figure 7.42, where the load-compression results for a MTQC fine mesh (8641 CPU sec) are clearly far better than those for a MTQ medium mesh (12882 CPU sec) at approximately 2/3 CPU cost.

7.3.5 DISCUSSION

The quasi-static axisymmetric crumpling of tubes has been modelled successfully. Results for four tubes are given in section 7.3.3 and compared with experiments. Generally load-compression curves, deformed geometries, and stress distributions showed good matching between predictions and experimental results.

Nevertheless a consistent tendency for overstiff solutions is present to a greater or lesser degree in most of the calculations. The load levels predicted in the load-compression curves are very close to the experimental values, but the predicted fold lengths are often too great. Two factors may be the cause of these differences: coarseness of the meshes and edge effects.

Finite element solutions give always upper bound energy approximations (Zienkiewicz, 1977), approaching gradually the true solutions upon mesh refinement. In section 7.3.4.3 it was shown that MTQC meshes did converge towards the experimental results. Some of the calculations would have benefited from finer meshes, although this was not attempted for reasons of cost.

Edge effects played an important role in most of the problems analyzed, where the number of folds produced varied between 2 and 4. Out of these, 2 folds occur always at the ends and may be heavily influenced by the interaction between platen and edge of tube. A complex plastic deformation process occurs at the tube edges when sliding against the platens, creating a characteristic rounded shape (figure 7.43a), which is not modelled properly by the meshes employed and the discrete contacts with Coulomb friction (figure 7.43b). Accurate representation of this phenomenon together with the overall
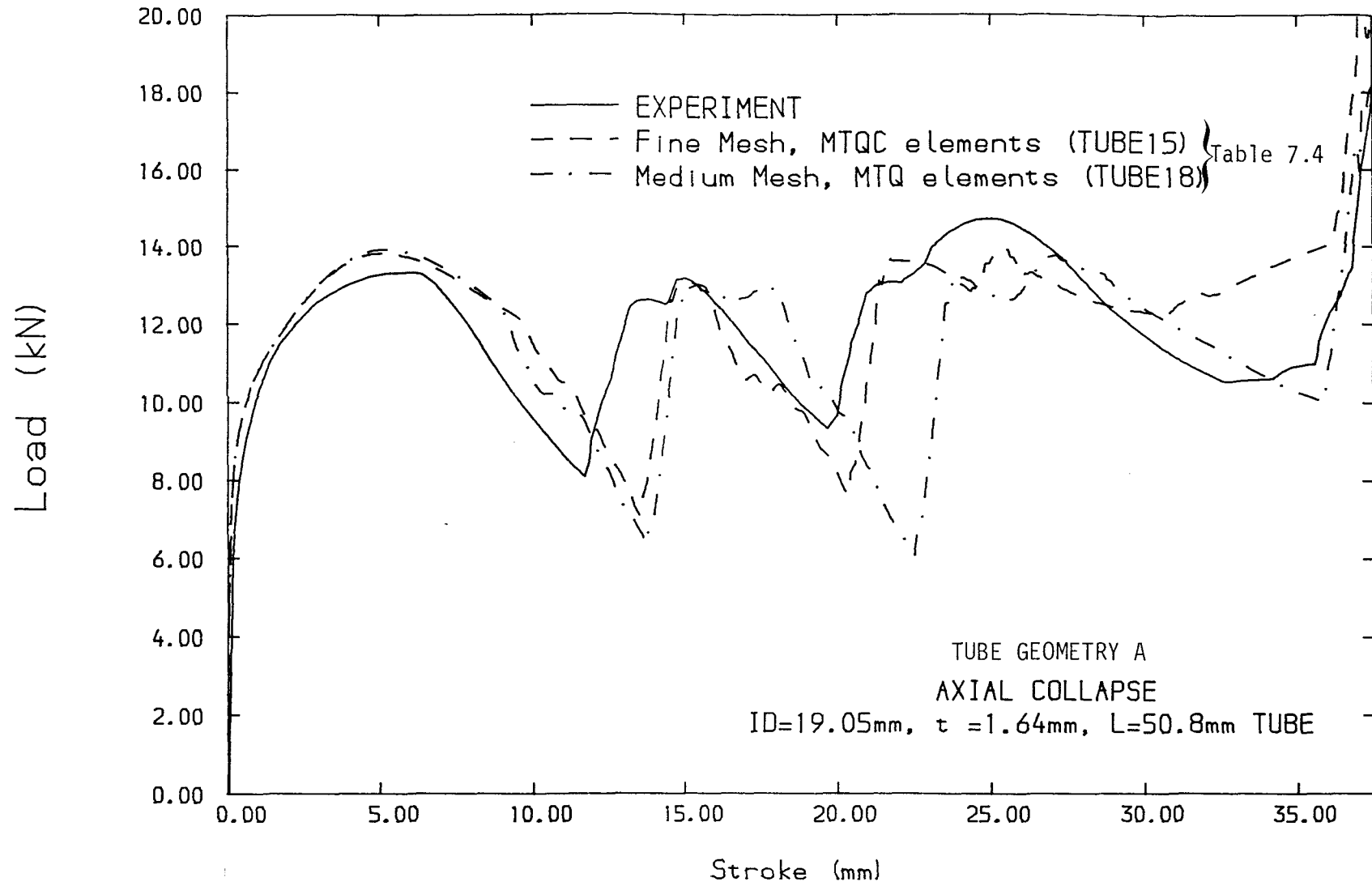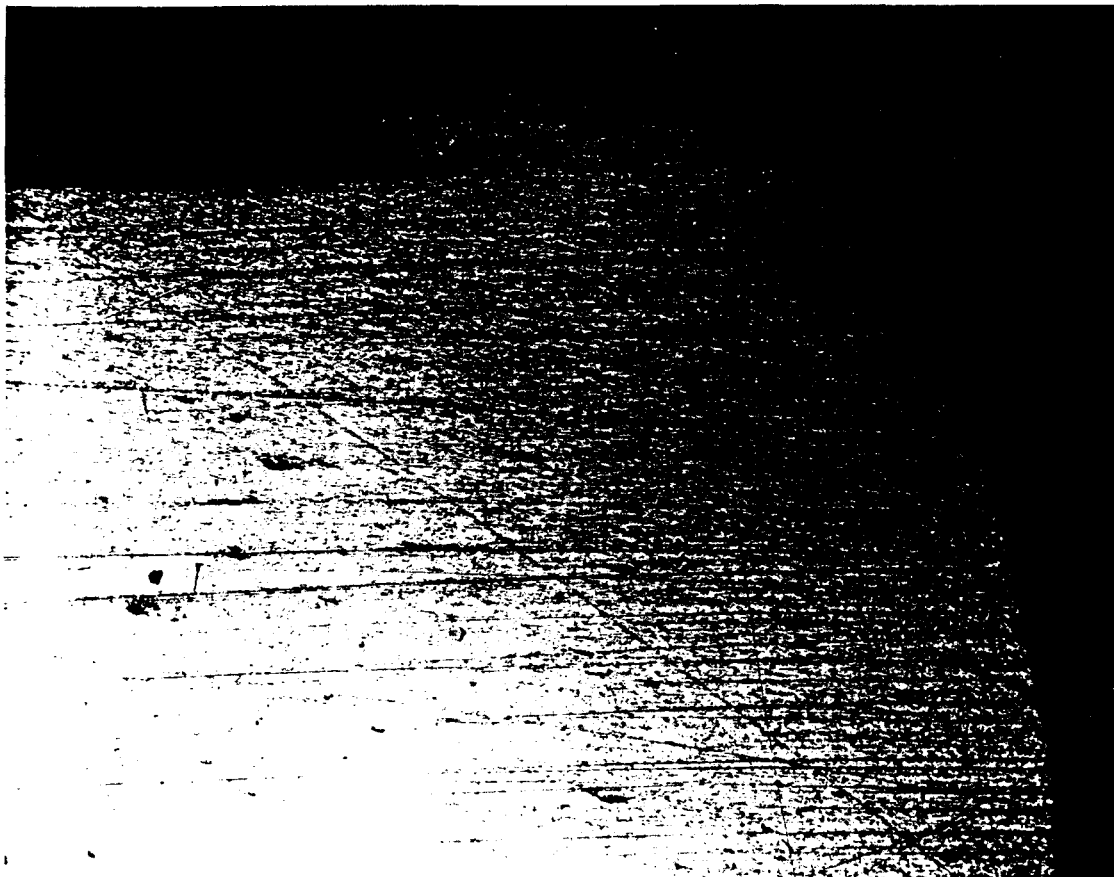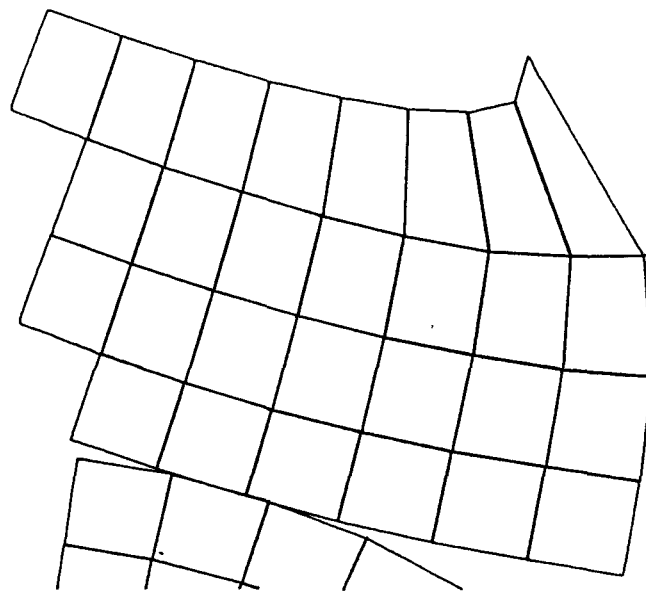
Figure 7.42: INFLUENCE OF ELEMENT TYPE ON NUMERICAL PREDICTIONS (4)

a) experimental shape

b) Calculated shape (TUBE21)

Figure 7.43: Local deformation from sliding at tube edges
(OD=38.1mm, t_o=1.65mm, L=50.8mm Tube) (geometry C)

crumpling analysis needs such locally fine meshes that computations would become uneconomic. This edge misrepresentation is bound to have a stiffening effect upon the end folds, therefore increasing the fold length.

The number of folds and the average collapse forces obtained in the calculations are compared with experimental results and predictions from Alexander (1960) (eqs. 7.2, 7.3) in table 7.3. Alexander's theory gives poor predictions as to the fold length for the thick tubes with high t_0/D ratios. This is probably due to the inadequacy for thicker tubes of Alexander's hinge/thin shell model. The average load predictions are closer to the experimental values. One must bear in mind however that a fairly arbitrary average value for Y was selected for equation (7.2).

Tube geometry	no. of folds			av. collapse load		
	eq(7.3)	expt	calc	eq(7.2) (*)	expt	calc
(A) ID=19.05mm,t_0=1.64mm,L=50.8mm	4.8	3	3	9.6	11.9	12.2
(B) ID=19.05mm,t_0=1.17mm,L=50.8mm	5.6	4	3.5	5.8	6.5	7.7
(C) OD=38.1 mm,t_0=1.65mm,L=50.8mm	3.4	3	2.25	13.6	13.8	16.1
(D) OD=25.4 mm,t_0=0.95mm,L=25.4mm	2.7	2.5	2	4.8	4.5	4.8

(*) for Y=175MPa, corresponding to 0.8 strain

Table 7.3: Summary of results for axisymmetric axial crumpling of tubes from theory by Alexander(1960), experiments, and numerical calculations.

Anal.	Geom. (+)	Mesh (++)	Element type (&&)	Frict. (μ)	Platen veloc. (m/s)	no of folds	Avge. Load P (kN) (*)	CPU (sec) (**)
TUBE1	E	Coarse,60x3	MTQC	0.0	40(&)	2	10.2	1040
TUBE2	E	Coarse,60x3	MTQC	0.1	40(&)	3	11.7	1414
TUBE3	E	Coarse,60x3	MTQC	0.2	40(&)	3	11.4	1364
TUBE4	E	Coarse,60x3	MTQC	0.3	40(&)	3	11.4	962
TUBE5	E	Coarse,60x3	MTQC	0.2	40	3	10.5	1079
TUBE6	E	Coarse,60x3	MTQ	0.2	40	3	9.9	1196
TUBE7	E	Coarse,60x3	MTQC	0.2	20	3	10.0	1758
TUBE8	E	Coarse,60x3	MTQC	0.2	10	3	9.8	3474
TUBE9	F	Coarse,100x3	MTQC	0.2	20	5	10.2	5333
TUBE10	B	Coarse,65x3	MTQC	0.2	20	3	7.2	2263
TUBE11	B	Coarse,65x3	MTQ	0.2	20	3	7.3	3734
TUBE12	B	Medium,130x3	MTQC	0.2	20	3 1/2	7.7	7167
TUBE13	A	Medium,90x3	MTQC	0.2	20	3	12.9	3352
TUBE14	D	Medium,80x3	MTQC	0.2	20	2	4.8	2664
TUBE15	A	Fine, 124X3	MTQC	0.2	20	3	12.2	8641
TUBE16	A	Medium,90x3	CST	0.2	20	1/2	22.2	2346
TUBE17	A	Coarse,45x3	MTQC	0.2	20	2 1/2	14.3	1035
TUBE18	A	Medium,90x3	MTQ	0.2	20	3	11.5	12882
TUBE19	C	Coarse,60x3	MTQC	0.2	20	2	14.8	1530
TUBE20	C	Fine, 124x4	MTQC	0.2	20	2 1/2	16.1	7732

(+) Geometry A: ID=19.05mm, t_0=1.64mm, L=50.8mm

Geometry B: ID=19.05mm, t_0=1.17mm, L=50.8mm

Geometry C: OD=38.10mm, t_0=1.65mm, L=50.8mm

Geometry D: OD=25.40mm, t_0=0.95mm, L=25.4mm

Geometry E: OD=38.10mm, t_0=1.22mm, L=50.8mm

Geometry F: OD=38.10mm, t_0=1.22mm. L=88.9mm

(++) For classification of meshes see section 7.3.2.1

(&) Velocity was applied without initial ramp for these cases

(&&) See section 4.2

(*) P = $[\int Pdx]/L$

(**) CPU times on a CRAY-1S

Table 7.4: Details of numerical analyses for axial tube collapse

The numerical model is not constrained by beam or thin shell assumptions, and therefore finds no problems in modelling the thick tubes, where in fact it gives better predictions. The load results are overstiff in all cases; however, for the second and third tubes in table 7.3 the relatively large difference with experiment is due to the shorter, stiffer incomplete folds at the end of the analysis.

7.4 MEDIUM VELOCITY (176m/s) TUBE IMPACT ANALYSIS

The impact of medium velocity hard and soft missiles on structures has been the object of some interest in the past few years. Extensive programs of experimental research have been undertaken at Meppen, FDG (e.g. Rudiger and Riech, 1983) and Winfrith, UK (e.g. Barr, 1983a, 1983b). The research is concerned with "medium" and "low" velocity impact, for which strain-rate effects are moderate.

A crashing aircraft consists principally of a soft tubular body with some smaller hard or semihard parts. It has been modelled at Winfrith and Meppen by tubular capped steel missiles with added masses, impacting at velocities between 150 and 300 m/s. In general the impact of such missiles produced concertina type crumpling. The axial direction of the impact and the extensive crumpling produced has prompted some one-dimensional empirical-numerical solutions (e.g. Bignon and Riera (1979), Hurley (1983)). These solutions, however, depend heavily on the interpretation of empirical data from crushing loads and strain-rate effects on collapse mechanisms, not providing therefore true general predictions.

The numerical procedures described in this thesis (chapter 4) are suitable for modelling the extensive axisymmetric crumpling produced by the impact of a tubular steel missile against a rigid surface. Such an analysis, corresponding to Winfrith experiment no. M111, is described here.

7.4.1 DESCRIPTION OF PROBLEM

The missile (fig. 7.44) consists of a thin spherical cap followed

makeweight
4.35Kg

V=176m/s

total mass 15Kg

Ø 150 mm

2.5mm   thicker pipe

1.6mm   thinner pipe

85mm

740 mm

625 mm

32mm
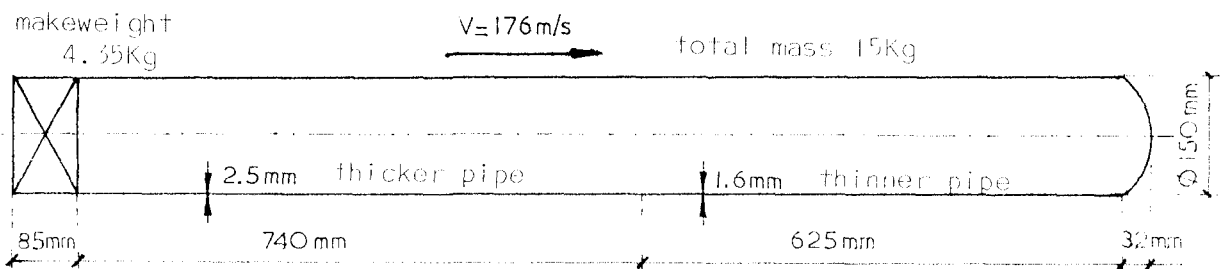
Figure 7.44: Geometry of tubular missile

Node 3890   Cell 5693

Node 400   Cell 5671

Figure 7.45: MESH FOR TUBULAR MISSILE CALCULATIONS (GENERAL VIEW)

by a pipe and, eventually, an end mass. The pipe is composed of two parts, each with a different thickness and slightly different material properties.

The missile was constructed of cold rolled mild steel sheet; apart from this fact, other explicit material data were scarce, being limited to the values of the yield stress and elongation at failure:

thickness	Yield stress	Elongation at failure
1.6 mm	308 MPa	29%
2.5 mm	270 MPa	24%

The missile impacts the target plane normally, with an axial velocity of 176 m/s. The target plane is assumed both rigid and frictionless.

7.4.2 NUMERICAL IDEALIZATION

Because of the axisymmetric character of the problem, MTQC toroidal elements (sect. 4.2.3) can be used to represent the body. The mesh consisted of 3901 nodes and 5771 triangular plane cells (2887 MTQC elements) (figures 7.45 and 7.46). The mesh was prepared using two quadrilaterals through the thickness of the spherical cap. In the tube section, three quadrilaterals through the thickness with approximate shape ratio 2:1 were taken, in order to represent accurately the concertina folding expected. For a small furthermost part of the tube where bending was not expected, the mesh was coarsened to two and one quadrilaterals through the thickness. The makeweight was represented with larger solid elements having the appropriate mass. The target was modelled as a rigid, frictionless stonewall.

The steel material was assumed to have a density of 7800 Kg/m^3, and an elastic-plastic stress-strain behaviour. The elastic part is characterized by a Young's modulus of 210 GPa and a Poisson's ratio of 0.3.

The plasticity was described by a Von Mises Yield surface and an
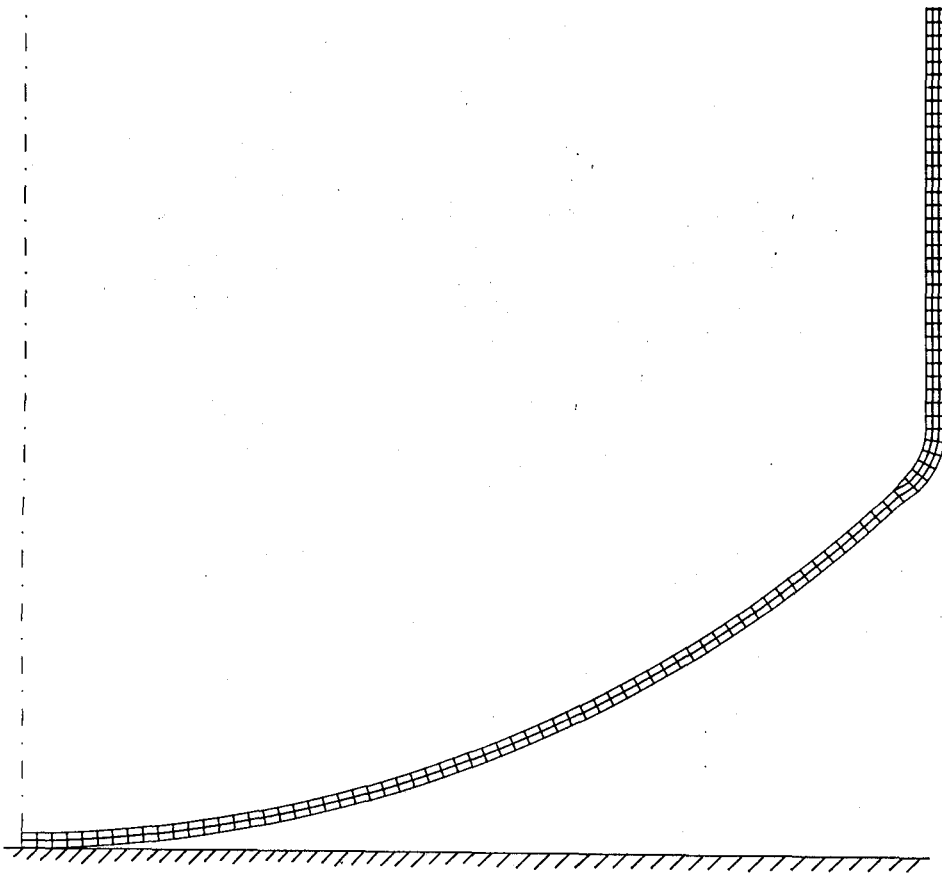
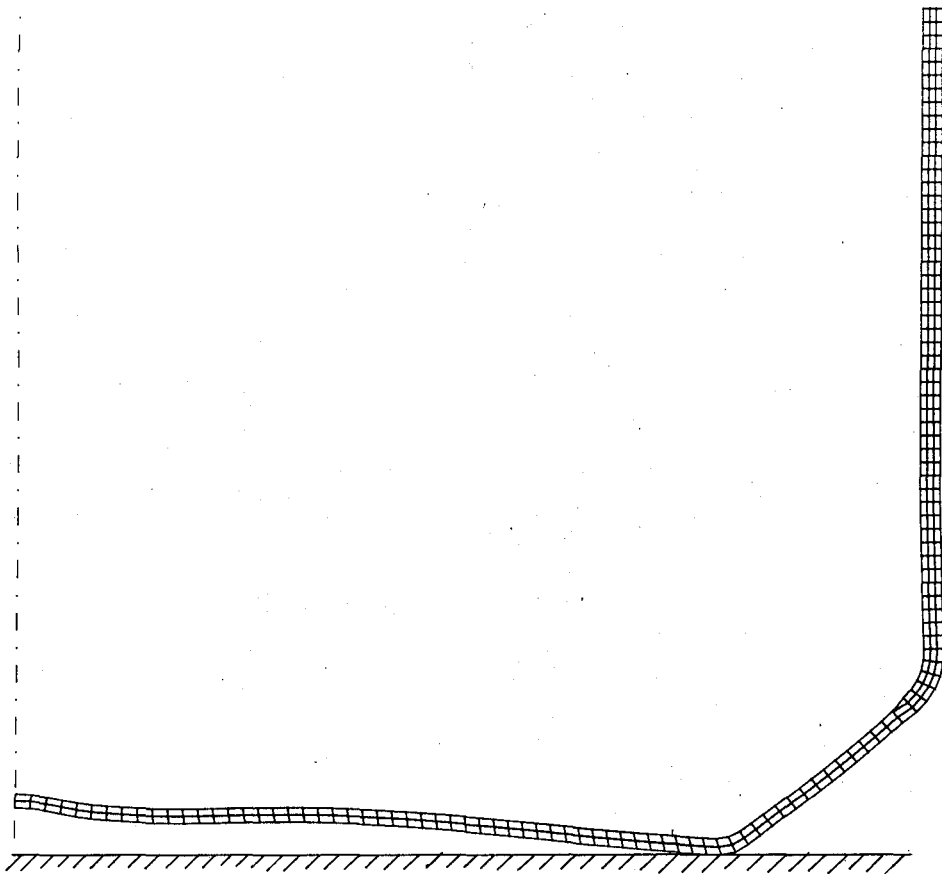Figure 7.46, MESH FOR TUBULAR MISSILE CALCULATIONS (DETAIL OF TIP)

Figure 7.47, TUBULAR MISSILE IMPACT - VIEW OF TIP AT 0.1msec

associative law. However, the radius of the Von Mises cylinder is not constant but changes with plastic strain and with strain-rate. At each time, the effective stress at yield is affected by a power law strain-hardening and a power law correction for strain-rate sensitivity, according to the expression:

$$Y = A\,\epsilon^n(1 + \dot{\epsilon}^m/B)$$

where A and n describe the hardening behaviour

for t_0=1.6mm (thinner pipe) A=495 MPa, n=0.17

for t_0=2.5mm (thicker pipe) A=470 MPa, n=0.17

B and m represent the strain-rate sensitivity

for both cases B=40.4 sec^{-m}, m=0.2

7.4.3 NUMERICAL RESULTS

The analysis was performed on a PRIME 750 computer. It was pursued up to a time of 2.5 msec, being interrupted then because of two reasons:

- the computer costs had become excessive, over 39 CPU days;
- further deformation of the missile would only involve repetition of the concertina folding mechanism already observed; not much additional information would be gained from the continuation of the analysis.

The number of computational cycles was 111336. Successive views of the deformed mesh are presented in figures 7.47 - 7.53 (details of missile tip) and 7.54 (general views). It can be seen that after an initial stage in which the spherical cap buckled inwardly (fig. 7.47), the rest of the deformation consists of the piling up of successive concertina folds (18 in total). All the folds were produced in the thinner tube section, the thicker part not having being reached at the time the analysis was stopped.

The resultant of the contact forces between missile and stonewall is plotted in figure 7.55 as a history of time. The initial part, up to 0.2 msec, corresponds to the buckling of the spherical cap, and is characterized by being very "noisy". The remainder consists of a
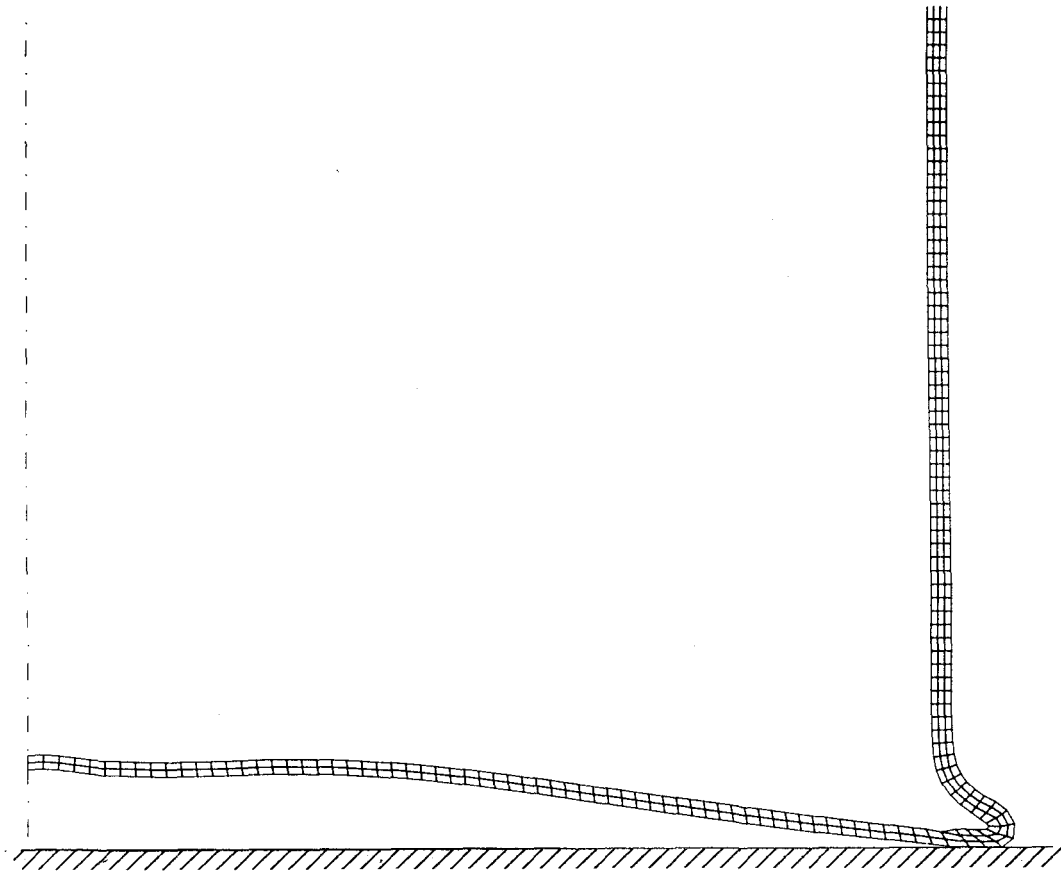
Figure 7.48: TUBULAR MISSILE IMPACT - VIEW OF TIP AT 0.2 msec
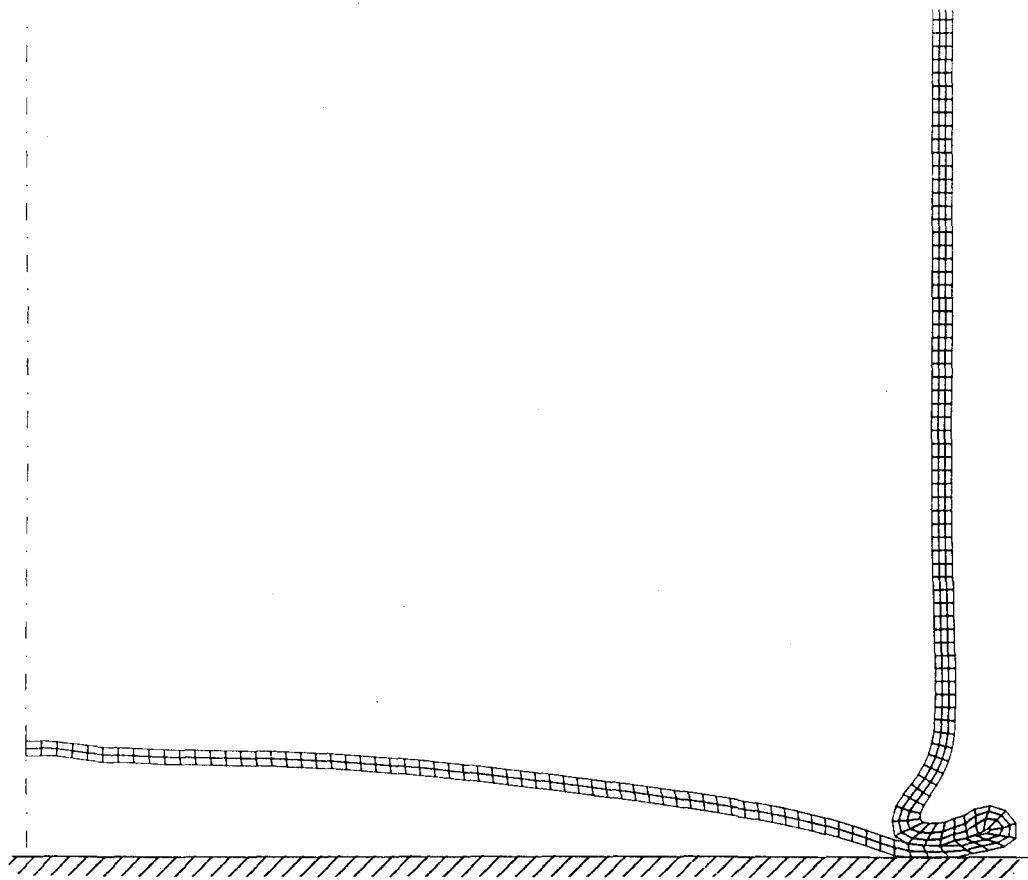
Figure 7.49: TUBULAR MISSILE IMPACT - VIEW OF TIP AT 0.25 msec
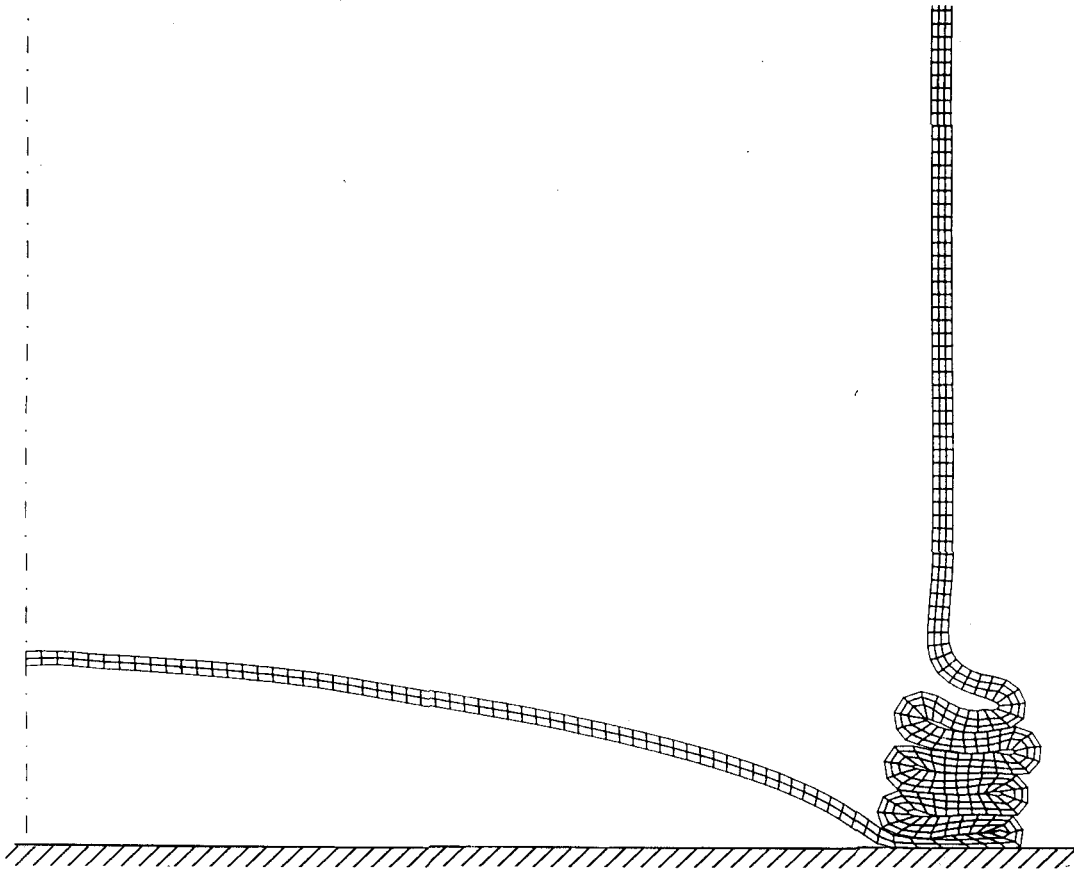
Figure 7.50: TUBULAR MISSILE IMPACT – VIEW OF TIP AT 0.6 msec
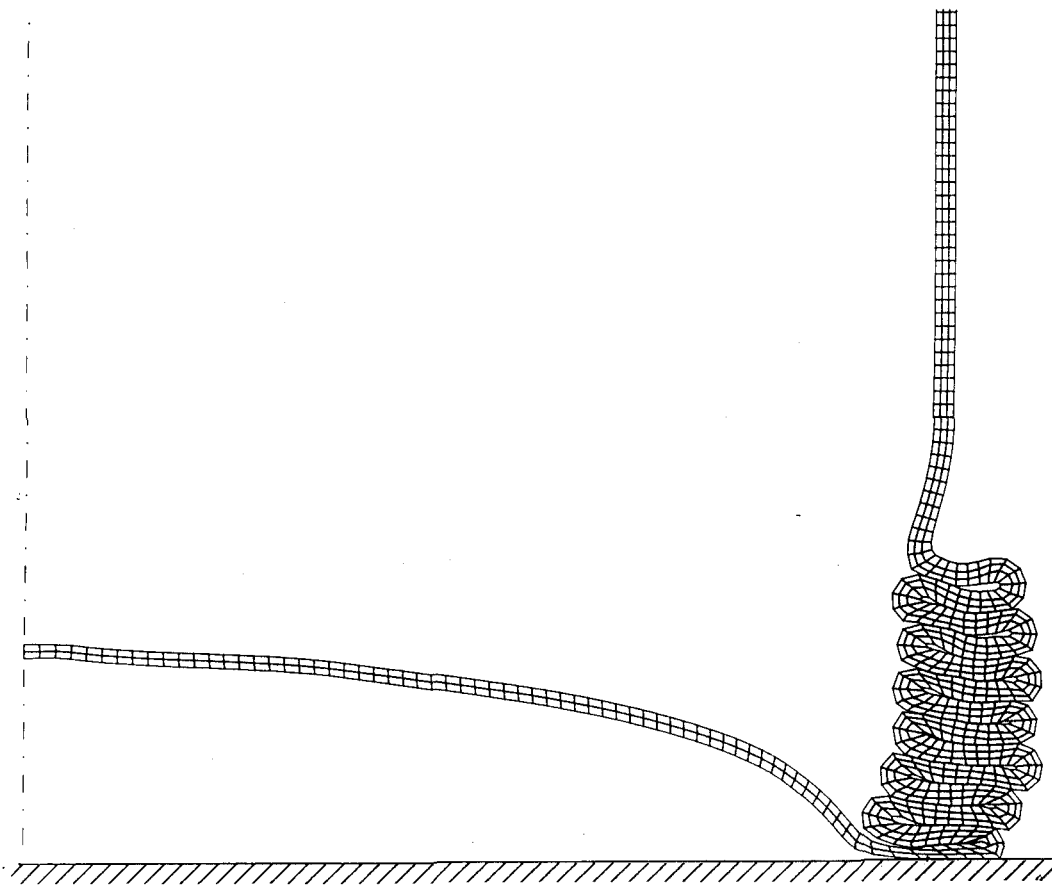
Figure 7.51: TUBULAR MISSILE IMPACT – VIEW OF TIP AT 1.0 msec
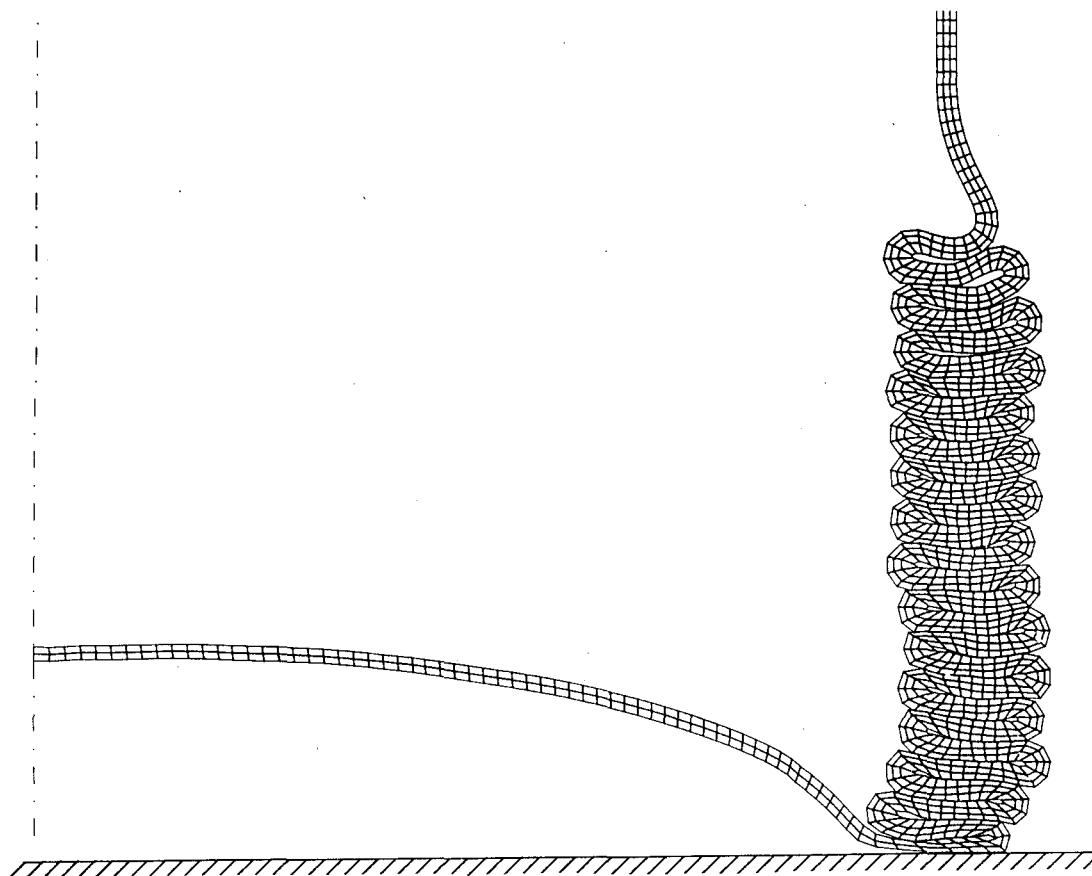
Figure 7.52: TUBULAR MISSILE IMPACT - VIEW OF TIP AT 2.0 msec
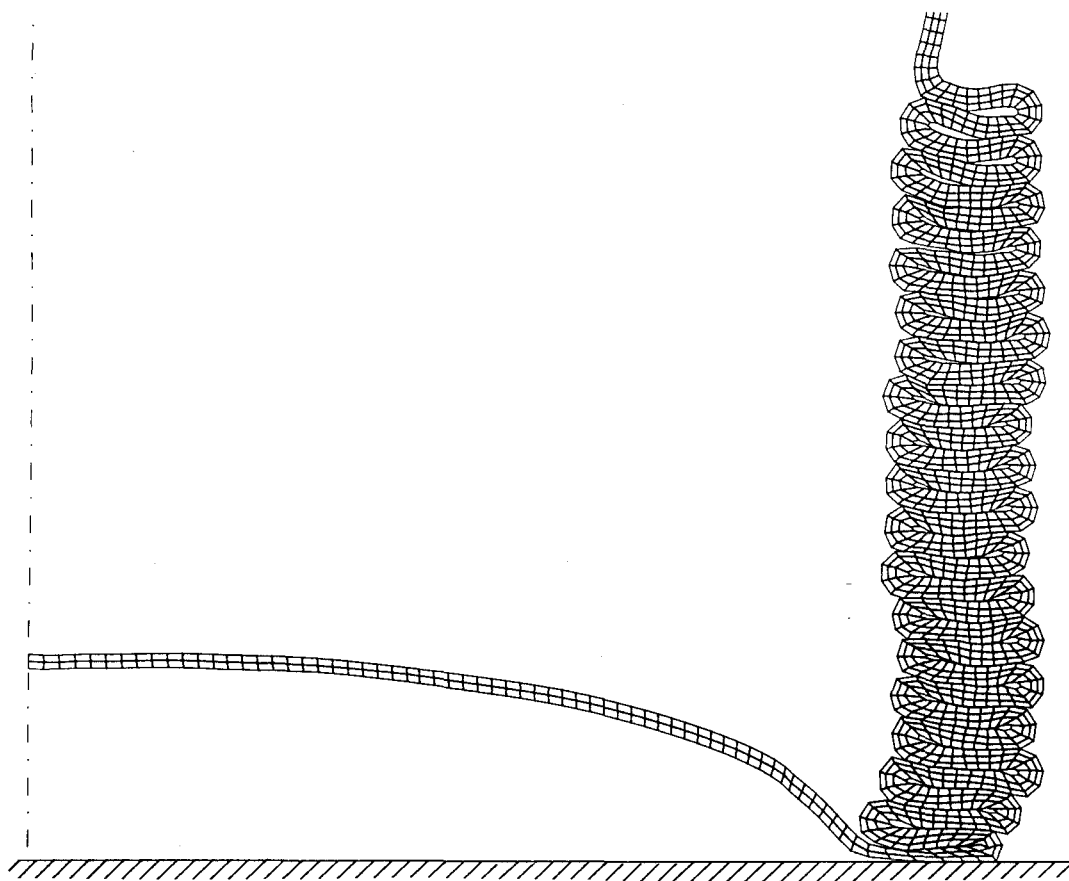
Figure 7.53: TUBULAR MISSILE IMPACT - VIEW OF TIP AT 2.5 msec

t=0.00msec   t=0.20msec   t=1.00msec   t=1.80msec

t=0.04msec   t=0.40msec   t=1.20msec   t=2.00msec

t=0.10msec   t=0.60msec   t=1.40msec   t=2.20msec

t=0.15msec   t=0.80msec   t=1.60msec   t=2.50msec

Figure 7.54: Tubular missile impact - succesive global views
of deformed mesh

Figure 7.55: TUBULAR MISSILE IMPACT – LOAD HISTORY ON TARGET
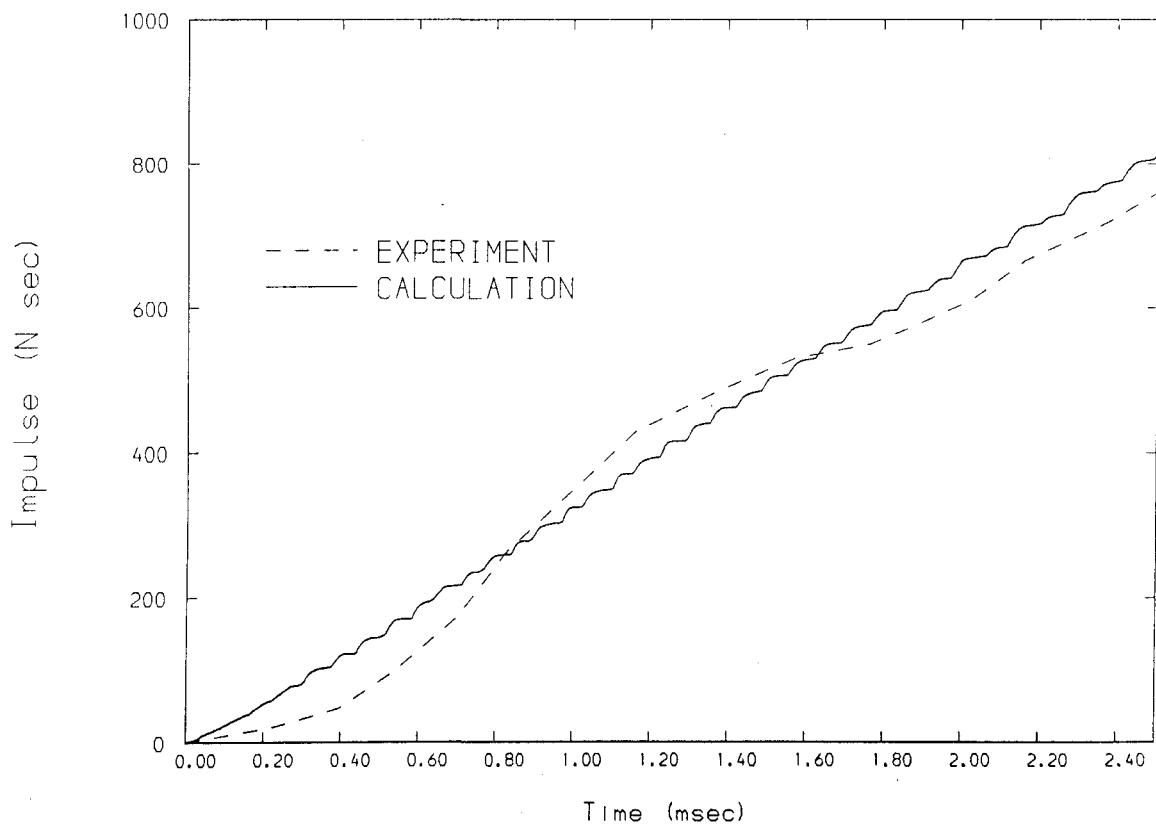
Figure 7.56: TUBULAR MISSILE IMPACT – IMPULSE HISTORY

number of peaks, two per full concertina fold. For each fold two hinges are formed: one external and one internal. The bending in these hinges corresponds to the less stiff periods (valleys), while for the periods in between, the loads are transmitted by the much stiffer axial compression mechanism (peaks).

The force was integrated with respect to time, obtaining the impulse history (figure 7.56). This constitutes a much smoother and nearly linear curve. It indicates a fairly constant collapse force.

Velocity histories are presented in figure 7.57 for two representative points. One corresponds to the back end of the missile, showing an approximately constant average deceleration. The second point corresponds to the folded section, showing an initial stage of slow deceleration followed by a sudden stoppage in the formation of the fold, continuing at zero velocity thereafter.

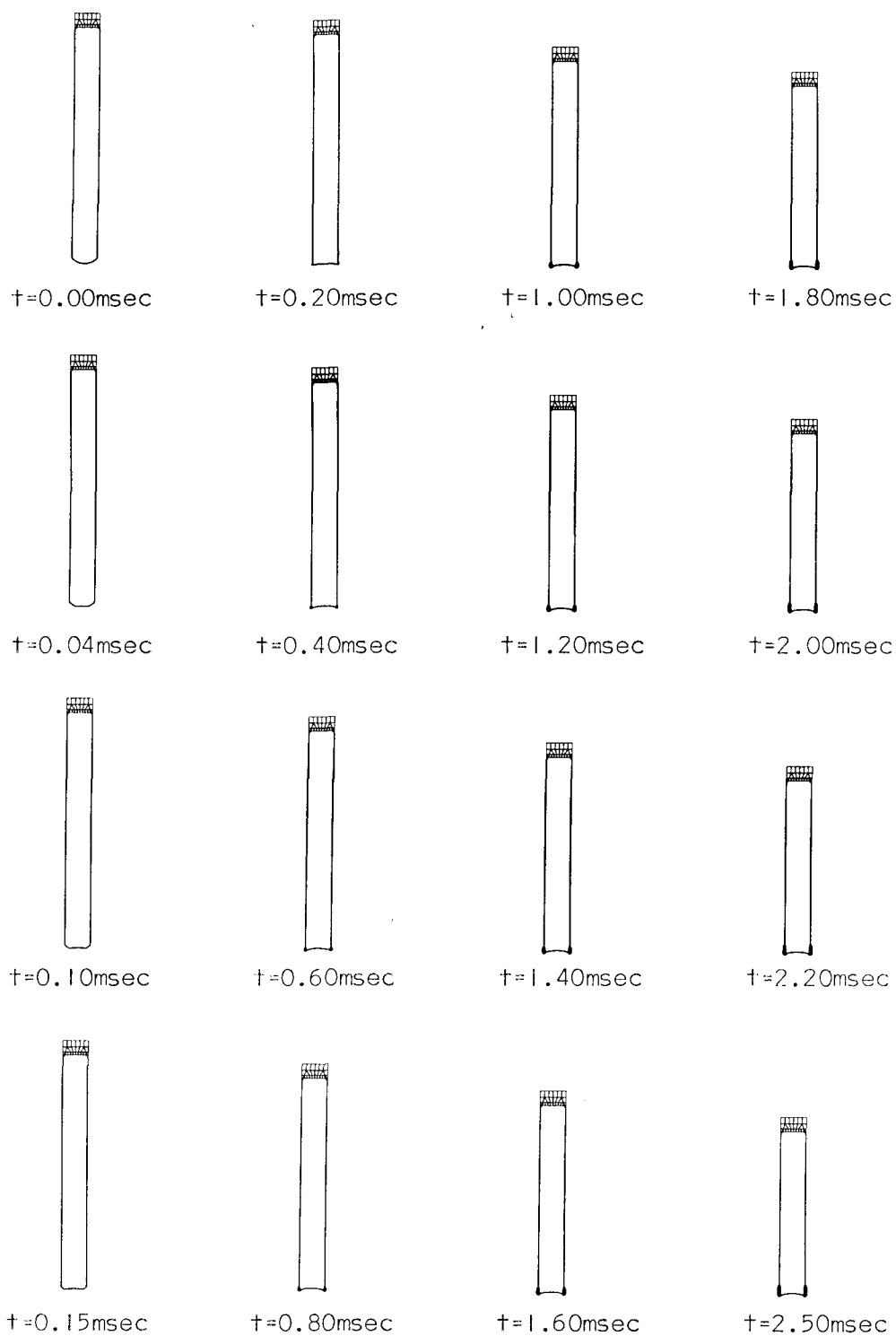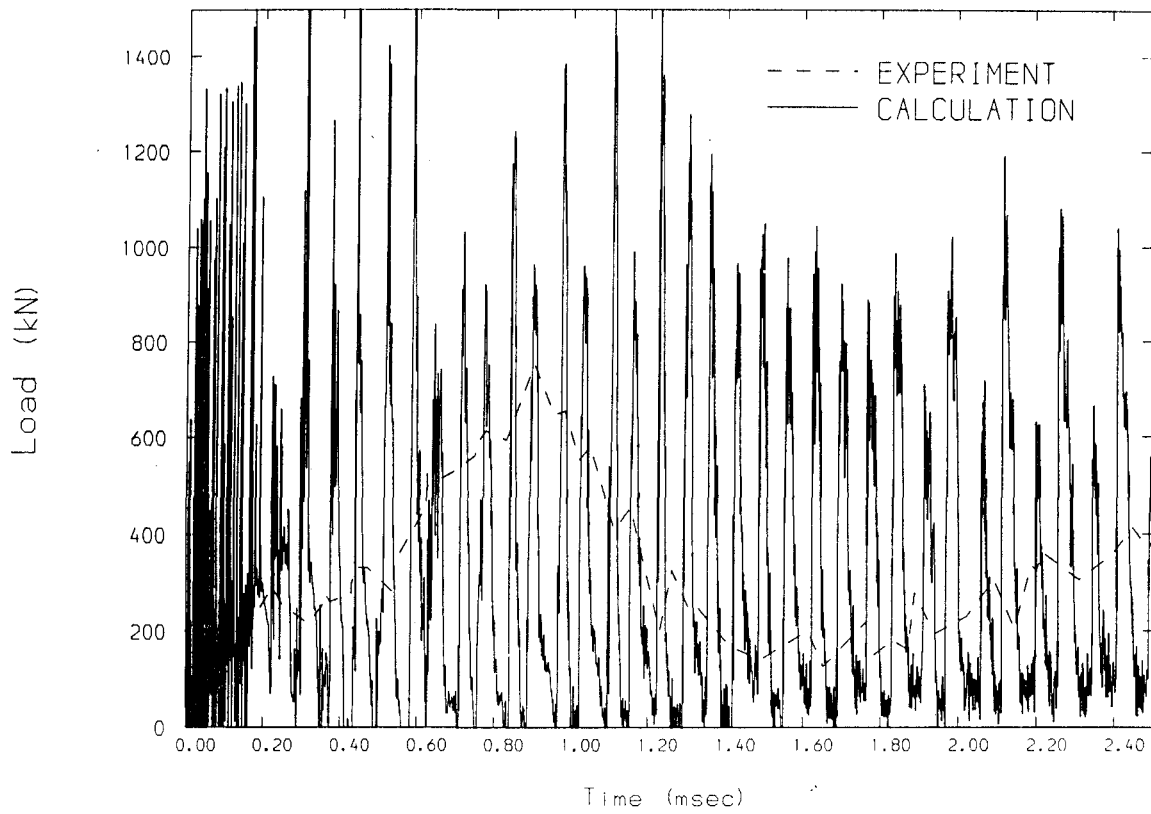Finally, histories of effective stresses are given in figure 7.58 for a point near to the nose which has suffered substantial plastic deformations in the folding, and for another point near the back which has behaved elastically, without reaching yield.

7.4.4 DISCUSSION

The concertina axisymmetric crumpling has been modelled on a large scale without any computational problems (apart from the cost), proving the robustness of the numerical algorithms and computer code. The sequential folding process is apparently very similar to the mechanisms already discussed for quasi-static analysis. However, considerably larger crushing load levels were observed for medium velocity crumpling than for quasi-static situations.

The experiment no. M111 at Winfrith produced 23 folds in the thin section of the tube and 6 further 4-lobed folds in the thicker section, leaving an undistorted tube length of 550 mm; contact time was 9.5 msec (data from Hurley, 1983).

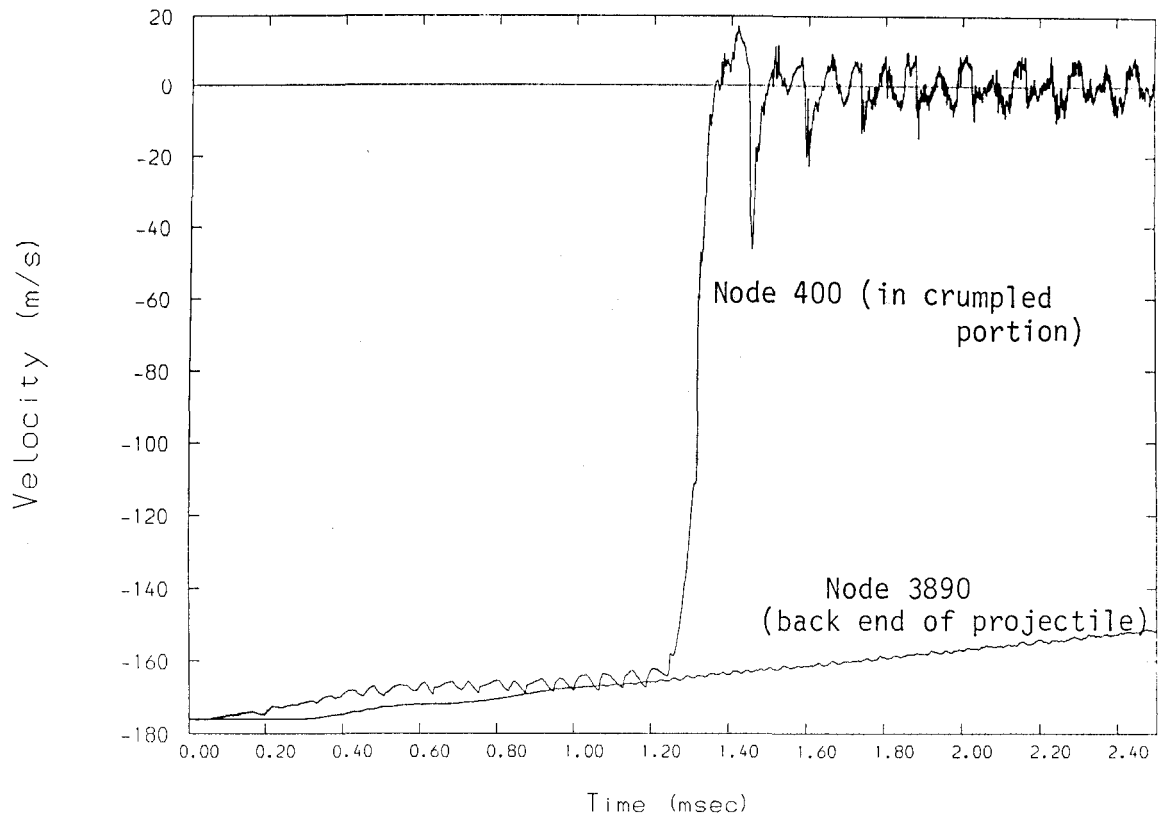The average fold length obtained in the experiment from the

Figure 7.57: TUBULAR MISSILE IMPACT – VELOCITY HISTORIES
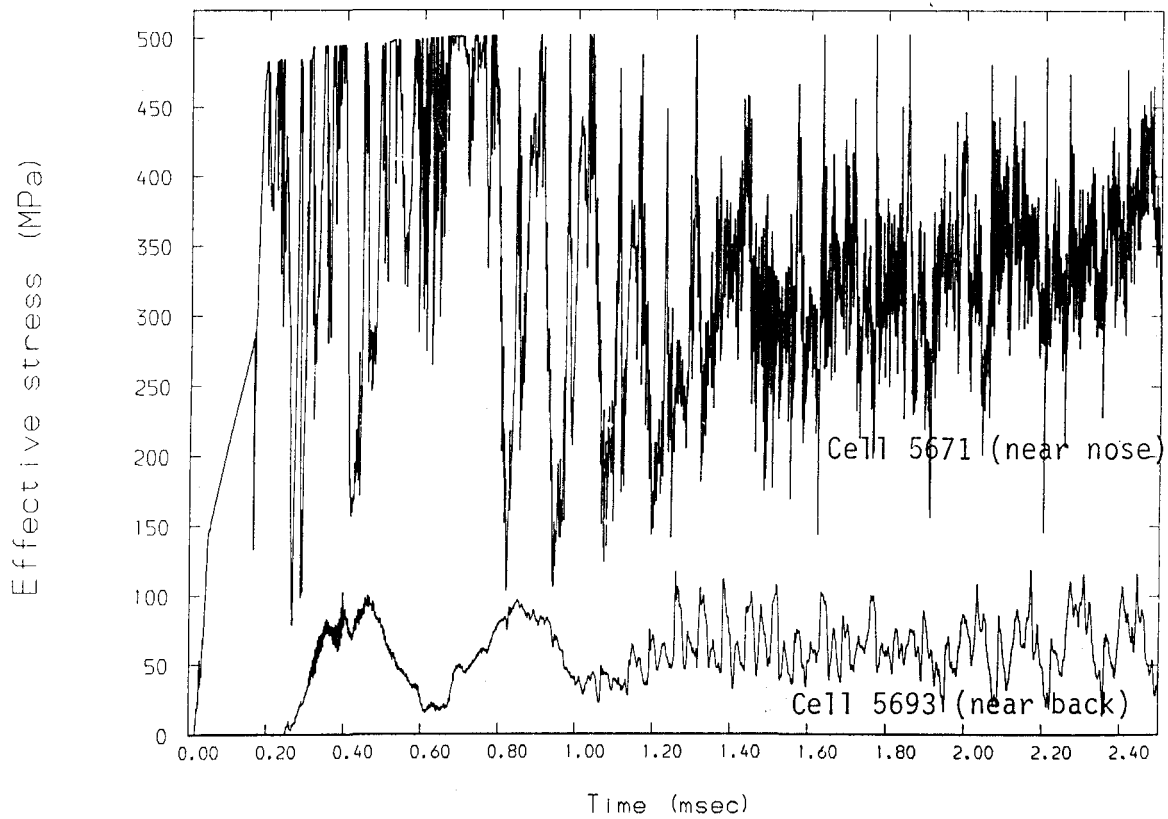
Figure 7.58: TUBULAR MISSILE IMPACT – STRESS HISTORIES

thinner pipe front section was

$$\bar{h}_{exp} = 27.2 \text{ mm}$$

This compares with an average value (based on 18 folds), obtained in the calculations of

$$\bar{h}_{calc} = 25.5 \text{ mm}$$

while the value obtained from equation (7.3) by Alexander (1960) is

$$\bar{h}_{Alex} = 29.3 \text{ mm}$$

Initially it was attempted to solve the problem with a mesh of MTQ elements (sect. 4.2.2). Although these elements worked satisfactorily for low velocity crumpling analyses (section 7.3.4.4), they proved unsuitable for this problem in which the velocity of deformation is substantially greater. Tangling over of the mesh occurred in the formation of the first fold, producing a negative volume in one of the triangular cells on the inner side of the fold (figs. 7.59a, 7.59b). This caused the computations to become unstable immediately (fig. 7.59c).

Previously, similar problems had been often observed when using Mixed Discretization procedures (MTQ in 2-D, MTB in 3-D) for very large deformation analyses, constituting a drawback for these procedures. It was this particular case which motivated the present research to find a corrected element; this element should preserve the capability for modelling incompressible plastic flow of the existing Mixed Discretization elements, but generating a greater resistance to tangling over. The result was the corrected mixed elements (MTQC in 2-D, MTPC in 3-D) presented in section 4.2.3, which have been used for this analysis.

The history of loads obtained from the calculations was substantially "noisier" than the experimental history (figure 7.55). Two factors are the cause for this difference. Firstly the finite rise time for the load-cell used in the experiments will have probably made it miss some of the very fast transients, although unfortunately no
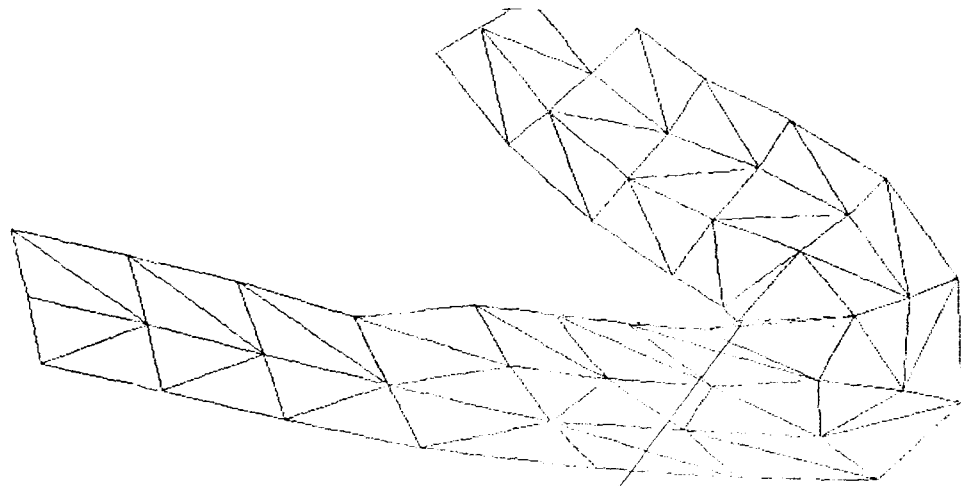
a) just prior to tangling over
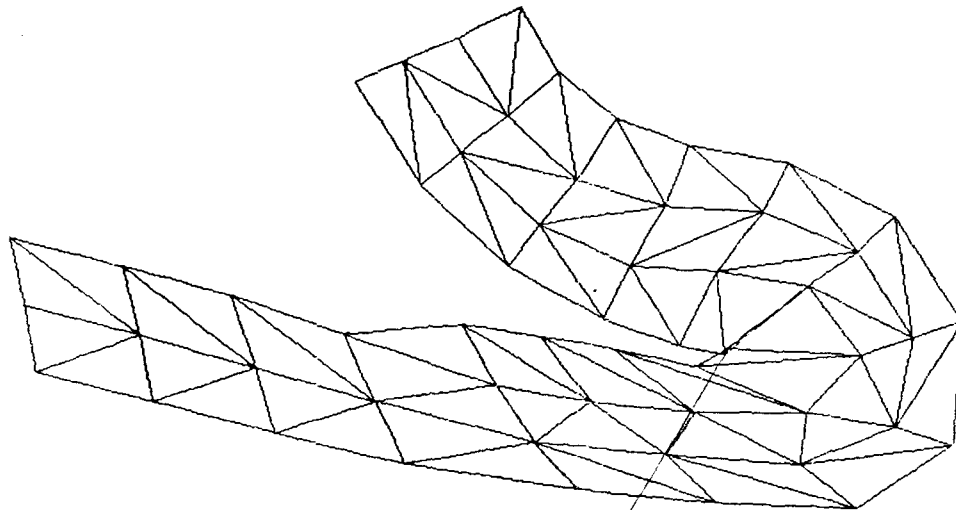
b) just after tangling over
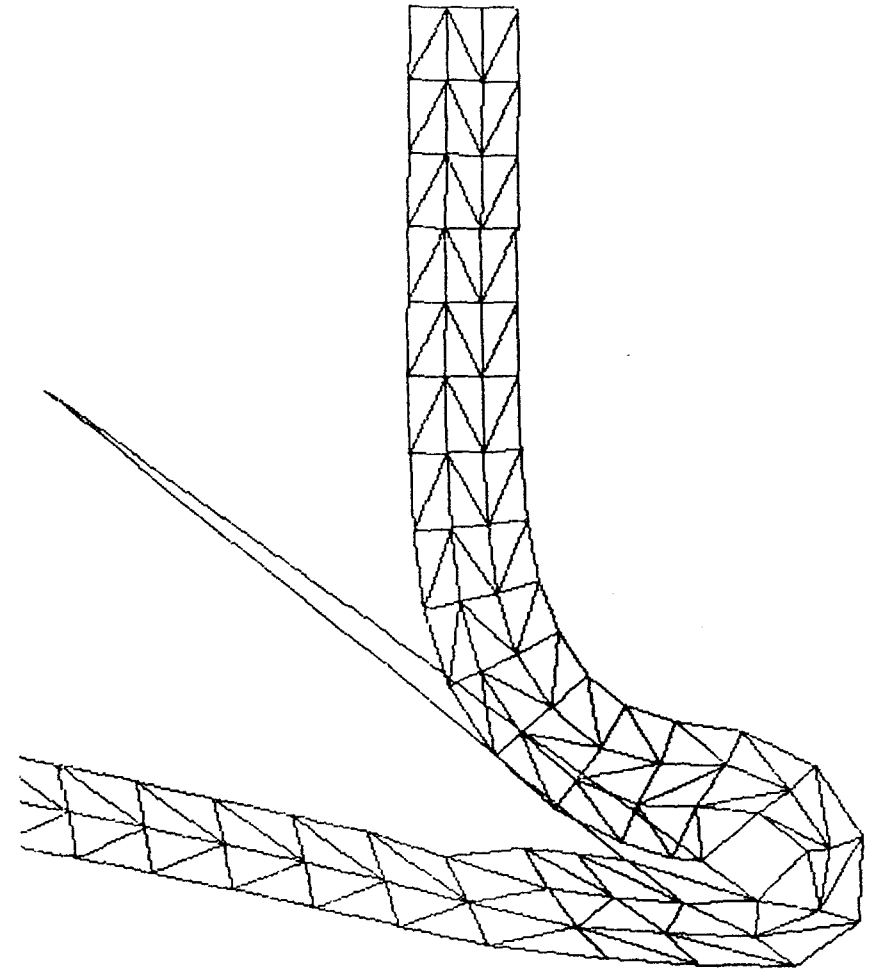
c) ensuing instability

Figure 7.59: Tubular missile impact calculations - tangling over of the mesh with MTQ elements

data are available to quantify this hypothesis. Secondly, the great number of artificial contact springs in the numerical model may have introduced some additional noise into the elastic folded region, which working in a linear non-dissipative regime, is naturally "noisy" on its own.

However, the time-average values of numerical and experimental loads proved to be remarkably close:

$$\bar{P}_{expt} = 338.4 \text{ kN}$$
$$\bar{P}_{calc} = 329.6 \text{ kN}$$

These averages were taken for the period comprised between 0.2 and 2.5 msec, which corresponds to the axisymmetric crumpling of the tube after the initial buckling of the spherical cap.

The dynamic inertia force from the deceleration of the folds was computed according to eqn. (7.8); the velocity v(t) introduced in this equation was the history of velocities at the top node (node 3890, figure 7.57). The time average of this inertia force, again referred to the period 0.2-2.5 msec, was

$$\bar{P}_i = 179.3 \text{ kN}$$

which, substracted from the value of the total force, P=329.6 kN, according to eqn. (7.5) leaves an average crushing force of

$$\bar{P}_c = 150.3 \text{ kN}$$

From these values it is apparent that the dynamic effects were important for this problem, the inertia forces being approximately 1/2 of the overall total forces, and of the same order as the forces originated by the crumpling process itself.

It is not possible to compute precisely the mean crushing force resulting from experiment as no data exist for velocity histories of the missile during the impact. However, the following considerations support the assumption of the experimental and numerical crushing forces being very similar. According to eqn. (7.9) the crushing force,

P_c, may be expressed as the difference between the total force, P, and the inertia force, P_i. It was seen above that the difference between experimental and numerical average total forces was small (2.6%). On the other hand, for the period analyzed, the deceleration has been small (from 176m/s to 152m/s, see fig. 7.57). The close match between numerical and experimental impulse histories (fig. 7.56) suggests that a similarly small deceleration would have happenned in experiment. As the inertia force, P_i, depends on the velocity (eqn. 7.8), it may be presumed that experimental and numerical crushing forces will be similar within an error of approximately 10%.

This "medium" velocity crushing force is considerably larger than that obtained from static tests performed on identical tubes (Hurley, 1983), which yielded a value of

$$P_c^{stat} = 61 \text{ kN}$$

This static value is consistent with the generally good quasi-static load predictions from eqn. (7.2) (Alexander, 1960). Considering an average value of Y = 476 MPa, which corresponds to 0.8 strain,

$$P_c^{Alex} = 71 \text{ kN}$$

Of this difference (150.3kN medium velocity, 61kN quasi-static), the strain-rate material hardening accounts only for a minor part. The strain-rate enhancement may be approximated as follows.

- time for the formation of one complete fold (two hinges):

$$t = (h-2t_0)/v = (27.2-3.2)10^{-3}m/(170m/s) = 1.41 \times 10^{-4} \text{ (sec.)}$$

- average strain-rate:

$$\Delta \epsilon = 2 \times 0.8 = 1.6$$
$$\dot{\epsilon} = \frac{\Delta \epsilon}{\Delta t} = 1.1 \times 10^4 \text{ (sec-1)}$$

- strain-rate enhancement factor:

$$1 + \dot{\epsilon}^m/B = 1+(1.1 \times 10^4)^{0.2}/40.4 = 1.16,$$

which corresponds to an increase of only 16%.

Even allowing for errors in these simplified considerations, the difference between quasi-stastic and medium velocity crushing loads is too large (approx. 100%) to be explained by strain-rate material hardening alone. This result is extremely interesting and suggests an inherently substantially greater energy dissipation for medium velocity tube crumpling, even for rate-insensitive materials. It is all the more notable since externally no apparent differences are appreciated between the crumpled geometries for low and medium velocity impact.

An explanation for this may be found in the pronounced non-linearity of the process. A final geometry which is substantially the same may be arrived at by distinct paths, associated with different amounts of dissipated energy.

7.5 **CONCLUSIONS**

1- Tubes subjected to axial collapse are efficient energy absorbers for impact situations. Experimental knowledge from the bahaviour of Aluminium tubes under quasi-static axial collapse was obtained from tests carried out mainly by Ghani (1982). Microhardness tests in sections of the crumpled tubes allowed the determination of yield stress (Y) distributions around the folds. These distributions were useful as a check of the numerical predictions.

2- The numerical modelling of quasi-static, axisymmetric axial collapse of tubes was approached with the non-linear explicit Finite Difference code (chapter 4). The numerical predictions (load-displacement curves, deformed geometries, stress distributions) compared well with experiment. The numerical code used constitutes a robust solution method for modelling what is a highly complex non-linear process, with very large strains and arbitrary tube-tube and tube-platen contacts. The simple, sound material model employed, based on Von Mises isotropic plasticity (chapter 6), also performed excellently.

3- An explicit (dynamic) solution method was applied successfully for modelling the quasi-static collapse, using velocity scaling in a controlled manner.

4- The numerical model proved sensitive to mesh refinement, specially in short tubes with few folds in the crumpling mechanism, for which end effects are important. An overall tendency for overstiff predictions (fold lengths too large) was detected. Convergence towards experimentally observed behaviour was achieved with mesh refinement.

5- The choice of appropriate elements for the numerical model was essential for successful predictions. CST elements (section 4.2.1) are totally unsuitable. CMTQ elements (section 4.2.3) provided the best results and the most robust meshes.

6- A medium velocity (176m/s) impact of a long tubular projectile, ocassioning large-scale crumpling, was modelled successfully, albeit at a high cost in computer resources. Results compare well with experiment, and indicate substantially greater levels of energy dissipation in the crumpling process than for quasi-static collapse.

CHAPTER 8

CONCLUSIONS AND SUGGESTIONS FOR FURTHER RESEARCH

8.1 CONCLUSIONS

8.2 SUGGESTIONS FOR FURTHER RESEARCH

8.2.1 Theoretical and numerical developments

8.2.2 Additional applications

8.1 __CONCLUSIONS__

1.   Explicit Finite Difference techniques, as used in this work, are advantageous for non-linear, short duration transient analysis (wave propagation type). They can be also useful in slow loading but steeply non-linear problems, in order to take advantage of their robustness and ease of implementation. In general, theoretical solid mechanics concepts and equations can be implemented straightforwardly. Many of the more rigorous stress update procedures necessary for implicit methods need not be used, as time-steps are restricted to very small values for stability. A Lagrangian mesh together with a Cauchy stress - velocity strain formulation are appropriate for low - medium velocity, large strain elastic-plastic problems with contacts.

2.   Meshes based on constant strain triangles or tetrahedra (CST) provide unacceptable results for incompressible plastic flow. Mixed Discretization procedures based on averaging the volumetric strains from several triangles/tetrahedra (Marti and Cundall, 1982) provide accurate predictions and are easily implemented into computer codes; however, tangling over of the mesh can occur in problems with very large distortions. A correction method is proposed here (section 4.2.3) for Mixed Discretization procedures, which maintains their ability for accurate plastic flow modelling, recovering the resistance to tangling over of CST meshes. Hence, a more robust and equally accurate alternative to Mixed Discretization is obtained.

3.   Tension tests are a simple and reliable means for obtaining large strain material stress-strain behaviour (chapter 6). Experimental data, together with some theoretical interpretation and results of numerical simulation tests, allowed a representative constitutive law for Aluminium to be established. A simple Von Mises plasticity model with power law hardening was employed. Results for more complex tube crumpling simulations showed the appropriateness of this material model.

4.   Numerical modelling of tube collapse mechanisms through axisymmetric sequential crumpling was successfully achieved (chapter 7) with the Explicit Finite Difference code developed (chapter 4). The contact algorihtms employed were successful and efficient in modelling

the interface between tube folds and between tube and platens. The resulting load-displacement curves and deformed geometries compare well with experimental data for quasi-static tube collapse. Stress distributions in crumpled tube sections were compared with experimental data derived from microhardness tests, with good results. The influence of some important aspects of the numerical model was ascertained:

- the model behaviour is overstiff (folds too long) if the mesh is not sufficiently refined;

- the choice of appropriate element types (CMTQ, sect. 4.2.3) was essential for efficient and successful modelling;

- The velocity scaling used (within the low velocity regime) allowed modelling of a quasi-static phenomenon with an explicit, dynamic procedure;

- end effects (deformation and folding at tube edges) may have a significant influence in some cases, being difficult to represent appropriately within a larger, global model.

5. Analysis of a steel tube medium velocity (176 m/s) impact (sect. 7.4) provided results which compare well with experimental data. The deformed geometry was similar to the low velocity case, but the crushing force was found to be significantly higher.

6. Computational costs for tube collapse simulations are high, although affordable for specialized safety or impact calculations.

8.2 SUGGESTIONS FOR FURTHER RESEARCH

A number of options are available for researchers interested in the topics dwelt upon in this thesis. Theoretical work along some of the lines suggested below would enhance the applicability of numerical simulation procedures to non-linear processes. Other suggestions involve the use of similar numerical methods as proposed here, widening the field of applications to other non-linear problems.

8.2.1 THEORETICAL AND NUMERICAL DEVELOPMENTS

- The choice of an objective stress rate for large strain analysis is not unique (section 2.5.1). Generally, the use of a particular stress rate is postulated and applied to the existing material data. It would be useful to study the influence of the different choices available, both in theoretical terms and for the practical implications in large strain engineering analyses.

- The material models employed here are restricted to simple Von Mises plastic materials with hardening. This could be extended to more sophisticated material models (sect. 2.2.7) appropriate for metals (distortion of yield surface, yield and failure surfaces), soils (dilatation, non-associativity, non-cylindrical yield surfaces, multiple surface idealizations) or concrete (cracking and failure criteria, non-cylindrical yield surfaces).

- More rigorous alternatives exist to the simple plastic radial return and stress update algorithms employed here (sections 4.5.2, 4.5.4). It would be useful to study the applicability and practical influence of these alternatives within explicit and implicit codes.

- Element by Element methods (Hughes, Levit and Winget (1983b), Ortiz, Pinsky and Taylor (1983)) are promising new alternatives for non-linear transient analysis. The main problem seems to be accuracy, and published applications are restricted to small academic examples. Such algorithms can be implemented without much effort into the architecture of an explicit code, in order to study their behaviour in practical terms for large scale engineering computations.

- For penalty method contact models, further research would be useful in order to increase the robustness and efficiency of the algorithms. This could include adaptative methods for determining contact stiffnesses, and improved search algorithms for automatic detection of contacts.

- Explicit time integration procedures could be used much more efficiently for static or quasi-static problems through the use of adaptative dynamic relaxation techniques (Underwood, 1983). In fact, relaxation techniques are also being proposed lately for use in equation-solving within implicit methods (e.g. Belytschko, 1983). It is possible that a relaxation algorithm could be found that was appropriate both for implicit equation-solving and for explicit dynamic relaxation. This would make possible the highly desirable combination of efficient explicit and implicit solution techniques within the same algorithm and computer code.

8.2.2 ADDITIONAL APPLICATIONS

- The thermomechanical coupling algorithm developed can be readily applied to study coupled phenomena, such as metal forming processes with generation of heat from plastic work and the consequent thermal stresses and material softening.

- Further use can be made of tension tests, coupled with numerical simulations, for more detailed investigations into material behaviour and failure modes in metals, and effects such as the influence of pores and mechanisms for void growth.

- The numerical techniques employed here could also be used for the study of lateral compression of tubes or tube assemblies (sect. 7.2.3.1), tube inversion (sect. 7.2.3.4), or diamond fold collapse (3-D model) (sect. 7.2.3.3).

- The crushing force for medium velocity impact (sect. 7.4) was significantly higher than that expected for low velocity or quasi-static collapse, both from theoretical and experimental results. It would be very interesting to study, experimentally and numerically, the influence of impact velocity on crushing mechanisms, both for rate-insensitive and rate-dependent materials.

REFERENCES

ALEXANDER, J.M. (1960): 'An approximate analysis of the collapse of thin cylindrical shells under axial loading', Quart. J. Mech. Appl. Math., Vol XIII(1), pp 10-15.

AL-HASSANI, S.T.S, JOHNSON, W., and LOWE, W.T. (1972): 'Characteristics of inversion tubes under axial loading', J. Mech. Eng. Sci., Vol 14, pp 370-381.

ANDREWS, K.R.F., ENGLAND, G.L. and GHANI, E. (1983): 'Classification of the axial collapse of cylindrical tubes under quasi-static loading', Int. J. Mech. Sci., Vol 25(9-10), pp 687-696.

ARGYRIS, J.H. and KELSEY, S. (1954): 'Energy thorems and structural analysis', aircraft eng., Oct. 1954.

BARR, P. (1983a): 'Studies of the effects of missile impacts on structures', Atom (UKAEA), Vol 318(April).

BARR, P. (1983b): 'Collapsing steel missile impact on concrete target', private communication, UKAEE Winfrith (UK).

BATHE, K.J., RAMM, E. and WILSON, E.L. (1975): 'Finite Element formulations for large deformation dynamic analysis', Int. J. Numer. Meth. Eng., Vol 9, pp 353-386.

BATHE, K.J. and WILSON, E.L. (1976): 'Numerical methods in Finite Element analysis', Prentice-Hall, New Jersey.

BELYTSCHKO, T. (1978): 'Explicit time-integration of structure-mechanical systems', in 'Advanced Structural Dynamics', J. Donea ed., Applied Science publishers, London, pp 97-122.

BELYTSCHKO, T. (1983): 'An overview of semidiscretization and time integration procedures', in 'Computational methods for transient analysis', eds. T. Belytschko and T.J.R. Hughes, North-Holland, Amsterdam.

BELYTSCHKO, T., HOLMES, N. and MULLEN, R. (1975): 'Explicit integration - stability, solution, properties, cost', in 'Finite Element Analysis of Nonlinear Structural Behaviour', T. Belytschko et al. eds., ASME AMD-Vol 14, N.Y., pp 1-23.

BELYTSCHKO, T. and KENNEDY, J.M. (1978): 'Computer models for subassembly simulation', Nucl. Eng. Design, Vol 49, pp 17-38.

BELYTSCHKO, T. and SCHOEBERLE (1975): 'On the unconditional stability of an implicit algorithm for nonlinear structural dynamics', J. Appl. Mech., Vol 42, pp 865-869.

BELYTSCHKO, T. and TSAY, C.S. (1982): 'WHAMSE - A program for three-dimensional nonlinear structural dynamics', Northwestern U., Ill., rept. NP-2250.

BERTHOLF, L.D. and BENZLEY, S.E. (1968): 'TOODY II - A computer program for two-dimensonal wave propagation', SC-RR-68-41, Sandia Laboratories, Albuquerque, New Mexico.

BIGNON, P. and RIERA, J.D. (1979): 'Verification of methods of analysis for soft missile impact', Informe de laboratorio CT-6/79, Curso de posgraduacao em Engenheria civil, U. Rio Grande do Sul, Brazil.

BILLINGTON, E.W. and TATE, A. (1981): 'The physics of deformation and flow', McGraw-Hill, New York.

BODNER, S.R. and SYMONDS, P.S. (1960): 'Plastic deformation in impact and impulsive loading of beams', in 'Plasticity', E.H. Lee and P.S. Symonds eds., Pergamon press, N.Y., pp 488-500.

BRIDGMAN, P.W. (1944): 'The stress distribution at the neck of a tensile specimen', Trans. Amer. Soc. Metals, Vol 32, pp 553-574.

BRIDGMAN, P.W. (1945): 'Effects of high hydrostatic pressure on the plastic properties of metals', Rev. of Modern Phys., Vol 17(1), pp 3-14.

BRIDGMAN, P.W. (1952): 'Studies in large plastic flow and fracture', McGraw-Hill, New York.

CARSLAW, W.S. and JAEGER, J.C. (1947): 'Conduction of heat in solids', Clarendon press, Oxford.

CHEN, W.H. (1971): 'Necking of a bar', Int. J. Solids & Struct., Vol 7(7), pp 685-717.

CLOUGH, R.W. (1960): 'The finite element in plane stress analysis', Proc. 2nd ASCE Conf. Electronic Computation, Pittsburgh Pa., Sept.

CLOUGH, R.W. and PENZIEN, J. (1975): 'Dynamics of structures', McGraw-Hill, Tokyo.

COTTRELL, A. (1975): 'An introduction to metallurgy, 2nd ed.', Edward Arnold, London.

COURANT, R. (1943): 'Variational methods for the solution of problems of equilibrium and vibrations', Bull. Amer. Math. Soc. 49, pp 1-23.

COURANT, R., FRIEDRICHS, K. and LEWY, H. (1928): 'On the partial differential equations of mathematical physics', Math. Ann., Vol 100, pp 32-74.

CRUSE, T.A. (1969): 'Numerical solutions in three-dimensional elastostatics', Int. J. Solids & Struct., Vol 5, pp 1259-1274.

CUNDALL, P.A. and MARTI, J. (1979): 'Some new developments in discrete numerical methods for dynamic modelling of jointed reck masses', 1979 RETC proceedings, chpt. 84, pp 1466-1484.

CURNIER, A. (1984): 'A theory of friction', Int. J. Solids & Struct., Vol 20(7), pp 637-647.

DAFALIAS, Y.F. (1983): 'Corotational rates for kinematic hardening at large plastic strains', J. Appl. Mech., Vol 50, pp 561-565.

DAVIDENKOV, N.N. and SPIRIDINOVA, N.I. (1946): 'Analysis of the state of stress in the neck of a tension specimen', Proc. Amer. Soc. for testing Mater., Vol 46, pp 1147-1158.

DE ROUVRAY,A., ARNADEAU,F., DUBOIS,J., CHEDMAIL,J.F. and HAUG,E. (1984): 'Numerical techniques and experimental validations for industrial applications', in 'Structural Impact and Crashworthiness', Vol 1, G.A.O. Davies ed., pp 193-242.

DERUNTZ, J.A. and HODGE, P.G. (1963): 'Crushing of a tube between rigid platens', J. Appl. Mech., Vol 30, pp 391-395.

DIETER, G.E. (1976): 'Mechanical Metallurgy, 2nd ed.', McGraw-Hill, New York.

DONEA, J., FASOLI-STELLA, P. and GIULIANI, S. (1977): 'Lagrangian and Eulerian Finite Element techniques for transient fluid-structure interaction problems', Trans. 4th SMIRT conf., paper B1/2, San Francisco, Aug. 1977.

DOSTAL, M., PHELAN, P., and TRBOJEVIC, V.M. (1985): 'Analysis of an accidental drop of LMFBR intermediate heat exchanger', Int. Mtg. on fast breeder reactor safety, Knoxville (Tennessee), Apr. 1985.

DRUCKER, D.C. (1951): 'A more fundamental approach to plastic stress-strain relations', Proc. 1st U.S. Nat. Congress Appl. Mech. (Chicago 1951), pp 487-491.

FLANAGAN, D.P. and BELYTSCHKO, T. (1981a): 'Simultaneous relaxation in structural dynamics', J. Eng. Mech. Div. (ASCE), Vol 107(Dec.),pp 1039-1055.

FLANAGAN, D.P. and BELYTSCHKO, T. (1981b): 'A uniform strain hexahedron and quadrilateral with orthogonal hourglass control', Int. J. Numer. Meth. Eng., Vol 17, pp 679-706.

FUNG, Y.C. (1965): 'Foundations of solid mechanics', Prentice-Hall, New Jersey.

GARCIA, F. (1981): 'Formulacion del metodo de las ecuaciones integrales de contorno en elastoplasticidad tridimensional', Doctoral thesis, ETSI Industriales, U. Politecnica Madrid.

GHANI, E. (1982): 'Static and dynamic collapse behaviour of cylindrical tubes and tube assemblies', Ph.D. Thesis, Dept. Civil Eng. King's Coll., U. of London.

GIULIANI, S. (1982): 'An algorithm for continuous rezoning of the hydrodynamic grid in Arbitrary Lagrangian-Eulerian computer codes', Nucl. Eng. Design, Vol 72, pp 205-212.

GOICOLEA, J.M. (1985a): 'PR2D - An Explicit Finite Difference Non-linear Thermo-mechanical code. User's guide', Dept. of Civil Eng., King's Coll., U. of London, rept. CE-85-01

GOICOLEA, J.M. (1985b): 'PR2DPL - A program for mesh plotting (user's guide)', Dept. Civil Eng., King's Coll., U. of London, rept. CE-85-02.

GOICOLEA, J.M. (1985c): 'CURVA - A program for graph drawing (user's guide)', Dept. Civil Eng., King's Coll., U. of London, rept. CE-85-03.

GOUDREAU, G.L. and HALLQUIST, J.O. (1982): 'Recent developments in large-scale Lagrangian Hydrocode technology', Comp. Meth. Appl. Mech. & Eng., Vol 33, pp 725-757.

GREEN, E.H. and NAGHDI, P.M. (1965): 'A general theory of an elastic-plastic continuum', Arch. Rat. Mech. Anal. 18.

GUIST, L.R. and MARBLE, D.P. (1966): 'Prediction of the inversion load of a circular tube', US NASA technical note TN D-3622.

HALLQUIST, J.O. (1979): 'NIKE2D: An implicit, finite deformation Finite Element code for analyzing the static and dynamic response of two-dimensional solids', Lawrence Livermore laboratory, U. of California, rept. UCRL-52678.

HALLQUIST, J.O. (1982a): 'User's manual for DYNA2D', Lawrence Livermore laboratory, U. of California, rept. UCID-18756.

HALLQUIST, J.O. (1982b): 'Theoretical manual for DYNA2D', Lawrence Livermore laboratory, U. of California, rept. UCID-19401.

HALLQUIST, J.O. (1982c): 'DYNA3D user's manual (nonlinear dynamic analysis of solids in three dimensions)', Lawrence Livermore laboratory, U. of California, rept. UCID-19592.

HALLQUIST, J.O., WERNE, R.W. and WILKINS, M.L. (1977): discussion to "High-velocity impact calculations in three dimensions" by G.R. Johnson (1977), J. Appl. Mech., Vol 99(4), pp 793-794.

HANCOCK, S.L. (1976): 'Finite Difference equations for PISCES-2DELK', Physics International company report TCAM-76-2

HERNALSTEEN, P. and LEBLOIS, L.C. (1976): 'The use of energy absorbers to protect structures against impact loading', Nucl. Eng. Design, Vol 37, pp 373-406.

HERRMANN, W. and BERTHOLF, L.D. (1983): 'Explicit Lagrangian Finite Difference methods', in 'Computational Methods for Transient Analysis', T. Belytschko and T.J.R. Hughes eds., North-Holland, Amsterdam.

HIBBIT, H.D., MARCAL, P.V. and RICE, J.R. (1970): 'A Finite Element formulation for problems of large strains and displacements', Int. J. Solids & Struct., Vol 6, pp 1069-1086.

HILL, R. (1950): 'The mathematical theory of plasticity', Clarendon press, Oxford.

HIRT, C.W., AMSDEN, A.A. and COOK, J.L. (1974): 'An Arbitrary Lagrangian-Eulerian computing method for all flow speeds', J. comput. phys., Vol 14, p 227.

HUGHES, T.J.R. (1983): 'Analysis of transient algorithms with particular reference to stability behaviour', in 'Computational methods for transient analysis', eds. T. Belytschko and T.J.R. Hughes, North-Holland, Amsterdam.

HUGHES, T.J.R., LEVIT, I. and WINGET, J. (1983a): 'Element-By-Element implicit algorithms for heat conduction', J. Eng. Mech. ASCE, Vol 109(2), pp 576-585.

HUGHES, T.J.R., LEVIT, I. and WINGET, J. (1983b): 'An Element-By-Element solution algorithm for problems of structural and solid mechanics', Comp. Meth. Appl. Mech. & Eng., Vol 36, pp 241-254.

HUGHES, T.J.R. and WINGET, J. (1980): 'Finite rotation effects in numerical integration of rate constitutive equations arising in large deformation analysis', Int. J. Numer. Meth. Eng., Vol 15(12), pp 1862-1867.

HURLEY, S. (1983): 'Dynamic crushing loads of thin-walled steel tubes', UKAEE Winfrith, private communication.

JOHNSON, G.R. (1976): 'Analysis of elastic-plastic impact involving severe distortions', J. Appl. Mech., Vol 98(3), pp 439-444.

JOHNSON, G.R. (1977): 'High-velocity impact calculations in three dimensions', J. Appl. Mech., Vol 99(1), pp 95-100.

JOHNSON, G.R. (1981): 'Recent developments and analyses associated with the .EPIC-2 and EPIC-3 codes', in '1981 advances in aerospace Struct. and Mater.', S.I. Wang and W.J. Renton eds., winter mtg. ASME, Washington D.C., Nov 1981, pp 142-147.

JOHNSON, W. (1972): 'Impact strength of materials', Arnold, London.

JOHNSON, W. and REID, S.R. (1978): 'Metallic energy dissipating systems', Appl. Mech. Rev., Vol 31(3), pp 277-288.

JOHNSON, W., REID, S.R. and REDDY, T.Y. (1977): 'The compression of crossed layers of thin tubes', Int. J. Mech. Sci., Vol 19, pp 423-437.

JOHNSON, W., REID, S.R. and SINGH, L.B. (1975): 'Experimental study of the rolling torus load delimiter', Int. J. Mech. Sci., Vol 17, pp 603-615.

JOHNSON, W., SODEN, P.D. and AL-HASSANI, S.T.S (1977): 'Inextensional collapse of thin-walled tubes under axial compression', J. Strain Anal., Vol 12(4), pp 317-330.

JONES, S.E., GILLIS, P.P. and SHALABY, A.H. (1979): 'Stress distributions in the vicinity of a neck', J. Appl. Phys., Vol 50(5), pp 3168-3173.

KALSI, G.S. and MARTI, J. (1985): 'Three-dimensional rezoning of Lagrangian meshes in elasto-plastic thermally coupled problems', to appear in Comp. Meth. Appl. Mech. & Eng.

KAPLAN, M.A. (1973): 'The stress and deformation in mild steel during axisymmetric necking', J. Appl. Mech., Vol 40, pp 271-276.

KEY, S.W. (1969): 'A variational principle for incompressible and early-incompressible anisotropic elasticity', Int. J. Solids & Struct., Vol 5, pp 951-964.

KEY, S.W. (1974): 'HONDO - A Finite Element computer program for the large deformation dynamic response of axisymmetric solids', Sandia Nat. laboratories, Albuquerque N.M., rept. 74-0039.

KEY, S.W. (1978): 'Transient response by time integration: review of implicit and explicit operators', in 'Advanced Structural Dynamics', J. Donea ed., Applied Science publishers, London, pp 15-41.

KOLSKY, H. (1953): 'Stress waves in solids', Clarendon press, Oxford.

KOSLOFF, D. and FRAZIER, G.A. (1978): 'Treatment of hourglass patterns in low order Finite Element codes', Int. J. Numer. Anal. Meth. Geomech., Vol 2, pp 57-72.

KRIEG, R.D. (1975): 'A practical two-surface plastic theory', J. Appl. Mech., Vol 97(E3), pp 641-646

KRIEG, R.D. and KEY, S.W. (1973): 'Transient shell response by numerical time integration', Int. J. Num. Meth. Eng., Vol 7, pp 273-286.

KRIEG, R.D. and KEY, S.W. (1976): 'Implementation of a time-independent plasticity theory into structural computer programs', in 'Constitutive equations in viscoplasticity', J.A. Stricklin and K.J. Saczalski eds., ASME winter mtg., New York, Dec. 1976.

KUKKOLA, T. (1976): 'Energy absorbers used against impact loading', Nucl. Eng. & Design, Vol 37, pp 407-412.

KUNAR, R. and MINOWA, N. (1981): 'A comparison between Finite Element and Finite Difference explicit formulations for triangular and quadrilateral plane strain elements', Int. J. Num. Anal. Meth. Geomech., Vol 5(2), pp 217-224.

LANDON, J.W. and QUINNEY, H. (1923): 'Experiments with the Hopkinson pressure bar', Proc. Royal Soc., A103, p622.

LEE, E.H. (1969): 'Elastic-plastic deformation at finite strains', J. Appl. Mech., Vol 36, pp 1-6.

LEE, E.H. and MALLETT, R.L. (1983): 'Stress analysis for anisotropic hardening in finite-deformation plasticity', J. Appl. Mech., Vol 50, pp 554-560.

LICHNEROWICZ, A. (1958): 'Elements de calcul tensoriel', Lib. Armand Colin, Paris.

McFARLAND, R.K. (1963): 'Hexagonal cell structures under postbuckling axial load', AIAA Journal, Vol 1(6), pp 1380-1385.

MAENCHEN, G. and SACK, S. (1964): 'The TENSOR code', in 'Methods of Computational Physics', B. Alder et al. eds., Academic press, New York, pp 181-210.

MALVERN, L.E. (1969): 'Introduction to the mechanics of a continuous medium', Prentice-Hall, New Jersey.

MAMALIS, A.G. and JOHNSON, W. (1983): 'The quasi-static crumpling of thin-walled circular cylinders and frustra under axial compression', Int. J. Mech. Sci., Vol 25, p 713.

MAMALIS, A.G., JOHNSON, W. and VIEGELAHN, G.L. (1984): 'The crumpling of steel thin-walled tubes under axial compression at elevated strain rates: some experimental results', Int. J. Mech. Sci., Vol 26(11-12), pp 537-547.

MARSDEN, J.E. and HUGHES, T.J.R. (1978): 'Topics in the mathematical foundations of elasticity', in 'Non-linear analysis and mechanics: Heriot-Watt symposium', Vol II, ed. R.J. Knops, Pitman, London.

MARSDEN, J.E. and HUGHES, T.J.R. (1983): 'Mathematical foundations of elasticity', Prentice-Hall, New York.

MARTI, J. (1981): 'PR3D - Theoretical basis (version 1P-1)', Principia Mechanica Ltd., London, rept. PR-TN-6.

MARTI, J. (1983): 'PR3D - Programmer's guide', Principia Mechanica Ltd., rept. PR-TN-4.32.

MARTI, J. and CUNDALL, P.A. (1980): 'Constitutive laws for dynamic modelling of soils', report to USAF weapons laboratory, Dames and Moore, London.

MARTI, J. and CUNDALL, P.A. (1982): 'Mixed Discretization procedure for accurate modelling of plastic collapse', Int. J. Numer. Anal. Meth. Geomech., Vol 6(1), pp 129-139.

MARTI, J., GOICOLEA, J.M., KALSI, G.S. and MACEY, G.E. (1984): 'Transient thermomechanical analysis with explicit schemes', in 'Numer. Meth. for Transient and Coupled Problems', R.W. Lewis et al. eds., Pineridge press, Swansea, UK.

MARTI, J., KALSI, G.S. and LAST, N. (1984): 'Three-dimensional calculations of missile impact', in 'Structural Impact and Crashworthiness', J.Morton ed., Vol 2, pp 310-319.

MROZ, Z. (1967): 'On the description of anisotropic work-hardening', J. Mech. and Phys. Solids, Vol 15, pp 163-175.

MROZ, Z. (1972): 'A description of work hardening of metals with application to variable loading', Proc. Int. Symp. on foundations of plasticity, A. Sawczuk ed., Noordhoff international.

MULLEN, R.L. and BELYTSCHKO, T. (1983): 'An analysis of an unconditionally stable explicit method', Computers & Structures, Vol 16, pp 691-696.

NADAI, A. (1946): discussion to 'Analysis of the state of stress in the neck of a tension specimen' by N.N. Davidenkov and N.I. Spiridinova (1946), Proc. Amer. Soc. for testing Mater., Vol 46, pp 1175-1178.

NAGTEGAAL, J.C. and DEJONG, J.E. (1981): 'Some computational aspects of elastic-plastic large strain analysis', Int. J. Numer. Meth. Eng., Vol 17, pp 15-41.

NAGTEGAAL, J.C. and DEJONG, J.E. (1982): 'Some aspects of non isotropic work hardening in finite strain plasticity', in 'Plasticity of metals at finite strain: theory, experiment and computation', E.H. Lee and R.L. Mallett eds., Div. Appl. Mech., Stanford U., California.

NAGTEGAAL, J.C., PARKS, D.M. and RICE, J.R. (1974): 'On numerically accurate Finite Element solutions in the fully plastic range', Comp. Meth. Appl. Mech. & Eng., Vol 4, pp 153-177.

NEEDLEMAN, A. (1972): 'A numerical study of necking in circular cylindrical bars', J. Mech. & Phys. Solids, Vol 20(2), pp 111-127.

NEMAT-NASSER, S. (1982): 'On finite deformation elasto-plasticity', Int. J. Solids & Struct., Vol 18(10), pp 857-872.

NEWMARK, N.M. (1959): 'A method of computation for structural dynamics', J. Eng. Mech. Division ASCE, Vol 85(EM3), pp 67-94.

NICHOLS, B.D., HIRT, C.W., and HOTCHKISS, R.S. (1980): 'SOLA-VOF: A solution Algorithm for transient fluid flow with multiple free boundaries', Los Alamos scientific laboratory, U. of California, rept. LA-8355.

NOH, W.F. (1964): 'CEL: A time-dependent, two-space dimensional, coupled Eulerian-Lagrange code', in 'Methods of Computational Physics', Vol 3, B. Alder et al. eds.,Academic press, New York, pp 117-179.

NORRIS, D.M., MORAN, B., SCUDDER, J.K., and QUINONES, D.F. (1978): 'A computer simulation of the tension test', J. Mech. & Phys. Solids, Vol 26, pp 1-19.

ORTIZ, M., PINSKY, P.M. and TAYLOR, R.L. (1983): 'Unconditionally stable Element-By-Element algorithms for dynamic problems', Comp. Meth. Appl. Mech. & Eng., Vol 36, pp 223-239.

ORTIZ, M. and POPOV, E.P. (1983): 'Distortional hardening rules for metal plasticity', J. Eng. Mech. (ASCE), Vol 109(4), pp 1042-1057.

ORTIZ, M. and SIMO, J.C. (1985): 'An analysis of a new class of integration algorithms for elasto-plastic constitutive relations', to appear in.Int. J. Numer. Meth. Eng.

OSIAS, J.R. and SWEDLOW, J.L. (1974): 'Finite elasto-plastic deformation-I; theory and numerical examples', Int. J. Solids & Struct., Vol 10, pp 321-339.

OWEN, D.R.J. and HINTON, E. (1980): 'Finite Elements in plasticity: theory and practice', Pineridge press, Swansea (UK).

PARK, K.C. (1982): 'An improved semi-implicit method for structural dynamic analysis', J. Appl. Mech., Vol 49(3), pp 589-593.

PERZYNA, P. (1963): 'The constitutive equqtions for rate sensitive plastic materials', Quart. Appl. Math., Vol 20, pp 321-332.

PINSKY, P.M., ORTIZ, M. and PISTER, K.S. (1983): 'Numerical integration of rate constitutive equations in finite deformation analysis', Comp. Meth. Appl. Mech. & Eng., Vol 40, pp 137-158.

PRAGER, W. (1956): 'A new method of analyzing stress and strain in work-hardening plastic solids', J. Appl. Mech., Vol 23, pp 493-496.

PRAGER, W. (1961): 'Introduction to the mechanics of continua', Ginn and company, Boston.

PRANDTL, L. (1920): 'Ueber die Haerte plasticher Koerper', Goettinger Nachr., Math.-Phys. Kl. 1920, pp 74-85.

PRANDTL, L. (1924): 'Spannungsverteilung in plastichen Koerpern', Proc. 1 Int. Congr. Appl. Mech. (Delft,1924), pp 43-54.

PREVOST, J.H. (1978): 'Plasticity theory for soil stress-strain behaviour', J. Eng. Mech. (ASCE), Vol 104(EM5), pp 1177-1194.

PRINCIPIA MECHANICA LTD. (1984): 'PRISM - User's quide (version 1C-2)', Principia Mechanica Ltd. (London), rept. PR-TN-29.11.

PRINCIPIA MECHANICA LTD. (1983): 'Impact analysis of the W.V.P. glass container', Principia Mechanica Ltd. (London), repts. 205-83, 217-83, 221-83.

PUGSLEY, A. and MACAULAY, M. (1960): 'The large-scale crumpling of thin cylindrical columns', Quart. J. Mech. Appl. Math., Vol XIII(1), pp 1-9.

REID, S.R. and REDDY, T. (1978): 'Effect of strain hardening on the lateral compression of tubes between rigid plates', Int. J. Solids & Struct., Vol 14, pp 213-225.

REUSS, E. (1930): 'Beruecksichtingung der elastichen Formaenderungen in der plastizitatstheorie', Zeits. Angew. Math. Mech. 10, pp 266-274.

RICHTMEYER, D. and MORTON, K.W. (1967): 'Difference methods for initial value problems (2nd ed.)', Interscience, New York.

RIZZO, F.J. (1967): 'An integral equation approach to boundary value problems of classical elastostatics', Quart. Appl. Math., Vol 25(1), pp 83-95.

RUBINSTEIN, R. and ATLURI, S.N. (1983): 'Objectivity of incremental constitutive relations over finite time-steps in computational finite deformation processes', Comp. Meth. Appl. Mech. and Eng., Vol 36, pp 277-290.

RUDIGGER, E. and RIECH, H. (1983): 'Experimental and theoretical investigations on the impact of deformable missiles onto reinforced concrete slabs', 7th SMIRT Conf. (Chicago Aug. 1983), paper J8/3.

SCHOFIELD, A.H. and WROTH, C.P. (1968): 'Critical state soil mechanics', McGraw-Hill.

SCHREURS, P. (1983): 'Numerical simulation of forming processes; The use of Arbitrary Lagrangian-Eulerian (AEL) formulation and the Finite Element method', Doctoral thesis, Technische Hogeschool Eindhoven, Netherlands.

SHRIVE, N.G., ANDREWS, K.R.F. and ENGLAND, G.L. (1984): 'The impact energy dissipation of cylindrical systems', in 'Structural Impact and Crashworthiness', Vol 2, J. Morton ed., pp 544-554.

SIMO, J.C. and ORTIZ, M. (1985): 'A unified approach to finite deformation elasto-plastic analysis based on the use of Hyperelastic constitutive equations', to appear in Comp. Meth. Appl. Mech. & Eng.

SOUTHWELL, R.V. (1940): 'Relaxation methods in theoretical physics', Oxford University press.

THOMAS, S.G., REID, S.R. and JOHNSON, W. (1976): 'Large deformations of thin-walled circular tubes under transversal loading', Int. J. Mech. Sci., Vol 18, pp 325-333.

THORNTON, P.H. and MAGEE, C.L. (1977): 'The interplay of geometric and material variables in energy absorption', J. Eng. Mater. and Tech. (transactions ASME), Vol 99(April), pp 114-120.

TRUESDELL, C. and TOUPIN, P.A. (1960): 'The classical field theories', in 'Handbuch der Physik', S. Flugge (ed.), Vol III(1), pp 226-858, Springer-Verlag, Berlin

TRUJILLO, D.H. (1972): 'An unconditionally stable explicit algorithm for structural dynamics', Int. J. Numer. Meth. Eng., Vol 11, pp 1579-1592.

TRUJILLO, D.H. (1975): 'An unconditionally stable explicit algorithm for Finite Element heat conduction analysis', Nucl. Eng. & Design, Vol 32, pp 110-120.

UNDERWOOD, P. (1983): 'Dynamic relaxation', in 'Computational Methods for Transient Analysis', T. Belytschko and T.J.R. Hughes eds., North-Holland, Amsterdam, pp 245-266.

VON MISES, R. (1913): 'Mechanik der festen Koerper im plastich deformablen Zustand', Goettinger Nachr., math-phys. Kl. 1913, pp 582-592.

WILKINS, M.L. (1964): 'Calculation of Elastic-plastic flow', in 'Methods of Computational Physics', Vol 3, B. Alder et al. eds., Academic press, New York, pp 211-263.

WILKINS, M.L. (1968): 'Third progress report of light armour program', Lawrence Livermore laboratory, U. of California, rept. UCRL-50460.

WILKINS, M.L. (1969): 'Calculation of Elastic-plastic flow', Lawrence Livermore laboratory, U. of California, rept. UCRL-7322.

WILKINS, M.L. (1978): 'Mechanics of penetration and perforation', Int. J. Eng. Sci., Vol 16, pp 793-807.

WILKINS, M.L., BLUM, R.E., CRONSHAGEN, E. and GRANTHAM, P. (1975): 'A method for computer simulation of problems is solid mechanics and gas dynamics in three dimensions and time', Lawrence Livermore Laboratory, U. of California, rept. UCRL-51574.

WILKINS, M.L. and GUINAN, M.W. (1973): 'Impact of cylinders on a rigid boundary', J. Appl. Phys., Vol 44(3), pp 1200-1206.

WILKINS, M.L., STREIT, R.D., and REAUGH, J.E. (1980): 'Cumulative strain-damage model of ductile fracture: simulation and prediction of engineering fracture tests', Lawrence Livermore laboratory, U. of California, rept. UCRL-53058.

YAGHMAI, S. and POPOV, E.P. (1971): 'Incremental analysis of large deflections of shells of revolution', Int. J. Solids & Struct., Vol 7, pp 1375-1393.

ZIEGLER, H. (1959): 'A modification to Prager's hardening rule', Quart. Appl. Math. 17, pp. 55-65.

ZIENKIEWICZ, O.C. (1977): 'The Finite Element method (3rd edition)', McGraw-Hill, Berkshire (UK).